

Sea Level Change in the Arctic Ocean

Quantifying Contributions to Present-Day Arctic Ocean Sea Level Change

PhD Thesis

Carsten Ankjær Ludwigsen



Sea Level Change in the Arctic Ocean

Quantifying Contributions to Present-Day Arctic Ocean Sea Level Change

PhD Thesis

September, 2020

By

Carsten Ankjær Ludwigsen

caanlu@space.dtu.dk

Supervision:

Prof. Ole Baltazar Andersen, DTU Space

Prof. Shfaqat Abbas Khan, DTU Space, (co-supervisor)

Copyright: Reproduction of this publication in whole or in part must include the customary bibliographic citation, including author attribution, report title, etc.

Cover photo: Rawpixel Ltd, 2018

Published by: DTU, Department of Geodesy and Earth Observation, Elektrovej, Building 328, 2800 Kgs. Lyngby Denmark
www.space.dtu.dk

Resumé

Det Arktiske Hav ligger i den region der oplever Jordens hurtigste temperaturstigninger og er samtidig det mest utilgængelige hav i verden. Afsmeltning af is, øget ferskvand og havopvarmning påvirker havniveauet i Arktisk og dens indflydelse på den globale oceancirkulation. Satellitmålinger af havniveau i Arktis er besværliggjort af varierende havis og store ismasseændringer på land. Denne ph.d.-afhandling har til formål at kvantificere de enkelte bidrag til havniveauændringer i Arktis og derved øge forståelsen af klimapåvirkningerne, samt validere fjernmålte havniveauændringer i det Arktiske Hav.

Radar altimetri har observeret havniveauændringer i Arktis siden 1991, men havisdækket reducerer antallet af observationer betydeligt. Altimetrimålinger bliver yderligere forværret af udfordringer ved at adskille yngre havis og smeltesøer oven på is fra sprækker mellem havis og åbent hav, med store lokale variationer imellem metoder til følge. Ocean masseændringer observeret af GRACE-satellitterne siden 2002 er påvirket af store massetab på land, som overskygger de mindre masseændringer i havet. Selvom forskellige procedurer er brugt til at separere ændringer på land fra dem i havet, varierer masseændringer imellem 2 til 15 mm per år i det indre Arktis. Ændringer i havniveauet forårsaget af ændringer i salinitet (halosterisk) og havtemperatur (termosterisk) er ofte estimeret fra forskellen mellem GRACE og altimetri, hvilket er en tvivlsom metode taget i betragtning af hvor tvetydige satellitprodukterne er.

I dette studie bruges en ny metode til at skabe et satellituafhængigt steriske havniveauprodukt, kaldet *DTU Steric*. Fra over 300.000 målte temperatur- og salinitetsprofiler dannes et arktisk temperatur og salinitets grid, som bruges til at beregne de steriske ændringer. Produktet viser at øget ferskvand i det Arktiske Hav giver tydelige havniveaustigninger ved den vestrussiske kyst (10-20 mm per år) og i Beauforthavet (10-15 mm per år). Opvarmning af havet giver en mere ensartet og svagere havniveaustigning (1-5 mm per år) i det meste af det Arktiske Hav, hvor koldere vand i den østrussiske del af Arktis giver et havniveaufald (2-4 mm per år).

Ved at kombinere *DTU Steric* og GRACE-'mascons' fra NASA JPL, opnås en god korrelation ($R = 0,61-0,76$) med altimetrimålinger. Store forskelle er dog især tydelige langs den russiske kyst. For at kunne validere resultaterne med tidevandsmålinger, kræver det nøjagtige estimer af vertikale landændringer (VLM). Især i Arktis, hvor VLM fra den forhistoriske isafsmeltning (GIA) og elastisk VLM fra ændringer i nutidens ismasser (PDIL), giver betydelig VLM som påvirker tidevandsmålerne. Ved at anvende en ismodel i høj opløsning fra 1995-2015 skabes en dynamisk elastisk VLM-model som dækker hele Arktis. Den målte VLM ved 54 GNSS-lokationer nord for 50 °N er forklaret ved at kombinere elastisk VLM med GIA. VLM-modellen viser, at elastisk VLM fra PDIL er betydelig selv i områder langt væk fra ismasser. I Danmark laver PDIL en landhævning på $\sim 0,5$ mm per år, hvilket modvirker havniveaustigningerne fra smeltende iskapper betydeligt.

Ved at anvende både *DTU Steric* og VLM-modellen vurderes havniveauændringer fra 1995-2015 målt fra altimetri og ved tolv VLM-korrigerede arktiske tidevandsmålere. I stedet for GRACE, bruges modellerede geoideændringer fra PDIL og GIA, samt et dynamisk massebidrag fra en oceanografisk model som estimat for massbidraget i Arktis. For 11 af 12 tidevandsmålere og for 98 % af det Arktiske Hav er havniveauændringerne forklaret indenfor usikkerheden (1σ). Usikkerhed forbundet med det dynamiske massebidrag og med de steriske havniveauændringer i områder med dårlig hydrografisk datadækning mindsker præcisionen. Ved at indrage seneste og kommende satellitmissioner kan valideringen af de præsenterede resultater forbedres betydeligt.

Abstract

The Arctic Ocean is in the region with the fastest warming on Earth and is also the most inaccessible ocean in the world. Deglaciation of ice, ocean freshening, ocean warming changes the Arctic Ocean sea level and the relation to the global ocean circulation. Satellite measurements of Arctic sea level is challenged by varying sea ice and large ice mass changes on land. This PhD-thesis aims to quantify each of the contributions to sea level change in the Arctic Ocean and thereby improve the comprehension of the effects of climate change and validate sea level observations from remote sensing on the Arctic Ocean.

Radar altimeters have observed sea level changes in the Arctic since 1991, but the sea ice cover significantly limits the observations. Challenges of separating younger sea ice and meltponds on top of ice from leads between sea ice floes and open ocean furthermore exacerbates altimetric observations, resulting in large discrepancies among products. Mass changes observed by the GRACE-satellites since 2002 are affected by large deglaciation on land that overshadows smaller changes in the ocean. Even though different procedures for separating changes on land and in ocean estimates of mass changes vary between 2 and 15 mm y^{-1} in the interior Arctic. To estimate sea level anomalies caused by changes in ocean salinity (halosteric) and temperature (thermosteric), studies often rely on the difference between GRACE and altimetry, which is an arguable approach considering the large ambiguity of the satellite products.

In this study, an original approach is taken to create a satellite independent steric sea level product, called *DTU Steric*. From over 300k temperature and salinity profiles is a Arctic temperature and salinity grid compiled, which is used to compute steric changes. The product shows increased freshwater in the Arctic Ocean gives a significant sea level rise at the west coast of the Russian Arctic (10-20 mm y^{-1}) and in the Beaufort Sea (10-15 mm y^{-1}). Ocean warming causes a more uniform and smaller sea level rise (1-5 mm y^{-1}) in most of the Arctic Ocean, while cooler water results in sea level fall in the east Russian Arctic (2 - 4 mm y^{-1}).

By combining *DTU Steric* and GRACE mascons from NASA JPL, good correlation ($R=0.61-0.76$) is reached with altimetric observations. Large discrepancies are however in particular evident along the Russian Arctic. To validate the results with tide gauges along the coast requires accurate estimates of vertical land movement (VLM). In particular in the Arctic, where glacial isostatic adjustment (GIA) from prehistoric deglaciation and elastic VLM from changes in present-day ice loading (PDIL), creates significant VLM that affects tide gauges. By applying a high-resolution ice model from 1995-2015, a dynamic Arctic-wide elastic VLM-model is created. The measured VLM at 54 GNSS-sites north of 50°N is explained by the elastic VLM-model with GIA. The model shows, that the elastic VLM from PDIL is non-negligible in regions far away from glaciated areas. In Denmark creates PDIL an uplift of ~ 0.5 mm y^{-1} , which is significantly mitigating the associated barystatic sea level rise.

Utilizing both *DTU Steric* and the VLM-product, are sea level trends from 1995-2015 from altimetry and at twelve VLM-corrected Arctic tide gauges assessed. Instead of GRACE, the modeled geoid changes from PDIL and GIA and dynamic mass changes from an oceanographic model are used as estimate for the mass component. For 11 of 12 tide gauges and 98% of Arctic Ocean is the sea level trend explained within the standard error (1σ). Uncertainties associated with the dynamic mass contribution and the steric height sin areas with poor hydrographic data coverage attenuates the precision. By applying latest and upcoming satellite-missions can significantly improve the validation of the results presented.

Preface

This thesis is submitted in fulfillment of the requirements for obtaining a PhD degree at DTU Space, National Space Institute, Technical University of Denmark. The research was carried out under the supervision of Professor Ole Baltazar Andersen and co-supervised by Professor Shfaqat Abbas Khan from DTU Space.

My research was funded by the EC Horizon 2020-project, Integrated Arctic Observation System (INTAROS), Grant Agreement no. 727890. In the third half year of my PhD, I was lead-author of the INTAROS report to deliverable 2.1, *Report on present observing capacities and gaps: ocean and sea ice observing system*, available at intaros.nersc.no.

During my research I got the opportunity to attend several conferences. I presented posters at EGU (2018, 2020), AGU (2018, 2019), Living Planet Symposium (2019), GRACE-FO Science Team Meeting (2019) and had a oral talk at Ocean Surface Topography Science Team (OSTST, Chicago, 2019). Planned oral presentations at ISAR-6 (Tokyo, 2020) and ESA CryoSat-2 workshop (Taormina, 2020) were canceled due to COVID-19. In September 2019, I gave an invited lecture at the Arctic PhD-Summer School in St. Petersburg.

From September 2018 to February 2019, I had my external research stay at CU Boulder with Shijie Zhong (Department of Physics) and Steve Nerem (Colorado Center for Astrodynamics Research). The plan was to utilize Shijie's GIA-modeling for different 3D-earth models, but computational challenges lead to a change to CCAR, where Steve Nerem invited me to become part of his group.

Included in this PhD Thesis are three journal papers (one in press, one accepted, one submitted (as the of status September 15, 2020), which lays out the research conducted during my PhD. Furthermore have I developed two Arctic products relevant for Arctic Ocean sea level research; a steric sea level product (DTU Steric) based on interpolated temperature and salinity profiles and a high resolution Arctic vertical land movement (VLM) product, which includes a high resolution model for glacial elevation change.

Carsten Ankjær Ludwigsen
September, 2020

Publications list

1. Ludwigsen, C. A., & Andersen, O. B. (Accepted/In press). Contributions to Arctic sea level from 2003 to 2015. *Advances in space research*. <https://doi.org/10.1016/j.asr.2019.12.027>
2. Ludwigsen, C. A., Khan, S. A., Andersen, O. B. & Marzeion, B. (Accepted). Vertical Land Motion from present-day deglaciation in the wider Arctic. *Geophysical Research Letters*.
3. Ludwigsen, C. A., Andersen, O. B. & Rose, S. K. (submitted). Assessment of 21 years of Arctic Ocean Sea Level Trends (1995-2015). *Ocean Science*.

Acknowledgements

During my PhD-program have I gotten unvaluable help from numerous resources. Most and foremost the largest thanks goes to my supervisor Ole B. Andersen, who gave me the opportunity to write my PhD-thesis with him. I would not have been able to accomplish this work without Ole's continuous assistance, encouragement and support. I have enjoyed the talks and discussions we have had during the last 3 years and in particular the time we have spent together on the numerous trips around Europe and in the United States.

Huge thanks to my co-supervisor, Abbas Khan, who was always available for discussions on glacial and solid earth dynamics. I particular appreciate his encouragements during the research and writing of the second paper.

During my visit at CU Boulder, I am thankful to Shijie Zhong for inviting me to come to Boulder. Although the plans changed and I moved to the group of Steve Nerem, the discussions we had on GIA-models really helped improve my understanding of the computational requirements. Special thanks to Steve Nerem and his group for including me in his great group of PhD-students. It was a really fruitful period of my PhD and I benefited a lot from our sea level discussions in the group.

Thanks to all the colleagues at the GEO-department at DTU Space and to the lunch club for reminding that lunch and coffee breaks are important. Special thanks to Stine Kildegaard Rose and Heidi Villadsen for taking the time to give feedback on the manuscript.

Most importantly I thank my wife, Marie. While I was finishing my PhD, she has taken the lion's share and carried our son. Her love and support means everything.

To my son, I am looking forward to finally meet you.

List of Figures

1.1	Schematic picture of the most important processes of Arctic Amplification. Direct processes are shown with orange arrows, remote processes are purple and inter-seasonal processes are indicated with orange/black arrows. Courtesy of Nature Climate Change, Cohen et al. (2020).	1
1.2	Left: Change of Greenland Ice Sheet as measured by GRACE from May 2002 to Aug 2016 from NASA Jet Propulsion Laboratory (2020). Right: March and September Sea ice concentration trend from 1979-2018 based on satellite images (Stroeve and Notz, 2018).	2
1.3	Sea level change from 1993 to 2019 as measured by satellite altimeters from NOAA (https://star.nesdis.noaa.gov/socd/lisa/SeaLevelRise).	3
1.4	Left: Map of the Arctic Ocean with named areas which are used throughout this thesis. Map is adapted from James et al. (2016). Bathymetry is from IBCAO3.0 (Jakobsson et al., 2012). Right: Map of the main surface currents in the Arctic domain and connections to the adjoining oceans. Map is taken from Arctic Monitoring and Assessment Programme (AMAP) report 1998 (AMAP, 1998), site: https://www.amap.no/documents/doc/surface-ocean-currents-in-the-arctic/566	4
1.5	Left: Leading pressure pattern of Arctic Oscillation Index from NOAA Climate Prediction Center. Right: Arctic Oscillation index since 1980. Monthly data from NOAA.	5
2.1	Matrix of relative sea level measurements (in meters) from 127 tide gauges from PSMSL since 1980, sorted from most east (top) to most west (bottom). White spots indicate where there is no data or to few measurements to make a meaningful annual mean.	8
2.2	Left: Map of the 127 tide gauges with data since 1980. The color indicates how many years since 1980 have valid data. Right: Chart showing the decline of tide-gauges since 1980. The drop from 2018 to 2019 is due to that the annual value for some tide-gauges have not yet been validated by PSMSL.	9
2.3	Location of active ARGO floats on 4th July 2020. From the Argo Program website (argo.ucsd.edu).	9
2.4	Left: Ocean temperature (C°) within at max 5m depth for all hydrographic data available since 1990 used for the DTU Steric product. Right: Same as left, but with salinity (psu).	10
2.5	Illustration of the principles of satellite altimetry. Both figures from www.altimetry.info	11

2.6	Left: Idealized illustration of the Brown waveform. Right: Real example of a waveform from Envisat, with power on y-axis and number of bins on the x-axis. Both figures from altimetry.info.	11
2.7	Left: Principle of SAR-operating mode of CryoSat-2 from Raney (2012). Right: CryoSat-2 operating mode masks in the Arctic from Quartly et al. (2019).	12
2.8	Example of waveforms (normalized) from open ocean, sea ice and a lead for (P)LRM and SAR-mode of Sentinel-3A. PLRM means 'pseudo Low Resolution Mode', which is SAR waveforms (Sentinel-3A operates only in SAR-mode) degraded to LRM. From Quartly et al. (2019), with image courtesy of Benjamin Loveday, Plymouth Marine Laboratory.	13
2.9	Left: Temporal extent of all altimeters covering the Arctic. The color indicates the type of altimeter attached to the satellite. (Adaptated from Quartly et al. (2019)) Right: Maximum latitude reached by satellite missions. Blue (66°N) indicates max latitude by th Jason/Topex/Poseidon-mission (sometimes refered to as reference missions), dark orange (81°N) for Sentinel-3A/B, green (81.5°N) for ERS-1/2, Envisat and SARAL, purple (86°N) for IceSat and orange (88°N) for CryoSat-2 and IceSat-2.	14
2.10	1991-2018 sea level trend (mm y^{-1}) based on altimetric observations from ERS-1, ERS-2, Envisat and CryoSat-2 from Rose et al. (2019). ERS-1 is processed with the ESA REAPER-retracker and ERS-2 and Envisat data are processed with the ALES+ retracker (Passaro et al., 2018), while CryoSat-2 is processed with the DTU LARS-retracker and RADS (Scharroo et al., 2013).	14
2.11	Vertical velocity at GNSS stations included in the ULR-6A product (Santamaría-Gómez et al., 2017a). Stations with insufficient data or that are highly non-linear are shown as blank circles. Figure is adapted from Santamaría-Gómez et al. (2017a).	16
2.12	1992-2018 trend ECCOr4v4 (Fukumori et al., 2019; Forget et al., 2015) [mm y^{-1}] for thermosteric height, halosteric height, OBP and SSH. Thermosteric and halosteric heights are derived products computed from ocean temperature and salinity grids in ECCOr4v4.	17
3.1	Maximum reached pressure (bar) for the T/S profiles included in this work (1 bar \approx 1 m depth), divided into 5-year intervals.	20
3.2	Yearly averaged halosteric sea level anomalies [m] for 2003-2014 (ref. period 1995-2015).	21
3.3	DTU Steric sea level timeseries compared to a CPOM Altimetry minus GRACE (JPL Mascons). From top: Barents Sea (71°- 78°N, 20°- 50°E), Beaufort Sea (71°- 78°N, -160°- -135°W), East Siberian Sea (71°- 78°N, 140°- 170°E). Right panel shows the average for every month and 1σ (dashed lines).	23

3.4	Sea level trend maps from 2003-2015 of halosteric, thermosteric, total steric and CPOM altimetry minus GRACE (JPL Mascons) [mm yr^{-1}]. Bottom maps shows the data density as a percentage of months with data in a 50 km radius.	24
3.5	1995-2015 ice mass loss [gigatonnes] from Greenland ice sheet, Antarctic ice sheet and glaciers included in this study. Right y-axis shows the global sea level equivalent [mm].	26
3.6	Height change profiles of an idealized glacier with varying b (in gigatonnes). Example glacier has $A=1000 \text{ km}^{-2}$ and spans from 0 to 2000 meters height (Z). The asterisks (*) marks the height of E	28
3.7	Left column: 2003-2015 average mass balance [Gt yr^{-1}] for glaciers on Svalbard from the model by Marzeion et al. (2012). Size of circle is proportional with glacier area. Right column: Equivalent water height (EWH) elevation change from 2003 to 2015 in m yr^{-1} resulting from the redistribution of the mass balance. The EWH elevation change is not comparable with actual ice elevation change, since no model for firn has been applied. The values on the map a proportional with mass changes (assumed density of 917 kg m^{-3}). Outlines of glaciers are indicated with dashed lines. Topography scale at the bottom.	29
3.8	Similar to figure 3.7, but for (from top) Novaya Zemlya, Iceland and the Alaska south-west coast.	30
3.9	Average ice elevation change [m yr^{-1}] from 2003-2015 for the Greenland Ice Sheet. Left colorbar indicates the topography [m].	31
3.10	Average ice elevation change [m yr^{-1}] from 1995-2015 for Antarctic Ice Sheet.	32
3.11	Left panel shows the VLM at global scale from each source [mm yr^{-1}]. Right panel shows the geoid change (\dot{G}) associated with the melting of each source [mm yr^{-1}].	34
3.12	Left: Uplift from the VLM-model [mm yr^{-1}]. Right: Uncertainty of the VLM-model [mm yr^{-1}].	34
3.13	Enlargement of elastic VLM (only uplift) in some glaciated regions in the Arctic (on different colorscales) [mm yr^{-1}].	35
3.14	Present-day deformation rates (mm yr^{-1}) from the GIA-model of Caron2018 (a) and ICE6G-D Peltier et al. (2018) (b). The difference between the GIA-models (Caron2018 minus ICE6G-D) is shown in (c). Uncertainty from Caron2018 is shown on a different colorscale (d)	37
3.15	Average trend [mm yr^{-1}] of elastic deformation caused by rotational feedback from 1995 to 2015.	38

List of Abbreviations

AO	Arctic Oscillation
ASL	Absolute (Geocentric) Sea Level
CM	Center of mass
CPOM	Centre of Polar Observation and Modelling
DTU	Technical University of Denmark
ECCO	Estimating the Circulation and Climate of the Ocean model
ERS 1/2	European Remote-Sensing Satellite 1 and 2
eVLM	elastic Vertical Land Movement
GF	Greens Function
GIA	Glacial Isostatic Adjustment
GMSL	Global Mean Sea Level
GNSS	Global Navigation Satellite System
GRACE	Gravity Recovery and Climate Experiment
ITP	Ice-Thetered Profiler
ITRF	International Terrestrial Reference System
JPL	Jet Propulsion Laboratory (NASA)
NOL	Non-tidal Ocean Loading
PSMSL	Permanent Service for Mean Sea Level
RADS	Radar Altimeter Database System
REAR	Regional EIAsitic Rebound calculator
RF	Rotational Feedback
RSL	Relative Sea Level
SLA	Sea level anomaly
SLE	Sea Level Equation
SLR	Sea level rise
SSH	Sea surface height
TG	Tide Gauge
VLM	Vertical Land Movement

Contents

Resumé (Danish Abstract)	ii
Abstract	iii
Preface	iv
Publication list	v
Acknowledgements	vi
List of Figures	vii
Nomenclature	ix
1 Introduction	1
1.1 The Arctic in a Changing Climate	1
1.2 The Arctic Ocean - the Overlooked Mediterranean at the Top of the World	2
1.3 Components of Sea Level Change	5
2 Data availability in the Arctic Ocean	7
2.1 In-situ measurements	7
2.2 Remote Sensing	10
2.3 GNSS	15
2.4 An oceanographic model: Estimating the Circulation and Climate of the Ocean	16
3 Developed Arctic Data Products	19
3.1 Steric Sea Level Change in the Arctic	19
3.2 Vertical Land Motion	25
4 Publication 1: Contributions to Arctic Sea Level	39
4.1 Preface	39
5 Publication 2: Vertical Land Motion from Present-Day Deglaciation in the Wider Arctic	53
5.1 Preface	53
5.2 Supporting Information for "Vertical Land Motion from Present-Day Deglaciation in the Wider Arctic"	74
6 Publication 3: Assessment of 1995-2015 Arctic Ocean Sea Level Trends	87
6.1 Preface	87
7 Conclusions and outlook	107

1 Introduction

1.1 The Arctic in a Changing Climate

The Arctic is the region on Earth most affected by anthropogenic climate change. Surface temperatures in the Arctic have over the last two decades increased with more than double the global average (Richter-Menge et al., 2017; Meredith et al., 2019), while two of the latest winters (2016 and 2018) have been 6 degrees above the 1981-2010 average (Meredith et al., 2019). In the latest summer (2020) parts of Siberia experienced the highest temperatures ever registered in the Arctic, with maximum temperatures measured in Verkhoyansk (67.33°N, 133.32°E) with 38 C° on June 20, 2020 (WMO, 2020), which is 15-20 C° above the 1981-2010 average for June. The main driver of the rapid Arctic warming (called Arctic Amplification, figure 1.1) is the decreasing albedo effect from reduced sea ice and snow cover (Pistone et al., 2019), but also enhanced atmospheric and ocean heat transport is favoring a warmer Arctic (Stuecker et al., 2018).

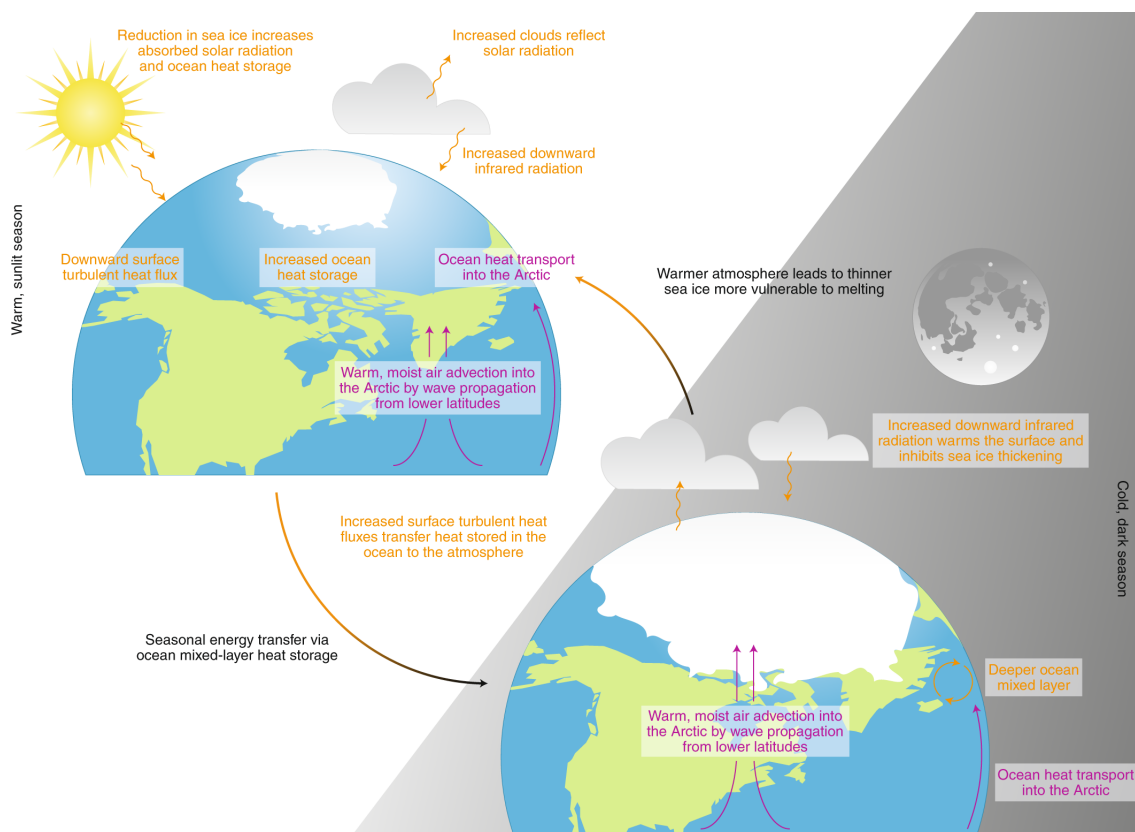


Figure 1.1: Schematic picture of the most important processes of Arctic Amplification. Direct processes are shown with orange arrows, remote processes are purple and inter-seasonal processes are indicated with orange/black arrows. Courtesy of Nature Climate Change, Cohen et al. (2020).

The warming Arctic has multiple consequences, with loss of ice on land and sea as the most prominent. The Gravity Recovery and Climate Experiment (GRACE), has measured Earth's gravity field since 2002. Estimates from GRACE of the mass loss of the Greenland Ice Sheet shows an average of 281 Gt y^{-1} from May 2002 to August 2016 equivalent to

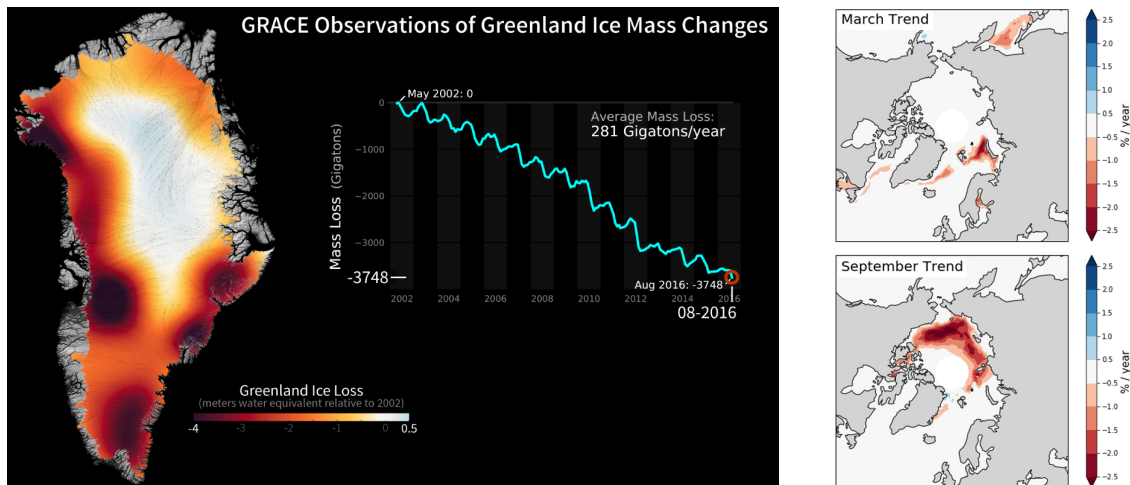


Figure 1.2: Left: Change of Greenland Ice Sheet as measured by GRACE from May 2002 to Aug 2016 from NASA Jet Propulsion Laboratory (2020). Right: March and September Sea ice concentration trend from 1979-2018 based on satellite images (Stroeve and Notz, 2018).

0.78 mm of global sea level rise (SLR) every year. For the same period Arctic glaciers outside Greenland lost 152.5 Gt y^{-1} of ice (eq. to 0.42 mm y^{-1} SLR) (Wouters et al., 2019), which is three-fourths of the global glacial ice loss.

Sea ice in the Arctic reaches its largest extent in March and lowest extent in September. The area of September sea ice has decreased with more than 12% per decade since 1979 (Onarheim et al., 2018), which is shown in figure 1.2. The loss of sea ice is particular evident in the Beaufort Sea and the East Siberian Sea (see figure 1.4 for a map of the Arctic Ocean). The share of sea ice older than 5 years has decreased from 30% to just 2% from 1979 to 2018 and first-year sea ice is now covering over half of the Arctic Ocean sea ice area, which is thinner and more vulnerable (Stroeve and Notz, 2018). While there is a natural variability in Arctic sea ice extent, at least 50% of the sea ice loss can be attributed to climate change (Meredith et al., 2019).

Decreasing land and sea ice also significantly affects the Arctic Ocean. Both processes release vast amounts of freshwater into the Arctic. Decreasing sea ice also enhances solar radiation reaching the ocean surface and opens up for increasing surface dynamics caused by wind stress over the Arctic Ocean (Watanabe and Hasumi, 2005; Giles et al., 2012; Martin et al., 2014).

All of the above mentioned processes alters the topography of the sea surface by either changing the mass or the density of the water column. Thus is the Arctic Ocean at the frontier of the most prominent effects of present-day climate change and understanding the causes of sea level change in the Arctic Ocean is understanding the consequences of climate change.

1.2 The Arctic Ocean - the Overlooked Mediterranean at the Top of the World

The Arctic Ocean represents less than 5% of the global ocean surface and less than 2% of the ocean volume (exact numbers depend on definition). Change in sea level has historically been observed with tide gauges along coasts with first records starting in the late 18th century in Europe. Historical records from the Permanent Service for Mean Sea

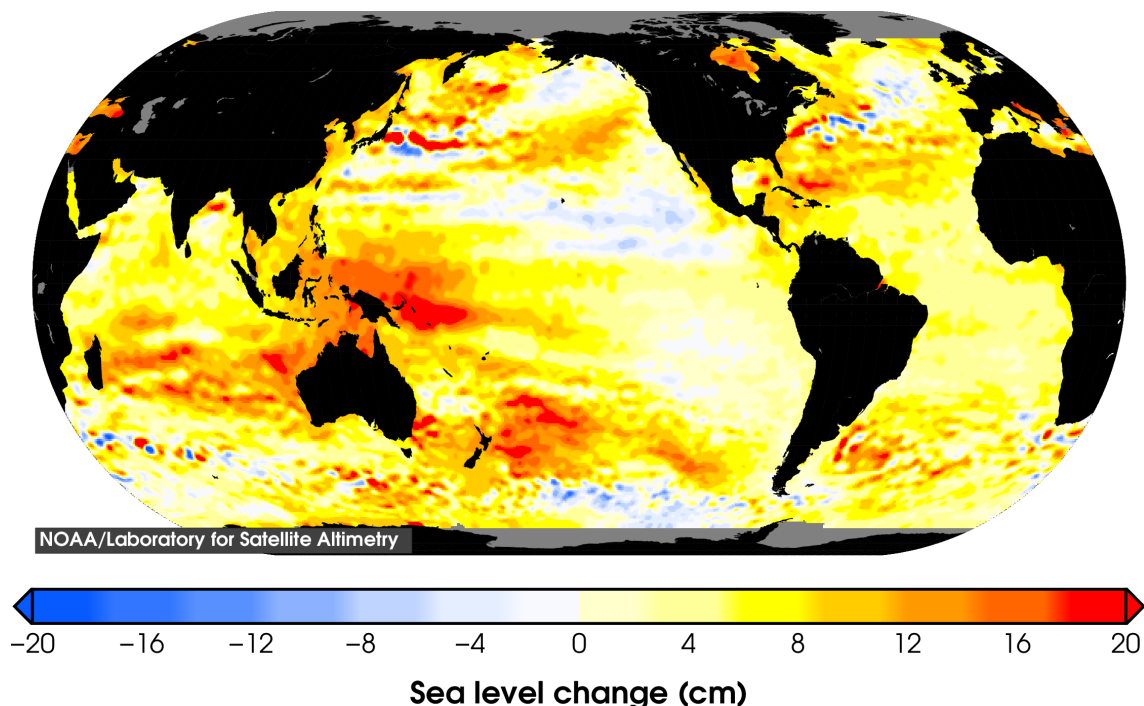


Figure 1.3: Sea level change from 1993 to 2019 as measured by satellite altimeters from NOAA (<https://star.nesdis.noaa.gov/socd/lisa/SeaLevelRise>).

Level (PSMSL, (Holgate et al., 2012)) show that tide gauges are unevenly distributed with most records in Europe and North America, which has made it difficult to compose a global sea level estimate. This changed in 1992 when satellite altimeters started measuring sea level and regional patterns of sea level change became visible (shown in figure 1.3). As figure 1.3 also shows, the polar regions are often blended and not considered in global mean sea level (GMSL) (Church and White, 2011; Fasullo and Nerem, 2018). One reason is that many of the satellites have an orbit inclination of 66° , thereby only covering between 66°N and 66°S . Even though multiple satellite missions provide continuous cover up to 82°N since 1991 (Rose et al., 2019), permanent and seasonal changing sea ice cover makes it challenging to get consistent measurements. GMSL (without the polar regions) has shown a trend of $3 \pm 0.4 \text{ mm y}^{-1}$ (Nerem et al., 2018) from 1993-2018. Nerem et al. (2018) detected an acceleration of $0.084 \pm 0.025 \text{ mm y}^{-2}$, which means, if the acceleration persists, that GMSL will in total rise $65 \pm 12 \text{ cm}$ from 2005 to 2100, with at least 78% originating from ice loss of Antarctica (0.0332 mm y^{-2}), Greenland (0.0236 mm y^{-2}) and glaciers (0.0094 mm y^{-2}).

Sea Level studies in the Arctic Ocean has in the past also relied on tide gauges (Proshutinsky et al., 2004, 2009; Henry et al., 2012), while in the last decade a number of satellite-based estimates of Arctic Sea Level has emerged (Prandi et al., 2012; Cheng et al., 2015; Armitage et al., 2016; Carret et al., 2017; Rose et al., 2019; Veng and Andersen, 2020).

The spatial pattern of Arctic sea level change is consistent among the studies. The most significant feature is the 'doming' (Regan et al., 2019) of the Beaufort Sea, with an rise up to 2 cm yr^{-1} (Giles et al., 2012; Armitage et al., 2016; Rose et al., 2019). It is caused by anticyclonic winds create an inwards Ekman transport (Giles et al., 2012; Armitage et al., 2016). The gyre is thereby accumulating freshwater from decreasing sea ice that is lighter than saline water, which results in a strong SSH-trend (Giles et al., 2012).

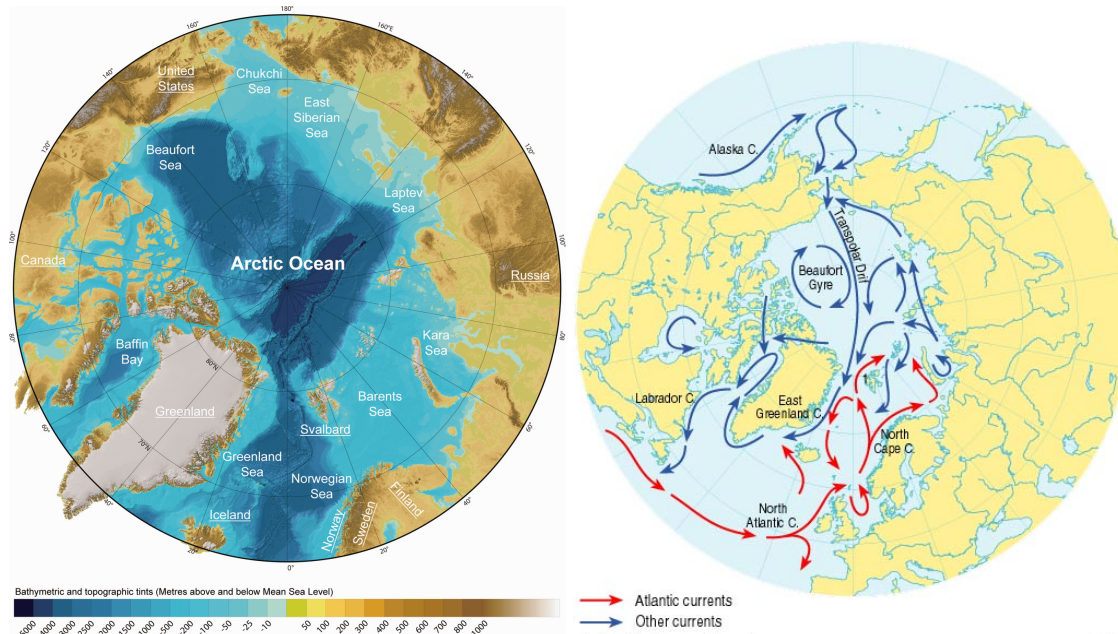


Figure 1.4: Left: Map of the Arctic Ocean with named areas which are used throughout this thesis. Map is adapted from James et al. (2016). Bathymetry is from IBCAO3.0 (Jakobsson et al., 2012). Right: Map of the main surface currents in the Arctic domain and connections to the adjoining oceans. Map is taken from Arctic Monitoring and Assessment Programme (AMAP) report 1998 (AMAP, 1998), site:<https://www.amap.no/documents/doc/surface-ocean-currents-in-the-arctic/566>.

Figure 1.4 shows the different seas and bathymetry of the Arctic Ocean. The seas along the Siberian Coast are shallow (<200 m deep), while the Beaufort Sea has depths below 1000 meters and the interior of the Arctic Ocean extends down to depths below 4000 meters. The Arctic Ocean is a mediterranean sea almost entirely surrounded by land. Atlantic waters enter the Arctic Ocean through the Fram Strait and Barents Sea, while a smaller inflow of pacific water comes through the Bering Strait into the Chukchi Sea, which again mostly exits through the Fram Strait. Although the Arctic Ocean is geographically limited by the surrounding land, the Greenland Sea, Norwegian Sea and Baffin Bay are included when discussing changes in the Arctic Ocean (Carret et al., 2017; Ludwigsen and Andersen, 2020; Raj et al., 2020).

Besides the Beaufort Gyre the main current in the Arctic Ocean is the Transpolar Drift, which leads water and sea ice from the East Siberian and Chukchi Seas across the Arctic Ocean and out through the Fram Strait (a.o. Armitage et al. (2018)).

1.2.1 Arctic Oscillation

Sea level in the Arctic Ocean correlates with the Arctic Oscillation (AO) (Armitage et al., 2016; Raj et al., 2020). The AO-index is defined from sea level pressure (SLP) anomalies north of 20°N (Thompson and Wallace, 1998). A positive AO-index favors a strong zonal SLP, high pressure in the North Atlantic and Pacific between 30 and 45 °N and low pressure over the Arctic, with the jet stream dividing the low and high pressure regions, which confines the cold air over the Arctic and enhances the circular wind pattern around the Arctic. In its negative phase the zonal SLP-differences are weakened, allowing for more cold Arctic air to penetrate southward and Arctic winds become more distorted. Daily and monthly values of AO-index is published by National Oceanic and Atmospheric Administrations (NOAA) and is strongly related to the North Atlantic Oscillation (NAO) (Wallace

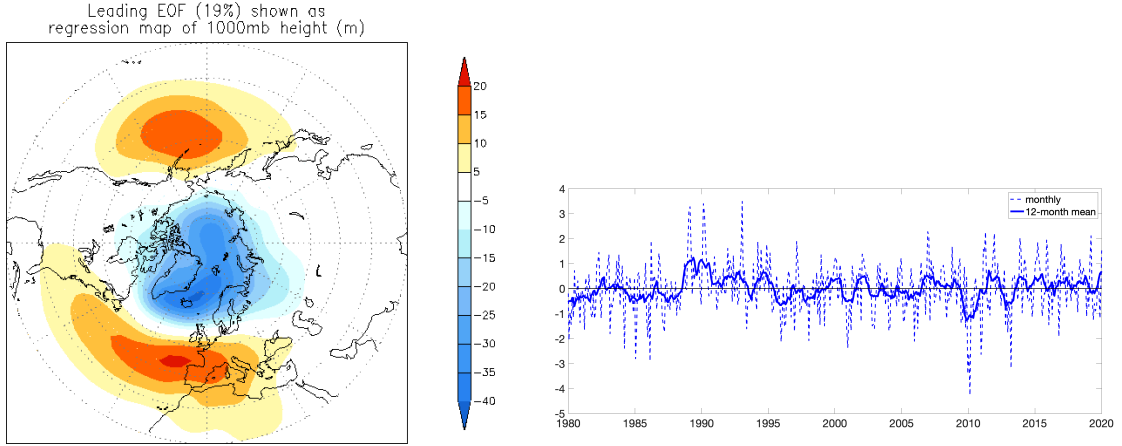


Figure 1.5: Left: Leading pressure pattern of Arctic Oscillation Index from NOAA Climate Prediction Center. Right: Arctic Oscillation index since 1980. Monthly data from NOAA.

and Gutzler, 1981).

During positive AO, a cyclonic wind pattern builds up sea level on the continental shelf of the Siberian Seas to the east, while negative AO-regimes favor a pattern with sea level fall in the Siberian Seas (Armitage et al., 2018).

1.3 Components of Sea Level Change

Longterm sea level change (SLC, \dot{S}), as measured by satellite altimetry, can be divided into components of sea level change due to change in mass \dot{S}_M and change in density, which is called steric sea level change \dot{S}_{ST} :

$$\dot{S} = \dot{S}_M + \dot{S}_{ST} \quad (1.1)$$

\dot{S}_{ST} is further divided into change of halosteric sea level, \dot{S}_{HS} which originates from changes in salinity and termosteric sea level change, \dot{S}_{TS} , which is due to changes in ocean temperature. While on global scale \dot{S}_{TS} is by far the largest steric component, \dot{S}_{HS} is significant in the Arctic, because the water expansion at low temperatures is limited and changes in freshwater are eminent in the Arctic (Morison et al., 2012).

The mass component, \dot{S}_M , can be split into the mass coming from present-day changes of landbased ice (\dot{S}_I), a component accounting for viscoelastic mantle flow from glacial isostatic adjustment (GIA) (\dot{S}_{GIA}), a barotropic component originating in wind forcing (\dot{S}_W) and a component that accounts for any other land-to-ocean mass flux that does not originate from ice (\dot{S}_C). While a lot of temporal and spatial variability comes from \dot{S}_W and \dot{S}_C (Calafat et al., 2012; Dangendorf et al., 2014), the main mass component of regional and long-term \dot{S} is \dot{S}_I (WCRP, 2018; Frederikse et al., 2018). Changes in atmospheric pressure, called Inverse Barometer (IB) is theoretically also a part of \dot{S}_M , but is often corrected for in altimetric SLA-products and hence included in \dot{S} (Rose et al., 2019).

$$\dot{S} = \underbrace{\dot{S}_I + \dot{S}_{GIA} + \dot{S}_W + \dot{S}_C}_{\text{mass components}} + \underbrace{\dot{S}_{HS} + \dot{S}_{TS}}_{\text{steric components}} \quad (1.2)$$

\dot{S}_I is not globally uniform because the changed loading also alters the geopotential field of Earth's surface, the geoid, due to the change in gravitational attraction from land-to-

ocean mass fluxes. Farrell and Clark (1976) wrote the temporal (t) and spatial (ω) sea level change associated with a changed loading on Earth's surface in a simple form as:

$$\dot{R}(\omega, t) = \dot{G}(\omega, t) - \dot{U}(\omega, t) + c. \quad (1.3)$$

where \dot{G} is the change in geoid height and \dot{U} is the vertical isostatic change of the solid earth that results from changed loading on Earth's surface, called Vertical Land Motion (VLM). The spatially invariant, c , ensures mass conservation. From equation 1.3 follows, that \dot{R} is the SLC that would be observed from a position on the solid earth, e.g. the coast and thus equivalent to the sea level measured by tide gauges. \dot{R} is commonly referred to as relative sea level (RSL) change. From a perspective of altimetry, sea level is measured with respect to Earth's center of mass (CM) (Wu et al., 2012), which is called absolute sea level (ASL) and is invariant of \dot{U} . Geoid-driven sea level change is caused by any mass changes on Earth and is sometimes referred to as \dot{N} (Spada, 2017) and hence is

$$\dot{N} = \dot{G} + c \quad (1.4)$$

\dot{N} can further be split into different sources of ice loading (e.g. Greenland, glaciers, Antarctica, \dot{S}_I) and GIA ($= \dot{S}_{GIA}$) which is done in chapter 3 and in the third publication (chapter 6).

c is equivalent to global-mean geocentric sea level change (Gregory et al., 2019) and includes the SLC from ice sheets averaged over the oceans (barystatic sea level change) and secondly, it includes the fact that U is changing the shape of the ocean basin, which in turn changes the sea level. From Spada (2017) c can be defined as:

$$c = -\frac{M_I \rho_w}{A_O} - \left\langle \frac{\phi}{g} - U \right\rangle \quad (1.5)$$

The first term is the barystatic sea level change, where M_I is the total mass of the changed surface loading, ρ_w is the density of ocean water and A_O is the ocean surface of the Earth. $\langle \dots \rangle$ marks the average over Earth's ocean surface. Because changes of shoreline is neglected, A_O is assumed to be a constant.

By rewriting equation 1.3 and assuming that \dot{S}_{SH} has no influence on the geoid, the ASL change (\dot{S}) is related to the RSL change (\dot{R}) by VLM (\dot{U}), which is essential when sea level from altimetry is compared to sea level measured by tide gauges.

$$\dot{S} = \dot{R} + \dot{U} \quad (1.6)$$

Similar to \dot{N} , \dot{U} can also be divided into different sources of change in surface loading, e.g. ice loading and GIA.

2 Data availability in the Arctic Ocean

This chapter focuses on the geophysical data that are used for this research of the Arctic Ocean. The main challenge of doing research in the Arctic and specifically the Arctic Ocean is the poor coverage of data due to the unfriendly environment and associated high costs. Continuous in-situ records require maintenance and robustness, which furthermore is challenged by strenuous accessibility. Data of the Arctic Ocean is separated into data from in-situ measurements and remote sensing. Additionally, one oceanographic model is presented which naturally is constrained by both in-situ data and remote sensing.

2.1 In-situ measurements

In-situ measurements have the advantage that minimal interpretation is necessary, since the physical property is measured on location. Before the satellite era (starting in 1991), in-situ measurements were the only source of repeated physical data in the Arctic.

2.1.1 Tide Gauges

Using tide gauges is the only direct way to measure sea level without using remote sensing. A tide gauge is fixed to the known local reference on land, which means it measures sea level change relative to Earth's surface and thus called relative sea level (RSL). PSMSL (psmsl.org, (Holgate et al., 2012)) is a global repository of long-term tide-gauge data, with a monthly or annual temporal resolution.

Since the 1980's 127 tide-gauges from PSMSL are located above 60°N, with around 100 of them located towards the Arctic Ocean or its connecting seas. A significant shut down of stations in particular in the Russian Arctic means that less than half of the stations have data in 75% of the years since 1980. Most stations with complete or near-complete sea level records are located along the Norwegian Coast.

2.1.2 Hydrographic data

Hydrographic data are measures of the physical properties of water. Throughout this work, we only use temperature and salinity measurements of the water column, so-called T/S-profiles to generate steric sea level heights. Since the beginning of year 2000, the ARGO-mission has created a mask of floats, that repeatedly obtains T/S-profiles from the surface down to 2000 meters depth. At present, nearly 4000 floats have been deployed by ARGO, but due to the sea ice cover in the Arctic, only very few T/S-profiles have been collected in the northern latitudes, and most of them in the Norwegian Sea with few in the Chukchi Sea (see figure 2.3 for a map of locations of ARGO floats at July 4th, 2020).

Buoys designed for Arctic environment that dive below the sea ice, so called Ice-Thetered Profilers (ITP) take consistent measurements below the sea ice down to 500-800 meters depth. They are deployed by Woods Hole Oceanography Institution (WHOI), and are mainly located in the Canadian Arctic and the Beaufort Sea. Most profiles in the Arctic Ocean are obtained from ships, that either breaks through the ice or sail in the ice-free ocean during the summer. These mission-based data collections, are creating a spatial and temporal bias, because areas with no or thin ice can be visited more frequently during summer months. The Unified Database for Arctic and Subarctic Hydrography (UDASH) (Behrendt et al., 2017), is a repository that collects all available T/S-profiles north of 60°N from 1980 to 2015. Data from the World Ocean Database, Institute of Marine Research in Norway, ARGO and ITP's from WHOI have been added to extend the dataset up to 2018.

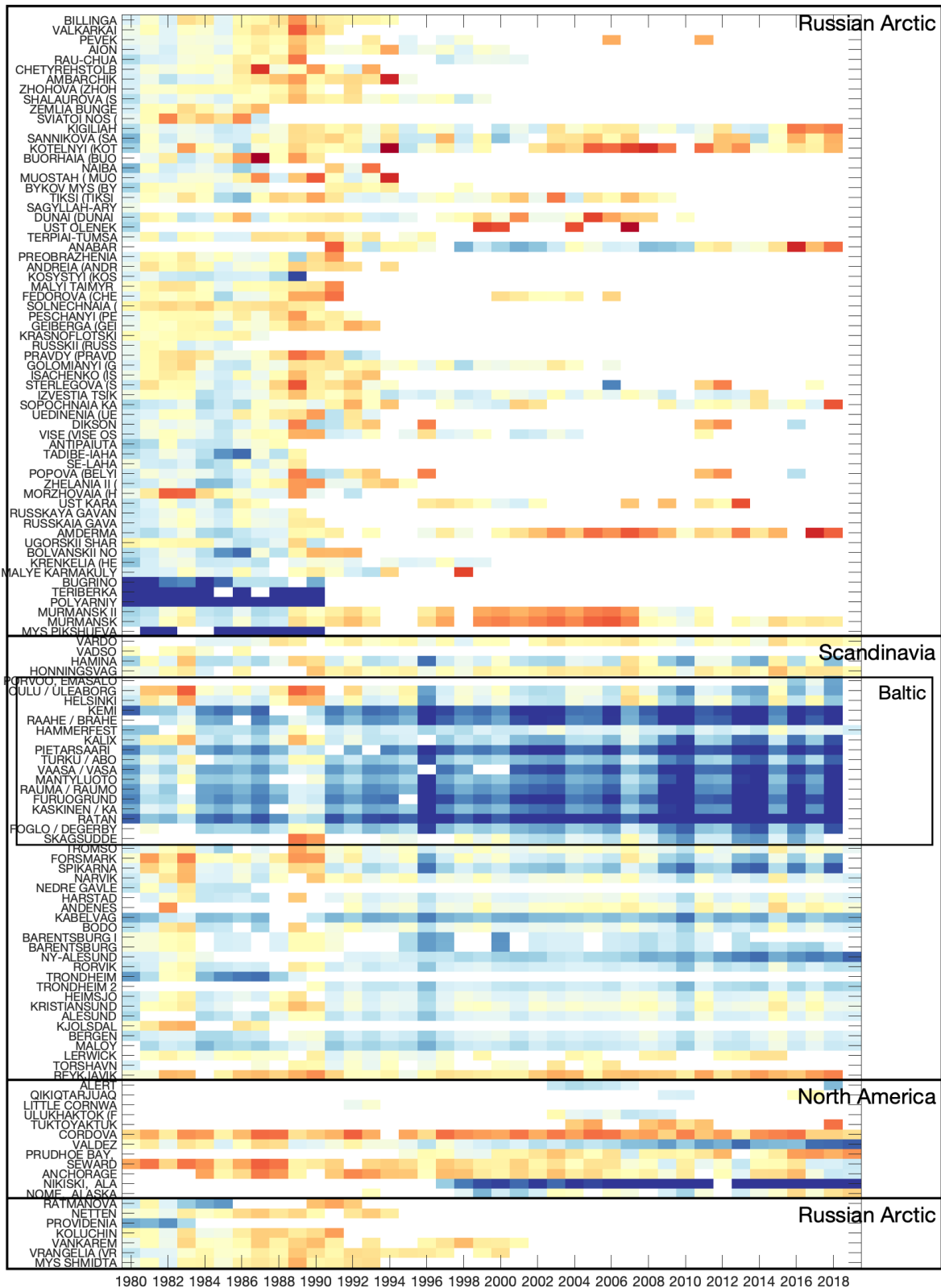


Figure 2.1: Matrix of relative sea level measurements (in meters) from 127 tide gauges from PSMSL since 1980, sorted from most east (top) to most west (bottom). White spots indicate where there is no data or too few measurements to make a meaningful annual mean.

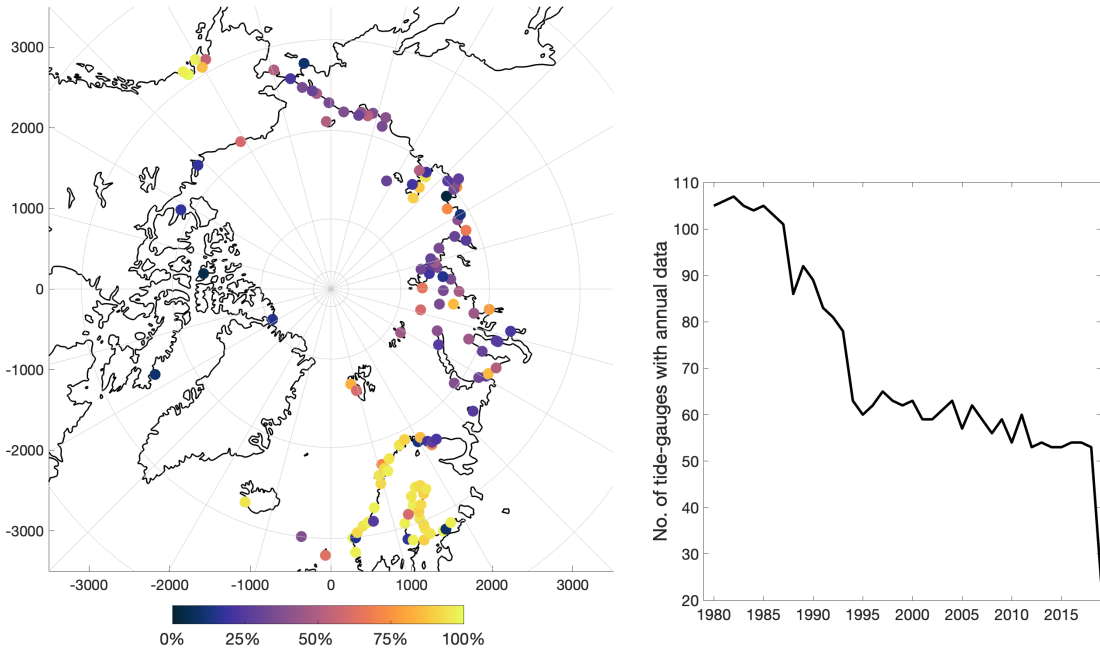


Figure 2.2: Left: Map of the 127 tide gauges with data since 1980. The color indicates how many years since 1980 have valid data. Right: Chart showing the decline of tide-gauges since 1980. The drop from 2018 to 2019 is due to that the annual value for some tide-gauges have not yet been validated by PSMSL.

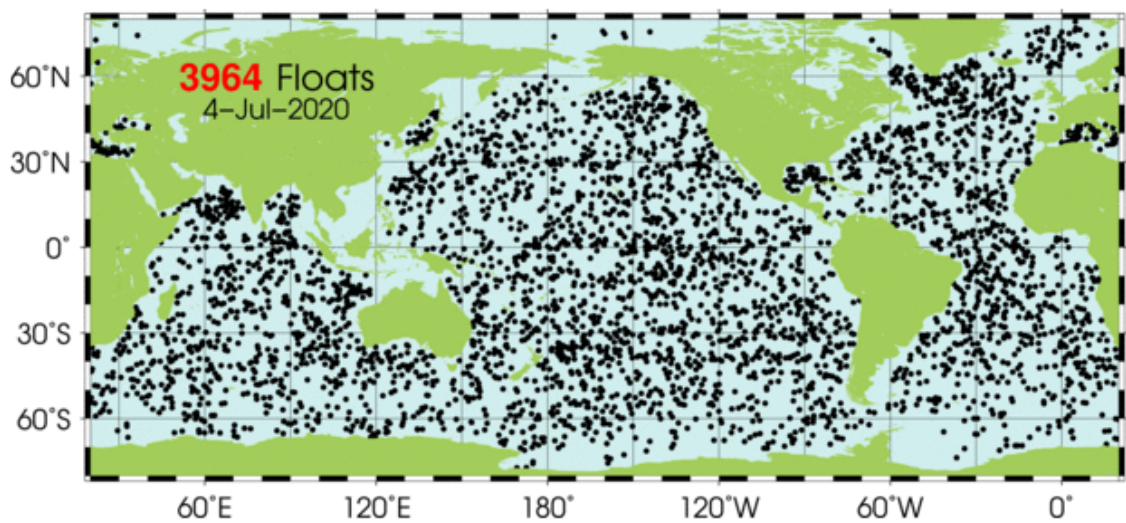


Figure 2.3: Location of active ARGO floats on 4th July 2020. From the Argo Program website (argo.ucsd.edu).

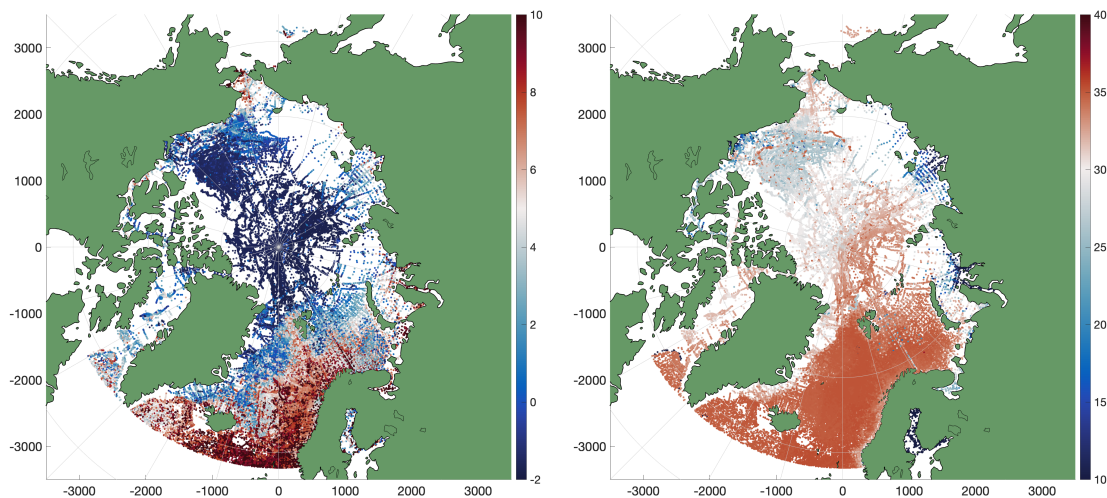


Figure 2.4: Left: Ocean temperature (C°) within at max 5m depth for all hydrographic data available since 1990 used for the DTU Steric product. Right: Same as left, but with salinity (psu).

Location and near-surface temperature and salinity for all available T/S-profiles from 1990-2018 is shown in figure 2.4. It is visible that the Arctic Ocean has sub-zero temperatures, going down to -2°C which is where sea water with average salinity freezes. Figure 2.4 also shows, that the Beaufort Gyre has fresher water with salinity values around 28 psu, which in turn has a warmer freezing temperature. Distinct is also the freshwater outflow from Russian rivers in the Arctic, with low salinity values in the Kara and Laptev Seas (a.o. Povalishnikova et al. (2018); Osadchiev et al. (2020)). In total, over 300k T/S-profiles are available in the Arctic from 1990-2018.

2.2 Remote Sensing

Measuring the Arctic Ocean from satellites is a convenient way to get repeated and consistent data with extensive spatial coverage. While measurements from flights and in some cases drones are also widely used in the Arctic, in particular for the purpose of validation and localized research, only remote sensing data from satellites are included in this work - more specifically satellite radar altimetry and gravitational measurements from GRACE.

2.2.1 Satellite Altimetry

Radar altimetry from satellites (henceforth called satellite altimetry) measures the travel time of the return radar pulse from a satellite orbiting in a known height relative to the reference ellipsoid. If the travel time is multiplied by the speed of light is the distance between the satellite and the surface obtained. Over the ocean, the height between the reference ellipsoid and the surface is called sea surface height (SSH). The change in SSH is equivalent to \dot{S} in equation 1.1. The shape and power of the reflected signal, the waveform, is used to estimate the range, but can also be used to estimate different physical surface properties, such as wind speed, significant wave-height (SWH) and surface type.

The altimeter transmits over 1000 pulses every second, but the waveforms are usually averaged over 1/20 second (20 Hz) before they are analyzed. The characteristic shape

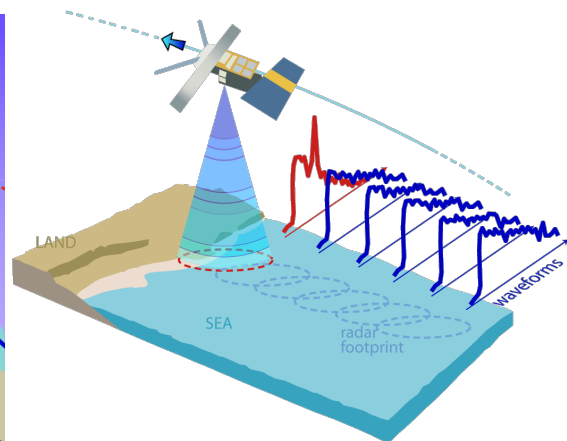
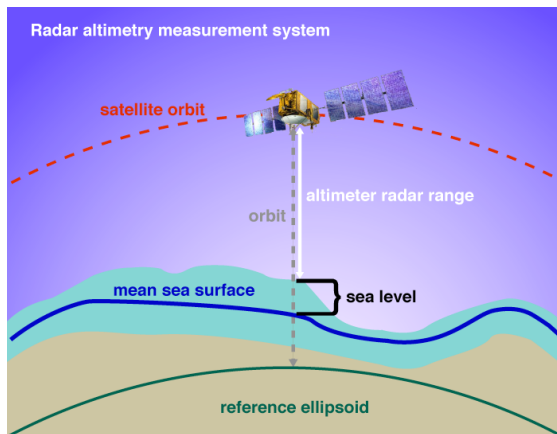


Figure 2.5: Illustration of the principles of satellite altimetry. Both figures from www.altimetry.info.

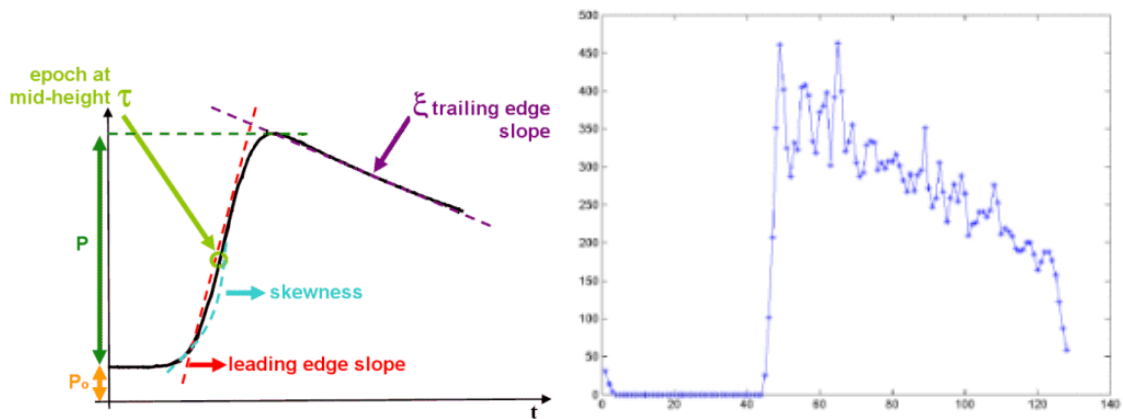


Figure 2.6: Left: Idealized illustration of the Brown waveform. Right: Real example of a waveform from Envisat, with power on y-axis and number of bins on the x-axis. Both figures from altimetry.info.

of the averaged ocean waveform in conventional altimetry can be described using the Brown-Hayne model (Brown, 1977; Hayne, 1980) (see figure 2.6). The half-amplitude specifies the travel time, while the amplitude is related to the backscatter coefficient, which again is related to the wind speed. The leading edge slope determines the SWH (steep slope means calm surface, hence small SWH).

Right illustration in figure 2.6, shows the characteristic waveform over open ocean. If the footprint of the radar pulse is partially or totally reflected by land the waveform becomes more rough and does not have the characteristics of the waveform in figure 2.6. For sea ice and land ice, the reflecting surface can have a similar waveform as the ocean, but usually with lower maximum amplitude (Gregory et al., 2019). Due to the in-homogeneous surface of in particular old sea ice and land ice, the waveform can also have a more wide and diffuse shape. Of particular interest in the Arctic, is the ability for the radar pulse to reach the ocean surface in cracks between sea ice floats, called leads. Besides being the only SSH-measurements in sea ice covered oceans, the leads are also important for calculating sea ice freeboard and thus essential for volume-estimates of sea ice (Tilling et al., 2018). The waveform from leads has a spike-like shape with high maximum power and steep leading and trailing edges (a.o. Peacock and Laxon (2004); Quarty et al.

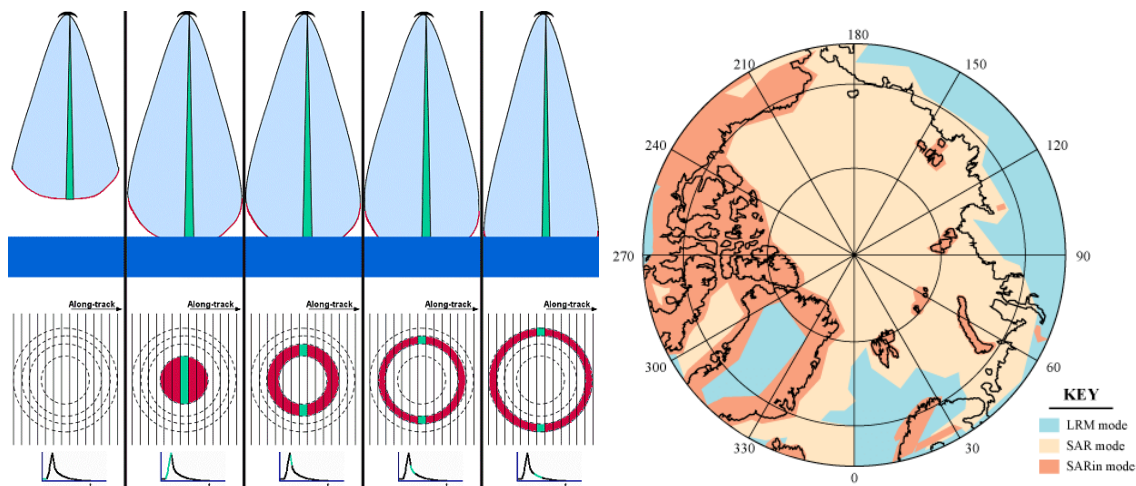


Figure 2.7: Left: Principle of SAR-operating mode of CryoSat-2 from Raney (2012). Right: CryoSat-2 operating mode masks in the Arctic from Quartly et al. (2019).

(2019)).

CryoSat-2 can switch between conventional altimetry (called 'Low-resolution mode' (LRM)) and SAR-altimetry (Synthetic Aperature Radar-mode) (Wingham et al., 2006). Additionally, CryoSat-2 has a SAR Interferometric (SARin) mode, which is useful in particular in coastal regions, where an extra antenna makes it possible to locate off-nadir signals (Wingham et al., 2006; Quartly et al., 2019). The different modes of CryoSat-2 are enabled after a defined mask, which is shown in figure 2.7.

CryoSat-2 operates in SAR-mode in coastal and sea ice regions (see map in figure 2.7). The delay-doppler method of SAR altimeters (Raney, 1998), looks at the same area from multiple pulses, as the satellite moves along track. When multiple looks are averaged, a narrow along track footprint is archived, which is a significant improvement compared to the round footprint from conventional altimeters. The narrow footprint and relative low noise, makes them ideal to discover leads in sea-ice regions.

The shape of a SAR waveform has a more steep trailing edge than conventional altimetry, because the area covered in SAR-mode is relatively small at the end of the radar pulse which reduces the noise that creates the trailing edge. As seen in figure 2.8 the waveform of sea ice is similar to that of open ocean, which is often the case for older sea ice. Young ice can have specular waveforms, that resembles the waveform from leads (Tilling et al., 2018). Often is the shape a mixture of different waveforms (Peacock and Laxon, 2004; Tilling et al., 2018). The ocean surface reflects more energy of the radar pulse, which helps to distinguish reflections from ocean (Tilling et al., 2018; Quartly et al., 2019).

Analysis of waveforms is called retracking. Differences in retracking is the most common difference between different altimetric sea level products. Furthermore, in order to obtain sea level change, the estimated range needs to be corrected for various geophysical corrections (tidal corrections), atmospheric corrections (ionosphere, wet and dry troposphere, inverse barometer) and sea state bias (dependent on SWH). To obtain sea level anomaly from altimetry, S , it follows that:

$$S = H - H_R - MSS - r, \quad (2.1)$$

where H is the satellite height above the reference ellipsoid, H_R is the retracked range and

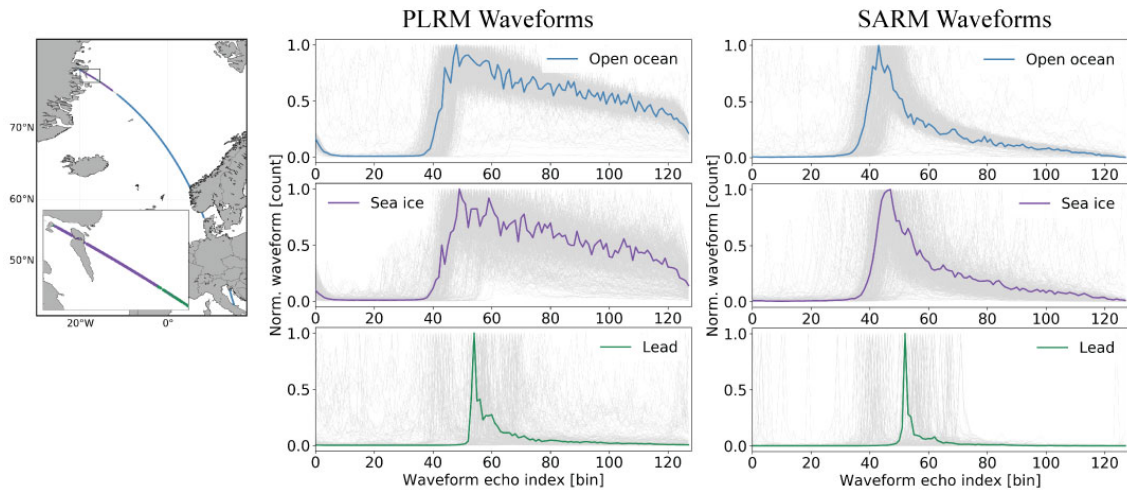


Figure 2.8: Example of waveforms (normalized) from open ocean, sea ice and a lead for (P)LRM and SAR-mode of Sentinel-3A. PLRM means 'pseudo Low Resolution Mode', which is SAR waveforms (Sentinel-3A operates only in SAR-mode) degraded to LRM. From Quartly et al. (2019), with image courtesy of Benjamin Loveday, Plymouth Marine Laboratory.

r is the sum of all corrections. MSS is the mean sea surface, which is S averaged over time (Andersen and Scharroo, 2011). Even though efforts are made to obtain as many measurements from leads as possible, the Arctic Ocean is poorly covered. Since 1991 various satellites cover the Arctic Ocean which together creates a complete timeseries from 1991 until present (figure 2.9).

Before CryoSat-2, the weekly coverage was below 20% in sea ice areas (divided into blocks of $2^\circ \times 1^\circ$) (Cheng et al., 2015). Nevertheless, different Arctic Sea Level products using different retracers (a.o. Naeije et al. (2000); Cheng et al. (2015); Armitage et al. (2016)) based on altimetric observations exist. Empirical retracers (e.g. the CPOM-altimetry product from Armitage et al. (2016)) uses statistics of the waveform to obtain the altimetric range, where physical retracers, like the ALES+ retracker (Passaro et al., 2018) used for the DTU Arctic sea level product (Rose et al., 2019), obtains the waveform properties by applying a physical model that best fits the waveform. Empirical retracers are simple to apply (Quartly et al., 2019), but lack the full physical description of the waveform that is given from the best-fit model of physical retracers.

A common distinguished feature in all products is the 'doming' of the Beaufort Gyre, which is also clearly visible in the most recent DTU Arctic SLA product from Rose et al. (2019), which is shown in figure 2.10. The DTU product used the ERS-1, ERS-2, Envisat and CryoSat-2 for creating an 28-year Arctic Ocean sea level record. Because ERS-1/2 and Envisat had an orbit inclination of 98.5° , the spatial coverage only extended up to 81.5°N . CryoSat-2 which was launched in 2010 has coverage up 88°N , and has thereby near full spatial coverage of the Arctic Ocean. The timeline and spatial extent of radar altimeters measuring in the Arctic is shown in figure 2.9.

The Radar Altimeter Database System (RADS, <http://rads.tudelft.nl/>, (Scharroo et al., 2013)), is a multi-mission database which aims to harmonize altimetric sea level data across satellites. It uses a modified version of the Brown-model to retrack waveforms and provides only 1-Hz altimetry. SAR mode for CryoSat-2 is degraded to a 'reduced SAR' version, which yields better alignment with LRM (Scharroo et al., 2013).

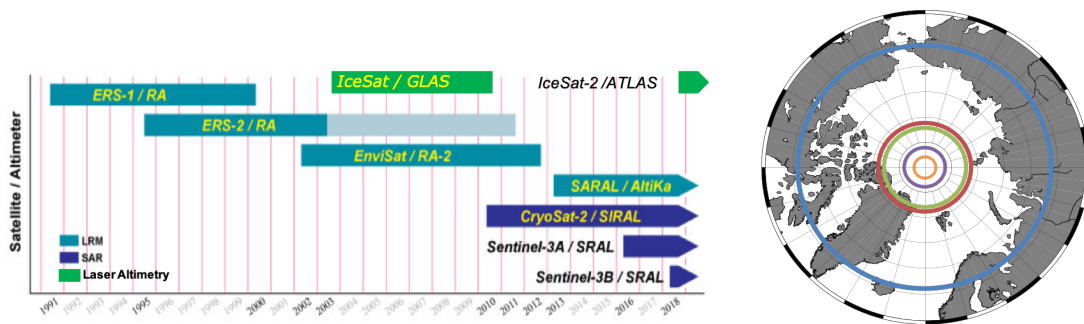


Figure 2.9: Left: Temporal extent of all altimeters covering the Arctic. The color indicates the type of altimeter attached to the satellite. (Adaptated from Quartly et al. (2019)) Right: Maximum latitude reached by satellite missions. Blue (66°N) indicates max latitude by th Jason/Topex/Poseidon-mission (sometimes refered to as reference missions), dark orange (81°N) for Sentinel-3A/B, green (81.5°N) for ERS-1/2, Envisat and SARAL, purple (86°N) for IceSat and orange (88°N) for CryoSat-2 and IceSat-2.

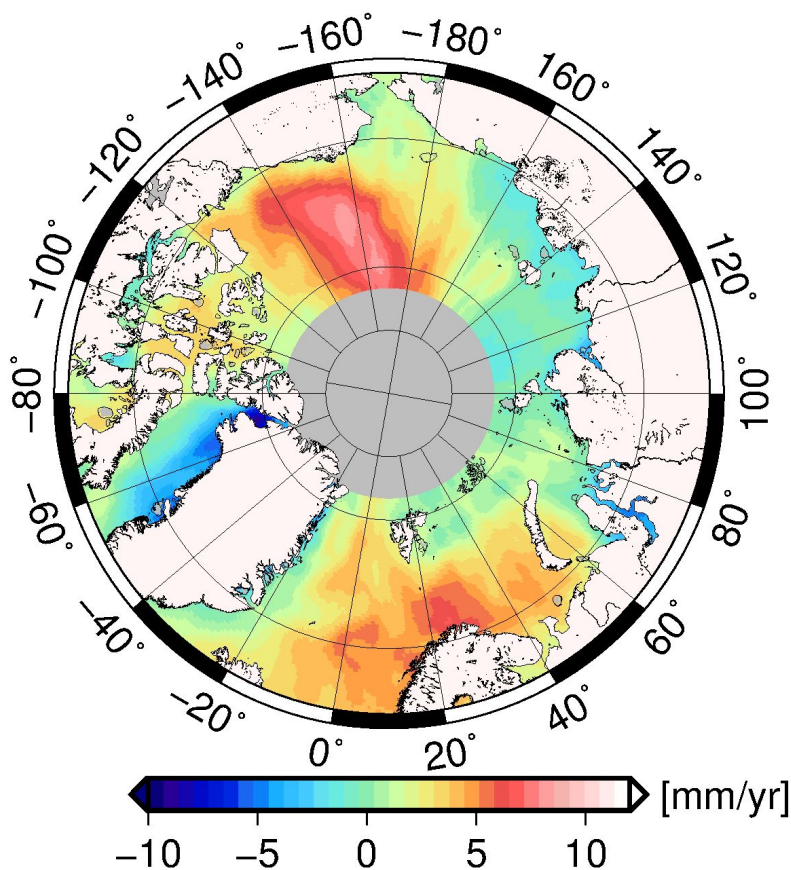


Figure 2.10: 1991-2018 sea level trend (mm yr^{-1}) based on altimetric observations from ERS-1, ERS-2, Envisat and CryoSat-2 from Rose et al. (2019). ERS-1 is processed with the ESA REAPER-retracker and ERS-2 and Envisat data are processed with the ALES+ retracker (Passaro et al., 2018), while CryoSat-2 is processed with the DTU LARS-retracker and RADS (Scharroo et al., 2013).

2.2.2 Gravitational measurements from GRACE

The Gravity Recovery and Climate Experiment (GRACE) was launched in 2002 and lasted until mid-2017. Since mid-2018, has the follow-on mission, GRACE-FO, succeeded GRACE with almost the same configuration. GRACE consists of two identical satellites separated at a distance of around 220 km in a polar orbit. The exact distance is monitored with microwave ranging. A small gravitational pull or push experienced by one of the satellites due to a gravitational anomaly, is measured as a change in separation distance (Tapley et al., 2004).

The Jet Propulsion Lab (JPL), NASA, Center for Space Research (CSR), University of Texas and GeoForschungsZentrum (GFZ), Potsdam all have data centers that produce monthly gravitational anomalies from GRACE given in spherical harmonics. The gravitational products from GRACE have a theoretical spatial resolution limit of 300-500 km (Tapley et al., 2004), which is coarse compared to satellite altimetry measurements. The coarse resolution also results in significant leakage effects (Chen et al., 2006). Ice sheet changes can be equivalent to several meters of water, while changes in the ocean often are in the magnitude of millimeters. Thereby is GRACE detecting changes in ice mass even though it is several hundreds km away from land.

The leakage effect is in particular significant in the Arctic Ocean because of the close proximity to Greenland and other glaciers. To avoid leakage, JPL, CSR and the Goddard Space Flight Center (GSFC) have constrained the measured gravity anomalies into mass concentration blocks (mascons) of the Earth's surface (Wiese et al., 2016; Luthcke et al., 2013; Save et al., 2016). For every mascon are geophysical constraints applied 'a priori' (Watkins et al., 2015). The block size varies between products, with JPL being most coarse with 3° equal area blocks, but with a coastal filter applied, so blocks in coastal areas are split between land and ocean. CSR-mascons are given in 0.5x0.5° (Save et al., 2016) while GSFC uses blocks with a radius of 67 km (Luthcke et al., 2013). Over the ocean are gravity anomalies from GRACE often expressed as changes in ocean bottom pressure (OBP), which is the same as the change in ocean mass of the total water column. Thereby can mass-driven changes in sea level be detected by GRACE (\dot{S}_M in equation 1.1). Trend estimates of OBP-change in the Arctic for the three different mascon-products are shown Ludwigsen and Andersen (2020) in chapter 4.

2.3 GNSS

Vertical displacement or Vertical Land Movement (VLM) measured by Global Navigation Satellite System (GNSS) located on land provides valuable information for multiple purposes. Foremost, is it a direct measurement of \dot{U} in equation 1.3, which implies that, when a GNSS receiver is located at the same location as a tide gauge, then \dot{N} can be measured by taking the sum of \dot{U} and \dot{R} (relative sea level measured by the tide gauge) (Wöppelmann et al., 2007). Secondly, measurements of vertical deformation from GNSS can be inverted to mass equivalent changes on the Earth's surface (Khan et al., 2010).

A consortium based at University La Rochelle (ULR) is publishing reanalyzed GNSS data Wöppelmann et al. (2007, 2009). The URL-6A-dataset (Santamaría-Gómez et al., 2017a), provides quality-controlled vertical and lateral velocities from 756 stations globally for a maximal time series of 19 years (1995 to 2014) shown in figure 2.11. They are referenced to the ITRF2008-reference frame (Altamimi et al., 2011), which is similar to the long-term CM-reference frame (Dong et al., 2003). For the Arctic, most GNSS-stations included in ULR-6A are found in Scandinavia, with reasonable coverage in Greenland and North America. As with the tide gauge data, the Russian Arctic is poorly covered.

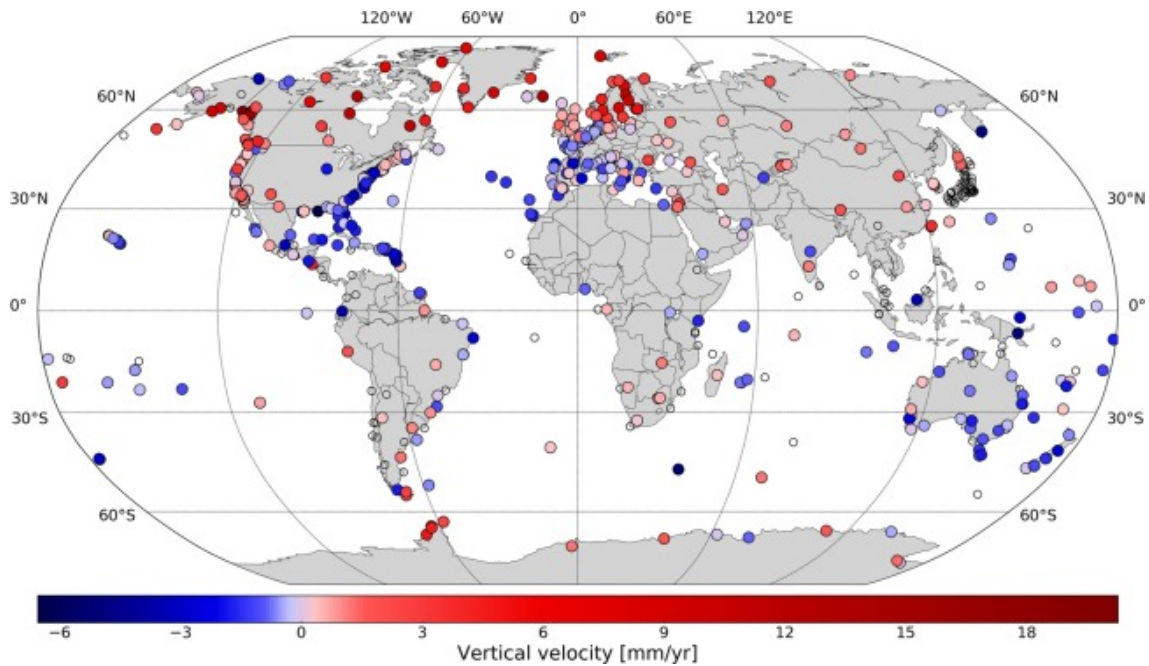


Figure 2.11: Vertical velocity at GNSS stations included in the ULR-6A product (Santamaría-Gómez et al., 2017a). Stations with insufficient data or that are highly non-linear are shown as blank circles. Figure is adapted from Santamaría-Gómez et al. (2017a).

2.4 An oceanographic model: Estimating the Circulation and Climate of the Ocean

The third and fourth release of the latest version of Estimating the Circulation and Climate of the Ocean (version 4) (Forget et al., 2015; Fukumori et al., 2019) is in this study used to compare with hydro-graphic data (ECCOV4r3) (Ludwigsen and Andersen, 2020) and estimate OBP (ECCOV4r4, third publication, chapter 6). ECCOV4 employs both GRACE, altimetry and selected in-situ data to constrain the oceanographic model. Ocean variables of temperature, salinity, OBP and SSH are provided in monthly datasets divided into 13 tiles with 90x90 equal area sized grids. The native resolution varies from 22 to 110 km (Forget et al., 2015), with the highest resolution in the high latitudes, while the resolution in depth varies from 10 meters to nearly 500 meters. Ocean columns of salinity and temperature from ECCO are converted to halosteric and thermosteric heights (see chapter 3 for details). Trends from 1992-2018 of SSH, OBP and steric heights for ECCOV4r4 are shown in figure 2.12.

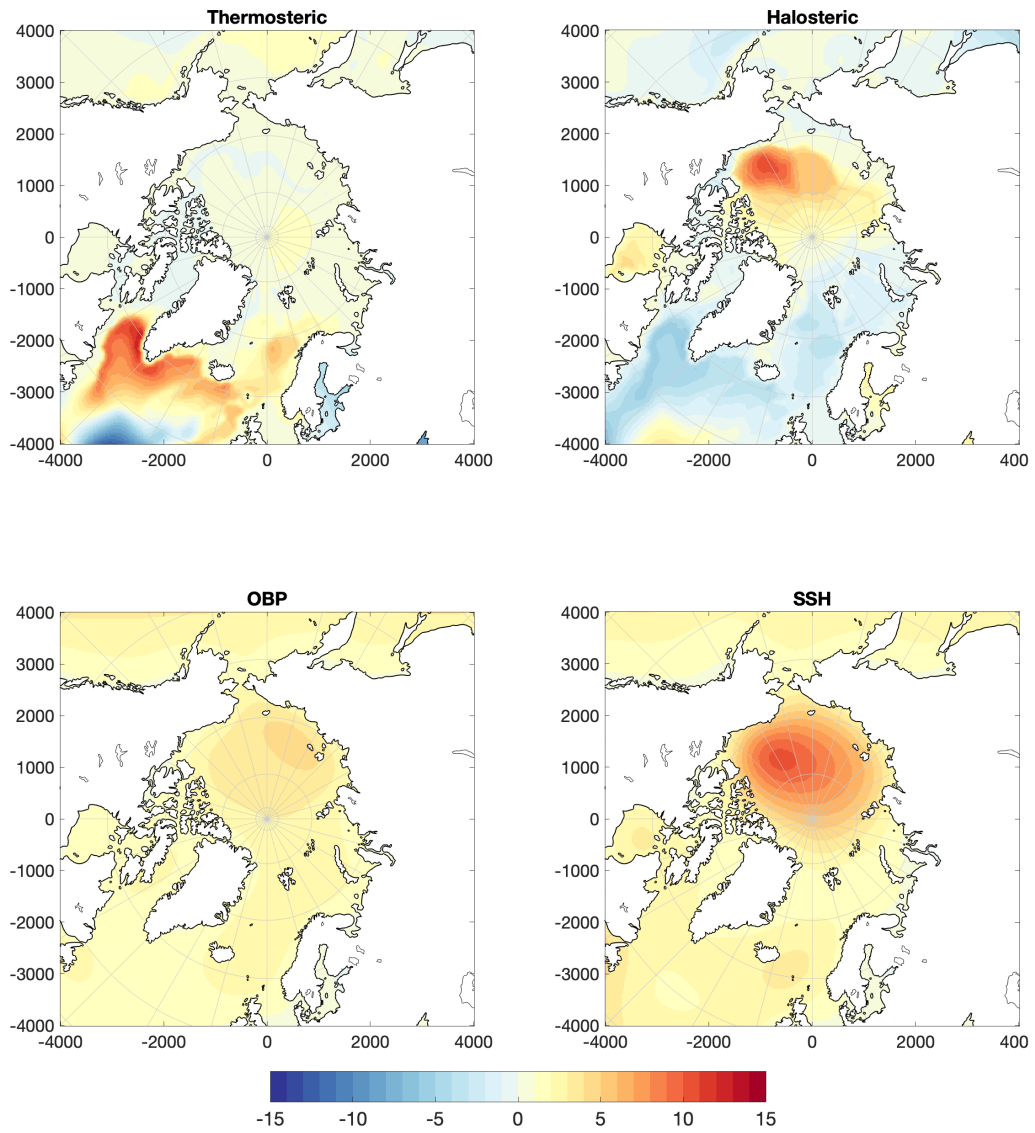


Figure 2.12: 1992-2018 trend ECCOr4v4 (Fukumori et al., 2019; Forget et al., 2015) [mm y^{-1}] for thermosteric height, halosteric height, OBP and SSH. Thermosteric and halosteric heights are derived products computed from ocean temperature and salinity grids in ECCOr4v4.

3 Developed Arctic Data Products

Two original Arctic products essential for assessing Arctic sea level change were developed. First, we developed a steric height product that interpolates all available temperature and salinity in-situ data in the Arctic, DTU Steric, to create a satellite-independent estimate of steric heights. Other existing steric height products are either based on oceanographic models (i.e. ECCO, Fukumori et al. (2019)) or simply the difference between ocean bottom pressure from GRACE and altimetry (i.e. Armitage et al. (2016))

Secondly, in order to align tide gauges with altimetry, accurate estimates of vertical land motion (VLM) is necessary. Because GNSS is not available in the proximity of all tide gauges, we developed a annual gridded Arctic-wide VLM product. Commonly, VLM is based on either only GIA (Henry et al., 2012), where large-scale VLM from present-day ice loading is neglected or derived from GRACE (Frederikse et al., 2018), which has significant spatial resolution limits.

3.1 Steric Sea Level Change in the Arctic

Steric sea level change, \dot{S}_{SH} describes the change in density and associated contraction or expansion of the water column caused by a change in water salinity or temperature. Following the notion of Gill and Niller (1973); Stammer (1997); Calafat et al. (2012); Ludwigsen and Andersen (2020), the change in steric heights are calculated as:

$$\dot{S}_{ST} = \dot{S}_{HS} + \dot{S}_{TS} \quad (3.1)$$

, where \dot{S}_H and \dot{S}_T defines the contribution from salinity change (halosteric) and temperature change (thermosteric) respectively. The parts of the right-hand side of equation 3.1, are defined as

$$S_{HS} = -\frac{1}{\rho_0} \int_{-H}^0 \beta S' dz \quad (3.2)$$

$$S_{TS} = \frac{1}{\rho_0} \int_{-H}^0 \alpha T' dz \quad (3.3)$$

where H denotes the minimum height (maximum depth (z)). S' and T' are defining salinity and temperature anomalies. The reference values used in Ludwigsen and Andersen (2020) are 0 C° and 35psu, which we assume to be Arctic-mean values. Since we only consider changes in sea level, the choice of reference values has no impact on the results. β represents the saline contraction coefficient and α the thermal expansion coefficient. The opposite sign of S_H is needed since β represents a contraction. α and β are functions of absolute salinity, conservative temperature and pressure, and is determined with help from the freely available Thermodynamic Equation of SeaWater 2010 (TEOS-10) software (Roquet et al., 2015).

The DTU Steric sea level product is created from more than 300.000 T/S profiles from 1980-2018. A large number of the profiles are taken from the UDASH-database (Behrendt et al., 2017), which has collected all available profiles from 1980-2015. Additionally the latest data from ARGO, Ice Thetered Profiles (ITP's) and other profiles included in the World Ocean Database are extending the temporal coverage to include 2018. Figure 3.1 shows the locations and maximum pressure of the hydrographic profiles divided into 5

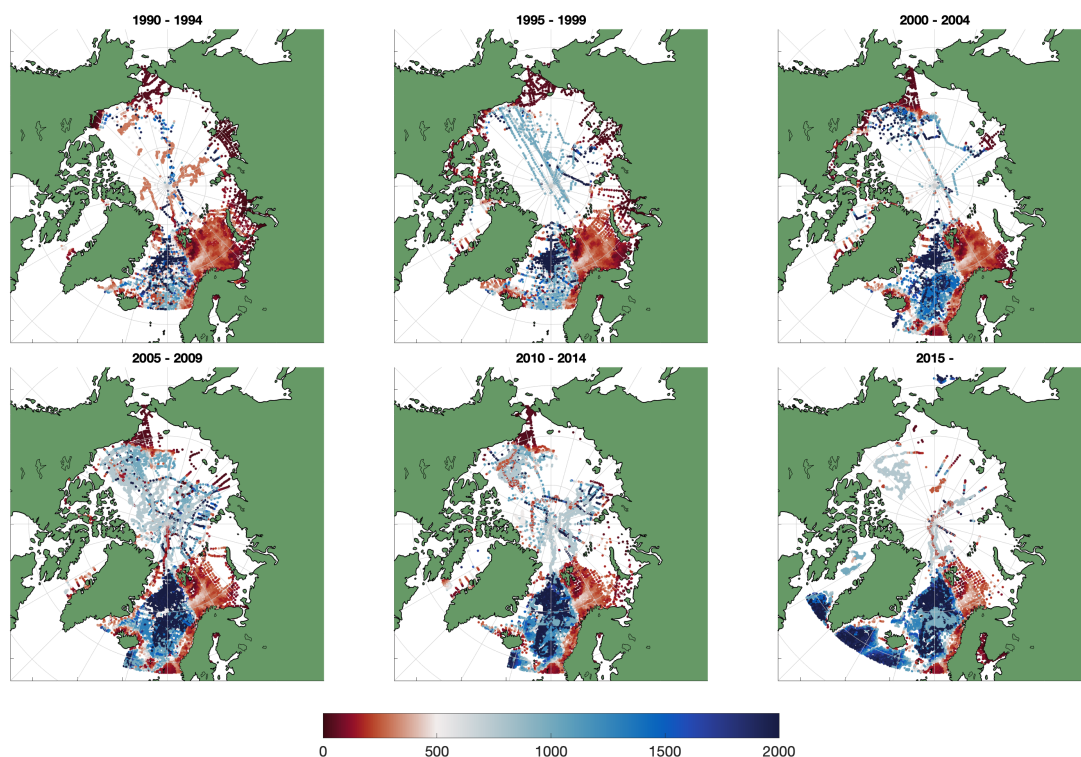


Figure 3.1: Maximum reached pressure (bar) for the T/S profiles included in this work (1 bar \approx 1 m depth), divided into 5-year intervals.

year intervals. In general does ice-free regions in the Norwegian and Greenland Sea show best coverage, while in particular the Laptev and East Siberian Seas are less represented. The Beaufort Sea and interior Arctic Ocean has better coverage than the Siberian coast, but are in some years also significantly lacking hydrographic data.

The process steps for creating DTU Steric are described in Ludwigsen and Andersen (2020). In short, T/S data are interpolated so that the vertical profiles makes physical sense, i.e. follows within 1σ the shape of a median profile in 100-km radius. Secondly, profiles are averaged into monthly 50x50 km blocks for 46 pressure intervals (10-bar steps from 10 to 200 bar, 50 bar steps from 250 to 1000 bar and 100 bar steps from 1100 to 2000 bar). The T/S values are horizontally interpolated by kriging, where-after spatial outliers are removed. Occurring gaps are filled with data from the same months in adjacent years, to preserve the seasonal variability, which is visible in figure 3.3.

Figure 3.2, shows how the halosteric sea level contribution varies from year to year. While a general freshening of the Beaufort Gyre is visible, we see that the inter-annual variations are large. Armitage and Davidson (2014) documented a decline in halosteric sea level from 2012 to 2014, that is dominated by 5-10 mm y^{-1} downward trend in the East Siberian and Laptev Seas. Because of inter-annual interpolation, is this drop recognized to a lesser extent in DTU Steric, but in particular from 2012 to 2013 is a decline of halosteric sea level in the East Siberian Sea visible.

The steric contribution to sea level change, has sometimes in literature been computed as the difference between ocean bottom pressure and sea level observed by altimetry (Morison et al., 2012; Armitage et al., 2016). DTU Steric is the only Arctic steric sea level

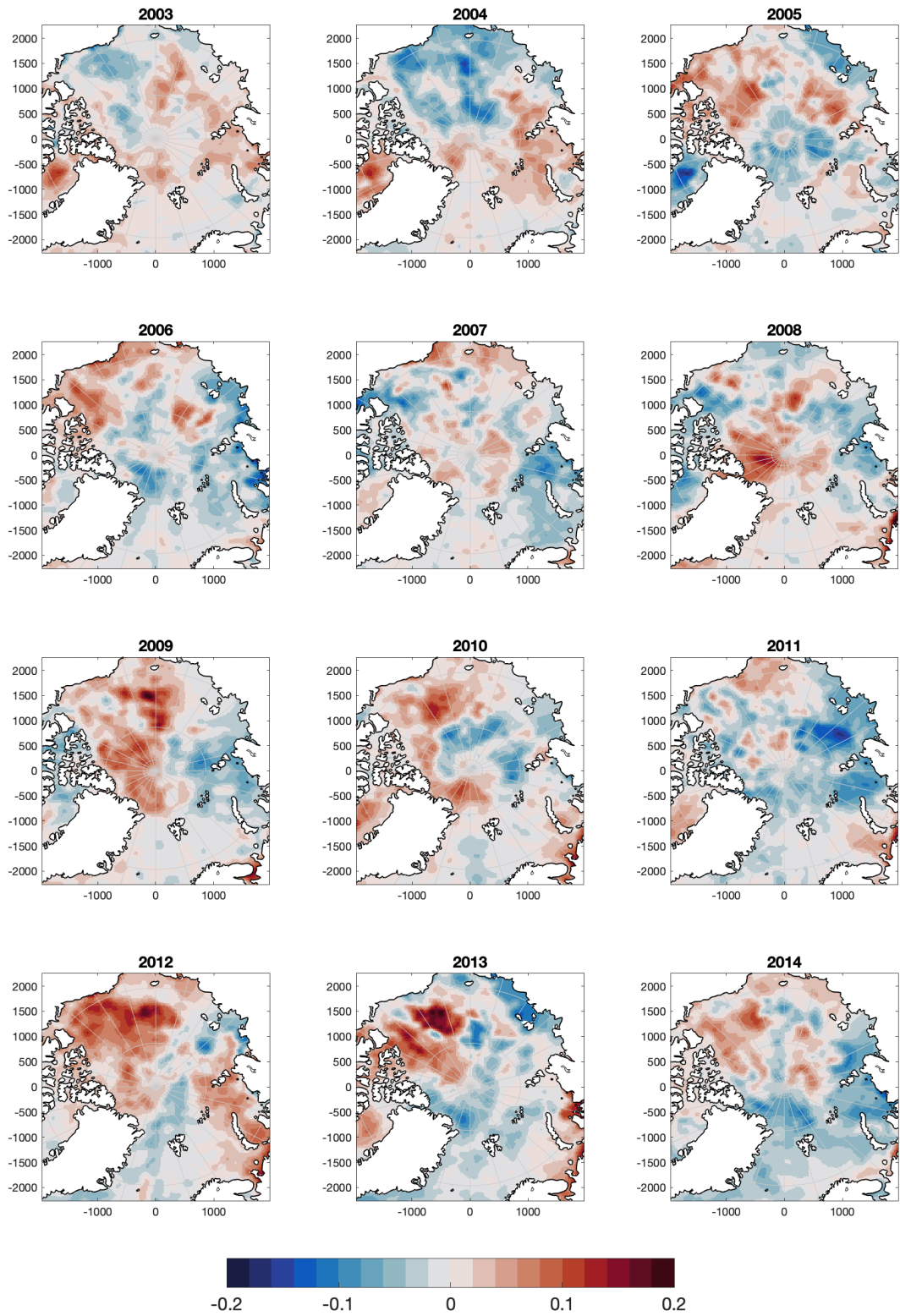


Figure 3.2: Yearly averaged halosteric sea level anomalies [m] for 2003-2014 (ref. period 1995-2015).

product that is based only on temperature and salinity profiles. The seasonal variations of the Barents, Beaufort and East Siberian Sea, is shown in figure 3.3, together with the difference between GRACE (JPL Mascons, (Wiese et al., 2016)) and SSH from altimetry (Armitage et al., 2016). Some of the differences originates in different bias' in the datasets, where altimetry has best data quality during winter due to fewer of meltponds on top of ice (Peacock and Laxon, 2004), the temperature and salinity data are more consistent during the summer months because of more data (Behrendt et al., 2017).

The 'doming' of the Beaufort Gyre is well captured in both satellite-based steric heights and the steric heights from DTU Steric. The average seasonal signal shows however a opposite pattern. For the Barents Sea, where the T/S data density is generally good (data density is shown in figure 3.4), the two datasets have opposite trends and DTU Steric data lacks some of the variability of the satellite-based estimate. In the East Siberian Sea, that has the lowest data density, is the seasonal signal well represented in both datasets, even though DTU Steric lacks winter data. Furthermore, are trends in the East Siberian Sea strongly opposite, where satellite-based products show a sea level decline, is DTU Steric increasing. Studies showing an increased freshwater contribution from river runoffs in the Russian Arctic (a.o. Povalishnikova et al. (2018)) indicates, that an increasing steric sea level contribution is more authentic.

Maps of the 2003-2015 halosteric and thermosteric sea level trend is shown in figure 3.4), together with the DTU Steric trend and the altimetry minus GRACE (satellite-based) steric trend. Altimetry data north of 81.5°N are interpolated, so they should only be compared with caution.

The DTU Steric dataset is available in netcdf-format here: <ftp://ftp.space.dtu.dk/pub/DTU19/STERIC/DTU19Steric.nc>.

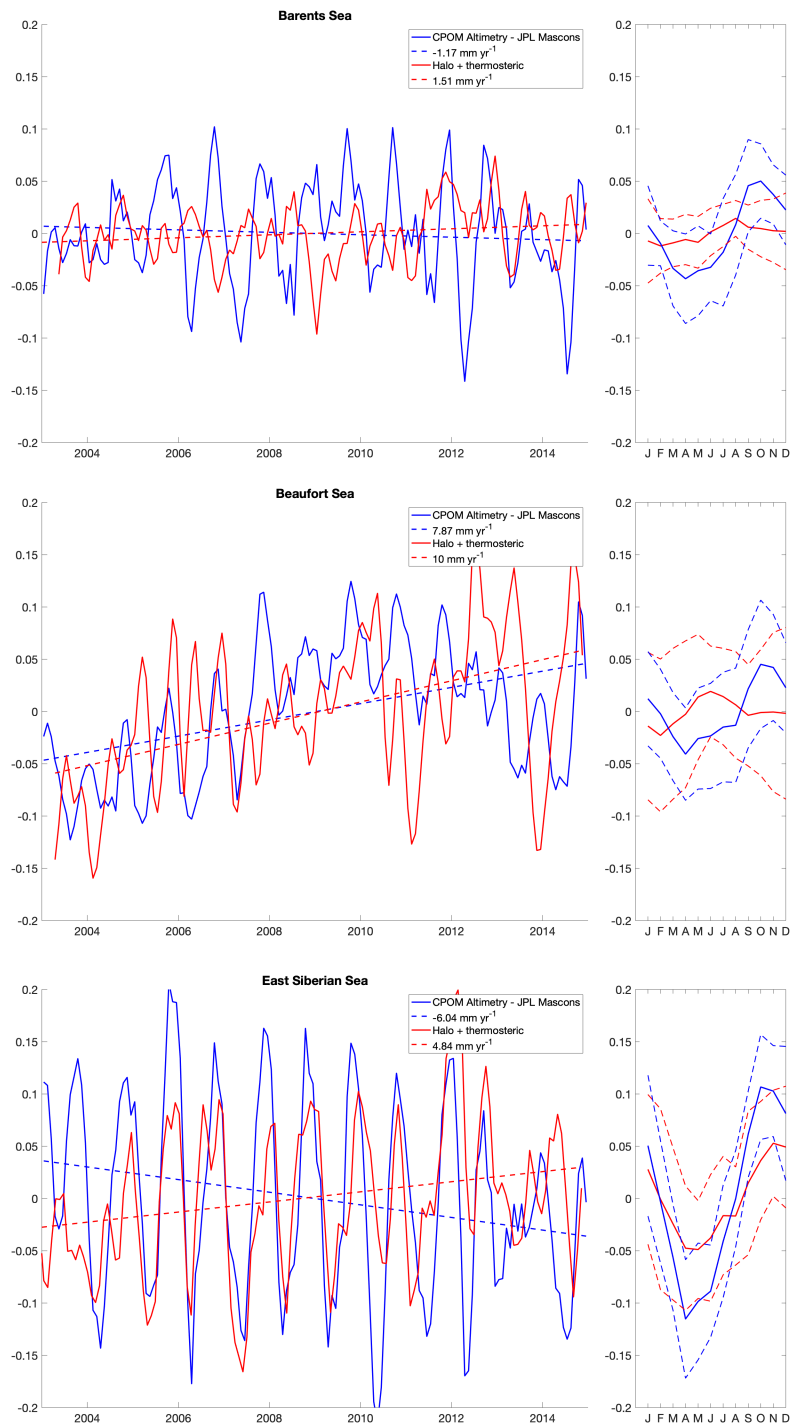


Figure 3.3: DTU Steric sea level timeseries compared to a CPOM Altimetry minus GRACE (JPL Mascons). From top: Barents Sea (71° - 78° N, 20° - 50° E), Beaufort Sea (71° - 78° N, -160° - -135° W), East Siberian Sea (71° - 78° N, 140° - 170° E). Right panel shows the average for every month and 1σ (dashed lines).

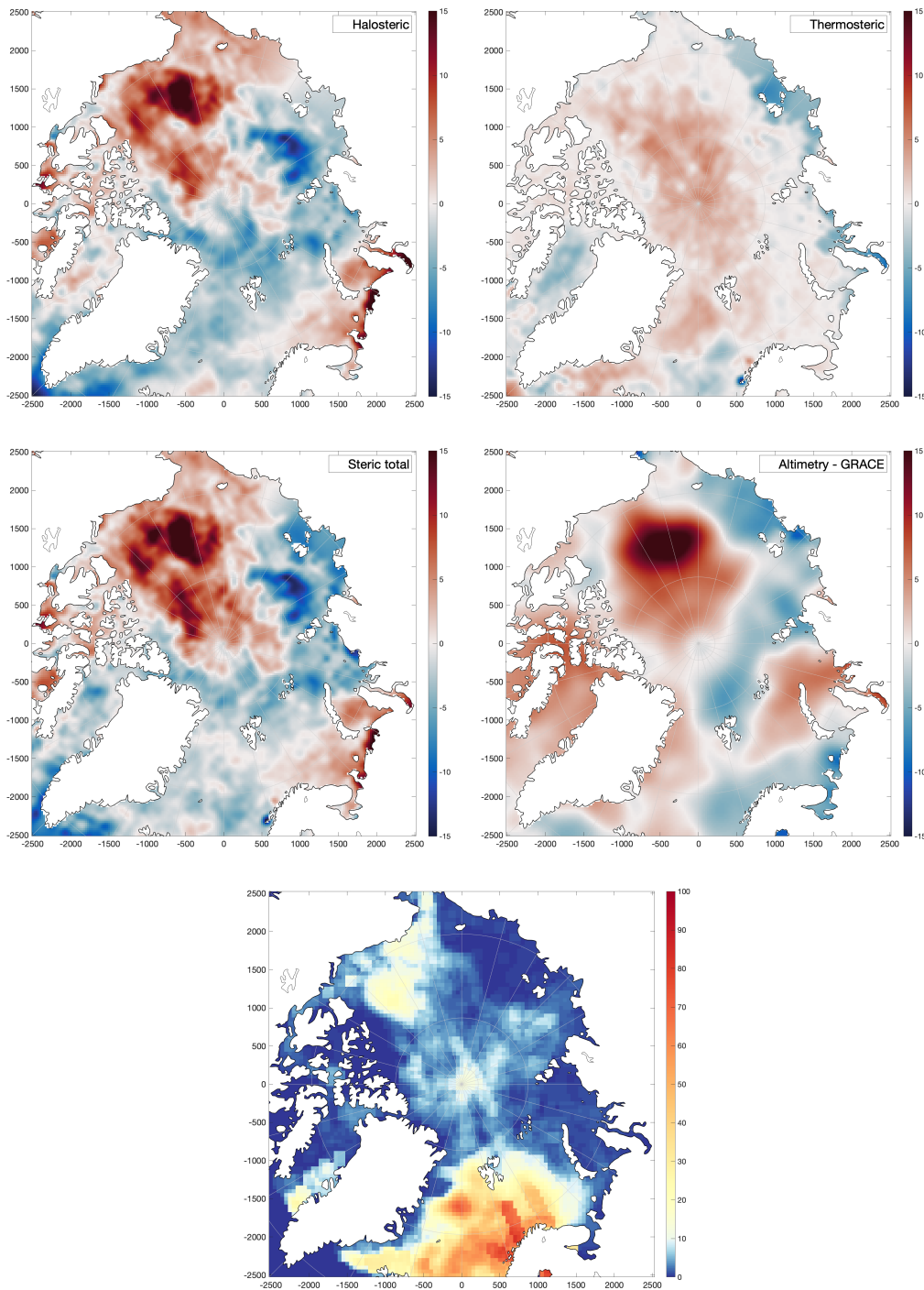


Figure 3.4: Sea level trend maps from 2003-2015 of halosteric, thermosteric, total steric and CPOM altimetry minus GRACE (JPL Mascons) [mm y^{-1}]. Bottom maps shows the data density as a percentage of months with data in a 50 km radius.

3.2 Vertical Land Motion

Quantifying Vertical Land Motion (VLM) is essential when relative sea level measurements from tide gauges with any other model or satellite-based estimates of sea level (e.g. Altimetry, GRACE, steric sea level). As written in chapter 1, VLM is a composite of multiple ongoing processes with GIA being the most prominent. While GIA (\dot{U}_{GIA}) has been modeled by the scientific community for decades (Peltier, 1974; Farrell and Clark, 1976), only in recent years has attention been given to the immediate elastic response to present-day ice loading (PDIL), \dot{U}_{PDIL} (Riva et al., 2017; Schumacher et al., 2018; Frederikse et al., 2019). In particular in the Arctic, where considerable land ice loss due to climate change is observed in every region (Moon et al., 2018), is the elastic vertical deformation essential for tide-gauge corrections. Estimates of ice loading changes from GRACE has recently been used to estimate elastic VLM (Frederikse et al., 2019). The limited spatial resolution of GRACE is however insufficient when tide gauges are located close to glaciated areas, since the mass loss from GRACE is spread over large areas which results in area-averaged uplift rates. Similar to other studies, we assume the viscoelastic GIA-like response from PDIL on annual scales is small (Bamber and Riva, 2010; Schumacher et al., 2018; Caron et al., 2018), but can accumulate to be significant after decades of deglaciation (Whitehouse et al., 2007). In regions with complex earth structures, like the West Antarctic Ice Sheet, can the viscous response from PDIL be significant today (Hay et al., 2017; Barletta et al., 2018; Powell et al., 2019). The uplift associated with GIA, \dot{U}_{GIA} , is here constrained to the viscoelastic uplift associated with the deglaciation on millennial scales starting 122 kyr ago (Caron et al., 2018).

We define total VLM-signal \dot{U}_{tot} as the sum of \dot{U}_{GIA} , \dot{U}_{PDIL} and VLM that is undefined from other sources of surface loading, \dot{U}_{other} :

$$\dot{U}_{tot} = \dot{U}_{PDIL} + \dot{U}_{GIA} + \dot{U}_{other} \quad (3.4)$$

The main focus of this section will be \dot{U}_{PDIL} , which it is original and a highly relevant consequence of a warming Arctic, since elastic VLM is directly affected by present-day deglaciation.

3.2.1 Present-day ice model

We divide the ice model of PDIL into a model for glaciers, Greenland ice sheet and Antarctic ice sheet. Glaciers and the Greenland Ice Sheet is constructed in a high-resolution 2x2 km grid. The elastic and gravitational signal from the southern hemisphere is small and almost spatially invariant in the Arctic and thus is the spatial resolution for Antarctica and southern hemisphere glaciers insignificant for the Arctic Ocean. The total mass loss of each of PDIL is shown in figure 3.5.

Glacial model

Parts of this section is also described in the supplementary material of Ludwigsen et al. (2020a), chapter 5.

Mass balance estimates from globally around 120.000 glaciers (excluding glaciers from Antarctica and Greenland) are provided by an updated model of Marzeion et al. (2012), which is constrained by direct mass balance estimates from Zemp et al. (2019). About 85% percent of the total global glacial mass loss is happening north of 50°N (Zemp et al., 2019).

Yearly glacial mass balance, b , (provided in gigatonnes per year, figure 3.6) is converted to change in equivalent water height (meters per year). For glaciers smaller than 4 km²,

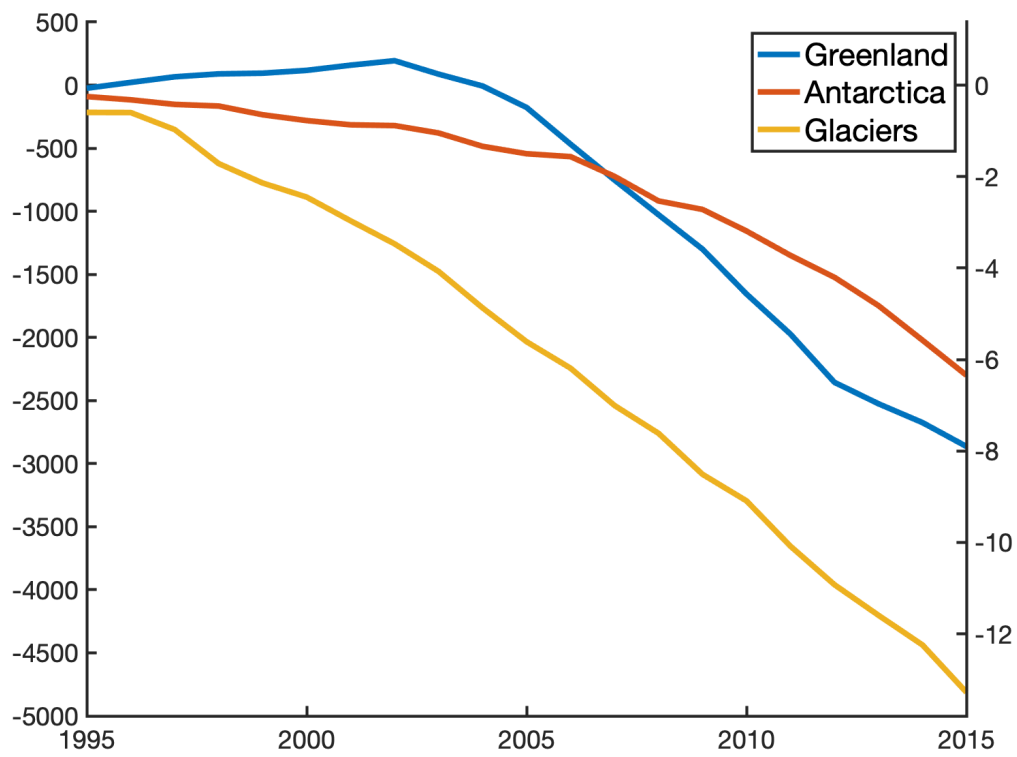


Figure 3.5: 1995-2015 ice mass loss [gigatonnes] from Greenland ice sheet, Antarctic ice sheet and glaciers included in this study. Right y-axis shows the global sea level equivalent [mm].

the ice loss is assumed equal over the area of the glacier, while for glaciers larger than 4 km², we combine glacial mass loss with shapefiles from the sixth version of the Rudolph Glacier Inventory (RGI 6.0) (RGI Consortium, 2017) and 1 arc-min topography, ETOPO1 from Amante and Eakins (2009). A distribution function, D , is created, so that glaciers experience the largest mass loss at the bottom of the glacier, which decreases with altitude. This pattern is recognizable for most glaciers losing mass and is also observed with altimetry (Nuth et al., 2010; Foresta et al., 2016; Ciraci et al., 2018). Since the model is not considering firn compaction, 1:1 comparison with altimetry would however be misleading. Maps of glacial mass balance and the resulting elevation change is shown in figure 3.7 and 3.8. The altitude, where the mass balance becomes positive is denoted as E , which is not directly related to the equilibrium line altitude. E is defined from \tilde{Z} is the median glacial height and \bar{h} is the average ice height change (in meters),

$$E = (1 - \bar{h})\tilde{Z} \quad (3.5)$$

, where \bar{h} is defined as

$$\bar{h} = b(\rho A)^{-1} \quad (3.6)$$

, where A is the area of the glacier, ρ is the density (917 kg m⁻³). The distribution function, D is defined as

$$D(i) = 1 - \exp\left(\frac{(2 - \bar{h})(E - Z(i))}{Z_{max}}\right) \quad (3.7)$$

D in equation 3.7, is normalized and multiplied with the mass balance, to ensure that mass is conserved:

$$\frac{dh(i)}{dt} = \frac{b}{\rho A_i} \frac{D(i)}{\sum_{i=1}^k D(i)} \quad (3.8)$$

here is A_i the specific area for the grid cell, i , which in this case is 4 km². Height change profiles with varying b of an idealized glacial example of equation 3.8 is shown in figure 3.6.

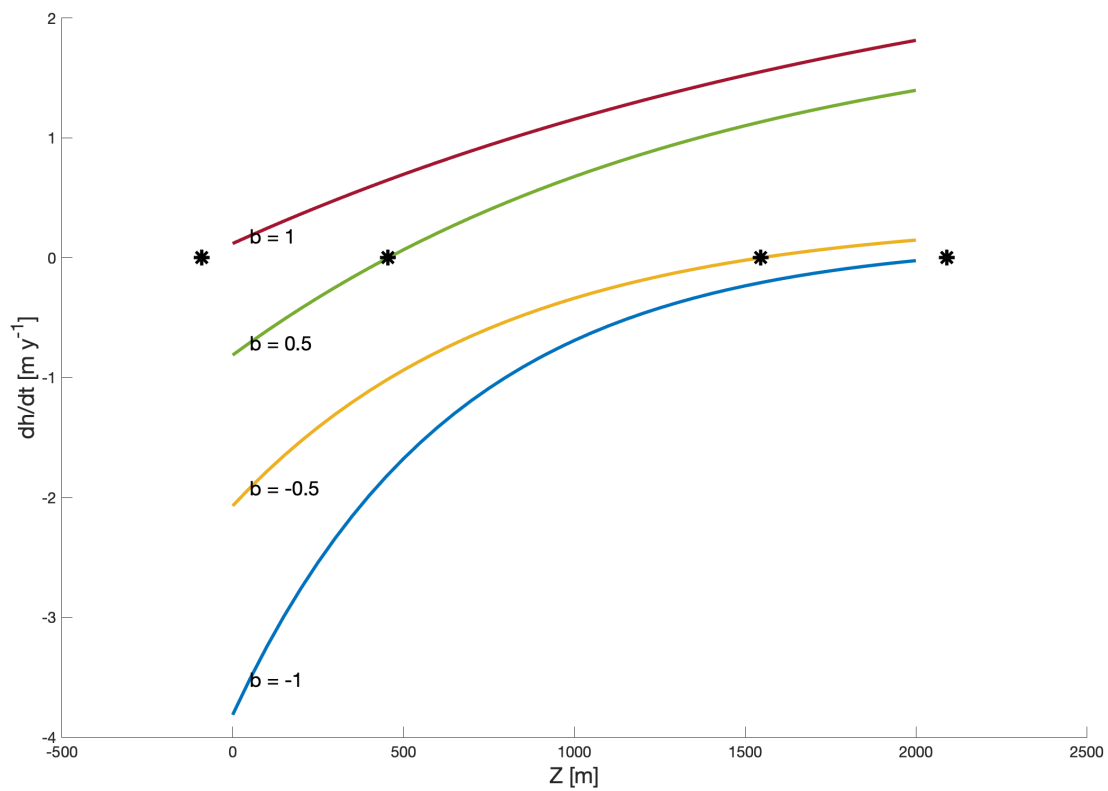


Figure 3.6: Height change profiles of an idealized glacier with varying b (in gigatonnes). Example glacier has $A=1000 \text{ km}^{-2}$ and spans from 0 to 2000 meters height (Z). The asterisks (*) marks the height of E .

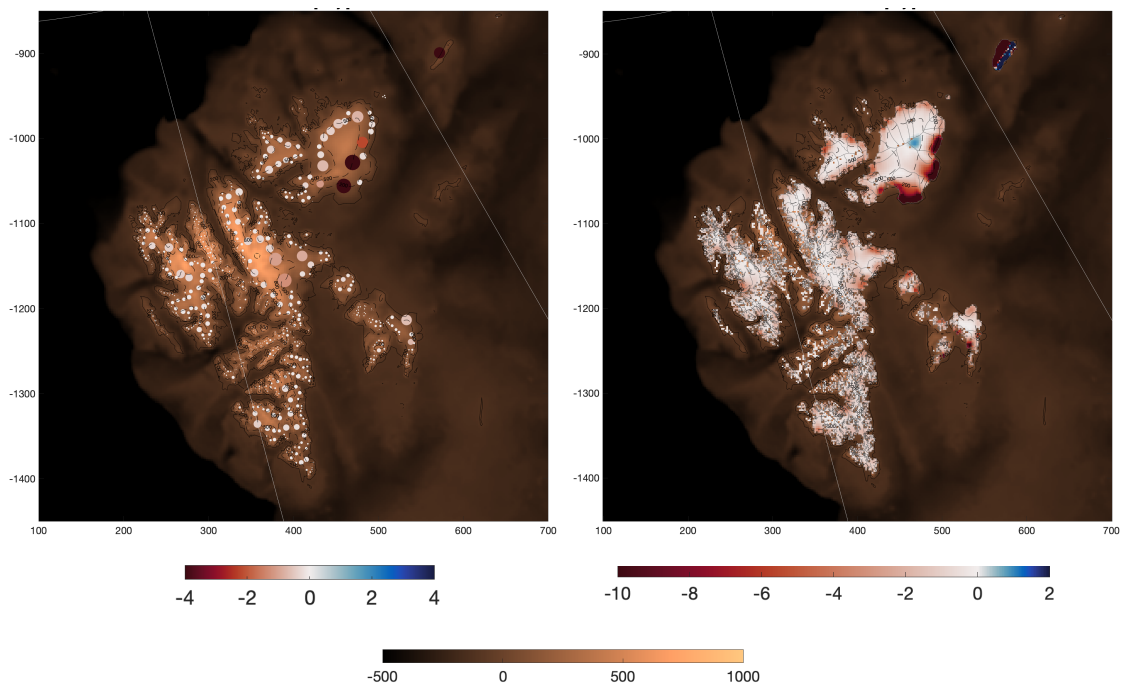


Figure 3.7: Left column: 2003-2015 average mass balance [Gt yr^{-1}] for glaciers on Svalbard from the model by Marzeion et al. (2012). Size of circle is proportional with glacier area. Right column: Equivalent water height (EWH) elevation change from 2003 to 2015 in m yr^{-1} resulting from the redistribution of the mass balance. The EWH elevation change is not comparable with actual ice elevation change, since no model for firn has been applied. The values on the map are proportional with mass changes (assumed density of 917 kg m^{-3}). Outlines of glaciers are indicated with dashed lines. Topography scale at the bottom.

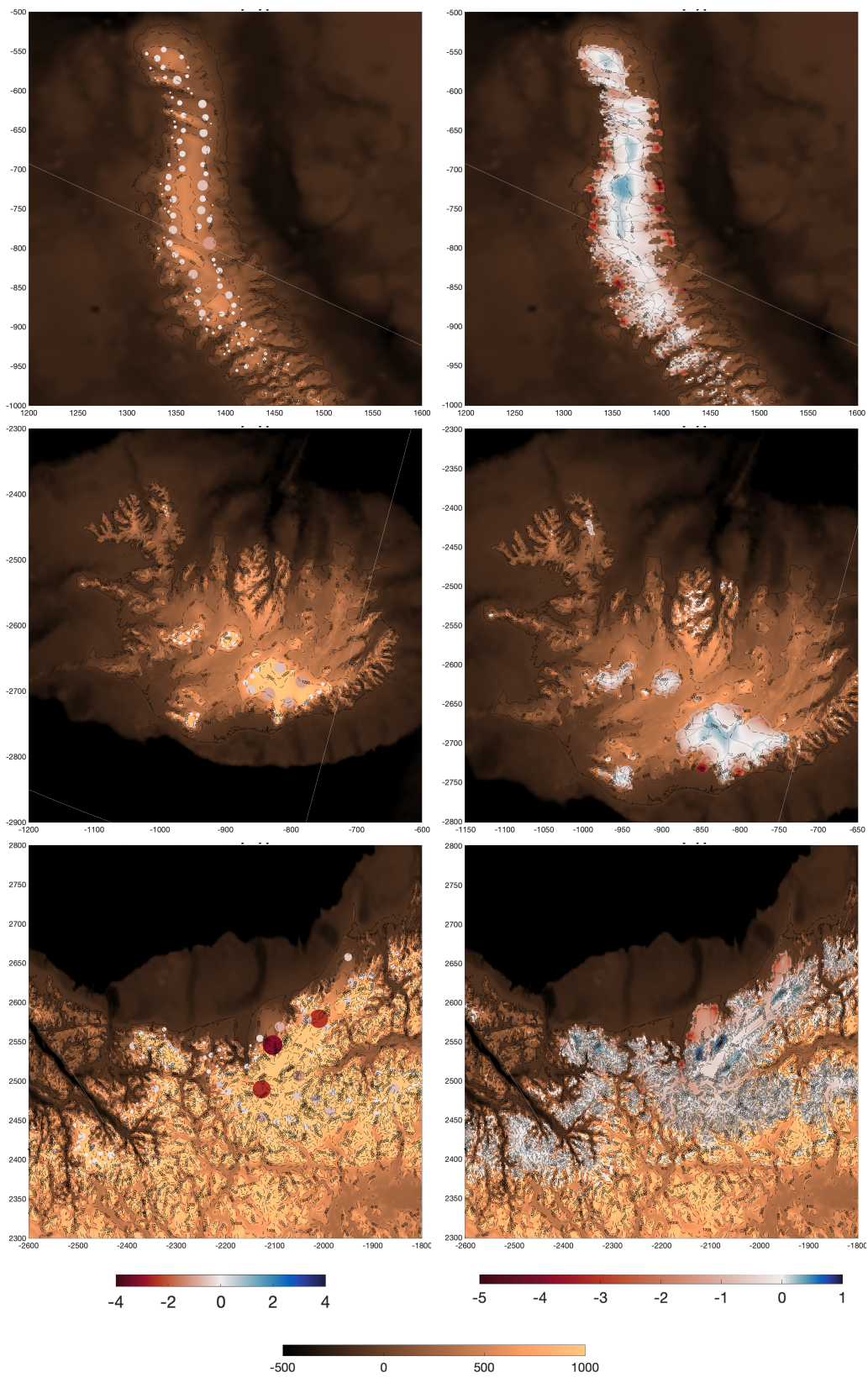


Figure 3.8: Similar to figure 3.7, but for (from top) Novaya Zemlya, Iceland and the Alaska south-west coast.

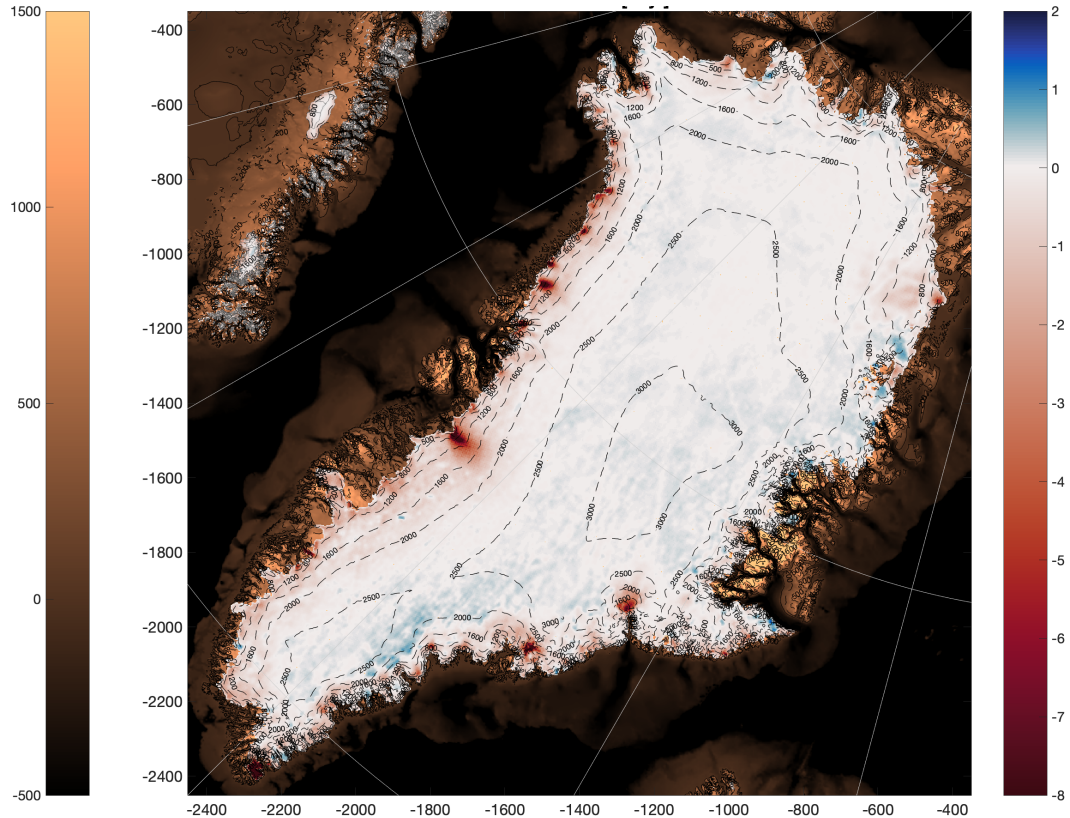


Figure 3.9: Average ice elevation change [m yr^{-1}] from 2003-2015 for the Greenland Ice Sheet. Left colorbar indicates the topography [m].

Greenland

Present-day elevation change of Greenland (with glaciers) is described in Ludwigsen et al. (2020a) and is based on an elevation model from Abbas Khan, DTU Space (Khan et al., 2014). Its method follows a procedure that was also used in Ewert et al. (2012); Smith et al. (2009); Kjeldsen et al. (2013). In short, it combines remote sensing data from Airborn Topographic Mapper (ATM) flights (Krabill, 2011), with ICESat data (Zwally et al., 2011) and CryoSat-2 (Helm et al., 2014). It has a native high resolution of 2×2 km and due to the use of altimeter data is it very well constrained from crossing satellite tracks (Khan et al., 2014). Ice elevation change (in equivalent water heights) is shown in figure 3.9.

Antarctica

The Antarctic contribution to Arctic ocean sea level is estimated from the elevation model by Schröder et al. (2019) which is given in a 10×10 km resolution. The Antarctic mass balance from 1995-2015 is -110 Gt yr^{-1} , which is in agreement with the IMBIE-estimate (Shepherd et al., 2018). The elevation change is based on top-of ice measurements, but is for the purpose of calculating the elastic response, scaled to match the total mass assuming an uniform ice-density (917 kg m^{-3}). Elevation change rates are shown in figure 3.10.

3.2.2 Elastic Vertical Land Motion

From the high resolution ice model, we can compute elastic VLM from PDIL, \dot{U}_{PDIL} . For the calculations we use the Regional ElAstic Rebound calculator (REAR) developed by Danielle Melini (Melini et al., 2015). It is designed for calculating the direct elastic response to changed surface loading (Farrell, 1972; Clark and Lingle, 1977), but it does not solve the sea level equation (Farrell and Clark, 1976) that also includes the viscoelastic deformation

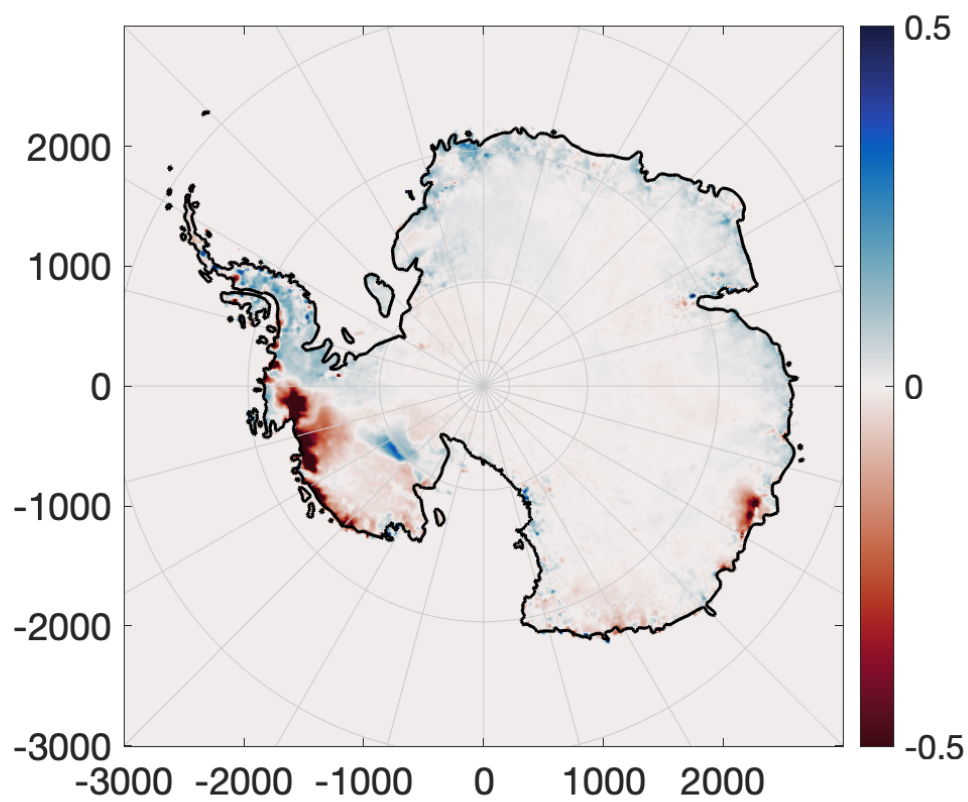


Figure 3.10: Average ice elevation change [m yr⁻¹] from 1995-2015 for Antarctic Ice Sheet.

and is usually gravitationally self-consistent (Milne and Mitrović, 1996), which among others would include the effect of ocean loading.

Contrary to GIA, where viscous mantle flow is happening over time, is \dot{U}_{PDIL} assumed to be an instantaneous elastic process (Peltier, 1974). We follow the theory of Farrell (1972) in the adaption of Melini et al. (2015). The elastic response to a disc surface loading can be expressed as Green's Functions (GF's) for vertical and horizontal displacement (u, v) and gravitational potential (ϕ).

$$\begin{Bmatrix} u \\ v \\ \phi \\ g \end{Bmatrix}(\psi) = \frac{3\rho_i}{\rho_e} H \sum_{\ell_{max}}^{\ell_{min}} \begin{Bmatrix} h'_\ell \\ l'_\ell \\ 1 + k'_\ell \end{Bmatrix} \frac{f_\ell(\alpha)}{2\ell + 1} \begin{Bmatrix} 1 \\ \frac{\delta}{\delta\psi} \\ 1 \end{Bmatrix} P_\ell(\cos \psi) \quad (3.9)$$

Here h'_ℓ , l'_ℓ and k'_ℓ are the Load Deformation Constant's (LDC's) or also called 'Love numbers' for spherical harmonic degree ℓ . LDC's define the properties of the Earth and comes predefined in the Earth model, described later. ψ is the angle-distance to the load (0=load center, 180=antipode), ρ_i , ρ_e , is respectively the average density of the load and Earth, H is the change in load thickness, f_ℓ is a shape-factor dependent on the radius of the load α and $P_\ell(\cos \psi)$ is the Legendre polynomial. The shape-factor is defined as (Melini et al., 2015):

$$f_\ell = \frac{P_{\ell+1}(\cos \alpha) - P_{\ell-1}(\cos \alpha)}{1 + \cos \alpha} \quad \text{if } \ell > 0. \quad (3.10)$$

Throughout this thesis, we do not consider horizontal displacement (v) from changes in surface loads, because it in general is a magnitude smaller than vertical displacement and has little impact on sea level change. From equation 3.9, the geoid height variation (equivalent to G in equation 1.3, chapter 1) and vertical displacement, U , at a location with co-latitude, θ and longitude λ is the sum of the GF's for every load (k):

$$\begin{Bmatrix} U \\ G \end{Bmatrix}(\theta, \lambda) = \sum_{k=1}^{N_d} \begin{Bmatrix} u_k \\ \phi_k \\ g \end{Bmatrix}(\psi_k) \quad (3.11)$$

where N_d is the number of disc loads.

The ice loading input of REAR is in an flexible point-format [co-lat lon dh/dt radius], where dh/dt is the ice elevation change and radius is the user defined radius of the circle-area that is represented by the point. A 2x2 km resolution (4 km²) equals a radius (α) of 1.128 km. REAR uses the Green's functions for elastic deformation and gravitational change described in chapter 1 (eq. 3.9 and 3.11). The loading deformation constants (LDC's) used for equation 3.9 are defined with respect to Earth's center of mass (CM). They are defined from the REF6371-model (Kustowski et al., 2007), which is an improved version of the commonly used PREM-model (Dziewonski and Anderson, 1981).

From 3.11 it is seen that both the elastic VLM, U and the elastic geoid change, G is a product of the GF's. Global maps of both \dot{U} and \dot{G} from the global icemodel described above is shown in figure 3.11.

The elastic VLM in the wider Arctic and the associated uncertainty is shown in figure 3.12 and for some selected glaciated regions in figure 3.13 (VLM only).

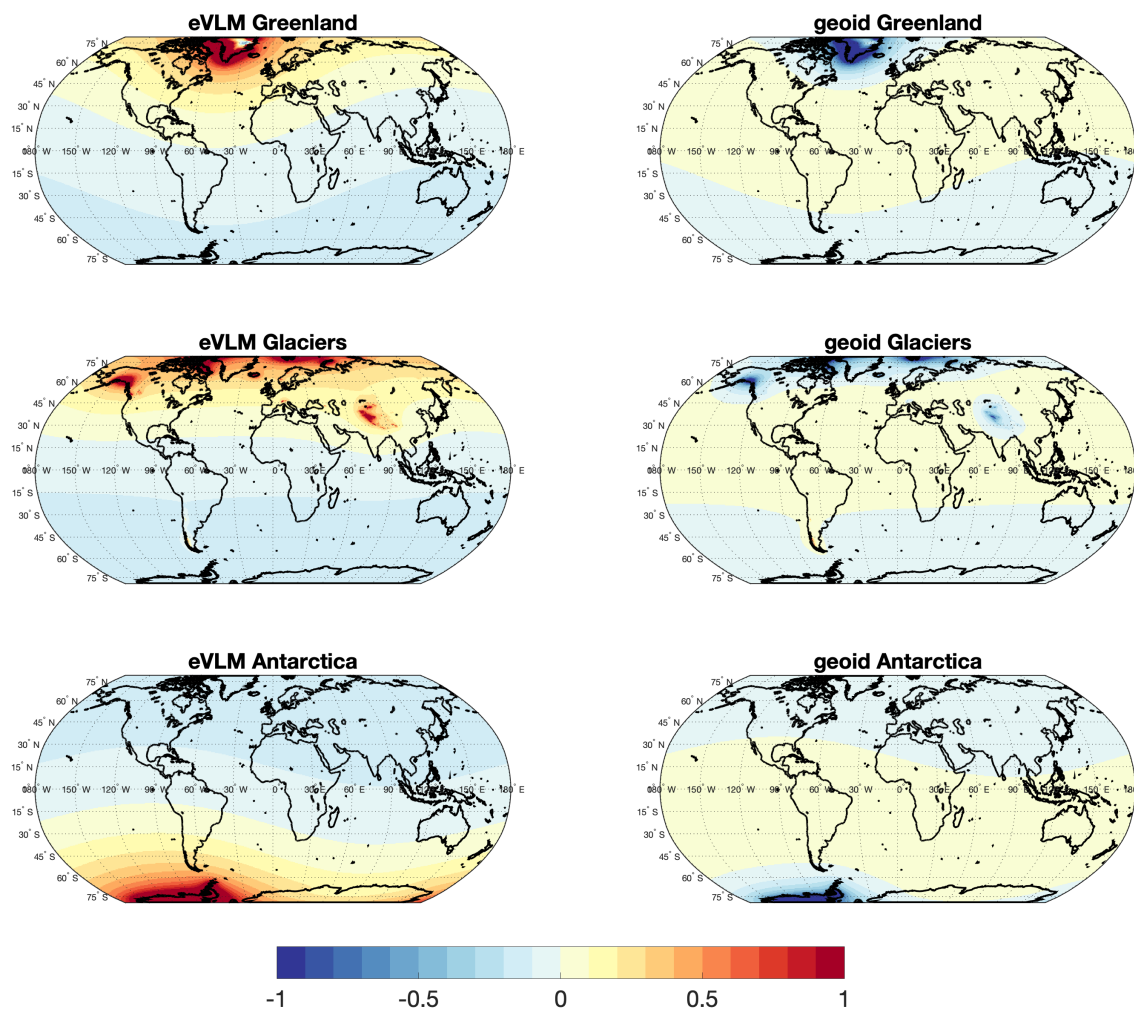


Figure 3.11: Left panel shows the VLM at global scale from each source [mm y^{-1}]. Right panel shows the geoid change (\dot{G}) associated with the melting of each source [mm y^{-1}].

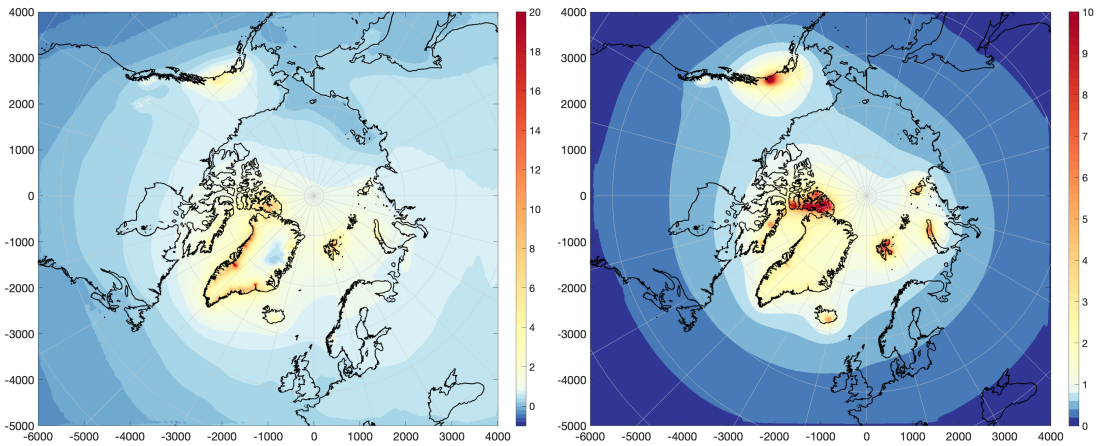


Figure 3.12: Left: Uplift from the VLM-model [mm y^{-1}]. Right: Uncertainty of the VLM-model [mm y^{-1}].

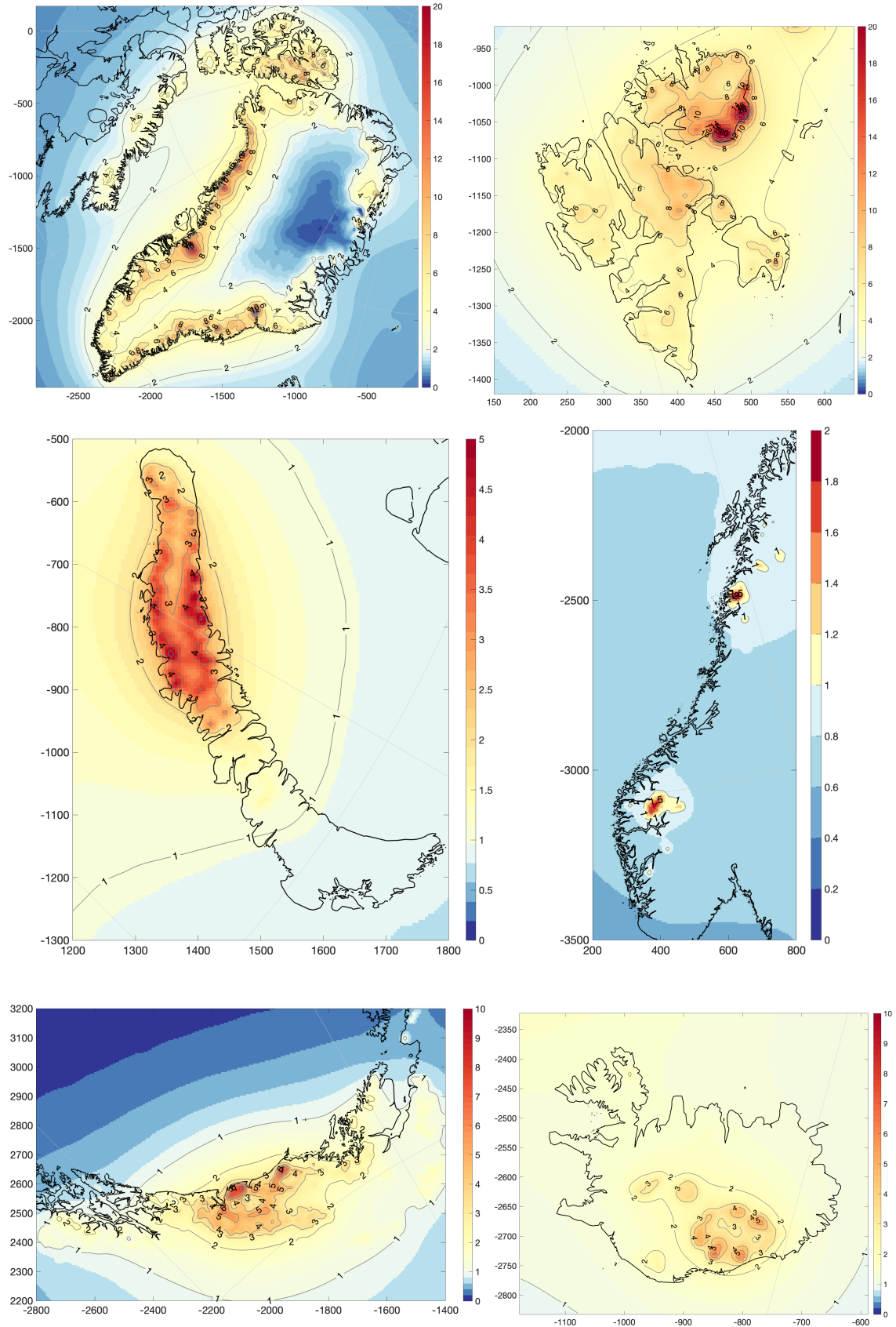


Figure 3.13: Enlargement of elastic VLM (only uplift) in some glaciated regions in the Arctic (on different colorscales) [mm y^{-1}].

3.2.3 GIA

To restore the complete VLM signal, we need to apply a model for glacial isostatic adjustment (GIA) which is the viscoelastic VLM caused by the unloading of ice after the last ice ages (typically 10-100 kyr ago) with last glacial maximum 21 Kyr ago. In publication 2 and 3, the Caron2018 GIA-model (Caron et al., 2018) has been used as the default GIA-model, while we also compare with the commonly used ICE6G-D-model (Peltier et al., 2015; Peltier et al., 2018).

The Caron2018-model utilized paleo-records of RSL and long-time TG and GNSS-data to construct a earth and ice-model that gives the statistical best fit to the data (Caron et al., 2018). The ICE6G-D GIA-model is actually an ice history model, which also is constrained with paleo-records and GNSS-uplift rates. Contrary to Caron2018, ICE6G-D uses a given earth model (VM5a) that is used to translate uplift rates to an ice loading history using the sea level equation (Farrell and Clark, 1976). The associated radial displacement (GIA) using the VM5a model is given as a by-product.

The two GIA-models and the difference between them is shown in figure 3.14. We see that they substantially disagree - in particular in North America where Caron2018 has 10 mm y⁻¹ higher rates than ICE6G-D, and in general is North America showing larger uplift rates in the Caron2018-model. Supplemental material in Caron et al. (2018) shows that GNSS and paleo records can be opposite considering their preferred viscosity profile, with paleo records in North America preferring high viscosities. The compromise gives higher viscosity values than GNSS-alone would predict, which means that the viscous deformation is not yet as relaxed which results in larger GIA uplift (from personal communication with L. Caron). The models disagree also in Greenland, where Caron2018-model poorly constrained, because of lack of paleo-records. Challenges in separating past and present ice dynamics, generally results in varying GIA-estimates in Greenland (Wake et al., 2016).

3.2.4 Other effects on VLM

The elastic VLM from present-day ice loading and viscoelastic VLM from GIA are the largest component of VLM. If the combined VLM-model should be aligned with GNSS on regional to global scales, we need to adjust for rotational feedback and non-tidal ocean loading (NOL). GNSS is referenced to ITRF2008 or ITRF2014, which is equivalent to the long-term average of center of mass (CM) (Dong et al., 2003). CM is also the reference frame of both the elastic calculations (defined by the LDC's) and the Caron2018-GIA model. However, are non-secular variations of GCM in center of figure (CF) (Dong et al., 2003), which means a detrended CM-CF translation is necessary to align GNSS with the constructed model.

The changes in loading from PDIL also changes the rotation of the pole, which causes an elastic deformation of the solid earth (Milne and Mitrovica, 1998; King and Watson, 2014). This rotational feedback (RF) was assumed to be at a near-constant rate on secular scales before the rapid present-day ice loss, since it was dominated by GIA (Milne and Mitrovica, 1998; King and Watson, 2014). The method of King and Watson (2014) is used to calculate RF from given daily C04 polar motion parameters from International Earth Rotation Service, available at <http://datacenter.iers.org>. RF in millimeters at a given latitude and longitude is according to King and Watson (2014) defined as:

$$\text{RF}(\text{lat}, \text{lon}) = -33 \sin(2\text{lat})((x_P - \bar{x}_P) \cos(\text{lon}) - (y_P - \bar{y}_P) \sin(\text{lon})) \quad (3.12)$$

, where x_P and y_P are provided by the C04 polar motion product given in arcsec. The reference values, \bar{x}_P, \bar{y}_P are defined as a cubic-fit from 1976–2010 and linear fit from 2010

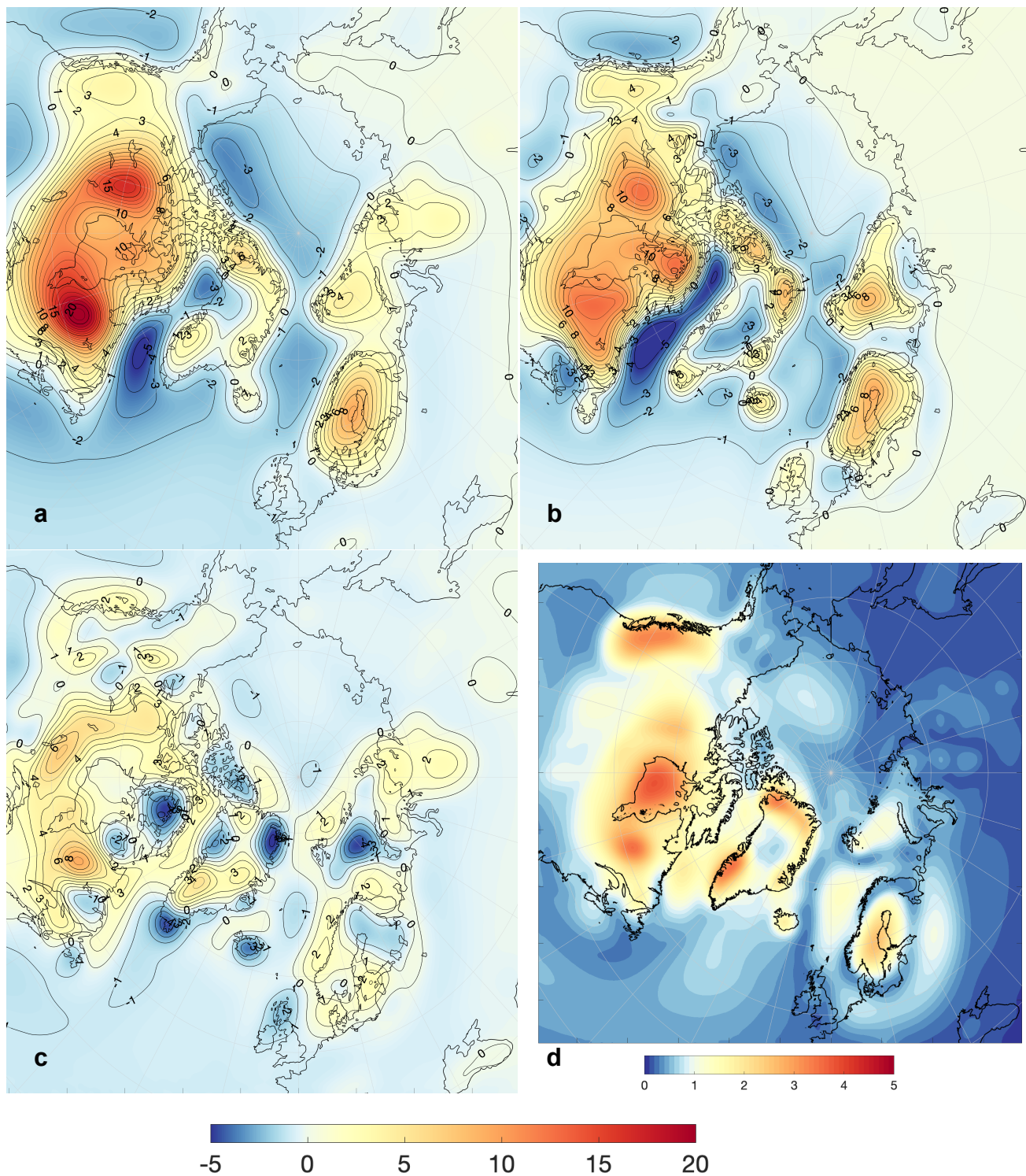


Figure 3.14: Present-day deformation rates (mm y^{-1}) from the GIA-model of Caron2018 (a) and ICE6G-D Peltier et al. (2018) (b). The difference between the GIA-models (Caron2018 minus ICE6G-D) is shown in (c). Uncertainty from Caron2018 is shown on a different colorscale (d)

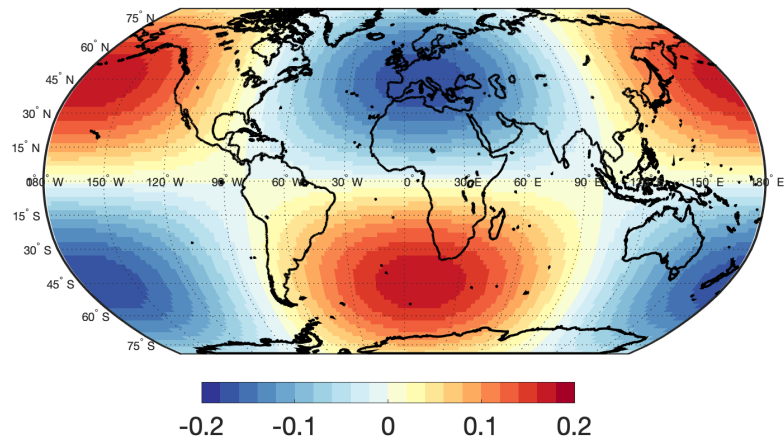


Figure 3.15: Average trend [mm y^{-1}] of elastic deformation caused by rotational feedback from 1995 to 2015.

(King and Watson, 2014). The average RF-trend from 1995 to 2015 is shown in figure 3.15.

Another effect on VLM is change in the terrestrial water storage (TWS) that causes an elastic deformation. While TWS locally can be the largest contribution to VLM (in particular in non-glaciated areas), the effect in the Arctic regions is limited. Frederikse et al. (2019) used GRACE-observations to estimate the TWS-caused elastic VLM effect to be $\pm 0.2 \text{ mm y}^{-1}$ in most of the Arctic, but with a uplift of $> 1 \text{ mm y}^{-1}$ in parts of North America.

4 Publication 1: Contributions to Arctic Sea Level

4.1 Preface

The first publication (Ludwigsen and Andersen, 2020) was published in *Advances of Space Research* in January 2020. It attempts to close the sea level budget in the Arctic, by utilizing the *DTU Steric* product that was developed during the first year of this PhD-project. It uses a straightforward approach, where ocean mass changes from GRACE-mascon products are combined with *DTU Steric* and compared with absolute sea level change estimates from satellite altimetry. Already in the early stages of the research it was realized, that neither different products of GRACE or altimetry were very consistent. Previous studies of Arctic Sea Level budget (Henry et al., 2012; Armitage et al., 2016; Carret et al., 2017) only utilized one altimetric sea level or GRACE mass product, which does not reflect the variance and uncertainty associated that becomes clear when using multiple independent estimates.

Three GRACE Mascon products and an ensemble mean are combined with both the DTU Steric product and steric calculations from the ECCOv4r3-oceanographic model (ECCOv4 was significantly improved from release 3 to release 4 in early 2020, which is the version showed in chapter 2) and compared to three versions (DTU, CPOM and RADS) of the 2003-2015 sea level trend based on satellite altimetry.

From 24 different combinations, this study showed that a combination of JPL Mascons (Wiese et al., 2016), the DTU Steric product and CPOM altimetry (Armitage et al., 2016) had the best spatial correlation ($R=0.76$) which clearly outperformed any combination with the ECCO-model. Thereby it was shown that the DTU Steric product, despite the lack of hydro-graphic data in some regions of the Arctic Ocean, was able to partially close the sea level budget and yield better correlation with altimetric observations.

C. A. Ludwigsen and O. B. Andersen, Contributions to Arctic sea level from 2003 to 2015, Advances in Space Research, <https://doi.org/10.1016/j.asr.2019.12.027>

Contributions to Arctic Sea Level from 2003-2015

Carsten A. Ludwigsen¹ and Ole B. Andersen²

*DTU Space, National Space Institute, Technical University of Denmark
Elektrovej 327, 2800 Kgs. Lyngby, Denmark*

1) *Corresponding author: caanlu@space.dtu.dk*

2) *oa@space.dtu.dk*

Abstract

As one of the most remote and inaccessible regions in the world, the sea level in the Arctic is still today in large parts uncertain. Sea level estimates from GRACE and satellite altimetry show disagreements in areas of the Arctic while only few in-situ measurements are present to validate satellite products. By using an independent in-situ based dataset of hydrographic data (DTUSteric), this study compares different available datasets from GRACE and altimetry. The best agreement ($R=0.76$) is reached between the combination of DTUSteric and the JPL Mascon solution and the altimetry product from Centre of Polar Observation and Modelling (CPOM). A large residual signal is found in the East Siberian Sea, an area with no in-situ observations and in general uncertain satellite observations. The spatial correlation coefficients ranging from 0.32-0.76 reflects a large number of unknowns and uncertainties, with coarse GRACE resolution, extensive interpolation and lack of in-situ data in parts of the Arctic Ocean and uncertainty of the altimetric products being the largest sources of error. In general, we recommended that satellite observations are used carefully in the Arctic. Even this study shows that steric estimates from in-situ observations to some extent can explain the gap between GRACE and altimetry, the observed sea level trend in significant regions of the Arctic cannot be validated with in-situ hydrographic data.

Keywords: Arctic, Sea Level, Climate Change, Ocean

1. Introduction

The Arctic region is experiencing the most rapid climate changes in the world (Blunden & Arndt, 2013; Box, et al., 2019). Change in water temperature and freshwater inflow can change patterns of ocean currents with effects on the North Atlantic Circulation (Proshutinsky, et al., 2015; Tedesco, et al., 2016). Thus, is analyzing changes in sea level important for understanding water mass exchange,

changing currents, freshwater flow and estimating sea ice freeboard (Wang, et al., 2017; Armitage, et al., 2018; Kwok & Morison, 2015).

Due to the inaccessible and remote location of the Arctic, large parts of the Arctic Ocean are rarely measured by in-situ observations. Since the first altimetric measurements by the ERS-1 mission in 1991, sea level change is used as a measure of spatio-temporal oceanographic variations, such as changing currents, freshwater content and water mass fluxes from land to ocean. However, due to an inclination of 98.5 degrees to the Earth's equatorial plane part of the Arctic Ocean is not reached with altimetry, referred to as the Arctic 'pole hole' above 82 deg latitude where the change of sea level is unknown. Since 2010, this has to some extent changed with Cryosat-2 (inclination 92 degrees). Additionally, altimetry is challenged by sea ice, which significantly limits the amount of exploitable observations. ERS-1/2 and Envisat both had low resolution altimeters that were not able to do stack analysis like CryoSat-2 is in SAR mode. The additional information gained by SAR altimetry is important to distinguish between return signals from melt ponds on top of sea ice and open ocean, which has similar waveforms. Furthermore, 20Hz SAR data from CryoSat-2 is far better in detecting sea level in leads between sea ice floes.

From mid 2002 to 2017 the Gravity Recovery and Climate Experiment (GRACE)-twin satellites measured the gravitational change of the Earth's surface. GRACE provides change of water mass without the challenges of sea ice, but can only determine signals with wavelengths of several hundred km's, whereby the rapid changes of melting land ice shadows the smaller ocean mass changes. Recently, the most common way of separating land and ocean signals from GRACE, has been by separating the gravitational signal into mass concentration blocks ('mascons') where geophysical constraints are implemented a priori (Wiese, et al., 2016; Luthcke, et al., 2013; Save, et al., 2016). In the following we use the term ocean bottom pressure (OBP) for sea level changes seen by GRACE, referring to pressure change at the bottom of the ocean induced by a change of mass in the water column.

GRACE observes eustatic sea level change, which must be complemented with steric sea level to enable a comparison with altimetry. Steric sea level is the change in ocean density induced by changing temperature and salinity (T/S). T/S values of the water column are measured regularly by the ARGO-program at mid to low latitude, but only few buoys reach the Arctic ocean because of sea ice cover (Behrendt, et al., 2017). T/S-profiles from campaign data and buoys designed for the Arctic environment provide some sparse information, but only very few regular measurements exist. Studies of steric sea level in the Arctic are consequently dependent on ocean models, which either is constrained by GRACE and/or satellite altimetry.

Recent studies by Armitage, et al. (2016), Andersen and Piccioni (2016) and Carret, et al. (2017), all attempt to close the Arctic Sea Level budget (the linear altimetric sea level trend being the sum of eustatic and steric sea level trend). All studies use a selected altimetric product, a selected steric sea level product (either models or few selected buoys), and a selected GRACE eustatic sea level product. Here we will demonstrate the importance of the choice of product, where in particular the different GRACE-products are showing large discrepancies (Carret, et al., 2017; WCRP Global Sea Level Budget Group, 2018) in the Arctic area which greatly affects the magnitude of residuals resulting from the Arctic sea level budget computation.

By using a satellite-independent estimate of steric sea level and an ocean model, we are able to compare three different GRACE-mascon products against three available altimetric sea level estimates in the Arctic and thereby consolidate the Arctic sea level in regions of good agreement and identify regions with inconsistencies among available Arctic sea level products.

2. Data

Ocean bottom pressure (OBP) derived from gravitational observations by GRACE are related to sea surface height (SSH) by the sea level budget equation:

$$\text{SSH} = \text{OBP} + H$$

Where H is the steric water column expansion caused by a change in temperature and salinity. Steric heights do not change the gravitational attraction of the ocean and is hence not seen by GRACE.

Table 1 shows the original temporal and spatial resolution of the different datasets used in this study. We limit the period of interest from January 2003 to December 2014, which is the common period for all used datasets. Datasets of OBP and steric heights have full coverage of the Arctic from up to 90N, while altimetry is limited to 82N. All datasets are interpolated into a monthly 50x50 km polar stereographic grid. When comparing ocean-wide averages, the OBP and the steric dataset is limited to 82N.

Table 1. Original temporal resolution, time span and spatial resolution of the products used in this study.

Product	Org. temporal	Time span	Org lat x lon (vertical)
GRACE:			
CSR	monthly	2003/01-2017/04	0.5x0.5 deg
JPL	monthly	2002/04-2017/04	0.5x0.5 deg
GSFC	monthly	2003/01-2016/06	~63 km radius
Altimetry:			
RADS	along track	continuous	1 hz along track
CPOM	monthly	2003/01-2014/12	0.25x0.75 deg
DTU	weekly	1991/06-2018/12	0.25x0.50 deg
Steric:			
ECCOv4	monthly	1992/01-2015/12	~50x100km (5m)
DTUSteric	monthly	1980/01-2017/12	50x50 km (10 m – 100 m)

2.1 Sea Surface Heights from Altimetry

SSH from 2003-2015 in the Arctic consists of data from the ESA-satellites Envisat (mid 2002 – April 2012) and CryoSat-2 (mid 2010 - present). Three different Arctic SSH datasets with different processing algorithms and different geophysical corrections (see Table 2) are used in this study.

RADS: SSHs retrieved from the Radar Altimeter Database System (RADS, (Scharroo, et al., 2013)). Envisat and so-called pseudo-LRM data from CryoSat-2 SAR mode (Scharroo, et al., 2013) CryoSat-2 are retracked using identical retrackers . Subsequent selection criteria when retrieving data from RADS are chosen after the principle of Cheng et al. (2015), so that a wider range of pulse peakiness and significant wave heights is accepted, thereby allowing for higher data density in sea ice covered regions. Cheng et al. (2015) showed that this is possible without compromising the accuracy of SSH anomalies. The RADS data are provided as along track data and consequently gridded into 50x50 km monthly mean grids. The

difference in the SSH mean fields in 2011 for Envisat and CryoSat-2 have been subtracted from the CryoSat-2 SSH data in an attempt to account for regional satellite bias in particular in sea-ice covered regions.

CPOM: Centre for Polar Observation and Modelling (CPOM) at University College London (UCL) provides SSH estimates using the retracking principle of Armitage et al., 2016 (Armitage, et al., 2016), which uses a multi-functional retracker that can both retrack open ocean and sea ice leads for both Envisat and CryoSat-2 and CryoSat-2 SAR data even though they have different operational modes (Armitage, et al., 2016; Armitage, et al., 2018).

DTU: The altimetric product developed by the Technical University of Denmark (DTU (Rose, et al., 2019)) uses a combination of different retrackers. ALES+ retracker (Passaro, et al., 2014) is used for Envisat. For CryoSat-2 an empirical sea-ice lead retracker in sea ice covered regions is complemented with RADS retracked data for open waters.

Table 2. Different models for geophysical corrections used for the altimetric products.

<i>Correction</i>	<i>RADS</i>	<i>CPOM</i>	<i>DTU</i>
Inverse Barometer	MOG2D	ECWMF	MOG2D
Wet Troposphere	ECWMF	ECWMF	Doris/GIM/Bent
Dry Troposphere	ECWMF	ECWMF	ECWMF
Sea State Bias	NOAA	CLS	ALES+/RADS (only open water)
Ionospheric correction	JPL GIM	CNES	ECWMF
Ocean Tide	GOT4.10	FES2004	FES2014
Solid/Pole Tide	IERS	Cartwright/Wahr	Cartwright/Wahr

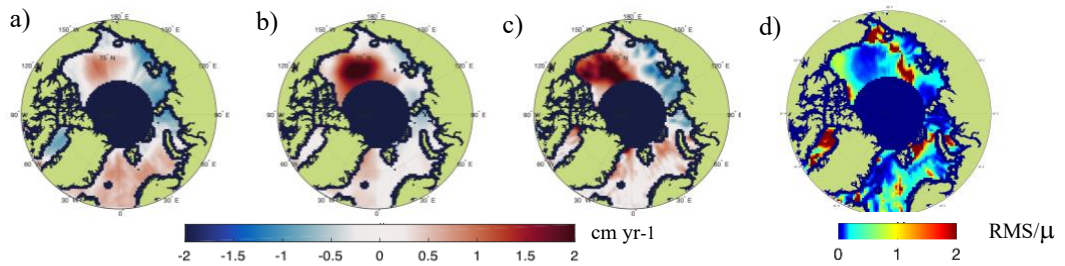


Figure 1. Sea level trends from 3 different altimetric products from 2003-2015. a) DTU (Rose et al., 2019), b) CPOM (Armitage et al., 2017), c) RADS and d) normalized Root Mean Square (RMS divided by the mean trend) between a-c. problematic

In Figure 1. Sea level trends from 3 different altimetric products from 2003-2015. a) DTU (Rose et al., 2019), b) CPOM (Armitage et al., 2017), c) RADS and d) normalized Root Mean Square (nRMS) of the grid cell-wise difference between the three sea level trend products is shown. A normalized Root Mean Square (nRMS) of the grid cell-wise difference between the three sea level trend products is shown in the Figure 1. Sea level trends from 3 different altimetric products from 2003-2015. a) DTU (Rose et al., 2019), b) CPOM (Armitage et al., 2017), c) RADS and d) normalized Root Mean Square (RMS divided by the mean trend) between a-c.d on a different color scale. The normalized RMS is computed as:

$$nRMS = \frac{RMS}{\mu} - 1,$$

where μ is the mean trend. It shows that the altimetric products in general align in the Beaufort Gyre, Siberian Seas and the North Atlantic, but some differences around Svalbard, in the Davis Strait and in a zone between the East Siberian Seas and the Beaufort Gyre are visible.

2.2 Ocean Bottom Pressure

We used the GRACE measurements of Earth's gravity field from mid 2002 to mid 2017. The Jet Propulsion Institute (JPL, (Wiese, et al., 2018; Watkins, et al., 2015; Wiese, et al., 2016)), Centre for Space Research (CSR, (Save, et al., 2016)) and Goddard Space Flight Center (GSFC, (Luthcke, et al., 2013)) provides Level-3 mascon products, where the signals are 'divided' between mass change signal from land and ocean. GRACE-solutions are all corrected for Glacial Isostatic Adjustment by the ICE6G (Peltier, et al., 2015) model and atmospheric loading by AOD1B (Flechtner, et al., 2014) from the German Research Centre for Geosciences (GFZ). Figure 2a-c the trends in OBP-pressure is displayed, while Figure 2d is showing a normalized RMS of the grid cell-wise difference between the three OBP-products, calculated similar to the nRMS of the altimetric products. Figure 2d reveals a large difference among the GRACE mascon products in the interior of the Arctic and in the East Siberian Seas.

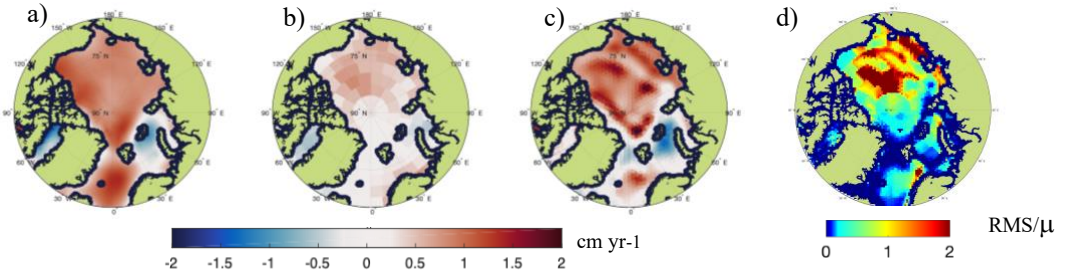


Figure 2. Sea level trends from 3 different GRACE mascon products from 2003-2015. a) GSFC (Luthcke, et al., 2013), b) JPL (Wiese, et al., 2016), c) CSR (Save, et al., 2016) and d) normalized RMS (RMS divided by the mean trend) between a-c.

2.3 Steric Heights

The ECCOv4r3 ocean model (Forget, et al., 2015; Fukumori, et al., 2017) provide modeled temperature and salinity estimates in a 4D grid. The same goes for the DTUSteric product from DTU, which is an interpolated product based on all available hydrographic in-situ data. For both products, the thermosteric (η_T s) and halosteric heights (η_H s) are calculated by integrating from ocean bottom (or max depth of 2000 meters) to ocean surface as below (Gill & Niiler, 1973; Stammer, 1997):

$$\eta_{Hs} = \int_P^0 \beta S' dz$$

$$\eta_{Ts} = - \int_P^0 \alpha T' dz$$

, where β is the saline contraction coefficient and α is thermal expansion coefficient, S' and T' is the salinity and temperature anomaly, with $T=0\text{C}$ and $S=35\text{psu}$ as reference values and P is the bottom pressure or pressure at 2000 m depth. α and β are determined with a 75-term polynomial expression, that are functions of absolute salinity, conservative temperature and pressure. They are found by using the TEOS-10 software (Roquet, et al., 2015) freely available at <http://www.teos-10.org>.

DTUSteric: Building on the extensive UDASH dataset (Behrendt, et al., 2017), a total of over 300.000 temperature and salinity profiles located north of 60th latitude spanning from 1980-2015 are used. Additional profiles from ARGO, World Ocean Database (WOD), Institute of Marine Research of Norway (IMR), and Ice-Tethered-Profiles (ITP) from Woods Hole Oceanographic Institution have been added to the UDASH dataset (possible duplicates have subsequently been removed). The following steps are taken to edit and derive the DTU monthly steric data set:

- 1) Profiles with more than 5 measurements and with a minimum depth of less than 10 meters, maximum depth more than 100 m and with salinity values of less than 45 psu and temperatures of less than 20 C-deg are selected.
- 2) A median-filter is used to interpolate all profiles into 10-meter intervals from 0-190-meter depth, 50-meter intervals from 200-900 meters and 100-meter intervals from 1000 to 2000 meters and the profiles are combined into monthly datasets.
- 3) Values are neglected if the temperature or salinity value is more than 3 standard deviations from the median in a 100 km horizontal radius. Occurring vertical gaps are filled by using a 5-depth level moving mean window.
- 4) The profiles are binned into a monthly 50x50 km stereographic grid for every depth level, creating a 4D dataset for temperature and salinity.
- 5) Horizontal gaps are filled by kriging interpolation and a bathymetry-function is applied to remove data where there is no ocean.
- 6) Step 3 is repeated for each grid cell but using data from adjacent years to fill gaps instead of vertical interpolation.
- 7) The steric heights are computed and the final grid is horizontal smoothed by taking a 100 km radius mean.

The interpolated 4D-product (3D for steric heights) is called DTU Arctic Ocean Steric Heights (DTUSteric), and is available at <ftp.space.dtu.dk/ARCTIC>.

ECCO: The consortium of Estimating the Circulation and Climate of the Ocean model version 4 release 3 (ECCOv4r3, (Fukumori, et al., 2017; Forget, et al., 2015)) is used as a model comparison for steric height estimates. It provides 1-degree grids of temperature and salinity at 50 depth levels from 1992-2015 and subsequently converted into steric heights. ECCO is constrained with selected hydrographic data, GRACE and altimetry, and is therefore not entirely independent from the other datasets.

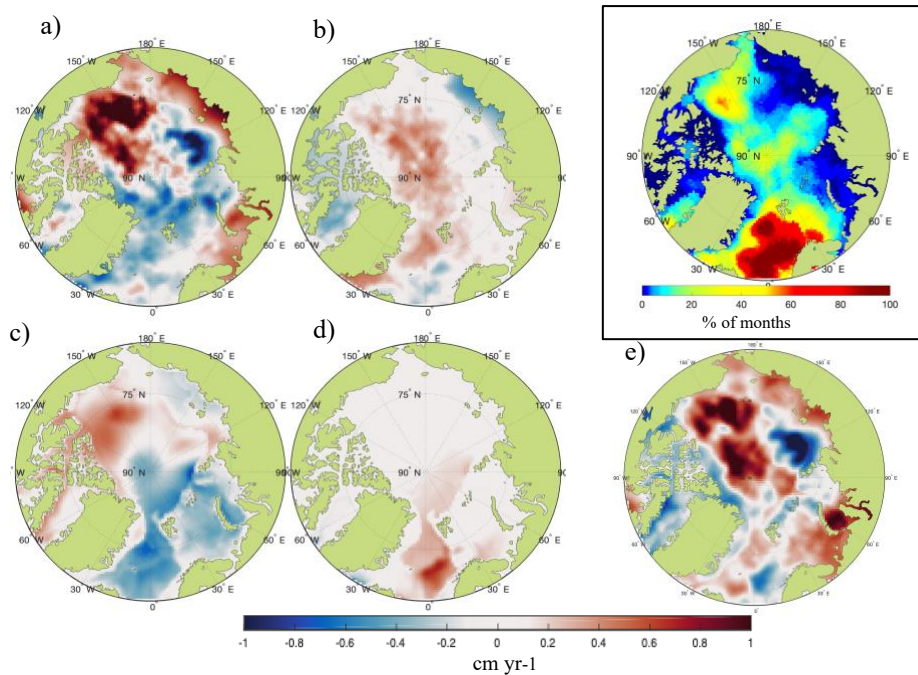


Figure 3. Steric sea level trends from 2003-2015. a) map the halosteric from DTUSteric. b) thermosteric from DTUSteric, c) halosteric by the ECCOv4r3 model, d) thermosteric from ECCOv4r3 [17]. e) is the residual map between DTUSteric and the ECCO-model (a+b minus c+d). In the upper right corner is the density of hydrographic data given in percentage of months with available data in a 100 km radius of each 50x50km grid node.

In Figure 3, the halosteric and thermosteric sea level trends for both ECCO and DTUSteric are shown. Figure 3e shows the difference between the total steric sea level trend, e.g. thermosteric + halosteric, of the two steric products. In the upper right corner of Figure 3, is the density of hydrographic data used for the DTUSteric product given as percentage of months with available data in a 100 km radius of each 50x50km grid node. It clearly shows the low data density in the interior of the Arctic, while the North Atlantic and the Beaufort Gyre has higher coverage of in-situ data.

3. Analysis

Various combinations between the three different mascon solutions, two steric and three altimetric SSH estimates are made. Additionally, we computed a mean of the three mascon solutions, called OBPmean. The spatial correlation coefficients (only computed over the ocean between 65N and 82N) are shown in Table 3. It indicates that the ‘best combination’ is found with the JPL mascons and the DTUSteric product relative to the CPOM altimetric product ($R=0.76$). The modelled steric product from ECCOv4r3 has general poor spatial correlation with any of the altimetric SSH estimates, regardless of the OBP solution used. CPOM has highest correlation with any of the OBP+DTUSteric solutions followed by RADS and the DTU solutions.

Table 3. Correlation coefficients between different combinations of trend maps of sea level contributions from steric and OBP compared with the three altimetric solutions.

OBP + Steric	RADS	DTU	CPOM
JPL + DTU Steric	0.61	0.35	0.76
JPL + ECCOv4 Steric	-0.16	0.40	-0.10
GSFC + DTU Steric	0.50	0.40	0.67
GSFC + ECCOv4 Steric	-0.10	0.37	0.00
CSR + DTU Steric	0.49	0.19	0.69
CSR + ECCOv4 Steric	-0.05	0.16	0.17
OBPmean + DTU Steric	0.54	0.32	0.74
OBPmean + ECCOv4 Steric	-0.11	0.33	0.04

The sum of the ‘best combination’ based on spatial correlation (JPL mascon + DTUsteric) is shown in Figure 4a. The Beaufort Gyre is particularly well seen with trends around 2 cm/yr. The residuals between the ‘best combination’ and CPOM altimetry (Figure 1b), which showed the highest correlation, is shown in Figure 4b.

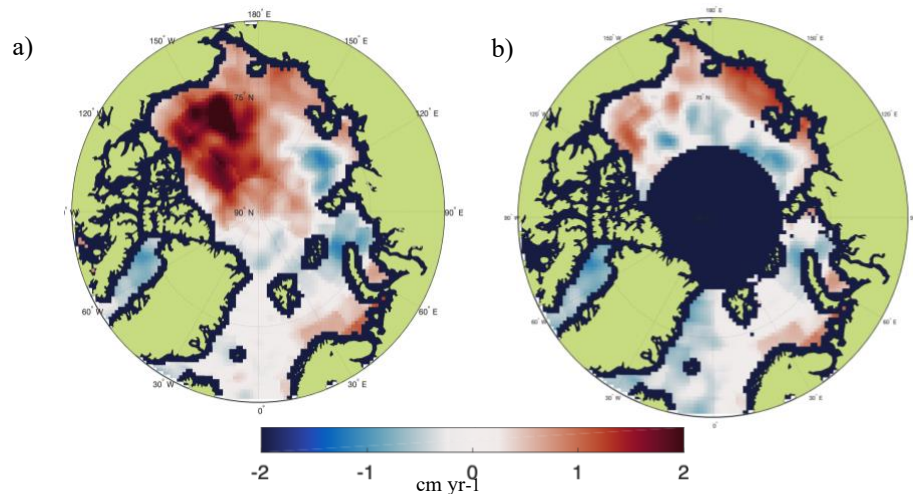


Figure 4. Maps of the “best combination” between sea level trends for OBP+steric and altimetry for 2003-2015. a) shows JPL mascons added the DTUsteric product and b) is the residual between a) and Figure 1b, SSH from CPOM altimetry (Figure 1b).

Good agreement in most interior parts of the Arctic Ocean is found. But large sections of the coastal areas, in particular in the East Siberian Sea, the OBP+DTUsteric product has an increasing trend, while altimetry-based sea level trends decrease. The pattern is consistent throughout all altimetric products. The GSFC and CSR OBP-products from GRACE have an even higher trend in the East Siberian Sea, which would increase the residual shown in Figure 4b. A comparative study by the WRCP Sea Level Budget Group (2018) showed global ocean mass trends among the mascon solution varying from 1.76-2.61 mm/yr with the JPL solution having the lowest value. Even though the mascon solutions are designed to separate land and ocean signals, the differences could be attributed to errors in leakage correction. This error is presumably larger in coastal areas or areas with large land signals (e.g. from Greenland), resulting in a general larger uncertainty in the Arctic. Specifically, in the eastern Siberia, Suzuki, et al, (2016) showed a negative GRACE-based terrestrial-water-storage trend caused

by increased evapotranspiration during the summer months. This is not yet fully understood due to limited availability of in-situ data, but might not be accounted for in the mascon-processing.

At the same time, there is almost no hydrographic information in the East Siberian Sea (as shown in Figure 3), with only very few measurements in the entire investigation period. Thus, is the signal seen in the DTUSteric product likely due to extrapolation of hydrographic data and hence is the increasing trend in the region influenced by the strong freshwater trend of the nearby Beaufort Gyre. Noteworthy is, that the ECCO-model is showing a decreasing trend, which agrees with the altimetric products. Since the ECCO-model as well has no in-situ information in the area and both GRACE and satellite altimetry is used as constraints (Fukumori, et al., 2017), we consider the signal more as a result of a budget calculation than as an independent contribution.

The temporal change of Arctic-wide averaged monthly sea level is shown in Figure 5, where DTU and CPOM seem to agree more, while the RADS products is showing greater interannual variability. The occasional lack of seasonal variability in DTUSteric can be explained due to the seasonal nature of in-situ data (primarily summer data). The seasonal variability is on the other hand represented in the mass changes from GRACE. However, as the mass change only account for about half of the seasonal variations we are not able to represent the seasonal signal seen in the altimetric data with the combined DTUSteric + JPL Mascon product.

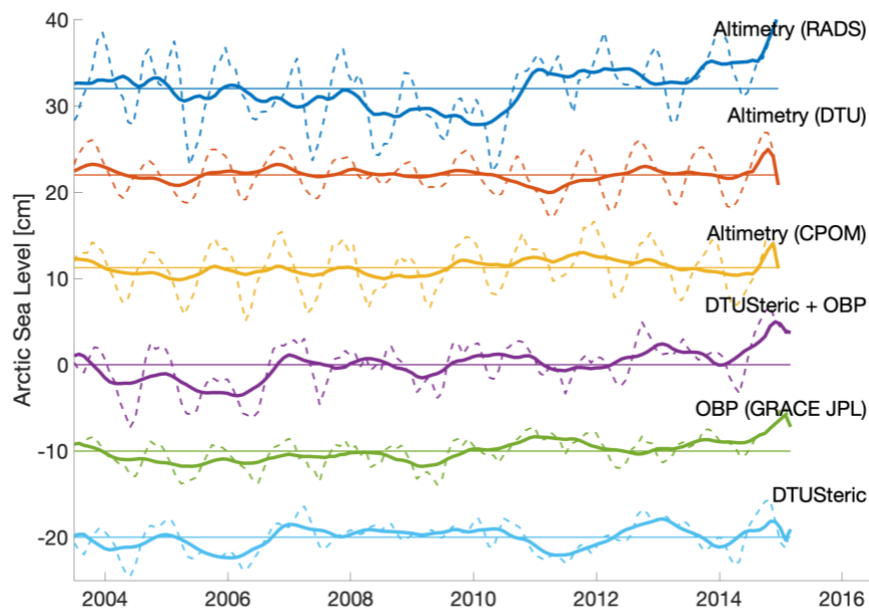


Figure 5. Three-month (dashed lines) and 13-month running mean (thick lines) sea level from 2003-2015 for the different SSH products and contributions to Arctic sea level change (values in cm). The timeseries are shifted arbitrarily for better visibility.

4. Discussion and Conclusion

Attempts from previous studies (Kwok & Morison, 2015; Armitage, et al., 2016) to validate altimetric sea level in areas of the Arctic show a similar pattern as this study. Armitage, et al. (2016) compared the CPOM sea level product to tide gauges in the Arctic. While good agreement was reached in the Beaufort Sea and Barents Sea, the

Kara, Laptev and East Siberian Seas had significant less correlation with tide gauge data. These are the same areas, where Figure 4 show large disagreement, confirming a large sea level uncertainty in those areas.

While Armitage, et al, (2016) found good agreements between selected hydrographic data (mainly Ice-Thetered-Profiles) and satellite derived steric heights (ALT-OBP), this study is the first that uses an Arctic-wide steric product that is independent of satellite data.

Both the ocean bottom pressure products from GRACE and the altimetric products show different spatial trend patterns and magnitudes as illustrated in Figure 2d and 3d. The best spatial correlation between the sum of the JPL mascons eustatic sea level change and the DTUSteric sea level change in a comparison with the the CPOM altimetry sea level change. If we ignore the ECCO-model, the correlation coefficients range from 0.32 to 0.76.

The DTU altimetry product uses special retracking of CryoSat-2-data, and is thereby able to retrieve sea level information within sea ice leads which improves spatio-temporal coverage in regions with shifting sea ice cover (Rose, et al., 2019). However, the merging of the data with different retrackers slightly degrade the spatial correlation in the sea level budget comparison. This could be caused by an unknown offset between the retrackers in the product. The products from CPOM and RADS have the advantage of using the same retracker for both Envisat and CryoSat-2, which can result in a more consistent transition from Envisat to CryoSat-2. However, as seen in Figure 5, RADS data jumps in 2011 which is likely due to intermission bias.

Regions with large residuals correlate well with regions with poor hydrographic data coverage. In particular, the coastal region of the East Siberian Sea is poorly covered with in-situ observations. At the same time is this region known to be the most challenging in terms of altimetry (Armitage, et al., 2016; Rose, et al., 2019), while the GRACE solutions also show different sea level trends (as seen in Figure 2).

EOF-calculations of GRACE-observed OBP anomalies applied by Wang et al, (2017) and Peralta-Ferriz, et al. (2014) and SSH anomalies by Armitage, et al. (2016), indicate that the leading annual EOF mode of SSH is mass driven, while the seasonal variability is dominated by steric changes. The leading mode has a significant East Siberia Sea - Central Arctic dipole similar what is seen in the residual map in Figure 4. This could imply that the post-processing of GRACE data applied for the JPL mascons are not able to detect the mass variability seen by standard GRACE L3 products processed after Chambers and Bonin (2012), which is used in the other studies.

The residual map in Figure 4b also resembles the pattern of figure 10 in Armitage, et al, (2016), showing satellite derived steric height changes from 2012-2014, where a large drop of steric heights are seen in the East Siberian Sea and along the coast in the Beaufort Sea area. Baccuse of sparse in-situ data and how the DTUSteric product is extrapolating both spatially and temporally, those fast changes are likely to fade.

The normalized RMS values show that the altimetric products disagree north of Siberia, around Svalbard, Davies Strait and around the Beaufort Gyre. Those areas are also known to be areas with changing sea ice and transition zones between first year and multi-year sea ice (Kwok, 2018). Contrary, OBP-products from GRACE disagree mostly in the interior of the Arctic and along the East Siberian Coast, indicating are more general uncertainty of the mass trend in the Arctic. The DTUSteric product is able to explain most of the signal seen by CPOM altimetry and JPL Mascons. This confirms the finding of other studies (Armitage, et al., 2016; Carret, et al., 2017; Rose, et al., 2019) that the Beaufort Gyre is mainly a halosteric signal.

The general low residuals between CPOM altimetry and OBP from JPL mascons + DTUSteric, even in the ice-covered part of the Arctic Ocean, gives confidence that the combination might be used as a proxy to close the 'pole hole' in altimetric observations north of 82N before 2011. Further investigations comparing CryoSat-2

between 82N and 88N with OBP + Steric including both GRACE and GRACE-Follow On to extend the time series should be made to confirm this theory.

Acknowledgements

The authors would like to thank T. Armitage and one anonymous reviewer for comments that greatly improved the manuscript. Also, a thank to S.K. Rose for preparing the DTU altimetric product, R. Scharroo for keeping the RADS database updated, the ECCO-consortium for the ECCOV4r3 model, A. Behrendt for creating the UDASH-database, B. Loomis and D. Wiese for providing of and discussions on the GRACE-mascons. Arctic dynamic topography data were provided by the Centre for Polar Observation and Modelling, University College London (www.cpom.ucl.ac.uk/dynamic_topography (Armitage, et al., 2016)).

The project is partly funded by the EU-INTAROS project (Grant agreement 727890) and the ESA-Climate Change Initiative Sea level budget closure (Expro RFP/3-14679/16/I-NB).

Bibliography

- Andersen, O. B. & Piccioni, G., 2016. Recent Arctic Sea Level Variations from Satellites.. *Frontiers in Marine Science*, Volume 3, p. 76. doi:10.3389/fmars.2016.00076.
- Armitage, T., Bacon, S. & Kwok, R., 2018. Arctic Sea Level and Surface Circulation Response to the Arctic Oscillation. *Geophysical Research Letters*, 45(13), pp. 6576–6584. doi:10.1029/2018GL078386.
- Armitage, T., Bacon, S., Ridout, A., Thomas, S., Aksenov, Y., Wingham, D., 2016. Arctic sea surface height variability and change from satellite radar altimetry and GRACE, 2003–2014. *Journal of Geophysical Research: Oceans*, 121(5), pp. 4303–4322. doi:10.1002/2015JC011579.
- Behrendt, A., Sumata, H., Rabe, B. & Schauer, U., 2017. UDASH – Unified Database for Arctic and Subarctic Hydrography. *Earth Syst. Sci. Data*, 10(2), pp. 1119–1138. doi:10.5194/essd-10-1119-2018.
- Blunden, J. & Arndt, D. S., 2013. State of the Climate in 2012. *Bull. Amer. Meteor. Soc.*, 94(8), p. 1–258. doi:10.1175/2013BAMSStateoftheClimate.1.
- Box, J. E., Colgan, W. T., Christensen, T. R. & et al, 2019. Key indicators of Arctic climate change: 1971–2017. *Environmental Research Letters*, 14(4), pp. 045010. doi:10.1088/1748-9326/aafc1b.
- Carret, A., Johannessen, J., Andersen, O., Michaël, A., Prandi, P., Blazquez, A. & Cazenave, A., 2017. Arctic Sea Level During the Satellite Altimetry Era.. *Surveys in Geophysics*, 38(1), pp. 251–275. doi:10.1007/s10712-016-9390-2.
- Chambers, D. P. & Bonin, J. A., 2012. Evaluation of Release-05 GRACE time-variable gravity coefficients over the ocean. *Ocean Science*, 8(5), pp. 859–868. doi:10.5194/os-8-859-2012.
- Cheng, Y., Andersen, O. B. & Knudsen, P., 2015. An Improved 20-Year Arctic Ocean Altimetric Sea Level Data Record. 38(2), p. 146–162. doi:10.1080/01490419.2014.954087.
- Flechtner, F., Dobsław, H. & Fagiolini, E., 2014. *AOD1B Product Description Document for Product Release 05, GRACE 327-750 (GR-GFZ-AOD-0001)*, Potsdam: GFZ German Research Centre for Geosciences Department 1: Geodesy.
- Forget, G., Campin, J-M., Heimbach, P., Hill, C., Ponte, R., Wunsch, C., 2015. ECCO version 4: an integrated framework for non-linear inverse modeling and global ocean state estimation.. *Geoscientific Model Development*, 8(10), pp. 3071–3104. doi:10.5194/gmd-8-3071-2015.
- Fukumori, I., Wang, O., Fenty, I., Forget, G., Heimbach, P., & Ponte, R., 2017. *2017: ECCO Version 4 Release 3*, Pasadena. doi: 1721.1/110380 : NASA JPL.
- Gill, A. E. & Niiler, P. P., 1973. The theory of the seasonal variability in the ocean. *Deep-Sea Res.*, 20(2), pp. 141–177. doi:10.1016/0011-7471(73)90049-1.
- Kwok, R., 2018. Arctic sea ice thickness, volume, and multiyear ice coverage: losses and coupled variability (1958–2018). *Environmental Research Letters*, 13(10), pp. 105005. doi:10.1088/1748-9326/aae3ec.
- Kwok, R. & Morison, J., 2015. Sea surface height and dynamic topography of the ice-covered oceans from CryoSat-2: 2011–2014. *J. Geophys. Res. Oceans*, 121(1), pp. 674–692. doi:10.1002/2015JC011357.
- Luthcke, S., Sabaka, T.J., Loomis, B., Arendt, A., McCarthy, J.J. & Camp, J., 2013. Antarctica, Greenland and Gulf of Alaska land-ice evolution from an iterated GRACE

global mascon solution. *Journal of Glaciology*, 59(216), pp. 613-631. doi:10.3189/2013JoG12J147.

Passaro, M., Cipollini, P., Vignudelli, S., Quartly, G., Snaith, H., 2014. ALES: A multi-mission adaptive subwaveform retracker for coastal and open ocean altimetry. *Remote Sensing of Environment*, 145(145), p. 173–189. doi:10.1016/j.rse.2014.02.008.

Peltier, W., Argus, D. & Drummond, R., 2015. Space geodesy constrains ice-age terminal deglaciation: The global ICE-6G_C (VM5a) model. *J. Geophys. Res. Solid Earth*, 120(1), pp. 450-487. doi:10.1002/2014JB011176.

Peralta-Ferriz, C., Morison, J., Wallace, J., Bonin, J., & Zhang, J., 2014. Arctic Ocean Circulation Patterns Revealed by GRACE. *J. Climate*, 4(27), pp. 1445–1468. doi:10.1175/JCLI-D-13-00013.1.

Proshutinsky, A., Dukhovskoy, D., Timmermans, M-L., Krishfield, R., Bamber, J., 2015. Arctic circulation regimes. *Phil. Trans. R. Soc.*, 373(2052), doi:10.1098/rsta.2014.0160.

Roquet, F., Madec, G., McDougall, T. & Barker, P., 2015. Accurate polynomial expressions for the density and specific volume of seawater using the TEOS-10 standard. *Ocean Modelling*, 90(90), pp. 29-43. doi:10.1016/j.ocemod.2015.04.002.

Rose, S., Andersen, O., Passaro, M., Ludwigsen, C., & Schwatke, C., 2019. Arctic Ocean Sea Level Record from the Complete Radar Altimetry Era: 1991–2018. *Remote Sensing*, 11(14), p. 1672. doi:10.3390/rs11141672.

Save, H., Bettadpur, S. & Tapley, B., 2016. High resolution CSR GRACE RL05 mascons. *J. Geophys. Res. Solid Earth*, 121(10), pp. 7547-7569. doi:10.1002/2016JB013007.

Scharroo, R., Leuliette, E. W., Lillibridge, J. L., Byrne, D., Naeije, M. C., Mitchum, G. T., 2013. *RADS: Consistent multi-mission products*. Venice, Italy, ESA SP-710.

Stammer, D., 1997. Steric and wind-induced changes in TOPEX/POSEIDON large-scale sea surface topography observations. *JGR Oceans*, 102(C9), pp. 20987-21009. doi:10.1029/97JC01475.

Suzuki, K., Matsuo, K. & Hiyama, T., 2016. Satellite gravimetry-based analysis of terrestrial water storage and its relationship with run-off from the Lena River in eastern Siberia. *International Journal of Remote Sensing*, 37(10), p. 2198–2210. doi:10.1080/01431161.2016.1165890.

Tedesco, M., Mote, T., Fettweis, X., Hanna, E., Jeyaratnam, J., Booth, J., Datta, R. & Briggs, K., 2016. Arctic cut-off high drives the poleward shift of a new Greenland melting record. *Nature Communications*, Volume 7, p. 11723. doi:10.1038/ncomms11723.

Wang, Z., Hamilton, J. & Su, J., 2017. Variations in freshwater pathways from the Arctic Ocean into the North Atlantic Ocean. *Progress in Oceanography*, Volume 155, pp. 54-73. doi:10.1016/j.pocean.2017.05.012.

Watkins, M.M., Wiese, D.N., Yuan, D.-N., Boening, C. & Landerer, F.W., 2015. Improved methods for observing Earth's time variable mass distribution with GRACE using spherical cap mascons. *J. Geophys. Res. Solid Earth*, 120(4), pp. 2648-2671. doi:10.1002/2014JB011547.

WCRP Global Sea Level Budget Group, 2018. Global sea-level budget 1993–present. *Earth Syst. Sci. Data*, 10(3), pp. 1551–1590. doi:10.5194/essd-10-1551-2018.

Wiese, D. N., Landerer, F. & Watkins, M., 2016. Quantifying and reducing leakage errors in the JPL RL05M GRACE mascon solution. *Water Resour. Res.*, 52(9), pp. 7490-7502. doi:10.1002/2016WR019344.

Wiese, D.N., Yuan, D.-N., Boening, C., Landerer, F. W., Watkins, M. M., 2018. *JPL GRACE Mascon Ocean, Ice, and Hydrology Equivalent Water Height Release 06 Coastal Resolution Improvement (CRI) Filtered Version 1.0. Ver. 1.0. PO.DAAC, CA, USA. et accessed 2019-02-22.* [Online]

Available at: http://grace.jpl.nasa.gov/data/get-data/jpl_global_mascons/ [Accessed 10 May 2019].

5 Publication 2: Vertical Land Motion from Present-Day Deglaciation in the Wider Arctic

5.1 Preface

The second publication that is accepted to be published in *Geophysical Research Letters* in September 2020 (Ludwigsen et al., 2020a). The objective was to create a Vertical Land Movement (VLM) model covering the entire Arctic, where GNSS-measurements are generally sparse and inconsistent. Accurate and reliable VLM-estimates are paramount for correcting tide gauge data if they should be compared to absolute sea level estimates from altimetry. The elastic calculations also show, how much of the sea level rise caused by present-day deglaciation is in fact mitigated by an associated elastic VLM in the Northern Regions.

A major achievement of this work was the conversion of total mass balance estimates of glaciers to a global glacial surface elevation change model in a 2x2 km grid, which is comparable to the resolution of models based on altimetric observations of the Greenland Ice sheet. The resolution is a factor 100 more dense than similar products based on GRACE-observations (e.g. Frederikse et al. (2019)), which are too coarse to be probably used in glaciated areas.

Yearly elastic uplift estimates from glaciers and Greenland were calculated with REAR (Melini et al., 2015) and combined with glacial isostatic adjustment (GIA) model from Caron et al. (2018). Rotational feedback (King et al., 2012) and non-tidal ocean loading (van Dam et al., 2012) was added to the resulting VLM-model. 2003-2015 VLM-trends from the model were compared to 54 wider-Arctic GNSS-sites from ULR (University La Rochelle) version 6a (Santamaría-Gómez et al., 2017b). Non-secular geocenter motion signal was removed from the GNSS-estimates in order to align the ITRF2008-reference of GNSS-measured VLM with the center of mass frame of the VLM-model.

The results showed good agreement between the VLM-model and GNSS - both in near and far field. However, the uniform elastic earth model used (REF6371 (Kustowski et al., 2007)) caused residuals in areas with low-viscosities (East-Greenland and Iceland). Also, local effects of VLM, like post-seismic deformation after a major earthquake in Alaska and significant deglaciation after the Little Ice Age caused disagreement between GNSS-measured VLM and the computed VLM-model. However, the residuals could be attributed to localized uplift predictions of other studies. Hence is the model also usable for detecting extraordinary circumstances causing VLM.

The publication includes supporting information, that follows after the main article, which includes uncertainty assessment and table with VLM-values at each GNSS-site. A version of the VLM-model in a 5x5km resolution (Ludwigsen et al., 2020b) is accessible from the open repository https://data.dtu.dk/articles/dataset/Arctic_Vertical_Land_Motion_5x5_km.

Vertical Land Motion from Present-Day Deglaciation in the Wider Arctic

Carsten Ankjær Ludwigsen¹, Shfaqat Abbas Khan¹, Ole Baltazar
Andersen¹ and Ben Marzeion²

¹DTU Space, Technical University of Denmark

²Institute of Geography and MARUM – Center for Marine Environmental Sciences, University of Bremen,
Germany

Key Points:

- Elastic VLM from present-day ice loss in the Arctic causes significant uplift of coastlines in North America and Northern Europe.
- A combined VLM-model that includes GIA and elastic VLM, yields good agreement with GNSS-stations in the wider Arctic.
- Residuals between GNSS and modeled VLM provides an approximation of extraordinary VLM caused by local circumstances.

Corresponding author: Carsten Ankjær Ludwigsen, caanlu@space.dtu.dk

Abstract

Vertical land motion (VLM) from past and ongoing glacial changes can amplify or mitigate ongoing relative sea level change. We present a high resolution VLM-model for the wider Arctic, that includes both present-day ice loading (PDIL) and glacial isostatic adjustment (GIA). The study shows that the non-linear elastic uplift from PDIL is significant ($0.5\text{-}1\text{ mm y}^{-1}$) in most of the wider Arctic and exceeds GIA at 15 of 54 Arctic GNSS-sites, including sites in non-glaciated areas of the North Sea region and the east coast of North America. Thereby the sea level change from PDIL (1.5 mm y^{-1}) is significantly mitigated from VLM caused by PDIL. The combined VLM-model was consistent with measured VLM at 85% of the GNSS-sites ($R=0.77$) and outperformed a GIA-only model ($R=0.64$). Deviations from GNSS-measured VLM can be attributed to local circumstances causing VLM.

Plain Language Summary

From 2003 to 2015, the Northern Hemisphere lost more than 6,000 gigatons of land ice, which added nearly 18 mm to the global mean sea level rise. Loss of land-based ice results in the vertical deformation of the Earth's surface. Ongoing rebounding or subsidence caused by the end of the last ice age is often assumed to govern vertical deformation. However, present-day ice loss from Greenland and Arctic glaciers also cause an immediate vertical deformation. By using a vertical deformation model, that includes both components, we can explain GPS-measured deformation occurring in the Arctic. Our results show that the present-day Arctic ice loss contribution to vertical deformation is approximately $0.5\text{ to }1\text{ mm y}^{-1}$ in the wider northern region. This exceeds deformation caused by the disappearance of the last ice ages at many coastal regions, including the North Sea region and the North American Atlantic coast. The present-day ice loss included in the VLM-model equals a global sea level rise of 1.5 mm y^{-1} , which means that 30-80% of the sea level rise caused by Arctic ice loss is mitigated by surface uplift caused by the same ice loss.

1 Introduction

The Arctic region is warming faster than any other region on Earth (Post et al., 2019). Deglaciation of Arctic land-based ice accounts for 70% of all barystatic sea level change (Abram et al., 2019) and has increased the sea level rise by 0.035 mm y^{-2} over the last three decades (Nerem et al., 2018). From 2003 to 2015 the Greenland Ice Sheet and adjoining glaciers produced 1 cm of sea level rise, while the contribution of other Arctic glaciers was 0.8 cm (Zemp et al., 2019).

Change in ice loading not only contributes to sea level change, but also alters Earth's solid surface, which commonly is called Vertical Land Motion (VLM). Accurate quantification of VLM and its causes is key for understanding relative sea level (RSL) (Watson et al., 2015; Wöppelmann & Marcos, 2016), which is the sea level change measured by tide gauges (TG).

VLM can be modeled for a given ice loading by employing the sea level equation of Farrell and Clark (1976) or in its elastic adaptation by Clark and Lingle (1977). viscoelastic relaxation of Earth's surface caused by past ice loading changes, also known as Glacial Isostatic Adjustment (GIA), has historically been the most important component of VLM (Farrell & Clark, 1976; Tushingham & Peltier, 1991; Milne & Mitrovica, 1998; Peltier et al., 2015) and is often assumed to be the key contributor to VLM in sea level studies from tide gauges (Church & White, 2011; Jevrejeva et al., 2014). This assumption is in particular inadequate in the Arctic region (Henry et al., 2012), where the change in present-day ice loading (PDIL) is extensive and the corresponding VLM equals GIA in order of magnitude.

Here we quantified the VLM resulting from changes in PDIL from 2003-2015 in the wider Arctic (the region above 50 deg latitude). After considering GIA, ocean loading, rotational feedback (RF) and non-secular geocenter motion, the total VLM uplift is predicted and compared to GNSS-measured VLM at 54 locations.

In recent years, data products from the Gravity Recovery And Climate Experiment (GRACE) satellite mission have been used to estimate PDIL and the corresponding VLM (Adhikari et al., 2016; Riva et al., 2017; Frederikse et al., 2019). While this is a reasonable estimate for regional and global VLM-patterns, the native resolution of GRACE is around 300-km half width at the equator (Tapley et al., 2004) which is insufficient for estimating VLM close to glaciers and ice sheets.

Here we combined a high-resolution (2x2 km) ice mass balance data in the Arctic to compute VLM from PDIL (VLM_{PDIL}), with a resolution that is suitable in both the near- and far-field in the Arctic region.

2 Data and Method

The solid-earth response of PDIL is assumed to be purely elastic and the viscoelastic response is considered to be negligible. This includes the ongoing solid-earth response from modern changes in ice loading prior to 2003, which is not considered in the applied GIA-models. In particular, the deglaciation after the Little Ice Age (LIA) that ended in the 19th century can create a GIA-like viscoelastic response that is not captured by GIA-models (Simon et al., 2018).

Contrary to studies using GRACE-measurements for ice loading, we used mass balance data from glaciers (Marzeion et al., 2012; Pfeffer et al., 2014; Zemp et al., 2019) that were transformed into an ice-elevation model (details in Supporting Information S1) with a 2x2 km spatial resolution by applying a mass balance distribution function and assuming a uniform density of 917 kg m^{-3} . Glaciers were combined with elevation changes from Greenland (updated version of the data from S. A. Khan et al. (2013), see section 2.1).

90 Separately, Antarctic yearly mass equivalent surface elevation changes for 2003-2015 from
 91 Schröder et al. (2019) were used to estimate the present-day Antarctic contribution to
 92 VLM in the Arctic.

93 The elastic VLM (VLM_{PDIL}) was computed with REAR (Regional Elastic Rebound
 94 calculator) (Melini et al., 2014, 2015). REAR calculates the elastic response to a disc
 95 load (Farrell, 1972) and assumes a solid, non-rotating and isotropic earth. Load Deformation
 96 Constants (LDC's) used for solving the Green's Functions were obtained from
 97 the REF6371 model by Kustowski et al. (2007) which is similar to the PREM-model (Dziewonski
 98 & Anderson, 1981), however the REF6371 model includes more realistic seismic properties
 99 of the crust (Kustowski et al., 2007). The LDC's from REAR are by default defined
 100 with respect to Earth's center of mass (CM-frame), which is consistent with the
 101 GIA-model of Caron et al. (2018). The ICE6G_D-model of Peltier et al. (2018) is refer-
 102 enced to the center of solid-earth (CE). The surface loading change included in GIA
 103 is however prehistoric and current viscoelastic mass transport induces a negligible CM-
 104 CE motion (King et al., 2012; Argus et al., 2014).

105 Rotational feedback (Milne & Mitrović, 1998) was added to the elastic VLM-model
 106 by using equation 1 and 2 from King and Watson (2014). Position changes of the pole
 107 (x_p, y_p) for ITRF2008 are available from IERS (Bizouard & Gambis, 2009). Since REAR
 108 is not solving the sea level equation (Farrell & Clark, 1976; Milne et al., 1999), it does
 109 not account for the effect of extra water mass added to the oceans because of PDIL, which
 110 results in a measurable deformation (van Dam et al., 2012; Santamaría-Gómez & Mémin,
 111 2015). Non-tidal ocean loading (NOL) is predicted by estimating the elastic deformation
 112 of ocean bottom pressure (OBP, shown in Figure S2.2 in Supporting Information)
 113 grids from the latest version of Estimating the Circulation and Climate of the Ocean (ECCO)
 114 project (version 4, release 4) (Fukumori et al., 2019; Forget et al., 2015).

115 GNSS data are referenced to ITRF2008 (Altamimi et al., 2011), which has secular
 116 trends in CM, while non-secular trends of ITRF are in center of figure (CF) (Dong
 117 et al., 2003). Therefore, when studying ongoing mass changes, we need to make a ITRF
 118 to CM translation by considering non-linear geocenter motion (GCM). GCM is obtained
 119 from first-order Stokes coefficients from 2002-2019 provided by Sun et al. (2016) avail-
 120 able from <https://grace.jpl.nasa.gov/data/get-data/geocenter/>, which are de-
 121 trended in order to make the ITRF to CM translation. An VLM-model (eq. 2) is cre-
 122 ated that is comparable to adjusted GNSS-measured VLM (eq. 3):

$$VLM_{ela}^{CM} = VLM_{PDIL}^{CM} + VLM_{NOL}^{CM} + VLM_{rot} \quad (1)$$

$$VLM_{model}^{CM} = VLM_{GIA}^{CM} + VLM_{ela}^{CM} \quad (2)$$

$$VLM_{GNSS}^{CM} = VLM_{GNSS}^{ITRF} - GCM^{ITRF-CM} \quad (3)$$

123 Where VLM_{ela}^{CM} is the elastic VLM-model, VLM_{GIA}^{CM} represents VLM caused by GIA,
 124 VLM_{rot} indicates the deformation caused by rotational feedback and VLM_{NOL} is the
 125 contribution from NOL. VLM_{GNSS}^{CM} is GNSS-measured VLM after non-secular geocen-
 126 ter motion is removed. Average VLM-rates from 2003-2015 are shown in Figure 1, while
 127 VLM_{model}^{CM} is evaluated against VLM_{GNSS}^{CM} in section 3. The contribution of Antarctic
 128 ice loading (including Southern Hemisphere glaciers) is shown together with the contri-
 129 bution of VLM_{NOL}^{CM} and VLM_{rot} in Figure S2.1 in Supporting Information.

130 Caron2018 (Caron et al., 2018) is the default GIA-model throughout this study.
 131 Caron2018 used 128000 forward models of different 1D Earth rheologies and ice eleva-
 132 tion histories to create a statistical distribution of the GIA signal representative of long
 133 term GNSS observations and relative sea level records from paleo RSL indicators. In some
 134 parts of the analysis, we include the ICE-6G_D GIA model of Peltier et al. (2018), since
 135 large discrepancies between the VLM_{model}^{CM} and VLM_{GNSS}^{CM} can be explained by the choice

136 of GIA-model. Recent study using an ensemble of simulations with 3D-earth rheologies
 137 (Li et al., 2020), seems to favor the results GIA-rates of Peltier et al. (2018).

138 Though we limited this study to the wider Arctic area, both the elastic VLM-components
 139 and GIA have a global impact. However, if we neglect the VLM caused by Antarctica,
 140 the VLM-signal from PDIL is relatively small ($< \pm 0.2 \text{ mm y}^{-1}$) outside the region of
 141 this study. The estimated uncertainty of the VLM_{model}^{CM} originates from the standard un-
 142 certainty of the ice model combined with a 10% uncertainty that represents the uncer-
 143 tainty from the REF6371 earth model (Wang et al., 2012).

144 While the ice model of Greenland is well constrained, mass balance errors of in-
 145 dividual glaciers from the glacial model can be large (several times the glacial signal).
 146 We therefore divide the glacial model into 25x25 km tiles, which reduces the uncertainty
 147 significantly, but might also introduce unrealistic low uncertainty in areas with large glacial
 148 signals or where glaciers are poorly constrained. Glaciers are, however, still the largest
 149 source of regional uncertainty (see Supporting Information Figure S3.1.). The Caron2018
 150 GIA-model has standard uncertainty estimates included in the product, while there is
 151 no uncertainty estimate associated with the ICE6G-model. Uncertainties of geocenter
 152 motion from Sun et al. (2016) contributes to the GNSS-uncertainty estimate. The spa-
 153 tial distribution of the uncertainty estimates are shown in Supporting Information Fig-
 154 ure S3.1.

155 2.1 Ice Loading

156 The main component of VLM_{PDIL} is the ice loading model and consist of a com-
 157 bined water equivalent elevation model from Greenland and mass balance estimates from
 158 glaciers. Rate of elevation change is shown in Supporting Information Figure S1.1. While
 159 only Northern Hemisphere ice history is created with high resolution, changes of Antarc-
 160 tic and Southern Hemisphere ice loading is computed on a $0.5 \times 0.5^\circ$ grid and included
 161 in the computation of VLM_{PDIL}^{CM} . The low resolution does not have any impact on VLM
 162 in the Arctic. The total mass loss of the Southern Hemisphere is 140 Gt y^{-1} , equiva-
 163 lent of to 0.38 mm y^{-1} barystatic sea level rise.

164 2.1.1 Glaciers

165 A total of 62,000 individual glaciers from the Randolph Glacier Inventory (RGI 6.0)
 166 (Pfeffer et al., 2014; RGI Consortium, 2017) located in North America, Russia, Scandi-
 167 navia (incl. Svalbard) and Iceland have been included in this study. Mass loss from in-
 168 cluded glaciers accounts for 95 % of the registered glacial mass loss of the Northern Hemi-
 169 sphere and constitutes 80% of the global glacial mass loss (Zemp et al., 2019).

170 Mass change estimates for each glacier were estimated using an updated version
 171 of a model reported in Marzeion et al. (2012). Direct mass balance observations (Zemp
 172 et al., 2019) were used to calibrate and validate the glacier model. The glacier model trans-
 173 lates information about atmospheric conditions into glacier mass change, while consid-
 174 ering various feedback mechanisms that occur between glacier mass balance and glacier
 175 geometry. Glacial mass balance was combined with a distribution function to calculate
 176 glacier-wide surface elevation change. This ensured that the lower parts of glaciers are
 177 thinning, while upper parts experience small elevation gains. This 'slope steepening' of
 178 glaciers is characteristic of glaciers of many regions (Nuth et al., 2010; Foresta et al., 2016;
 179 Ciraci et al., 2018) and is assumed to apply to all glaciers included in this study (see Sup-
 180 porting Information S1 for an enhanced description of glacial elevation change).

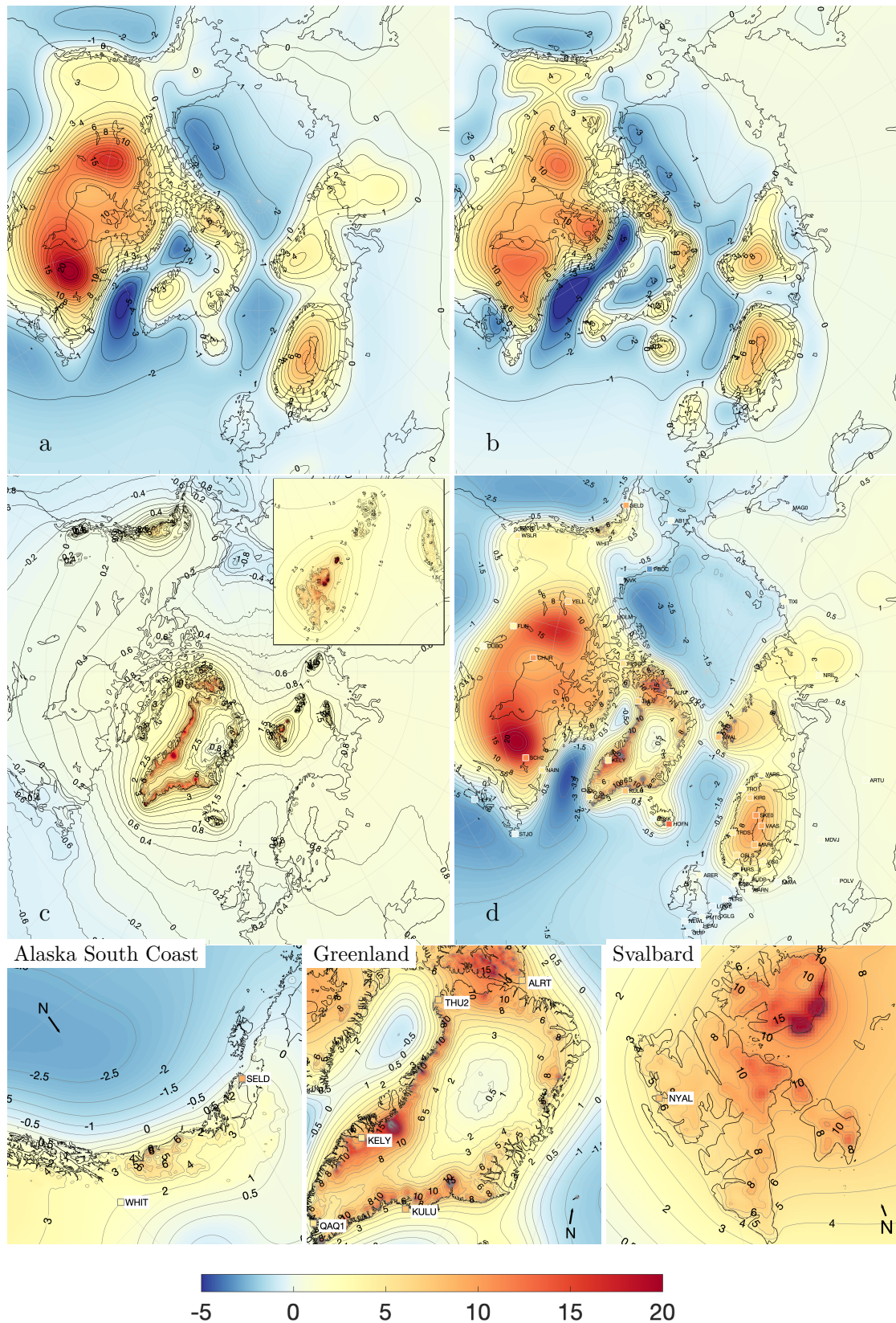


Figure 1. Average VLM-rates (mm y^{-1}) for 2003-2015 using the GIA-model of Caron2018(Caron et al., 2018) (a) and ICE6G_D (Peltier et al., 2018) (b). Modeled elastic rebound from contemporary land ice loss (including ocean loading and corrected for rotational feedback) (VLM_{ela}^{CM}) with enlargement of Svalbard is displayed in (c). The total VLM-model, VLM_{model}^{CM} , (a + c), with the square color representing average GNSS-determined VLM-rates (d). Enlargements of the south coast of Alaska, Greenland and Svalbard of (d) is shown in the bottom three panels. Spatial distribution of uncertainty estimates of (a),(c) and (d) are shown in

181 2.1.2 Greenland

182 Glacial ice history was combined with elevation change of the Greenland Ice Sheet
 183 and adjoining glaciers. We estimated the rate of ice volume change from 2003-2015 by
 184 using altimeter surveys from NASA’s ATM flights (Krabill, 2011) that took place be-
 185 tween 2003 and 2015 supplemented with high-resolution Ice, Cloud and land Elevation
 186 Satellite (ICESat) data (Zwally et al., 2011) from 2003-2009 and CryoSat-2 data from
 187 2011-2015 (Helm et al., 2014). Our procedure for deriving ice surface elevation changes
 188 has previously been described in detail by S. A. Khan et al. (2013) and is similar to the
 189 method used by, e.g. Ewert et al. (2012); Smith et al. (2009) and Kjeldsen et al. (2013).
 190 We used the observed ice elevation change rates to interpolate (using collocation) ice el-
 191 evation changes onto the 2x2 km spatial grid.

192 2.2 GNSS data

193 Timeseries of vertical deformation and uncertainty estimates of 54 GNSS-sites from
 194 the sixth release of the consortium led by University of La Rochelle (ULR-6) (Santamaría-
 195 Gómez et al., 2017) were used. A detailed map and timeseries of all GNSS-sites are shown
 196 in Supporting Information Figure S4.1 and Figure S5.1. ULR-6 includes 125 GNSS-sites
 197 located within the area of interest, but only GNSS-sites with data for at least 120 of 156
 198 months from 2003 to 2015 known not to be impacted by human activities were selected.
 199 One GNSS site was selected based on lowest observed standard deviation of timeseries
 200 when multiple GNSS sites were located within 100 km of each other. Nome (AT11), Es-
 201 bjerg City (ESBC) and Magadan (MAG0) were exempted from the temporal selection
 202 criteria, because of their location which has a special interest for interpretation.

203 Annual averages and combined uncertainties were calculated for each GNSS-site
 204 from the vertical component and standard uncertainty included in URL-6a. Hereafter,
 205 the linear trend was calculated for the years available between 2003 and 2015.

206 3 Evaluating the VLM model

207 From Figure 1 it is seen that the VLM-model is dominated by the pattern of the
 208 GIA-model, with rates above 20 mm y^{-1} east of the Hudson Bay and another local max-
 209 imum of over 15 mm y^{-1} in north-west Canada. The elastic rebound is evident in most
 210 of the Arctic, particular in Greenland with large areas exceeding 10 mm y^{-1} , with max-
 211 imum value at Jakobshavn Isbræ (69.1N, 49.5W) with an average modeled uplift of 40
 212 mm y^{-1} . Large areas around Svalbard and Alaska have modeled elastic VLM-rates of
 213 more than 8 mm y^{-1} . The uncertainty is significantly larger in glaciated regions than
 214 in the far field (see Figure 3.1 in Supporting Information).

215 Most depression zones are found over the ocean, with the Beaufort Sea and Labrador
 216 Sea subsiding with 2 mm y^{-1} and the Norwegian Sea with 1.5 mm y^{-1} . Subsiding coastal
 217 areas are found in North America, where Nova Scotia and most of the US east- and west
 218 coast subsides with more than 1 mm y^{-1} , while smaller subsidence (0.0 - 0.5 mm y^{-1})
 219 is found in Northern Europe along the North Sea and Atlantic coastlines. From Figure
 220 1 we see that most subsiding areas are caused by GIA.

221 Figure 2 shows that VLM_{model}^{CM} predicts VLM within the range of VLM_{GNSS}^{CM} at 46
 222 of 54 GNSS locations considered. The mean absolute error (MAE) for the 54 GNSS-sites
 223 was 1.39 mm y^{-1} (1.29 mm y^{-1} for ICE6G_D), which was 0.59 mm y^{-1} (0.56 mm y^{-1})
 224 better than MAE from only VLM_{GIA} . For 32 of the 54 GNSS-sites considered was the
 225 VLM-model with Caron2018 outperforming the ICE6G_D GIA model, thus was Caron2018
 226 selected as the default GIA-model in this study.

227 Barystatic sea level change for VLM_{PDIL} was 1.5 mm y^{-1} (ice loss-mediated global
 228 average sea level change (excl. Antarctica)). As shown in Figure 2, elastic VLM values

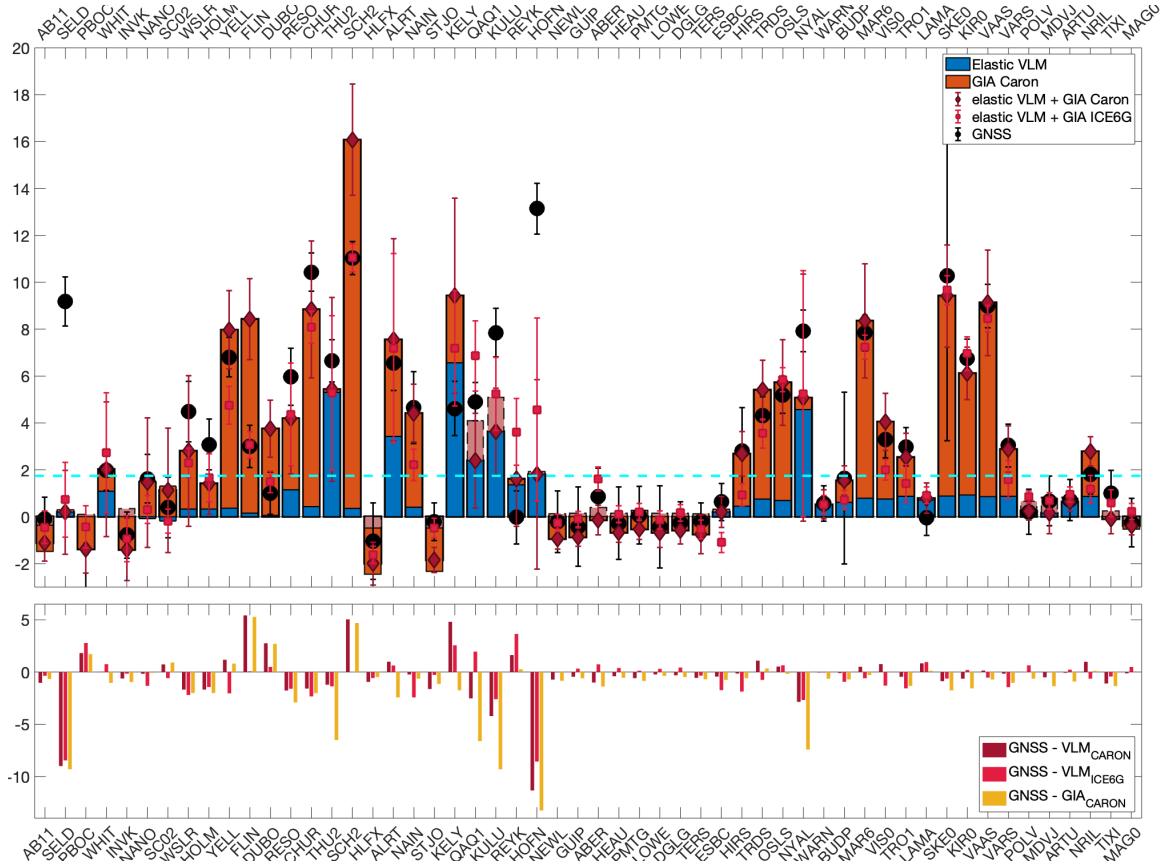


Figure 2. Average VLM change (mm y^{-1}) from 2003-2015 determined using the elastic VLM model (blue) and GIA (red) at the 54 GNSS-sites from Figure 1 and Supporting Information Figure S4.1 are shown (top). Sites are listed from most west (left) to most east (right). The dotted-cyan line indicates the average barystatic sea level rise ($\sim 1.85 \text{ mm y}^{-1}$) from the ice loss used in this study. The total modeled VLM uncertainty are indicated with red error bars and the GNSS-measured VLM is shown with black errorbars. Light red indicates locations in which GIA is negative and overlaps the positive elastic VLM. Residuals between GNSS-measured VLM (VLM_{GNSS}^{CM}) and the VLM-model (VLM_{model}^{CM}) (blue) and GIA (red) are shown (bottom). The average of the absolute residuals (equivalent to mean absolute error) are 1.54 mm y^{-1} and 1.89 mm y^{-1} respectively. All values used in this figure are included within Table S4.1 in Supporting Information.

229 between $0.5\text{-}1 \text{ mm y}^{-1}$ were observed at many far field GNSS-sites in this study and partly
 230 mitigated the barystatic sea level change.

231 The effect of non-cryospheric mass change is not included in VLM_{model}^{CM} . In par-
 232 ticular terrestrial water storage (TWS) causes a small uplift over large parts of North Amer-
 233 ica ($0.4 - 0.8 \text{ mm y}^{-1}$) and North-Central Siberia ($0.2 - 0.4 \text{ mm y}^{-1}$), while TWS is caus-
 234 ing a subsidence in most of Scandinavia of $0.2 - 0.4 \text{ mm y}^{-1}$ (Frederikse et al., 2019).

235 Glaciated regions show particularly large residuals between the predicted VLM and
 236 VLM measured by GNSS (Figure 3), but also exhibit the largest associated uncertain-
 237 ties of GNSS estimates. Predicted VLM at 30 of 54 GNSS-sites are within a range of 0.75
 238 mm y^{-1} to GNSS (the three center bins in the right panel of Figure 3), while there is
 239 an equal amount of under- and overestimates and hence no obvious bias. The most sig-

240 nificant discrepancies between measured and predicted VLM is explained in the follow-
 241 ing for every region.

242 3.1 North America

243 Alaska is located in the transition zone between GIA-uplift and GIA-subsidence,
 244 which is also reflected in the GNSS-rates. Nome (AB11), Prudhoe Bay (PBOC) and In-
 245 uvik (INVK) all experience an GIA-subsidence that is larger than the elastic uplift. While
 246 Nome and INVK are well matched with VLM_{GNSS}^{CM} , PBOC has the largest measured sub-
 247 sidence ($-3.2 \pm 1.6 \text{ mm yr}^{-1}$), while VLM_{model}^{CM} only shows a subsidence of $0.8 \pm 1.4 \text{ mm yr}^{-1}$.
 248 An extraordinary subsidence is likely caused by oil extraction in the Prudhoe Bay area.

249 The Alaska south coast accounts for more than 25% of the total glacial melt and
 250 is naturally dominated by elastic uplift while the uplift from GIA is below 1 mm yr^{-1} .
 251 Seldovia (SELD) shows an observed average rate of $9.2 \pm 1.0 \text{ mm yr}^{-1}$, while VLM_{ela}^{CM}
 252 is only $0.9 \pm 1.6 \text{ mm yr}^{-1}$ and GIA-rate $-0.1 \pm 0.8 \text{ mm yr}^{-1}$. Seldovia is located on the
 253 Kenai Peninsula close to the Kenai Fjords, which experienced an accelerated glacial ice
 254 loss in the 20th century (VanLooy et al., 2006). This is, however, not enough to explain
 255 the increased measured uplift. GIA-estimates vary in the region (Larsen et al., 2005; Hu
 256 & Freymueller, 2019), but is not more than around $1\text{-}2 \text{ mm yr}^{-1}$. The residual seems
 257 explained by a postseismic signal following the Prince Willam Sound Earthquake in 1964
 258 (Cohen & Freymueller, 2001; Huang et al., n.d.) which is still causing a local uplift on
 259 this side of the peninsula. The residuals estimates this effect to be 8.4 mm yr^{-1} from
 260 2003-2015, which is slightly less than the value found by Cohen and Freymueller (2001)
 261 of 9.3 mm yr^{-1} from 1994-2001. This rebound is expected to decay further over time,
 262 but will still be relevant for decades to come (Cohen & Freymueller, 2001; Huang et al.,
 263 n.d.).

264 Discrepancies between GNSS and modeled VLM in central North America, are likely
 265 due to uncertain GIA-estimates. A significantly better alignment between VLM_{model}^{CM} and
 266 GNSS is reached if Caron2018 is replaced by ICE-6G. The GIA-overestimate of Caron2018
 267 in North America has been demonstrated by other studies (Schumacher et al., 2018; Fred-
 268 erikse et al., 2019) and is likely caused by large differences between estimated viscosity
 269 properties of paleo-RSL indicators and GNSS in North America (Caron et al., 2018). TWS-
 270 change causes a small uplift below 1 mm yr^{-1} over large parts of North America (Frederikse
 271 et al., 2019), which enhances the difference between VLM_{model}^{CM} and VLM_{GNSS}^{CM} .

272 3.2 Greenland

273 Four GNSS-sites on Greenland and Alert (ALRT) on Baffin Island measure a sig-
 274 nificant elastic uplift. While Pittuffik/Thule (THU2) and ALRT agree with VLM_{model}^{CM} ,
 275 Kangerlussuaq (KELY) is overestimated quite a bit and VLM_{model}^{CM} at Kulusuk (KULU)
 276 and Qaqortoq (QAQ1) is below VLM_{GNSS}^{CM} . GIA on Greenland is poorly constrained in
 277 Caron2018, which can exaggerate VLM-estimates from GIA. A low-viscosity zone stretch-
 278 ing from Iceland beneath Southeast Greenland (S. A. Khan et al., 2016) enables a sig-
 279 nificant viscoelastic rebound caused by ice loss since LIA (S. Khan et al., 2014).

280 3.3 Iceland

281 The two GNSS-sites on Iceland show very different uplift rates of $0.0 \pm 1.1 \text{ mm}$
 282 yr^{-1} in Reykjavik (REYK) and $13.1 \pm 1.1 \text{ mm yr}^{-1}$ at Hoefn (HOFN) at the southern
 283 edge of the largest ice cap on Iceland, Vatnajökull. VLM_{model}^{CM} overestimates the rebound
 284 in Reykjavik while it largely underestimates it at Hoefn. Similar to south east Green-
 285 land a soft viscoelastic mantle layer (Fleming et al., 2007) creates a present-day viscoelas-
 286 tic signal that is much larger than the ones predicted by the GIA-model. A thin crust,
 287 also means that the uplift decreases faster with distance to the glacier (Fleming et al.,

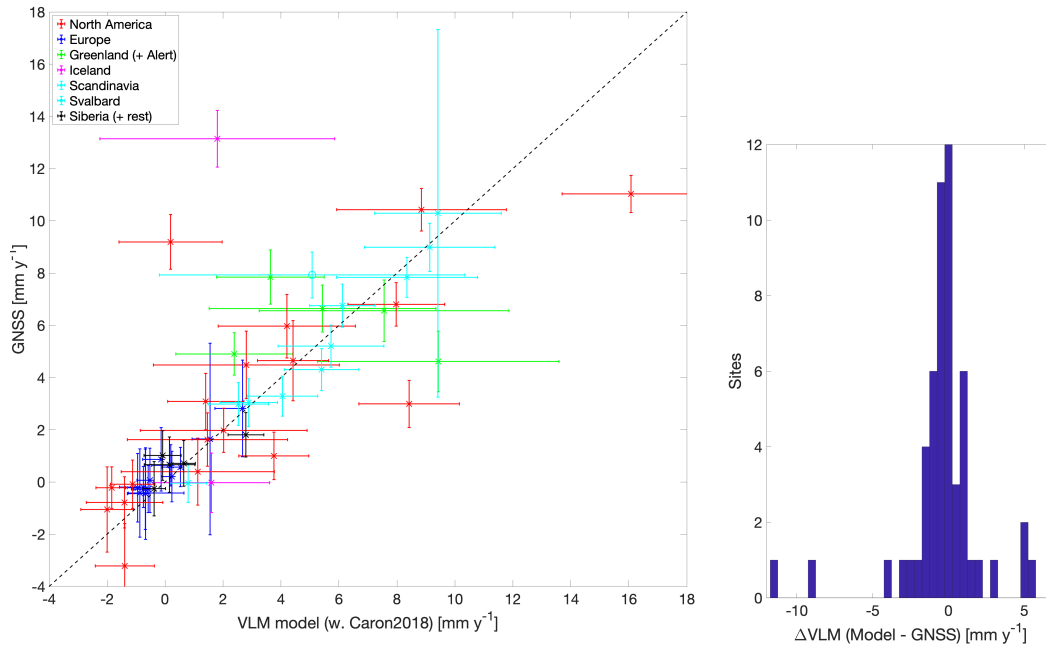


Figure 3. VLM_{GNSS}^{CM} versus VLM_{model}^{CM} including associated uncertainties for all GNSS-sites. If the cross is above the dashed line the VLM_{model}^{CM} underestimate compared to VLM_{GNSS}^{CM} . A histogram of the difference between VLM_{model}^{CM} and VLM_{GNSS}^{CM} (in intervals of 0.5 mm y^{-1}) is shown in the right panel.

288 2007; Sørensen et al., 2017), which could explain why Reykjavik shows little vertical de-
 289 formation despite being less than 100 km from glaciers.

290 3.4 Svalbard

291 The majority of land in Svalbard is covered with ice, and VLM is highly affected
 292 by ongoing ice-mass changes. At Ny Ålesund (NYAL), located on the west coast, VLM_{model}^{CM}
 293 is dominated by VLM_{ela}^{CM} of $4.9 \pm 5.3 \text{ mm yr}^{-1}$ and VLM_{GIA} of $0.5 \pm 0.4 \text{ mm yr}^{-1}$. In
 294 total this is 2.6 mm yr^{-1} short of observed VLM_{GNSS}^{CM} . While ICE6G and Caron2018
 295 agree within $\pm 0.2 \text{ mm yr}^{-1}$, more focused, but older studies predict a slightly higher
 296 GIA contribution of around 1.5 mm yr^{-1} (Sato et al., 2006; Kierulf et al., 2009). Also
 297 on Svalbard, significant post-LIA deglaciation (Grove, 2001) is likely contributing to an
 298 ongoing uplift (Mémin et al., 2014; Rajner, 2018). The effect is still uncertain (Rajner,
 299 2018) and Mémin et al. (2014) estimated the post-LIA rebound to be $2\text{-}5 \text{ mm yr}^{-1}$ in
 300 the beginning of 21st century, which explains the residual of 2.6 mm yr^{-1} .

301 3.5 Northern Europe and Scandinavia

302 GIA is dominating the vertical deformation in Scandinavia (Figure 1). Even though
 303 small glaciers exist in Norway, the elastic effect is very local and has almost negligible
 304 effect on the GNSS-sites in this study. However, VLM_{ela}^{CM} is still significant, and improves
 305 the correlation with observed VLM_{GNSS}^{CM} compared to a GIA-only model. This becomes
 306 more prominent for GNSS-sites in areas, where GIA is less dominant. Esbjerg (ESBC)
 307 on the west coast of Denmark is close to the zero-line of Caron2018, but is still measur-
 308 ing an uplift of about 0.6 mm yr^{-1} , which is equal to the rate from VLM_{ela}^{CM} .

309 In Northern Europe, Caron2018 models a subsidence, which is mitigated by an elas-
 310 tic uplift caused by present day ice melt. Generally, VLM_{model}^{CM} is consistent with VLM_{GNSS}^{CM}
 311 in the North Sea and the Baltic region, while an VLM-model using ICE6G is at odds
 312 at several locations.

313 3.6 Siberia

314 Only a few available GNSS measurements exist in eastern Europe and Siberia. Caron2018
 315 is also challenged by limited resources of paleo sea-level records, which makes the GIA-
 316 model more dependent on the existing GNSS-records. It is commonly anticipated that
 317 Siberia had little or no ice during the last glacial cycle (Whitehouse et al., 2007), except
 318 north central Siberia and in the shallow waters in the Barents Sea between Svalbard and
 319 Novaya Zemlya (Root et al., 2015).

320 Also VLM_{ela}^{CM} is generally smaller than around 0.5 mm yr^{-1} . While the VLM_{GNSS}^{CM}
 321 is within the uncertainty-range of VLM_{model}^{CM} for the Siberian GNSS-sites (Arti (ARTU),
 322 Norilsk (NRIL), Tixi (TIXI) and Magadan (MAG0)), a GIA-only model fits the GNSS
 323 measurements better which is likely due to increased dependence on GNSS in Caron2018.

324 4 Discussion and Conclusion

325 VLM of the wider Arctic region occurs mainly as a result GIA and elastic VLM.
 326 Though this study is limited to the area surrounding the Arctic, VLM caused by deglacia-
 327 tion produces global effects (Riva et al., 2017; Kleinherenbrink et al., 2018; Frederikse
 328 et al., 2019). By combining deglaciation that occurred since the last glacial maximum
 329 (GIA) and present-day changes in land ice (elastic VLM), the VLM-model provides a
 330 realistic estimate of VLM in the Arctic. By evaluating 54 GNSS-sites using a combined
 331 VLM-model, we found that measured uplift of GNSS can be explained by either prehis-
 332 toric or present-day changes in land ice volume. For 46 of the GNSS sites, residuals be-
 333 tween GNSS-measured VLM values and the VLM-model were smaller than associated
 334 uncertainties.

335 The 2x2-km spatial resolution of the used ice-model was much higher than simi-
 336 lar gravimetric satellite observations from GRACE (Adhikari et al., 2019). Increased spa-
 337 tial resolution improves VLM predictions accuracy in glaciated regions significantly, as
 338 local elastic deformation tends to dominate regional averages observed via GRACE (Frederikse
 339 et al., 2019). A VLM-model to GNSS comparison also indicated that the VLM-model
 340 was inadequate in some regions due to local causes of VLM that were not included in
 341 the VLM-model, such as subsurface properties, past seismic activity or 19–20th century
 342 ice-loss (Mémin et al., 2014; Rajner, 2018).

343 In non-glaciated areas, GNSS measurements generally agree well with the VLM-
 344 model. Contour lines shown in Figure 1, indicate that elastic uplift is centered around
 345 Greenland, except when close to other glaciated regions (e.g. Alaska and Svalbard), de-
 346 spite the fact that total Arctic glaciers mass loss is comparable with that of Greenland.
 347 Hence, the elastic uplift caused by ice melt in Greenland significantly affects the entire
 348 wider Arctic region, which includes coastlines of Northern Europe and the North Amer-
 349 ican Atlantic.

350 Riva et al. (2017) showed that elastic uplift caused by ice loss in Greenland causes
 351 a subsidence in the Southern Hemisphere. Similar, it is assumed that Antarctic ice loss
 352 will cause a subsidence in the Northern Hemisphere. Antarctic ice loss averaged 105 Gt
 353 y^{-1} from 2003-2015 (Schröder et al., 2019), and resulted in an elastic subsidence of less
 354 than 0.1 mm y^{-1} in the Northern Hemisphere. Since ice loss has the potential to occur
 355 rapidly in the future (Hay et al., 2017; Edwards et al., 2019), VLM caused by Antarc-

356 tic ice loss will be increasingly significant, and may be important for future coastal sea
357 level projections in the Northern Hemisphere.

358 Acknowledgments

359 We wish to thank Lambert Caron, Matt King and one anonymous reviewer for their con-
360 structive and helpful comments, which greatly improved the manuscript. Thanks to Danielle
361 Melini (Melini et al., 2014), for creating the REAR-code, which facilitated the creation
362 of the VLM-model. We also greatly appreciate the work of L. Caron (Caron et al., 2018)
363 on the Caron2018 GIA-model available from the NASA JPL website ([https://ves1.jpl
364 .nasa.gov/solid-earth/gia/](https://ves1.jpl.nasa.gov/solid-earth/gia/)) and R. Peltier on the ICE-6G_D model (Peltier et al.,
365 2018). elastic VLM and both GIA-models is available in a Arctic 5x5 km grid at [data
366 .dtu.dk/articles/Arctic_Vertical_Land_Motion_5x5_km_/12554489](http://data.dtu.dk/articles/Arctic_Vertical_Land_Motion_5x5_km_/12554489). The project
367 was partially funded by the EU-INTAROS project (Grant agreement no. 727890) and
368 the ESA-Climate Change Initiative Sea level budget closure (Expro RFP/3-14679/16/I-
369 NB).

370 References

- 371 Abram, N., Adler, C., Bindoff, N., Cheng, L., Cheong, S.-M., Cheung, W., ... Zhai,
372 P. (2019, 09). Summary for policymakers. in: IPCC special report on the
373 ocean and cryosphere in a changing climate..
- 374 Adhikari, S., Ivins, E. R., Frederikse, T., Landerer, F. W., & Caron, L. (2019).
375 Sea-level fingerprints emergent from grace mission data. *Earth System Science
376 Data*, 11(2), 629–646. Retrieved from [https://www.earth-syst-sci-data
377 .net/11/629/2019/](https://www.earth-syst-sci-data.net/11/629/2019/) doi: 10.5194/essd-11-629-2019
- 378 Adhikari, S., Ivins, E. R., & Larour, E. (2016). Issm-sesaw v1.0: mesh-based compu-
379 tation of gravitationally consistent sea-level and geodetic signatures caused by
380 cryosphere and climate driven mass change. *Geoscientific Model Development*,
381 9(3), 1087–1109. Retrieved from [https://www.geosci-model-dev.net/9/
382 1087/2016/](https://www.geosci-model-dev.net/9/1087/2016/) doi: 10.5194/gmd-9-1087-2016
- 383 Altamimi, Z., Collilieux, X., & Métivier, L. (2011). Itrf2008: an improved solution
384 of the international terrestrial reference frame. *Journal of Geodesy*, 85(8), 457–
385 473. Retrieved from <https://doi.org/10.1007/s00190-011-0444-4> doi: 10
386 .1007/s00190-011-0444-4
- 387 Argus, D., Peltier, W., Drummond, R., & Moore, A. (2014). The antarctica compo-
388 nent of postglacial rebound model ice-6g_c (vm5a) based on gps positioning,
389 exposure age dating of ice thicknesses, and relative sea level histories. *Geo-
390 physical Journal International*, 198(1), 537-563. Retrieved from [https://www
391 .scopus.com/inward/record.uri?eid=2-s2.0-84905924704&doi=10.1093%
392 2fgji%2fggu140&partnerID=40&md5=10f1208c9a63c67153b06b8bd607a133](https://www.scopus.com/inward/record.uri?eid=2-s2.0-84905924704&doi=10.1093%2fgji%2fggu140&partnerID=40&md5=10f1208c9a63c67153b06b8bd607a133)
393 (cited By 149) doi: 10.1093/gji/ggu140
- 394 Bizouard, C., & Gambis, D. (2009, 06). The combined solution c04 for earth ori-
395 entation parameters consistent with international terrestrial reference frame
396 2005. In (Vol. 134, p. 265-270). doi: 10.1007/978-3-642-00860-3_41
- 397 Caron, L., Ivins, E. R., Larour, E., Adhikari, S., Nilsson, J., & Blewitt, G. (2018).
398 Gia model statistics for grace hydrology, cryosphere, and ocean science. *Geo-
399 physical Research Letters*, 45(5), 2203-2212. Retrieved from [https://agupubs
400 .onlinelibrary.wiley.com/doi/abs/10.1002/2017GL076644](https://agupubs.onlinelibrary.wiley.com/doi/abs/10.1002/2017GL076644) doi: 10.1002/
401 2017GL076644
- 402 Church, J., & White, N. (2011). Sea-level rise from the late 19th to the
403 early 21st century. *Surveys in Geophysics*, 32(4-5), 585-602. Re-
404 trieved from [https://www.scopus.com/inward/record.uri?eid=2-s2.0
405 -80053195533&doi=10.1007%2fs10712-011-9119-1&partnerID=40&md5=
406 a6a2b9bb53f622e9bf4b3266a27d54f0](https://www.scopus.com/inward/record.uri?eid=2-s2.0-80053195533&doi=10.1007%2fs10712-011-9119-1&partnerID=40&md5=a6a2b9bb53f622e9bf4b3266a27d54f0) (cited By 737) doi: 10.1007/

- s10712-011-9119-1
- 407
408 Ciraci, E., Velicogna, I., & Sutterley, T. C. (2018). Mass balance of novaya
409 zemlya archipelago, russian high arctic, using time-variable gravity from
410 grace and altimetry data from icesat and cryosat-2. *Remote Sensing*, 10(11).
411 Retrieved from <https://www.mdpi.com/2072-4292/10/11/1817> doi:
412 10.3390/rs10111817
- 413 Clark, J. A., & Lingle, C. S. (1977). Future sea-level changes due to west antarctic
414 ice sheet fluctuations. *Nature*, 269(5625), 206–209. Retrieved from <https://doi.org/10.1038/269206a0> doi: 10.1038/269206a0
- 415
416 Cohen, S. C., & Freymueller, J. T. (2001). Crustal uplift in the south central
417 alaska subduction zone: New analysis and interpretation of tide gauge obser-
418 vations. *Journal of Geophysical Research: Solid Earth*, 106(B6), 11259–11270.
419 Retrieved from [https://agupubs.onlinelibrary.wiley.com/doi/abs/](https://agupubs.onlinelibrary.wiley.com/doi/abs/10.1029/2000JB900419)
420 10.1029/2000JB900419 doi: 10.1029/2000JB900419
- 421 Dong, D., Yunck, T., & Heflin, M. (2003). Origin of the international terrestrial
422 reference frame. *Journal of Geophysical Research: Solid Earth*, 108(B4).
423 Retrieved from [https://agupubs.onlinelibrary.wiley.com/doi/abs/](https://agupubs.onlinelibrary.wiley.com/doi/abs/10.1029/2002JB002035)
424 10.1029/2002JB002035 doi: 10.1029/2002JB002035
- 425 Dziewonski, A. M., & Anderson, D. L. (1981). Preliminary reference earth model.
426 *Physics of the Earth and Planetary Interiors*, 25(4), 297 - 356. Retrieved from
427 <http://www.sciencedirect.com/science/article/pii/0031920181900467>
428 doi: [https://doi.org/10.1016/0031-9201\(81\)90046-7](https://doi.org/10.1016/0031-9201(81)90046-7)
- 429 Edwards, T., Brandon, M., Durand, G., Edwards, N., Golledge, N., Holden, P., ...
430 Wernecke, A. (2019, 02). Revisiting antarctic ice loss due to marine ice-cliff
431 instability. *Nature*, 566, 58–64. doi: 10.1038/s41586-019-0901-4
- 432 Ewert, H., Groh, A., & Dietrich, R. (2012, September). Volume and mass changes of
433 the Greenland ice sheet inferred from ICESat and GRACE. *Journal of Geody-
434 namics*, 59–60, 111–123. doi: 10.1016/j.jog.2011.06.003
- 435 Farrell, W. E. (1972). Deformation of the earth by surface loads. *Re-
436 views of Geophysics*, 10(3), 761–797. Retrieved from [https://agupubs](https://agupubs.onlinelibrary.wiley.com/doi/abs/10.1029/RG010i003p00761)
437 [.onlinelibrary.wiley.com/doi/abs/10.1029/RG010i003p00761](https://agupubs.onlinelibrary.wiley.com/doi/abs/10.1029/RG010i003p00761) doi:
438 10.1029/RG010i003p00761
- 439 Farrell, W. E., & Clark, J. A. (1976). On postglacial sea level. *Geophysical Journal
440 of the Royal Astronomical Society*, 46(3), 647–667. Retrieved from [https://](https://onlinelibrary.wiley.com/doi/abs/10.1111/j.1365-246X.1976.tb01252.x)
441 onlinelibrary.wiley.com/doi/abs/10.1111/j.1365-246X.1976.tb01252.x
442 doi: 10.1111/j.1365-246X.1976.tb01252.x
- 443 Fleming, K., Martinec, Z., & Wolf, D. (2007, 01). Glacial-isostatic adjustment and
444 the viscosity structure underlying the vatnajökull ice cap, iceland. *Pure and
445 Applied Geophysics*, 164, 751–768. doi: 10.1007/s00024-007-0187-6
- 446 Foresta, L., Gourmelen, N., Pálsson, F., Nienow, P., Björnsson, H., & Shepherd, A.
447 (2016). Surface elevation change and mass balance of icelandic ice caps derived
448 from swath mode cryosat-2 altimetry. *Geophysical Research Letters*, 43(23),
449 12,138–12,145. Retrieved from [https://agupubs.onlinelibrary.wiley.com/](https://agupubs.onlinelibrary.wiley.com/doi/abs/10.1002/2016GL071485)
450 [doi/abs/10.1002/2016GL071485](https://agupubs.onlinelibrary.wiley.com/doi/abs/10.1002/2016GL071485) doi: 10.1002/2016GL071485
- 451 Forget, G., Campin, J.-M., Heimbach, P., Hill, C. N., Ponte, R. M., & Wunsch, C.
452 (2015). Ecco version 4: an integrated framework for non-linear inverse model-
453 ing and global ocean state estimation. *Geoscientific Model Development*, 8(10),
454 3071–3104. Retrieved from [https://gmd.copernicus.org/articles/8/3071/](https://gmd.copernicus.org/articles/8/3071/2015/)
455 2015/ doi: 10.5194/gmd-8-3071-2015
- 456 Frederikse, T., Landerer, F. W., & Caron, L. (2019). The imprints of con-
457 temporary mass redistribution on local sea level and vertical land motion
458 observations. *Solid Earth*, 10(6), 1971–1987. Retrieved from [https://](https://www.solid-earth.net/10/1971/2019/)
459 www.solid-earth.net/10/1971/2019/ doi: 10.5194/se-10-1971-2019
- 460 Fukumori, I., Wang, O., Fenty, I., Forget, G., Heimbach, P., & Ponte, R. M. (2019).
461 Ecco version 4 release 4 dataset. <https://ecco.jpl.nasa.gov/drive>. (Ac-

- 462 cessed: 2020-06-25)
- 463 Grove, J. (2001, 01). The initiation of the "little ice age" in regions round the north
464 atlantic. *Climatic Change*, *48*, 53-82. doi: 10.1023/A:1005662822136
- 465 Hay, C. C., Lau, H. C. P., Gomez, N., Austermann, J., Powell, E., Mitrovica,
466 J. X., ... Wiens, D. A. (2017). Sea level fingerprints in a region of com-
467 plex earth structure: The case of wais. *Journal of Climate*, *30*(6), 1881-
468 1892. Retrieved from <https://doi.org/10.1175/JCLI-D-16-0388.1> doi:
469 10.1175/JCLI-D-16-0388.1
- 470 Helm, V., Humbert, A., & Miller, H. (2014). Elevation and elevation change of
471 greenland and antarctica derived from cryosat-2. *The Cryosphere*, *8*(4), 1539-
472 1559. Retrieved from <https://www.the-cryosphere.net/8/1539/2014/> doi:
473 10.5194/tc-8-1539-2014
- 474 Henry, O., Prandi, P., Llovel, W., Cazenave, A., Jevrejeva, S., Stammer, D., ...
475 Koldunov, N. (2012). Tide gauge-based sea level variations since 1950 along
476 the norwegian and russian coasts of the arctic ocean: Contribution of the steric
477 and mass components. *Journal of Geophysical Research: Oceans*, *117*(C6).
478 Retrieved from [https://agupubs.onlinelibrary.wiley.com/doi/abs/](https://agupubs.onlinelibrary.wiley.com/doi/abs/10.1029/2011JC007706)
479 [10.1029/2011JC007706](https://agupubs.onlinelibrary.wiley.com/doi/abs/10.1029/2011JC007706) doi: 10.1029/2011JC007706
- 480 Hu, Y., & Freymueller, J. T. (2019). Geodetic observations of time-variable glacial
481 isostatic adjustment in southeast alaska and its implications for earth rhe-
482 ology. *Journal of Geophysical Research: Solid Earth*, *124*(9), 9870-9889.
483 Retrieved from [https://agupubs.onlinelibrary.wiley.com/doi/abs/](https://agupubs.onlinelibrary.wiley.com/doi/abs/10.1029/2018JB017028)
484 [10.1029/2018JB017028](https://agupubs.onlinelibrary.wiley.com/doi/abs/10.1029/2018JB017028) doi: 10.1029/2018JB017028
- 485 Huang, K., Hu, Y., & Freymueller, J. T. (n.d.). Decadal viscoelastic postseismic
486 deformation of the 1964 mw9.2 alaska earthquake. *Journal of Geophysical Re-*
487 *search: Solid Earth*, *n/a*(n/a), e2020JB019649. Retrieved from [https://](https://agupubs.onlinelibrary.wiley.com/doi/abs/10.1029/2020JB019649)
488 agupubs.onlinelibrary.wiley.com/doi/abs/10.1029/2020JB019649
489 [\(e2020JB019649 2020JB019649\)](https://agupubs.onlinelibrary.wiley.com/doi/abs/10.1029/2020JB019649) doi: 10.1029/2020JB019649
- 490 Jevrejeva, S., Moore, J., Grinsted, A., Matthews, A., & Spada, G. (2014). Trends
491 and acceleration in global and regional sea levels since 1807. *Global and Plan-*
492 *etary Change*, *113*, 11-22. Retrieved from [https://www.scopus.com/inward/](https://www.scopus.com/inward/record.uri?eid=2-s2.0-84890953576&doi=10.1016%2fj.gloplacha.2013.12.004&partnerID=40&md5=67194675f8fc061f1bb025a9fb67361f)
493 [record.uri?eid=2-s2.0-84890953576&doi=10.1016%2fj.gloplacha.2013](https://www.scopus.com/inward/record.uri?eid=2-s2.0-84890953576&doi=10.1016%2fj.gloplacha.2013.12.004&partnerID=40&md5=67194675f8fc061f1bb025a9fb67361f)
494 [.12.004&partnerID=40&md5=67194675f8fc061f1bb025a9fb67361f](https://www.scopus.com/inward/record.uri?eid=2-s2.0-84890953576&doi=10.1016%2fj.gloplacha.2013.12.004&partnerID=40&md5=67194675f8fc061f1bb025a9fb67361f) (cited By
495 85) doi: 10.1016/j.gloplacha.2013.12.004
- 496 Khan, S., Kjeldsen, K., Kjær, K., Bevan, S., Luckman, A., Aschwanden, A., ...
497 Fitzner, A. (2014). Glacier dynamics at helheim and kangerdlugssuaq glaciers,
498 southeast greenland, since the little ice age. *Cryosphere*, *8*, 1497-1507. (CC
499 Attribution 3.0 License) doi: 10.5194/tc-8-1497-2014
- 500 Khan, S. A., Kjær, K. H., Korsgaard, N. J., Wahr, J., Joughin, I. R., Timm, L. H.,
501 ... Babonis, G. (2013). Recurring dynamically induced thinning during
502 1985 to 2010 on upernavik isstrøm, west greenland. *Journal of Geophys-*
503 *ical Research: Earth Surface*, *118*(1), 111-121. Retrieved from [https://](https://agupubs.onlinelibrary.wiley.com/doi/abs/10.1029/2012JF002481)
504 agupubs.onlinelibrary.wiley.com/doi/abs/10.1029/2012JF002481 doi:
505 10.1029/2012JF002481
- 506 Khan, S. A., Sasgen, I., Bevis, M., van Dam, T., Bamber, J. L., Wahr, J., ...
507 Munneke, P. K. (2016). Geodetic measurements reveal similarities between
508 post-last glacial maximum and present-day mass loss from the greenland ice
509 sheet. *Science Advances*, *2*(9). Retrieved from [https://advances.sciencemag](https://advances.sciencemag.org/content/2/9/e1600931)
510 [.org/content/2/9/e1600931](https://advances.sciencemag.org/content/2/9/e1600931) doi: 10.1126/sciadv.1600931
- 511 Kierulf, H. P., Plag, H.-P., & Kohler, J. (2009, 10). Surface deformation induced by
512 present-day ice melting in Svalbard. *Geophysical Journal International*, *179*(1),
513 1-13. Retrieved from <https://doi.org/10.1111/j.1365-246X.2009.04322.x>
514 doi: 10.1111/j.1365-246X.2009.04322.x
- 515 King, M. A., Keshin, M., Whitehouse, P. L., Thomas, I. D., Milne, G., & Riva,
516 R. E. M. (2012). Regional biases in absolute sea-level estimates from tide

- 517 gauge data due to residual unmodeled vertical land movement. *Geophysical*
 518 *Research Letters*, 39(14). Retrieved from <https://agupubs.onlinelibrary>
 519 [.wiley.com/doi/abs/10.1029/2012GL052348](https://agupubs.onlinelibrary.wiley.com/doi/abs/10.1029/2012GL052348) doi: 10.1029/2012GL052348
- 520 King, M. A., & Watson, C. S. (2014, 09). Geodetic vertical velocities affected by re-
 521 cent rapid changes in polar motion. *Geophysical Journal International*, 199(2),
 522 1161-1165. Retrieved from <https://doi.org/10.1093/gji/ggu325> doi: 10
 523 .1093/gji/ggu325
- 524 Kjeldsen, K. K., Khan, S. A., Wahr, J., Korsgaard, N. J., Kjær, K. H., Bjørk, A. A.,
 525 ... van Angelen, J. H. (2013). Improved ice loss estimate of the northwestern
 526 greenland ice sheet. *Journal of Geophysical Research: Solid Earth*, 118(2),
 527 698-708. Retrieved from [https://agupubs.onlinelibrary.wiley.com/doi/](https://agupubs.onlinelibrary.wiley.com/doi/abs/10.1029/2012JB009684)
 528 [abs/10.1029/2012JB009684](https://agupubs.onlinelibrary.wiley.com/doi/abs/10.1029/2012JB009684) doi: 10.1029/2012JB009684
- 529 Kleinherenbrink, M., Riva, R., & Frederikse, T. (2018). A comparison of methods
 530 to estimate vertical land motion trends from gnss and altimetry at tide gauge
 531 stations. *Ocean Science*, 14(2), 187-204. Retrieved from [https://www.scopus](https://www.scopus.com/inward/record.uri?eid=2-s2.0-85044121271&doi=10.5194/2fos-14-187-2018&partnerID=40&md5=dbe85241ab9f3400fe3f655c42918079)
 532 [.com/inward/record.uri?eid=2-s2.0-85044121271&doi=10.5194/2fos-14](https://www.scopus.com/inward/record.uri?eid=2-s2.0-85044121271&doi=10.5194/2fos-14-187-2018&partnerID=40&md5=dbe85241ab9f3400fe3f655c42918079)
 533 [-187-2018&partnerID=40&md5=dbe85241ab9f3400fe3f655c42918079](https://www.scopus.com/inward/record.uri?eid=2-s2.0-85044121271&doi=10.5194/2fos-14-187-2018&partnerID=40&md5=dbe85241ab9f3400fe3f655c42918079) (cited
 534 By 6) doi: 10.5194/os-14-187-2018
- 535 Krabill, W. B. (2011). *Icebridge atm l2 icesn elevation, slope, and roughness,*
 536 *[1993-2012]*. (Boulder, Colorado: NASA Distributed Active Archive Center
 537 at the National Snow and Ice Data Center) doi: 10.5067/ICESAT/GLAS/
 538 DATA225
- 539 Kustowski, B., Dziewoński, A. M., & Ekström, G. (2007, 10). Nonlinear Crustal
 540 Corrections for Normal-Mode Seismograms. *Bulletin of the Seismological Soci-*
 541 *ety of America*, 97(5), 1756-1762. Retrieved from [https://doi.org/10.1785/](https://doi.org/10.1785/0120070041)
 542 [0120070041](https://doi.org/10.1785/0120070041) doi: 10.1785/0120070041
- 543 Larsen, C. F., Motyka, R. J., Freymueller, J. T., Echelmeyer, K. A., & Ivins, E. R.
 544 (2005). Rapid viscoelastic uplift in southeast alaska caused by post-little ice
 545 age glacial retreat. *Earth and Planetary Science Letters*, 237(3), 548 - 560.
 546 Retrieved from [http://www.sciencedirect.com/science/article/pii/](http://www.sciencedirect.com/science/article/pii/S0012821X05004152)
 547 [S0012821X05004152](http://www.sciencedirect.com/science/article/pii/S0012821X05004152) doi: <https://doi.org/10.1016/j.epsl.2005.06.032>
- 548 Li, T., Wu, P., Wang, H., Steffen, H., Khan, N. S., Engelhart, S. E., ... Horton, B. P.
 549 (2020). Uncertainties of glacial isostatic adjustment model predictions in north
 550 america associated with 3d structure. *Geophysical Research Letters*, 47(10),
 551 e2020GL087944. Retrieved from [https://agupubs.onlinelibrary.wiley](https://agupubs.onlinelibrary.wiley.com/doi/abs/10.1029/2020GL087944)
 552 [.com/doi/abs/10.1029/2020GL087944](https://agupubs.onlinelibrary.wiley.com/doi/abs/10.1029/2020GL087944) (e2020GL087944 2020GL087944) doi:
 553 10.1029/2020GL087944
- 554 Marzeion, B., Jarosch, A. H., & Hofer, M. (2012). Past and future sea-level change
 555 from the surface mass balance of glaciers. *The Cryosphere*, 6(6), 1295-1322.
 556 Retrieved from <https://www.the-cryosphere.net/6/1295/2012/> doi:
 557 10.5194/tc-6-1295-2012
- 558 Melini, D., Gegout, P., King, M., Marzeion, B., & Spada, G. (2015, 08). On the
 559 rebound: Modeling earth's ever-changing shape. *Eos Transactions American*
 560 *Geophysical Union*, 96. doi: 10.1029/2015EO033387
- 561 Melini, D., Spada, G., Gegout, P., & King, M. (2014, 01). *Rear - a regional elastic*
 562 *rebound calculator. user manual for version 1.0.* Retrieved from [http://hpc](http://hpc.rm.ingv.it/rear)
 563 [.rm.ingv.it/rear](http://hpc.rm.ingv.it/rear)
- 564 Milne, G. A., & Mitrovica, J. X. (1998, 04). Postglacial sea-level change on a ro-
 565 tating Earth. *Geophysical Journal International*, 133(1), 1-19. Retrieved
 566 from <https://doi.org/10.1046/j.1365-246X.1998.1331455.x> doi:
 567 10.1046/j.1365-246X.1998.1331455.x
- 568 Milne, G. A., Mitrovica, J. X., & Davis, J. L. (1999, 11). Near-field hydro-isostasy:
 569 the implementation of a revised sea-level equation. *Geophysical Journal Inter-*
 570 *national*, 139(2), 464-482. Retrieved from [https://doi.org/10.1046/j.1365-](https://doi.org/10.1046/j.1365-246x.1999.00971.x)
 571 [246x.1999.00971.x](https://doi.org/10.1046/j.1365-246x.1999.00971.x) doi: 10.1046/j.1365-246x.1999.00971.x

- 572 Mémin, A., Spada, G., Boy, J.-P., Rogister, Y., & Hinderer, J. (2014, 05). Decadal
573 geodetic variations in Ny-Ålesund (Svalbard): role of past and present ice-mass
574 changes. *Geophysical Journal International*, 198(1), 285-297. Retrieved from
575 <https://doi.org/10.1093/gji/ggu134> doi: 10.1093/gji/ggu134
- 576 Nerem, R. S., Beckley, B. D., Fasullo, J. T., Hamlington, B. D., Masters, D., &
577 Mitchum, G. T. (2018). Climate-change-driven accelerated sea-level rise de-
578 tected in the altimeter era. *Proceedings of the National Academy of Sciences*,
579 115(9), 2022–2025. Retrieved from [https://www.pnas.org/content/115/9/](https://www.pnas.org/content/115/9/2022)
580 2022 doi: 10.1073/pnas.1717312115
- 581 Nuth, C., Moholdt, G., Kohler, J., Hagen, J. O., & Käab, A. (2010). Svalbard
582 glacier elevation changes and contribution to sea level rise. *Journal of*
583 *Geophysical Research: Earth Surface*, 115(F1). Retrieved from [https://](https://agupubs.onlinelibrary.wiley.com/doi/abs/10.1029/2008JF001223)
584 agupubs.onlinelibrary.wiley.com/doi/abs/10.1029/2008JF001223 doi:
585 10.1029/2008JF001223
- 586 Peltier, W., Argus, D., & Drummond, R. (2015). Space geodesy constrains ice age
587 terminal deglaciation: The global ice-6g-c (vm5a) model. *Journal of Geo-*
588 *physical Research: Solid Earth*, 120(1), 450-487. Retrieved from [https://www](https://www.scopus.com/inward/record.uri?eid=2-s2.0-85027948080&doi=10.1002%2f2014JB011176&partnerID=40&md5=29a7ce38c5cf3872d2276981d2f6b34f)
589 [.scopus.com/inward/record.uri?eid=2-s2.0-85027948080&doi=10.1002%](https://www.scopus.com/inward/record.uri?eid=2-s2.0-85027948080&doi=10.1002%2f2014JB011176&partnerID=40&md5=29a7ce38c5cf3872d2276981d2f6b34f)
590 [2f2014JB011176&partnerID=40&md5=29a7ce38c5cf3872d2276981d2f6b34f](https://www.scopus.com/inward/record.uri?eid=2-s2.0-85027948080&doi=10.1002%2f2014JB011176&partnerID=40&md5=29a7ce38c5cf3872d2276981d2f6b34f)
591 (cited By 326) doi: 10.1002/2014JB011176
- 592 Peltier, W. R., Argus, D. F., & Drummond, R. (2018, February). Comment on "An
593 Assessment of the ICE-6G_C (VM5a) Glacial Isostatic Adjustment Model"
594 by Purcell et al. *Journal of Geophysical Research (Solid Earth)*, 123(2), 2019-
595 2028. doi: 10.1002/2016JB013844
- 596 Pfeffer, W. T., Arendt, A. A., Bliss, A., Bolch, T., Cogley, J. G., Gardner,
597 A. S., ... et al. (2014). The randolph glacier inventory: a globally com-
598 plete inventory of glaciers. *Journal of Glaciology*, 60(221), 537–552. doi:
599 10.3189/2014JoG13J176
- 600 Post, E., Alley, R. B., Christensen, T. R., Macias-Fauria, M., Forbes, B. C., Gooseff,
601 M. N., ... Wang, M. (2019). The polar regions in a 2c warmer world. *Sci-*
602 *ence Advances*, 5(12). Retrieved from [https://advances.sciencemag.org/](https://advances.sciencemag.org/content/5/12/eaaw9883)
603 [content/5/12/eaaw9883](https://advances.sciencemag.org/content/5/12/eaaw9883) doi: 10.1126/sciadv.aaw9883
- 604 Rajner, M. (2018). Detection of ice mass variation using gnss measurements
605 at svalbard. *Journal of Geodynamics*, 121, 20 - 25. Retrieved from
606 <http://www.sciencedirect.com/science/article/pii/S0264370718300450>
607 doi: <https://doi.org/10.1016/j.jog.2018.06.001>
- 608 RGI Consortium. (2017). *Randolph Glacier Inventory – A Dataset of Global Glacier*
609 *Outlines: Version 6.0: Technical Report*. ([https://doi.org/10.7265/N5-RGI](https://doi.org/10.7265/N5-RGI-60)
610 -60)
- 611 Riva, E., Frederikse, T., King, A., Marzeion, B., & Van Den Broeke, R. (2017).
612 Brief communication: The global signature of post-1900 land ice wastage
613 on vertical land motion. *Cryosphere*, 11(3), 1327-1332. Retrieved
614 from [https://www.scopus.com/inward/record.uri?eid=2-s2.0-](https://www.scopus.com/inward/record.uri?eid=2-s2.0-85020484420&doi=10.5194%2ftc-11-1327-2017&partnerID=40&md5=077251aec38900cef0ec0ecdd2b1eded)
615 [85020484420&doi=10.5194%2ftc-11-1327-2017&partnerID=40&md5=](https://www.scopus.com/inward/record.uri?eid=2-s2.0-85020484420&doi=10.5194%2ftc-11-1327-2017&partnerID=40&md5=077251aec38900cef0ec0ecdd2b1eded)
616 [077251aec38900cef0ec0ecdd2b1eded](https://www.scopus.com/inward/record.uri?eid=2-s2.0-85020484420&doi=10.5194%2ftc-11-1327-2017&partnerID=40&md5=077251aec38900cef0ec0ecdd2b1eded) (cited By 11) doi: 10.5194/
617 tc-11-1327-2017
- 618 Root, B. C., Tarasov, L., & van der Wal, W. (2015). Grace gravity observations
619 constrain weichselian ice thickness in the barents sea. *Geophysical Research*
620 *Letters*, 42(9), 3313-3320. Retrieved from [https://agupubs.onlinelibrary](https://agupubs.onlinelibrary.wiley.com/doi/abs/10.1002/2015GL063769)
621 [.wiley.com/doi/abs/10.1002/2015GL063769](https://agupubs.onlinelibrary.wiley.com/doi/abs/10.1002/2015GL063769) doi: 10.1002/2015GL063769
- 622 Santamaría-Gómez, A., Gravelle, M., Dangendorf, S., Marcos, M., Spada, G., &
623 Wöppelmann, G. (2017). Uncertainty of the 20th century sea-level rise due
624 to vertical land motion errors. *Earth and Planetary Science Letters*, 473, 24 -
625 32. Retrieved from [http://www.sciencedirect.com/science/article/pii/](http://www.sciencedirect.com/science/article/pii/S0012821X17303060)
626 [S0012821X17303060](http://www.sciencedirect.com/science/article/pii/S0012821X17303060) doi: <https://doi.org/10.1016/j.epsl.2017.05.038>

- 627 Santamaría-Gómez, A., & Mémin, A. (2015, 05). Geodetic secular velocity errors
628 due to interannual surface loading deformation. *Geophysical Journal Inter-*
629 *national*, *202*(2), 763-767. Retrieved from [https://doi.org/10.1093/gji/](https://doi.org/10.1093/gji/ggv190)
630 [ggv190](https://doi.org/10.1093/gji/ggv190) doi: 10.1093/gji/ggv190
- 631 Sato, T., Okuno, J., Hinderer, J., MacMillan, D. S., Plag, H.-P., Francis, O., ...
632 Fukuda, Y. (2006, 06). A geophysical interpretation of the secular displace-
633 ment and gravity rates observed at Ny-Ålesund, Svalbard in the Arctic—effects
634 of post-glacial rebound and present-day ice melting. *Geophysical Journal In-*
635 *ternational*, *165*(3), 729-743. Retrieved from [https://doi.org/10.1111/](https://doi.org/10.1111/j.1365-246X.2006.02992.x)
636 [j.1365-246X.2006.02992.x](https://doi.org/10.1111/j.1365-246X.2006.02992.x) doi: 10.1111/j.1365-246X.2006.02992.x
- 637 Schröder, L., Horwath, M., Dietrich, R., Helm, V., van den Broeke, M. R., & Ligten-
638 berg, S. R. M. (2019). Four decades of antarctic surface elevation changes
639 from multi-mission satellite altimetry. *The Cryosphere*, *13*(2), 427–449.
640 Retrieved from <https://www.the-cryosphere.net/13/427/2019/> doi:
641 [10.5194/tc-13-427-2019](https://doi.org/10.5194/tc-13-427-2019)
- 642 Schumacher, M., King, M., Rougier, J., Sha, Z., Khan, S. A., & Bamber, J.
643 (2018). A new global gps data set for testing and improving modelled gla-
644 uplift rates. *Geophysical Journal International*, *214*(3), 2164-2176. Re-
645 trieved from [https://www.scopus.com/inward/record.uri?eid=2-s2](https://www.scopus.com/inward/record.uri?eid=2-s2.0-85050475763&doi=10.1093%2fgji%2fggy235&partnerID=40&md5=0b6d3ed0cdf0208346d1d8bb4bed2c40)
646 [.0-85050475763&doi=10.1093%2fgji%2fggy235&partnerID=40&md5=](https://www.scopus.com/inward/record.uri?eid=2-s2.0-85050475763&doi=10.1093%2fgji%2fggy235&partnerID=40&md5=0b6d3ed0cdf0208346d1d8bb4bed2c40)
647 [0b6d3ed0cdf0208346d1d8bb4bed2c40](https://www.scopus.com/inward/record.uri?eid=2-s2.0-85050475763&doi=10.1093%2fgji%2fggy235&partnerID=40&md5=0b6d3ed0cdf0208346d1d8bb4bed2c40) (cited By 5) doi: 10.1093/gji/ggy235
- 648 Simon, K. M., Riva, R. E. M., Kleinenbrink, M., & Frederikse, T. (2018). The
649 glacial isostatic adjustment signal at present day in northern europe and the
650 british isles estimated from geodetic observations and geophysical models.
651 *Solid Earth*, *9*(3), 777–795. Retrieved from [https://www.solid-earth.net/](https://www.solid-earth.net/9/777/2018/)
652 [9/777/2018/](https://www.solid-earth.net/9/777/2018/) doi: 10.5194/se-9-777-2018
- 653 Smith, B. E., Fricker, H. A., Joughin, I. R., & Tulaczyk, S. (2009). An inventory of
654 active subglacial lakes in antarctica detected by icesat (2003–2008). *Journal of*
655 *Glaciology*, *55*(192), 573–595. doi: 10.3189/002214309789470879
- 656 Sun, Y., Riva, R., & Ditmar, P. (2016). Optimizing estimates of annual variations
657 and trends in geocenter motion and j2 from a combination of grace data and
658 geophysical models. *Journal of Geophysical Research: Solid Earth*, *121*(11),
659 8352-8370. Retrieved from [https://agupubs.onlinelibrary.wiley.com/](https://agupubs.onlinelibrary.wiley.com/doi/abs/10.1002/2016JB013073)
660 [doi/abs/10.1002/2016JB013073](https://agupubs.onlinelibrary.wiley.com/doi/abs/10.1002/2016JB013073) doi: 10.1002/2016JB013073
- 661 Sørensen, L. S., Jarosch, A. H., Adalgeirsdóttir, G., Barletta, V. R., Forsberg, R.,
662 Pálsson, F., ... Jóhannesson, T. (2017, 01). The effect of signal leakage
663 and glacial isostatic rebound on GRACE-derived ice mass changes in Ice-
664 land. *Geophysical Journal International*, *209*(1), 226-233. Retrieved from
665 <https://doi.org/10.1093/gji/ggx008> doi: 10.1093/gji/ggx008
- 666 Tapley, B. D., Bettadpur, S., Watkins, M., & Reigber, C. (2004). The gravity re-
667 covery and climate experiment: Mission overview and early results. *Geophys-*
668 *ical Research Letters*, *31*(9). Retrieved from [https://agupubs.onlinelibrary](https://agupubs.onlinelibrary.wiley.com/doi/abs/10.1029/2004GL019920)
669 [.wiley.com/doi/abs/10.1029/2004GL019920](https://agupubs.onlinelibrary.wiley.com/doi/abs/10.1029/2004GL019920) doi: 10.1029/2004GL019920
- 670 Tushingham, A. M., & Peltier, W. R. (1991). Ice-3g: A new global model of late
671 pleistocene deglaciation based upon geophysical predictions of post-glacial re-
672 lative sea level change. *Journal of Geophysical Research: Solid Earth*, *96*(B3),
673 4497-4523. Retrieved from [https://agupubs.onlinelibrary.wiley.com/](https://agupubs.onlinelibrary.wiley.com/doi/abs/10.1029/90JB01583)
674 [doi/abs/10.1029/90JB01583](https://agupubs.onlinelibrary.wiley.com/doi/abs/10.1029/90JB01583) doi: 10.1029/90JB01583
- 675 van Dam, T., Collilieux, X., Wuite, J., Altamimi, Z., & Ray, J. (2012). Nonti-
676 dal ocean loading: amplitudes and potential effects in gps height time series.
677 *Journal of Geodesy*, *86*(11), 1043–1057. Retrieved from [https://doi.org/](https://doi.org/10.1007/s00190-012-0564-5)
678 [10.1007/s00190-012-0564-5](https://doi.org/10.1007/s00190-012-0564-5) doi: 10.1007/s00190-012-0564-5
- 679 VanLooy, J., Forster, R., & Ford, A. (2006). Accelerating thinning of kenai
680 peninsula glaciers, alaska. *Geophysical Research Letters*, *33*(21). Retrieved
681 from <https://agupubs.onlinelibrary.wiley.com/doi/abs/10.1029/>

- 2006GL028060 doi: 10.1029/2006GL028060
- 682 Wang, H., Xiang, L., Jia, L., Jiang, L., Wang, Z., Hu, B., & Gao, P. (2012).
 683 Load love numbers and green's functions for elastic earth models prem,
 684 iasp91, ak135, and modified models with refined crustal structure from
 685 crust 2.0. *Computers & Geosciences*, 49, 190 - 199. Retrieved from
 686 <http://www.sciencedirect.com/science/article/pii/S0098300412002245>
 687 doi: <https://doi.org/10.1016/j.cageo.2012.06.022>
 688
- 689 Watson, C. S., White, N. J., Church, J. A., King, M. A., Burgette, R. J., & Legresy,
 690 B. (2015, JUN). Unabated global mean sea-level rise over the satellite altimeter
 691 era. *NATURE CLIMATE CHANGE*, 5(6), 565+.
- 692 Whitehouse, P. L., Allen, M. B., & Milne, G. A. (2007, 08). Glacial isostatic ad-
 693 justment as a control on coastal processes: An example from the Siberian
 694 Arctic. *Geology*, 35(8), 747-750. Retrieved from <https://doi.org/10.1130/G23437A.1>
 695 doi: 10.1130/G23437A.1
- 696 Wöppelmann, G., & Marcos, M. (2016). Vertical land motion as a key to under-
 697 standing sea level change and variability. *Reviews of Geophysics*, 54(1), 64-92.
 698 Retrieved from [https://agupubs.onlinelibrary.wiley.com/doi/abs/](https://agupubs.onlinelibrary.wiley.com/doi/abs/10.1002/2015RG000502)
 699 [10.1002/2015RG000502](https://agupubs.onlinelibrary.wiley.com/doi/abs/10.1002/2015RG000502) doi: 10.1002/2015RG000502
- 700 Zemp, M., Huss, M., Thibert, E., Eckert, N., McNabb, R., Huber, J., ... Cog-
 701 ley, J. G. (2019). Global glacier mass changes and their contributions
 702 to sea-level rise from 1961 to 2016. *Nature*, 568(7752), 382-386. doi:
 703 [10.1038/s41586-019-1071-0](https://doi.org/10.1038/s41586-019-1071-0)
- 704 Zwally, H. J., Schutz, R., Bentley, C., Bufton, J., Herring, T., Minster, J., ...
 705 Thomas, R. (2011). *Glas/icesat l2 antarctic and greenland ice sheet altimetry*
 706 *data v031*. (Boulder, Colorado: NASA Distributed Active Archive Center at
 707 the National Snow and Ice Data Center) doi: 10.5067/CPRXXK3F39RV

708 **References of Supporting Information:**

- 709 Caron, L., Ivins, E. R., Larour, E., Adhikari, S., Nilsson, J., & Blewitt, G. (2018).
 710 GIA model statistics for grace hydrology, cryosphere, and ocean science. *Geo-*
 711 *physical Research Letters*, 45(5), 2203-2212. Retrieved from [https://agupubs](https://agupubs.onlinelibrary.wiley.com/doi/abs/10.1002/2017GL076644)
 712 [.onlinelibrary.wiley.com/doi/abs/10.1002/2017GL076644](https://agupubs.onlinelibrary.wiley.com/doi/abs/10.1002/2017GL076644) doi: 10.1002/
 713 2017GL076644
- 714 Cohen, S. C., & Freymueller, J. T. (2001). Crustal uplift in the south central
 715 alaska subduction zone: New analysis and interpretation of tide gauge obser-
 716 vations. *Journal of Geophysical Research: Solid Earth*, 106(B6), 11259-11270.
 717 Retrieved from [https://agupubs.onlinelibrary.wiley.com/doi/abs/](https://agupubs.onlinelibrary.wiley.com/doi/abs/10.1029/2000JB900419)
 718 [10.1029/2000JB900419](https://agupubs.onlinelibrary.wiley.com/doi/abs/10.1029/2000JB900419) doi: 10.1029/2000JB900419
- 719 Fleming, K., Martinec, Z., & Wolf, D. (2007, 01). Glacial-isostatic adjustment and
 720 the viscosity structure underlying the vatnajökull ice cap, iceland. *Pure and*
 721 *Applied Geophysics*, 164, 751-768. doi: 10.1007/s00024-007-0187-6
- 722 Frederikse, T., Landerer, F. W., & Caron, L. (2019). The imprints of con-
 723 temporary mass redistribution on local sea level and vertical land motion
 724 observations. *Solid Earth*, 10(6), 1971-1987. Retrieved from [https://](https://www.solid-earth.net/10/1971/2019/)
 725 www.solid-earth.net/10/1971/2019/ doi: 10.5194/se-10-1971-2019
- 726 Grove, J. (2001, 01). The initiation of the "little ice age" in regions round the north
 727 atlantic. *Climatic Change*, 48, 53-82. doi: 10.1023/A:1005662822136
- 728 Hu, Y., & Freymueller, J. T. (2019). Geodetic observations of time-variable glacial
 729 isostatic adjustment in southeast alaska and its implications for earth rhe-
 730 ology. *Journal of Geophysical Research: Solid Earth*, 124(9), 9870-9889.
 731 Retrieved from [https://agupubs.onlinelibrary.wiley.com/doi/abs/](https://agupubs.onlinelibrary.wiley.com/doi/abs/10.1029/2018JB017028)
 732 [10.1029/2018JB017028](https://agupubs.onlinelibrary.wiley.com/doi/abs/10.1029/2018JB017028) doi: 10.1029/2018JB017028
- 733 Kierulf, H. P., Plag, H.-P., & Kohler, J. (2009, 10). Surface deformation induced by
 734 present-day ice melting in Svalbard. *Geophysical Journal International*, 179(1),

- 735 1-13. Retrieved from <https://doi.org/10.1111/j.1365-246X.2009.04322.x>
 736 doi: 10.1111/j.1365-246X.2009.04322.x
- 737 King, M. A., & Watson, C. S. (2014, 09). Geodetic vertical velocities affected by re-
 738 cent rapid changes in polar motion. *Geophysical Journal International*, 199(2),
 739 1161-1165. Retrieved from <https://doi.org/10.1093/gji/ggu325> doi: 10
 740 .1093/gji/ggu325
- 741 Larsen, C. F., Motyka, R. J., Freymueller, J. T., Echelmeyer, K. A., & Ivins, E. R.
 742 (2005). Rapid viscoelastic uplift in southeast alaska caused by post-little ice
 743 age glacial retreat. *Earth and Planetary Science Letters*, 237(3), 548 - 560.
 744 Retrieved from [http://www.sciencedirect.com/science/article/pii/
 745 S0012821X05004152](http://www.sciencedirect.com/science/article/pii/S0012821X05004152) doi: <https://doi.org/10.1016/j.epsl.2005.06.032>
- 746 Mémin, A., Spada, G., Boy, J.-P., Rogister, Y., & Hinderer, J. (2014, 05). Decadal
 747 geodetic variations in Ny-Ålesund (Svalbard): role of past and present ice-mass
 748 changes. *Geophysical Journal International*, 198(1), 285-297. Retrieved from
 749 <https://doi.org/10.1093/gji/ggu134> doi: 10.1093/gji/ggu134
- 750 Peltier, W., Argus, D., & Drummond, R. (2015). Space geodesy constrains ice age
 751 terminal deglaciation: The global ice-6g-c (vm5a) model. *Journal of Geo-
 752 physical Research: Solid Earth*, 120(1), 450-487. Retrieved from [https://www
 753 .scopus.com/inward/record.uri?eid=2-s2.0-85027948080&doi=10.1002%
 754 2f2014JB011176&partnerID=40&md5=29a7ce38c5cf3872d2276981d2f6b34f](https://www.scopus.com/inward/record.uri?eid=2-s2.0-85027948080&doi=10.1002%2f2014JB011176&partnerID=40&md5=29a7ce38c5cf3872d2276981d2f6b34f)
 755 (cited By 326) doi: 10.1002/2014JB011176
- 756 Pfeffer, W. T., Arendt, A. A., Bliss, A., Bolch, T., Cogley, J. G., Gardner,
 757 A. S., ... et al. (2014). The randolph glacier inventory: a globally com-
 758 plete inventory of glaciers. *Journal of Glaciology*, 60(221), 537-552. doi:
 759 10.3189/2014JoG13J176
- 760 Rajner, M. (2018). Detection of ice mass variation using gnss measurements
 761 at svalbard. *Journal of Geodynamics*, 121, 20 - 25. Retrieved from
 762 <http://www.sciencedirect.com/science/article/pii/S0264370718300450>
 763 doi: <https://doi.org/10.1016/j.jog.2018.06.001>
- 764 Root, B. C., Tarasov, L., & van der Wal, W. (2015). Grace gravity observations
 765 constrain weichselian ice thickness in the barents sea. *Geophysical Research
 766 Letters*, 42(9), 3313-3320. Retrieved from [https://agupubs.onlinelibrary
 767 .wiley.com/doi/abs/10.1002/2015GL063769](https://agupubs.onlinelibrary.wiley.com/doi/abs/10.1002/2015GL063769) doi: 10.1002/2015GL063769
- 768 Sato, T., Okuno, J., Hinderer, J., MacMillan, D. S., Plag, H.-P., Francis, O., ...
 769 Fukuda, Y. (2006, 06). A geophysical interpretation of the secular displace-
 770 ment and gravity rates observed at Ny-Ålesund, Svalbard in the Arctic—effects
 771 of post-glacial rebound and present-day ice melting. *Geophysical Journal In-
 772 ternational*, 165(3), 729-743. Retrieved from [https://doi.org/10.1111/
 773 j.1365-246X.2006.02992.x](https://doi.org/10.1111/j.1365-246X.2006.02992.x) doi: 10.1111/j.1365-246X.2006.02992.x
- 774 Schröder, L., Horwath, M., Dietrich, R., Helm, V., van den Broeke, M. R., & Ligten-
 775 berg, S. R. M. (2019). Four decades of antarctic surface elevation changes
 776 from multi-mission satellite altimetry. *The Cryosphere*, 13(2), 427-449.
 777 Retrieved from <https://www.the-cryosphere.net/13/427/2019/> doi:
 778 10.5194/tc-13-427-2019
- 779 Shepherd, A., Ivins, E., Rignot, E., Smith, B., van den Broeke, M., Velicogna, I., ...
 780 Wouters, B. (2018). Mass balance of the antarctic ice sheet from 1992 to 2017.
 781 *Nature*, 558(7709), 219-222. doi: 10.1038/s41586-018-0179-y
- 782 Sun, Y., Riva, R., & Ditmar, P. (2016). Optimizing estimates of annual variations
 783 and trends in geocenter motion and j2 from a combination of grace data and
 784 geophysical models. *Journal of Geophysical Research: Solid Earth*, 121(11),
 785 8352-8370. Retrieved from [https://agupubs.onlinelibrary.wiley.com/
 786 doi/abs/10.1002/2016JB013073](https://agupubs.onlinelibrary.wiley.com/doi/abs/10.1002/2016JB013073) doi: 10.1002/2016JB013073
- 787 Swenson, S., Chambers, D., & Wahr, J. (2008). Estimating geocenter varia-
 788 tions from a combination of grace and ocean model output. *Journal of
 789 Geophysical Research: Solid Earth*, 113(B8). Retrieved from <https://>

- 790 agupubs.onlinelibrary.wiley.com/doi/abs/10.1029/2007JB005338 doi:
791 10.1029/2007JB005338
- 792 Sørensen, L. S., Jarosch, A. H., Adalgeirsdóttir, G., Barletta, V. R., Forsberg, R.,
793 Pálsson, F., ... Jóhannesson, T. (2017, 01). The effect of signal leakage
794 and glacial isostatic rebound on GRACE-derived ice mass changes in Ice-
795 land. *Geophysical Journal International*, 209(1), 226-233. Retrieved from
796 <https://doi.org/10.1093/gji/ggx008> doi: 10.1093/gji/ggx008
- 797 Tushingham, A. M., & Peltier, W. R. (1991). Ice-3g: A new global model of late
798 pleistocene deglaciation based upon geophysical predictions of post-glacial rel-
799 ative sea level change. *Journal of Geophysical Research: Solid Earth*, 96(B3),
800 4497-4523. Retrieved from [https://agupubs.onlinelibrary.wiley.com/](https://agupubs.onlinelibrary.wiley.com/doi/abs/10.1029/90JB01583)
801 [doi/abs/10.1029/90JB01583](https://agupubs.onlinelibrary.wiley.com/doi/abs/10.1029/90JB01583) doi: 10.1029/90JB01583
- 802 VanLooy, J., Forster, R., & Ford, A. (2006). Accelerating thinning of kenai
803 peninsula glaciers, alaska. *Geophysical Research Letters*, 33(21). Retrieved
804 from [https://agupubs.onlinelibrary.wiley.com/doi/abs/10.1029/](https://agupubs.onlinelibrary.wiley.com/doi/abs/10.1029/2006GL028060)
805 [2006GL028060](https://agupubs.onlinelibrary.wiley.com/doi/abs/10.1029/2006GL028060) doi: 10.1029/2006GL028060
- 806 Whitehouse, P. L., Allen, M. B., & Milne, G. A. (2007, 08). Glacial isostatic ad-
807 justment as a control on coastal processes: An example from the Siberian
808 Arctic. *Geology*, 35(8), 747-750. Retrieved from [https://doi.org/10.1130/](https://doi.org/10.1130/G23437A.1)
809 [G23437A.1](https://doi.org/10.1130/G23437A.1) doi: 10.1130/G23437A.1

5.2 Supporting Information for "Vertical Land Motion from Present-Day Deglaciation in the Wider Arctic"

Supporting Information for "Vertical Land Motion from Present-Day Deglaciation in the Wider Arctic"

Carsten Ankjær Ludwigsen¹, Shfaqat Abbas Khan¹, Ole Baltazar
Andersen¹ and Ben Marzeion²

¹DTU Space, Technical University of Denmark

²Institute of Geography and MARUM Center for Marine Environmental Sciences, University of Bremen,
Germany

Contents of this file

1. S1 - Description of glacier ice model
2. S2 - Influence of rotational feedback, geocenter motion and Antarctic ice loading
3. S3 - Spatial distributions of of the VLM-model error
4. S4 - VLM at GNSS-sites
5. S5 - Timeseries of vertical deformation at all GNSS sites
6. S6 - Contribution of elastic uplift and GIA to Arctic VLM

S1 Description of glacier ice model

As initial conditions, we use glacier outlines obtained from RGI6.0 (Pfeffer et al., 2014). The time stamp of these outlines differs between glaciers, but is typically around the year 2000. To obtain results before this time, the model uses an iterative process to find the glacier geometry in the year of initialization (e.g., 1901) that results in the observed glacier geometry in the year of the outlines time stamp (e.g., 2000) after the model was run forward.

The model relies on monthly temperature and precipitation anomalies to calculate the specific mass balance of each glacier. Here, we use the mean of seven different re-analysis products as boundary conditions. Temperature is used to estimate the ablation of glaciers following a temperature-index melt model, and to estimate the solid fraction of total precipitation, which is used to estimate accumulation.

Mass balance data for each glacier is distributed over the glacier according to a mathematical approximation, assuming conservation of mass and that the glacier has a elevation gain at the top which becomes a elevation decline further down the glacier. The altitude where the elevation change goes from positive to negative, E , is approximated by a simple function of the glacial altitude (Z) and the averaged ice height change, ($\bar{h} = \rho b A^{-1}$), and ρ is the ice density (917 kg m^{-3}). Note that E is different from the equilibrium line altitude (ELA).

$$E = (1 - \bar{h}) \tilde{Z} \quad (\text{S1})$$

where \tilde{Z} is the median glacial height. For every glacier we define a distribution function, $D(i)$, where i represents a grid cell of the glacier:

$$D(i) = 1 - \exp\left(\frac{(2-\bar{h})(E-Z(i))}{Z_{max}}\right) \quad (\text{S2})$$

For all glaciers, is the elevation change assumed to be exponentially declining with height, $Z(i)$. The fraction in the exponential term makes sure that glaciers that on average gains

Corresponding author: Carsten Ankjær Ludwigsen, caanlu@space.dtu.dk

32 up to 2 m height, will have an elevation loss in the bottom of the glacier and elevation
 33 gain at the top, unless E is equal or to Z_{max} , in which case, the whole glacier will be loos-
 34 ing height.

35 The elevation change, dh/dt , is found by normalizing D , multiplying with the to-
 36 tal mass balance, b , and converted to a height change by dividing with $\rho = 917 \text{ kg m}^{-3}$.

$$\frac{dh(i)}{dt} = \frac{b}{\rho} \hat{D}(i) \quad \text{where,} \quad (\text{S3})$$

$$\hat{D}(i) = \frac{D(i)}{\sum_{i=1}^k D(i)} \quad (\text{S4})$$

37 **S1.1 Data availability**

38 The ice model is available as a NetCDF-4 file on [data.dtu.dk/articles/Arctic](https://data.dtu.dk/articles/Arctic_Vertical_Land_Motion_5x5_km_/12554489)
 39 [_Vertical_Land_Motion_5x5_km_/12554489](https://data.dtu.dk/articles/Arctic_Vertical_Land_Motion_5x5_km_/12554489).

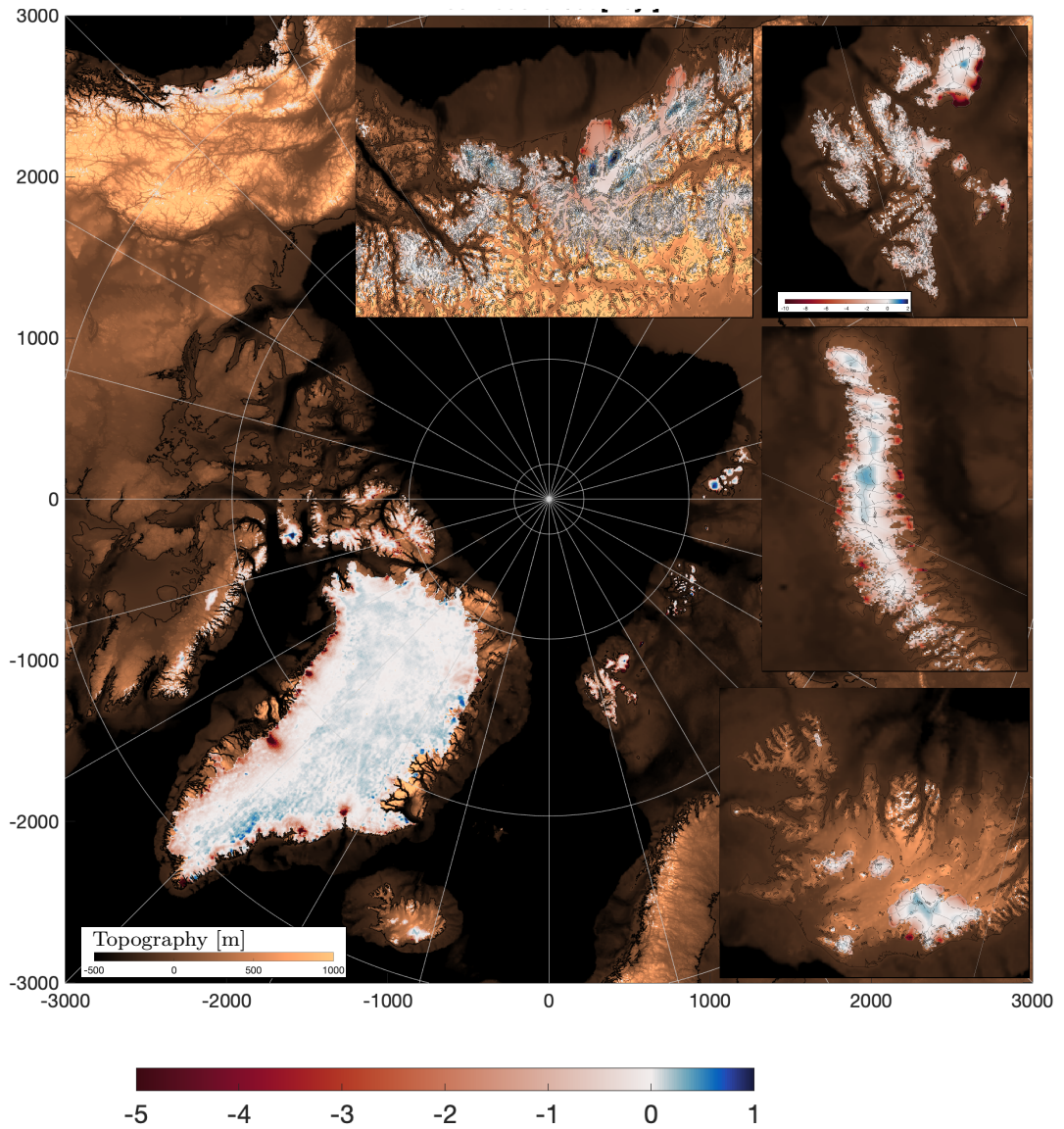


Figure S1.1. Ice elevation change from 2003 to 2015 in m yr^{-1} (red-blue scale) resulting from the redistribution explained above. The most interesting regions (Alaskan Coast, Svalbard (on a wider colorscale), Novaya Zemlja and Iceland) are enlarged. There is no significant ice loss in mainland Siberia. The elevation change is not comparable with actual elevation change, since no model for firn has been applied. The values on the map are proportional with mass changes (assumed density of 917 kg m^{-3})

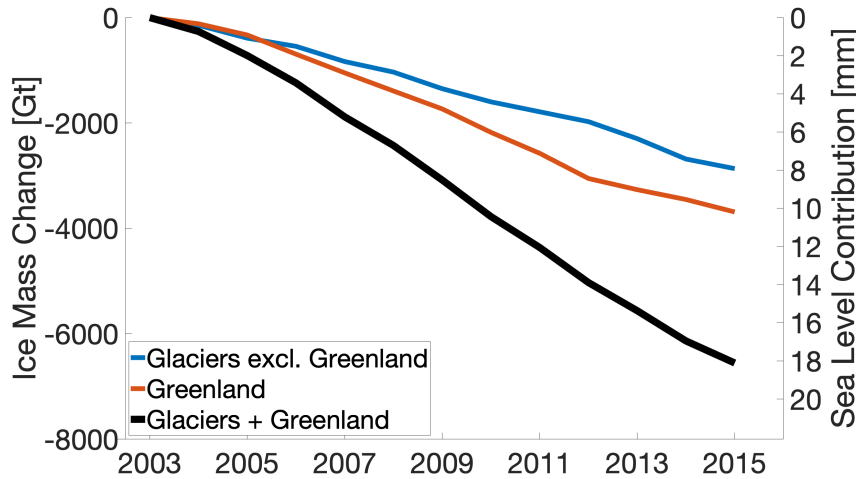


Figure S1.2. Ice loss from Greenland (including peripheral glaciers) and Arctic glaciers that goes in to the VLM calculations.

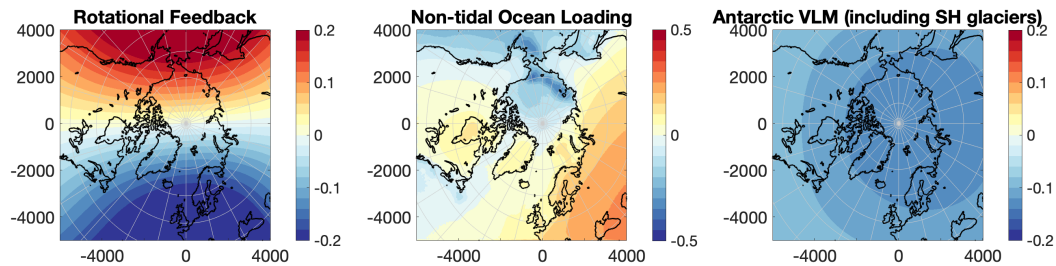


Figure S2.1. 2003-2015 average trends of rotational feedback, Non-tidal ocean loading and Antarctic elastic VLM fingerprint [mm yr^{-1}].

40 **S2 Influence of rotational feedback, ocean loading and Antarctic ice loss**

41 Rotational feedback is calculated using the eq.1 and eq.2 by King and Watson (2014).
 42 Pole positions x_p, y_p used in the calculations are available from <https://datacenter.iers.org/eop.php>. The Geocenter Motion subtracted from GNSS calculated as described in (Swenson et al., 2008) uses the degree-1 stokes coefficients based on the calculations by Sun et al. (2016) are available from <https://grace.jpl.nasa.gov/data/get-data/geocenter/>. The associated uncertainty of the geocenter motion has been added to the GNSS-error estimate. The elastic VLM effect of Antarctic Ice Loss is estimated from elevation changes by Schröder et al. (2019), which had an average mass loss of 105 Gt yr^{-1} between 2003 and 2015 which agrees well with the result of IMBIE (Shepherd et al., 2018).
 49
 50

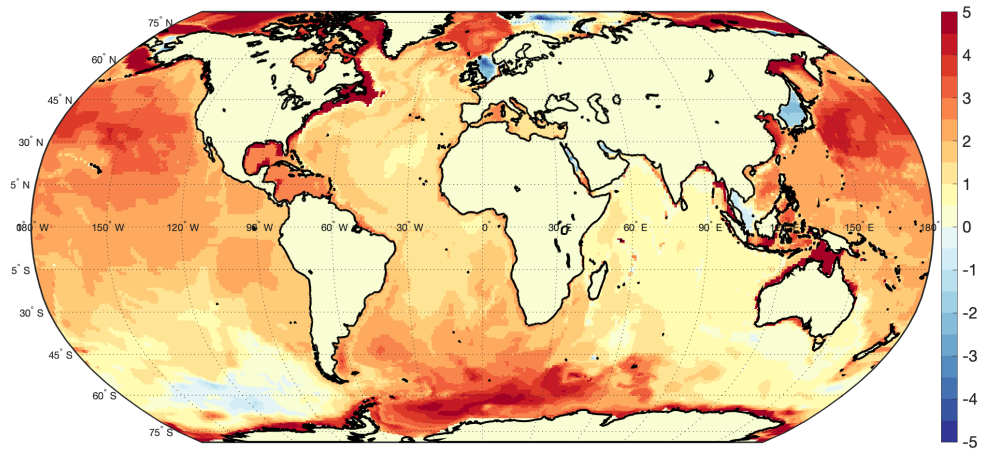


Figure S2.2. 2003-2015 ocean mass trend [mm/y] from ECCOv4r4 OBP used to estimate the effect of NOL.

51 **S3 Spatial distributions of of the VLM-model error**

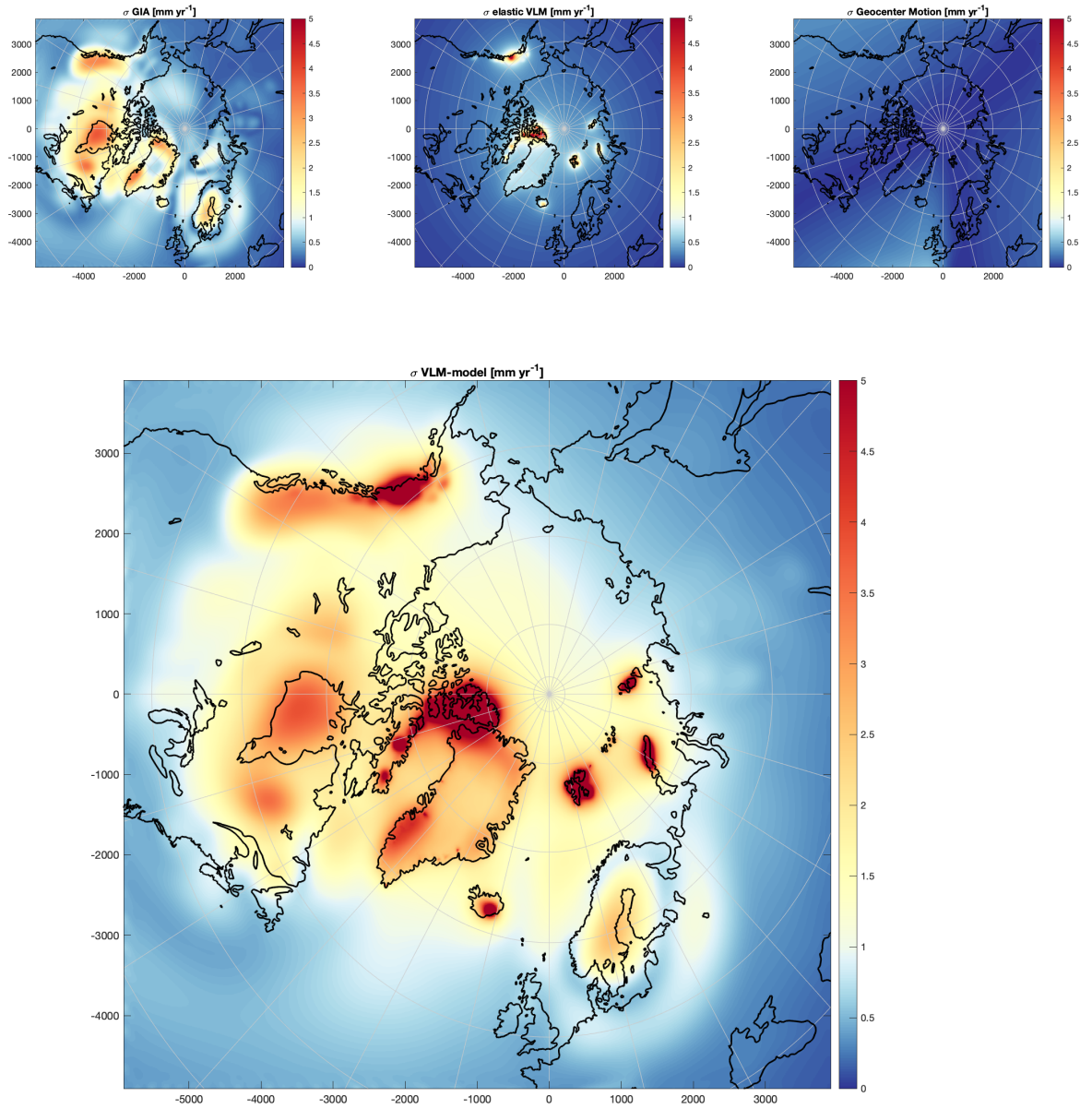


Figure S3.1. Standard deviation (σ) of GIA, elastic VLM and Geocenter Motion and combined for the total VLM-model [mm/yr] for 2003-2015.

52 **S4 VLM at GNSS-sites**

53 In this section, we explain the VLM measured by GNSS in comparison to the VLM-
 54 model for the regions covered in this study.

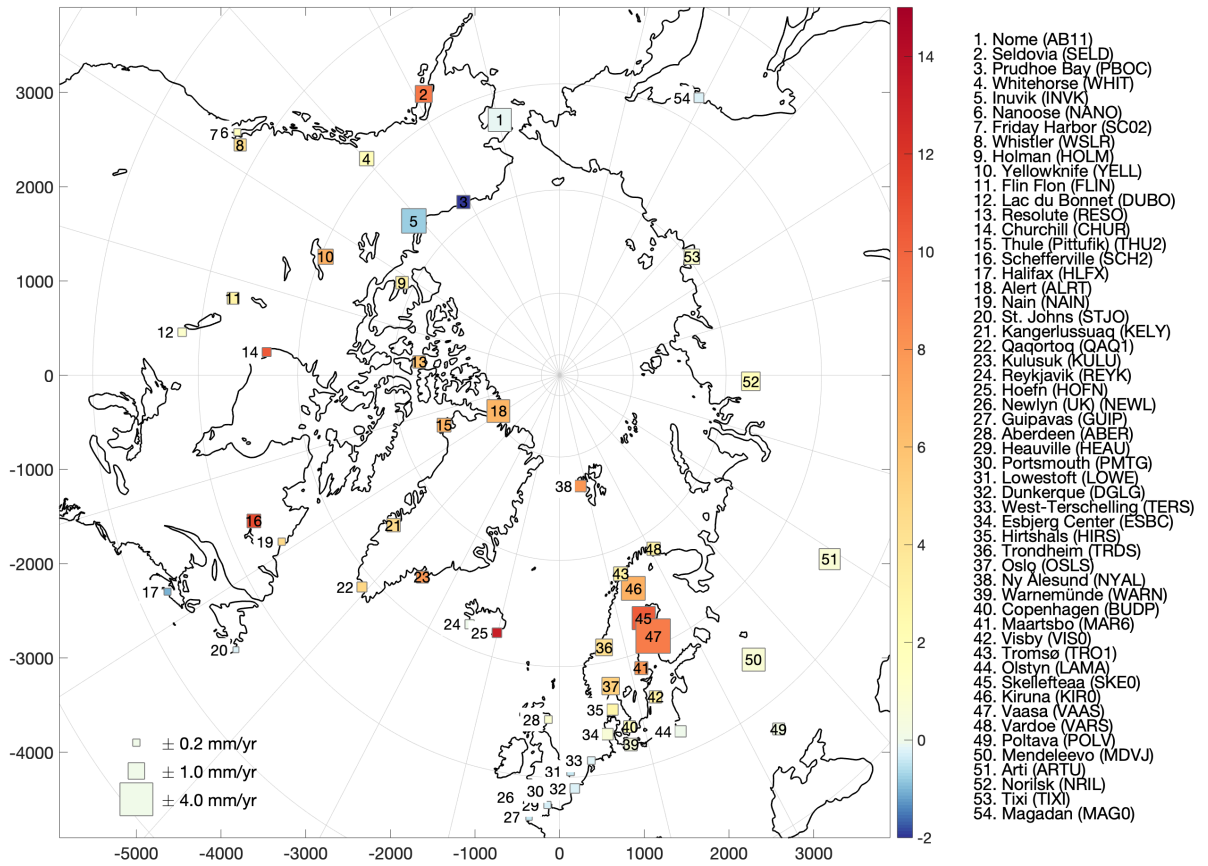


Figure S4.1. Location and name (and IGS abbreviation) of the 42 GNSS-sites used in this study ordered from most west to most east. The color indicates the linear trend from 2003-2015 [mm yr^{-1}], while the size of the square is proportional with the standard error (as estimated in the URL6-product).

55 **S5 Timeseries of vertical deformation at all GNSS sites**

56 Figure S5.1 shows both measured and modeled vertical deformation from 2003-2015
 57 of each individual GNSS-site. It also reflects, how elastic VLM is changing year by year,
 58 while GIA is linear.

59 **S6 Contribution of elastic VLM and GIA**

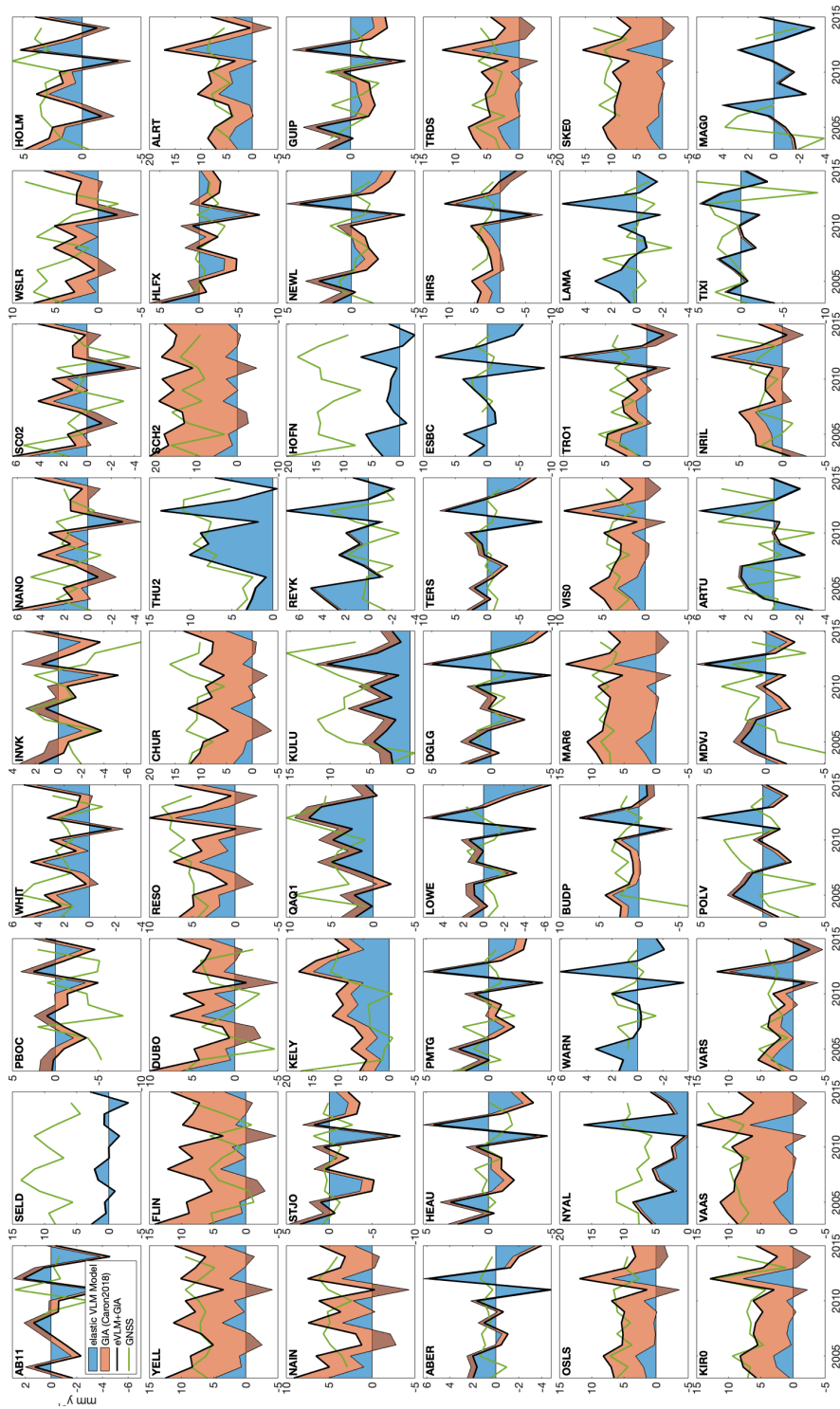


Figure S5.1. Measured and predicted year-to-year VLM-change [mm y^{-1}] from 2003 to 2015 for the 54 GNSS locations. GNSS is shown by the green line and the VLM model by the black line. The red and blue areas indicate the part of the VLM model that is elastic and GIA.

	IGS id	Abbr.	elastic VLM	Caron2018	VLM-model	GNSS VLM	Residual
Nome	4	AB11	-0.4 ± 0.7	-0.8 ± 0.3	-1.1 ± 1.0	-0.1 ± 0.9	-1.0 ± 1.4
Seldovia	517	SELD	0.3 ± 1.6	-0.1 ± 0.8	0.2 ± 2.4	9.2 ± 1.0	-9.0 ± 2.6
Prudhoe Bay	433	PBOC	0.1 ± 0.9	-1.5 ± 0.5	-1.4 ± 1.4	-3.2 ± 1.6	1.8 ± 2.1
Whitehorse	651	WHIT	1.1 ± 2.6	0.9 ± 1.3	2.0 ± 3.9	2.0 ± 0.8	0.0 ± 4.0
Inuvik	232	INVK	0.3 ± 1.0	-1.7 ± 0.9	-1.4 ± 1.9	-0.8 ± 1.0	-0.6 ± 2.1
Nanoose	341	NANO	-0.1 ± 0.6	1.5 ± 2.7	1.5 ± 3.3	1.6 ± 1.0	-0.2 ± 3.4
Friday Harbor	508	SC02	-0.2 ± 0.5	1.3 ± 2.6	1.1 ± 3.1	0.4 ± 1.3	0.7 ± 3.4
Whistler	656	WSLR	0.3 ± 0.6	2.5 ± 3.1	2.8 ± 3.8	4.5 ± 1.3	-1.7 ± 4.0
Holman	218	HOLM	0.3 ± 1.0	1.1 ± 0.8	1.4 ± 1.8	3.1 ± 1.1	-1.7 ± 2.1
Yellowknife	664	YELL	0.4 ± 0.8	7.6 ± 1.5	8.0 ± 2.3	6.8 ± 0.8	1.2 ± 2.4
Flin Flon	168	FLIN	0.2 ± 0.6	8.3 ± 1.6	8.4 ± 2.2	3.0 ± 0.9	5.4 ± 2.4
Lac du Bonnet	143	DUBO	0.1 ± 0.5	3.7 ± 1.1	3.8 ± 1.6	1.0 ± 0.9	2.8 ± 1.8
Resolute	477	RESO	1.1 ± 2.2	3.1 ± 0.9	4.2 ± 3.1	6.0 ± 1.2	-1.8 ± 3.3
Churchill	106	CHUR	0.4 ± 0.7	8.4 ± 2.8	8.8 ± 3.5	10.4 ± 0.8	-1.6 ± 3.6
Thule (Pittufik)	583	THU2	5.3 ± 3.3	0.1 ± 2.1	5.4 ± 5.4	6.6 ± 0.9	-1.2 ± 5.5
Schefferville	510	SCH2	0.4 ± 0.6	15.7 ± 2.3	16.1 ± 2.9	11.0 ± 0.7	5.0 ± 3.0
Halifax	211	HLFX	-0.5 ± 0.4	-1.5 ± 0.8	-2.0 ± 1.2	-1.1 ± 1.6	-0.9 ± 2.0
Alert	27	ALRT	3.4 ± 4.0	4.1 ± 1.5	7.6 ± 5.6	6.6 ± 1.2	1.0 ± 5.7
Nain	340	NAIN	0.4 ± 0.7	4.0 ± 1.0	4.4 ± 1.7	4.6 ± 1.5	-0.2 ± 2.3
St. Johns	548	STJO	-0.5 ± 0.4	-1.4 ± 0.3	-1.8 ± 0.8	-0.2 ± 0.8	-1.6 ± 1.1
Kangerlussuaq	247	KELY	6.6 ± 2.5	2.9 ± 3.4	9.4 ± 5.8	4.6 ± 1.2	4.8 ± 5.9
Qaqortoq	467	QAQ1	4.1 ± 1.5	-1.7 ± 1.4	2.4 ± 2.8	4.9 ± 0.8	-2.5 ± 3.0
Kulusuk	265	KULU	5.1 ± 1.6	-1.5 ± 1.0	3.6 ± 2.6	7.8 ± 1.0	-4.2 ± 2.8
Reykjavik	479	REYK	1.4 ± 1.4	0.2 ± 1.4	1.6 ± 2.8	-0.0 ± 1.1	1.6 ± 3.1
Hoefn	215	HOFN	1.9 ± 3.9	-0.1 ± 1.0	1.8 ± 4.9	13.1 ± 1.1	-11.3 ± 5.1
Newlyn (UK)	347	NEWL	0.1 ± 0.4	-1.1 ± 0.2	-0.9 ± 0.6	-0.2 ± 1.3	-0.7 ± 1.4
Guipavas	202	GUIP	0.2 ± 0.3	-1.0 ± 0.2	-0.9 ± 0.6	-0.4 ± 1.7	-0.4 ± 1.8
Aberdeen	10	ABER	0.4 ± 0.5	-0.5 ± 0.4	-0.1 ± 0.9	0.9 ± 1.2	-1.0 ± 1.5
Heauville	206	HEAU	0.1 ± 0.3	-0.8 ± 0.2	-0.7 ± 0.6	-0.3 ± 1.5	-0.4 ± 1.6
Portsmouth	446	PMTG	0.3 ± 0.4	-0.8 ± 0.3	-0.5 ± 0.6	0.1 ± 1.2	-0.6 ± 1.4
Lowestoft	286	LOWE	0.1 ± 0.4	-0.8 ± 0.5	-0.7 ± 0.9	-0.4 ± 1.8	-0.2 ± 2.0
Dunkerque	134	DGLG	0.2 ± 0.4	-0.7 ± 0.5	-0.6 ± 0.8	-0.3 ± 0.9	-0.3 ± 1.2
West-Terschelling	568	TERS	0.1 ± 0.4	-0.9 ± 0.7	-0.8 ± 1.1	-0.2 ± 0.8	-0.6 ± 1.4
Esbjerg Center	153	ESBC	0.3 ± 0.4	-0.1 ± 0.5	0.2 ± 0.9	0.6 ± 0.8	-0.4 ± 1.2
Hirtshals	210	HIRS	0.4 ± 0.5	2.2 ± 0.8	2.7 ± 1.3	2.8 ± 1.9	-0.1 ± 2.3
Trondheim	596	TRDS	0.8 ± 0.6	4.6 ± 1.1	5.4 ± 1.7	4.3 ± 0.8	1.1 ± 1.9
Oslo	378	OSLS	0.7 ± 0.5	5.0 ± 1.8	5.7 ± 2.3	5.2 ± 0.8	0.5 ± 2.4
Ny Ålesund	370	NYAL	4.6 ± 5.3	0.5 ± 0.4	5.1 ± 5.7	7.9 ± 0.9	-2.9 ± 5.7
Warnemünde	647	WARN	0.6 ± 0.4	-0.1 ± 0.5	0.5 ± 0.9	0.6 ± 0.8	-0.0 ± 1.2
Copenhagen	75	BUDP	0.6 ± 0.4	0.9 ± 0.5	1.6 ± 0.9	1.6 ± 3.7	-0.1 ± 3.8
Maartsbo	306	MAR6	0.8 ± 0.5	7.6 ± 2.4	8.3 ± 2.9	7.8 ± 0.8	0.5 ± 3.0
Visby	639	VIS0	0.8 ± 0.4	3.3 ± 1.1	4.0 ± 1.6	3.3 ± 0.8	0.8 ± 1.8
Tromsø	599	TRO1	0.9 ± 0.8	1.7 ± 0.7	2.5 ± 1.5	3.0 ± 0.8	-0.5 ± 1.7
Olstyn	274	LAMA	0.7 ± 0.4	0.1 ± 0.5	0.8 ± 0.9	-0.0 ± 0.7	0.8 ± 1.2
Skelleftea	534	SKE0	0.9 ± 0.6	8.5 ± 2.1	9.4 ± 2.7	10.3 ± 7.0	-0.9 ± 7.5
Kiruna	252	KIR0	0.9 ± 0.7	5.2 ± 0.9	6.1 ± 1.6	6.8 ± 0.8	-0.6 ± 1.8
Vaasa	625	VAAS	0.9 ± 0.6	8.3 ± 2.2	9.1 ± 2.7	9.0 ± 0.9	0.1 ± 2.9
Vardoe	630	VAR5	0.9 ± 0.8	2.0 ± 0.6	2.9 ± 1.4	3.0 ± 0.9	-0.2 ± 1.7
Poltava	452	POLV	0.7 ± 0.3	-0.4 ± 0.3	0.2 ± 0.5	0.2 ± 1.0	0.0 ± 1.1
Mendeleevo	323	MDVJ	0.8 ± 0.4	-0.7 ± 0.8	0.2 ± 1.2	0.7 ± 1.1	-0.5 ± 1.6
Arti	36	ARTU	0.8 ± 0.3	-0.2 ± 0.2	0.6 ± 0.6	0.7 ± 0.9	-0.1 ± 1.0
Norilsk	360	NRIL	0.9 ± 0.6	1.9 ± 0.2	2.8 ± 0.8	1.8 ± 0.8	1.0 ± 1.2
Tixi	587	TIXI	0.2 ± 0.6	-0.3 ± 0.3	-0.1 ± 0.9	1.0 ± 1.0	-1.1 ± 1.3
Magadan	298	MAG0	-0.2 ± 0.3	-0.2 ± 0.2	-0.4 ± 0.5	-0.3 ± 1.0	-0.1 ± 1.2

Table S4.1. Measured and modelled VLM for each GNSS-site in mm yr^{-1} . VLM-model is the sum of elastic VLM and GIA VLM.

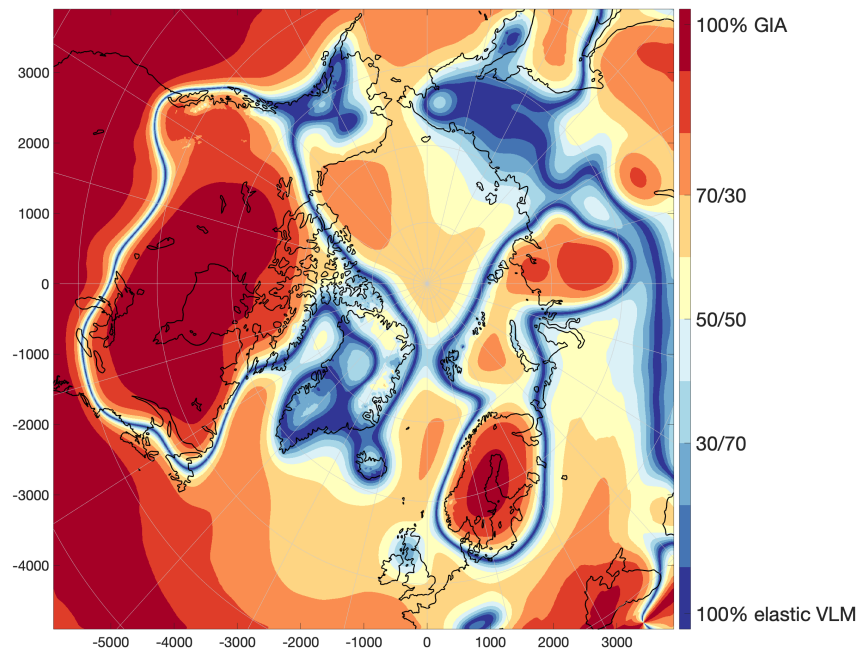


Figure S6.1. Percentage contribution of GIA-rate and elastic VLM-rate to total VLM-rate (in absolute terms) are shown. Red colors indicate areas in which GIA dominates VLM, while blue colors indicate areas in which elastic VLM is dominant.

60 **References**

- 61 King, M. A., & Watson, C. S. (2014, 09). Geodetic vertical velocities affected by re-
 62 cent rapid changes in polar motion. *Geophysical Journal International*, *199*(2),
 63 1161-1165. Retrieved from <https://doi.org/10.1093/gji/ggu325> doi: 10
 64 .1093/gji/ggu325
- 65 Pfeffer, W. T., Arendt, A. A., Bliss, A., Bolch, T., Cogley, J. G., Gardner,
 66 A. S., ... et al. (2014). The randolph glacier inventory: a globally com-
 67 plete inventory of glaciers. *Journal of Glaciology*, *60*(221), 537552. doi:
 68 10.3189/2014JoG13J176
- 69 Schröder, L., Horwath, M., Dietrich, R., Helm, V., van den Broeke, M. R., & Ligten-
 70 berg, S. R. M. (2019). Four decades of antarctic surface elevation changes
 71 from multi-mission satellite altimetry. *The Cryosphere*, *13*(2), 427-449.
 72 Retrieved from <https://www.the-cryosphere.net/13/427/2019/> doi:
 73 10.5194/tc-13-427-2019
- 74 Shepherd, A., Ivins, E., Rignot, E., Smith, B., van den Broeke, M., Velicogna, I., ...
 75 Wouters, B. (2018). Mass balance of the antarctic ice sheet from 1992 to 2017.
 76 *Nature*, *558*(7709), 219-222. doi: 10.1038/s41586-018-0179-y
- 77 Sun, Y., Riva, R., & Ditmar, P. (2016). Optimizing estimates of annual variations
 78 and trends in geocenter motion and j_2 from a combination of grace data and
 79 geophysical models. *Journal of Geophysical Research: Solid Earth*, *121*(11),
 80 8352-8370. Retrieved from [https://agupubs.onlinelibrary.wiley.com/
 81 doi/abs/10.1002/2016JB013073](https://agupubs.onlinelibrary.wiley.com/doi/abs/10.1002/2016JB013073) doi: 10.1002/2016JB013073
- 82 Swenson, S., Chambers, D., & Wahr, J. (2008). Estimating geocenter varia-
 83 tions from a combination of grace and ocean model output. *Journal of
 84 Geophysical Research: Solid Earth*, *113*(B8). Retrieved from [https://
 85 agupubs.onlinelibrary.wiley.com/doi/abs/10.1029/2007JB005338](https://agupubs.onlinelibrary.wiley.com/doi/abs/10.1029/2007JB005338) doi:
 86 10.1029/2007JB005338

6 Publication 3: Assessment of 1995-2015 Arctic Ocean Sea Level Trends

6.1 Preface

The third publication is submitted to Ocean Science in September 2020. It combines the gained results of the first and second publication, by integrating a tide gauge assessment into an updated attempt to close the Arctic sea level budget and identify the causes for Arctic sea level change. Instead of using a GRACE-data for the mass estimates, the study of this publication attempts to estimate the mass contribution for each source of PDIL from the ice-model used in (Ludwigsen et al., 2020a), GIA and dynamic effects from the ECCOv4r4-model.

This approach bypasses the use of GRACE for mass estimates which gives the advantage of a longer timeseries. Furthermore showed the analysis of (Ludwigsen and Andersen, 2020) that GRACE-estimates are inconsistent and affected by problems due to leakage effects from land-based mass changes. The mass contribution is estimated by combining the gravitational change associated with the VLM and GIA with estimates of changed atmospheric surface pressure. A dynamic contribution is estimated from the difference between Ocean Bottom Pressure estimates of ECCOv4r4 and the sum of the other mass contributions. As in the first publication (chapter 4) the steric sea level is given by the *DTU Steric* product.

1995-2015 (21 years) trends of sea level are compared with the altimetric data from (Rose et al., 2019) and VLM-corrected sea level trends at 12 tide gauges. Because the combined total mass component is equal to the ECCO OBP-estimate, comparisons are also made without the dynamic component.

The spatial trend maps of the derived sea level trend estimates including dynamic sea level change agrees well with altimetry and tide gauges. The difference between products is in almost the entire Arctic smaller than the associated uncertainty. However is the uncertainty also large (above 10 mm y^{-1}) in the areas with largest discrepancies among products (i.e. the Siberian Seas). The main sources of uncertainty are associated with the steric product and dynamic estimate, while also the altimetric sea level estimate is uncertain in particular in the Russian Arctic.

In the Norwegian Sea, where all products are well-constrained, yields the derived sea level estimate better agreement with the tide gauge-measured sea level trend than sea level observations from altimetry at the 2 of 3 Norwegian tide gauges. Also is it seemingly difficult for altimetry to capture the increased freshwater-outflow from west Siberia that is visible in *DTU Steric* and is also reflected in nearby tide gauges.

Assessment of 21 years of Arctic Ocean Absolute Sea Level Trends (1995-2015)

Carsten Ankjær Ludwigsen¹, Ole Baltazar Andersen¹, and Stine Kildegaard Rose¹

¹DTU Space, Elektrovej 328, 2800 Kgs. Lyngby, Denmark

Correspondence: Carsten Ankjær Ludwigsen (caanlu@space.dtu.dk)

Abstract. The Arctic Ocean is at the frontier of the fast changing climate in the northern latitudes. As the first study, we assess the different mass and steric components of the observed sea level trend from both absolute sea level (ASL) from altimetry and tide gauges, without using gravimetric observations from GRACE. This approach permits a longer time series and avoids problems with errors from leakage effects in GRACE-products. ASL is equal to mass-driven sea level added with steric sea level, while tide gauge based sea level are also corrected with novel estimates of vertical land movement. Calculations of the mass component from present-day deglaciation, shows that deglaciation rises Arctic sea level with more than 1 mm y⁻¹, while the steric contribution is between -5 and 15 mm y⁻¹ with large spatial variability, with the halosteric signal dominating the pattern. A dynamic mass contribution is derived from the Estimating Circulation and Climate of the Oceans (ECCO)-model (version 4 release 4), which varies between -1 and 2 mm y⁻¹. The combined mass and steric product agrees (within uncertainty) with ASL-trends observed from altimetry in 99% of the Arctic, although large uncertainties originate from poor data coverage in the steric data and large variability in the dynamic product. A comparison with ASL trends observed at tide gauges agrees with mass+steric at 11 of 12 tide gauge sites.

1 Introduction

The Arctic is globally the region with the fastest changing climate and is warming twice the rate of the global average. The resulting deglaciation of land and sea ice and ocean freshening all changes the sea level, hence is understanding sea level in the Arctic Ocean paramount for mapping consequences of climate change.

Spatial assessments of the sea level budget of the Arctic has in previous studies shown to be difficult (Henry et al., 2012; Armitage et al., 2016; Carret et al., 2017; Ludwigsen and Andersen, 2020; Raj et al., 2020), because both satellite observations and in-situ observations are less consistent than in low and mid-latitudes and challenged by the Arctic environment and fast-changing climate. Observations from the Gravity Recovery And Climate Experiment (GRACE) offer the only direct Arctic-wide measurements of the mass component, but discrepancies of over 10 mm y⁻¹ (Ludwigsen and Andersen, 2020) exist among different GRACE-products (Wiese et al., 2016; Save et al., 2016; Luthcke et al., 2013), and previous studies often choose the solution that fits the altimetric results (Carret et al., 2017; Raj et al., 2020). A cross-comparison of different combinations of GRACE, steric products and altimetry (Ludwigsen and Andersen, 2020), showed that the Arctic sea level budget using an

25 interpolated DTU steric product and a mass-product from the GRACE-satellites (GRACE JPL mascons (Wiese et al., 2016))
for 2003 to 2015 agreed well spatially with an altimetry-product from CPOM (Armitage et al., 2016).

Changes in absolute sea level (ASL) can be divided into two main contributions; changed water column density due to
changes in salinity or temperature, which is called *steric change* and *mass change* (also called Ocean Bottom Pressure) due
to changes of the gravitational field, land-to-ocean water mass flux and dynamic changes from changing wind stress and
30 atmospheric pressure.

$$\text{ASL} = \text{Steric} + \text{Mass} \quad (1)$$

Tide gauges (TG) gives direct measurements of sea level relative to the solid earth - called relative sea level (RSL). ASL
measured by satellite altimetry is measured relative to the Earth's center. The difference between ASL and RSL is defined by
the deformation of the solid Earth - called vertical land movement (VLM).

35 $\text{ASL} = \text{RSL} + \text{VLM} \quad (2)$

Bypassing GRACE makes it possible to extend the time series to 21 years from 1995-2015, which generally is 8 years more
than assessments using GRACE (Armitage et al., 2016; Carret et al., 2017; Raj et al., 2020) which was first launched in mid
2002. This has the advantage, that non-secular and non-seasonal effects of the Arctic Oscillation, which tends to dominate the
dynamic mass contribution (Henry et al., 2012; Armitage et al., 2018) gets smaller.

40 **2 Altimetry**

The DTU/TUM Arctic altimetric dataset (Rose et al., 2019) provides an independent estimate of ASL change. For the 1995-
2015 period, both ERS-1, ERS-2, Envisat (limited to 81.5°N) and Cryo-Sat-2 (limited to 88°N) is used. It combines results
of different retracers as well as conventional and SAR-altimetry, which may lead to biases (Rose et al., 2019). In particular
ERS-1/2 has a relative low spatial resolution and thereby limiting the measurements from leads (open-ocean inbetween the
45 sea ice floes) in sea ice. Also difficulties to distinguish between melt ponds on top of the sea ice and leads were shown to be
difficult. The used DTU altimetry product is not corrected for IB and is spatially limited southward to 65°N. The altimetric sea
level trend is shown in the right map of figure 5.

3 Tide Gauge data

Tide gauges with a consistent time series are few and unevenly distributed in the Arctic (Henry et al., 2012; Limkilde Svendsen
50 et al., 2016). Locations with both TG and GNSS to measure VLM is even rarer. As a substitute for GNSS-measurements, we
correct TG with the VLM-model described in (Ludwigsen et al., 2020a), which offers accurate VLM predictions for the Arctic
area.

Twelve TG's are selected in the Arctic region from the PSMSL-database (Holgate et al., 2012) (displayed in figure 1).
The selection is based on visual inspection of the monthly time series and to ensure that as many regions of the Arctic is

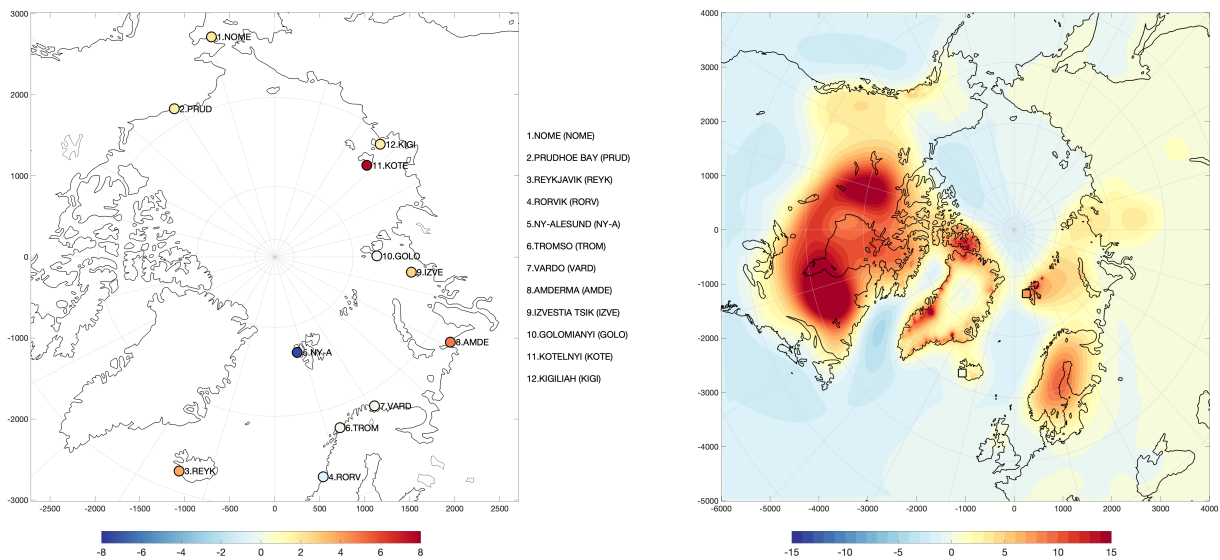


Figure 1. Left: 1995-2015 RSL trend [mm y^{-1}] and location of the selected tide gauges of this study. Right: 1995-2015 VLM-trend [mm y^{-1}] from the model of Ludwigsen et al. (2020b). The VLM-trend from the GNSS-sites at Reykjavik and Ny-Ålesund is shown with squared markers.

55 represented as possible. A 3-month averaged time series from 1995-2015 of every TG and the linear trend is shown in figure 2 and is corrected for VLM by using the VLM-model (Ludwigsen et al., 2020b) or, as in the case for Ny-Alesund and Reykjavik, using nearby GNSS for VLM (see figure 1). Reykjavik (64.2°N), Nome (64.5°N), and Rorvik (64.9°N) are located off the edge of the DTU/TUM Arctic altimetry dataset (Rose et al., 2019), which only extends to 65°N , but are nevertheless included to extend the spatial distribution of the TG-sites.

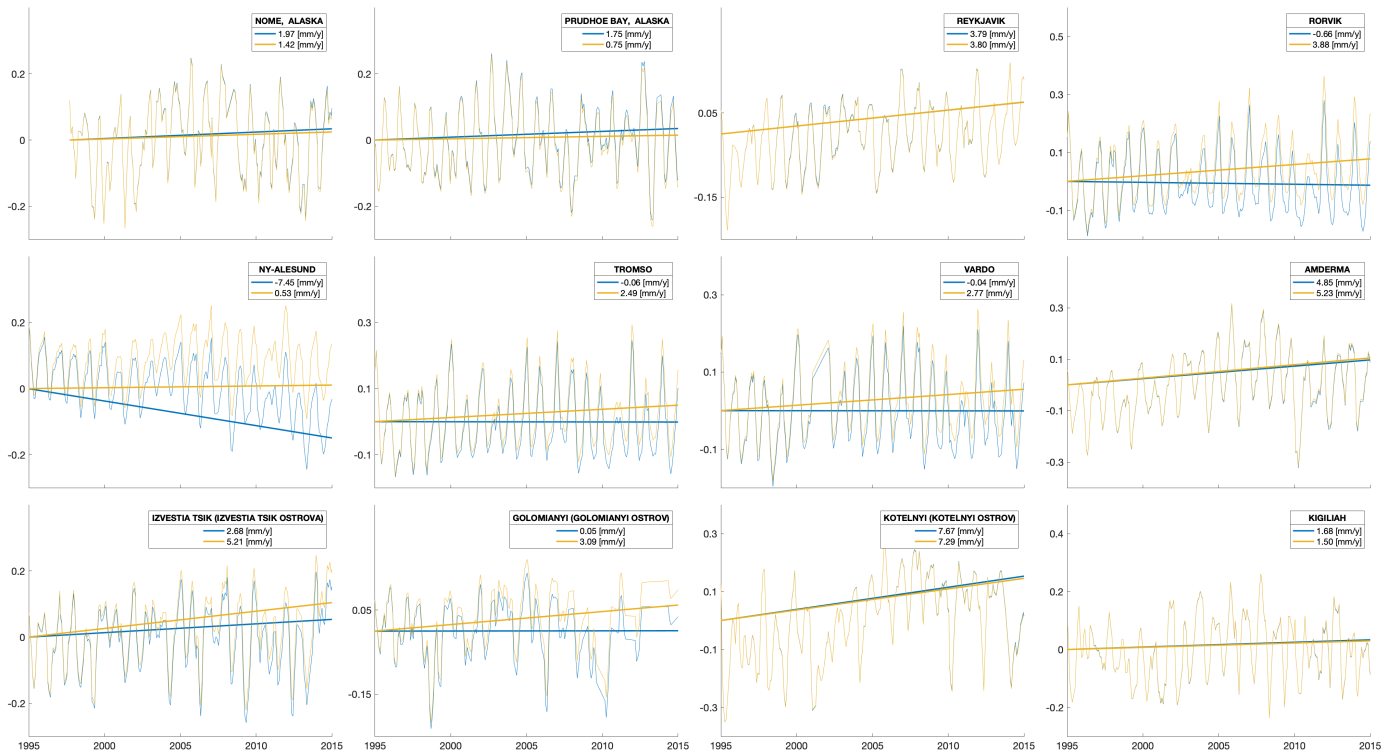


Figure 2. Relative sea level [m] from 1995-2015 registered at the 12 tide gauge from the PSMSL-database (Holgate et al., 2012)]. Blue line represents the 3-month running average, while the thick line is the linear trend (trend estimate [mm y^{-1}] shown in legend). Yellow line represents the absolute sea level and trend, equal to the blue line corrected for VLM with a VLM-model (Ludwigsen et al., 2020b) (except Ny-Ålesund and Reykjavik that are corrected with GNSS).

60 TG-trends are determined with least-squares method using months with data between 1995 and 2015 and the VLM-correction is interpolated onto the monthly TG-time series. From figure 2, we see that trends in the Arctic vary with nearly $\pm 1 \text{ cm y}^{-1}$, with Ny-Ålesund on Svalbard having a negative sea level trend of -7.45 mm y^{-1} , while Kostelnyi Island between the Laptev and East Siberian Sea shows a positive trend of 7.67 mm y^{-1} .

The VLM-model utilizes the Caron2018 GIA-model (Caron et al., 2018) which is added to an annual elastic VLM-model from 1995-2015 change in present-day ice loading (PDIL). As shown in Ludwigsen and Andersen (2020), Ny-Ålesund and Reykjavik experience extraordinary VLM, caused by substantial deglaciation during the Little Ice Age (Svalbard) and low mantle viscosities (Iceland and Greenland), that is not restored in the VLM-model. Therefore, are the two sites corrected with nearby GNSS instead of the VLM-model. GNSS is uncertain at Prudhoe Bay, where it measures a significant subsidence, that is significantly different from the VLM-model. This is probably caused by near-by construction or oil depletion sites. However, 70 the tide gauge is located on a peninsula reaching into the Beaufort Sea 10 km away from the GNSS-location, which is why the VLM-model is trusted over the GNSS-measurement.

4 Steric contribution

The DTU steric sea level change is computed as described in Ludwigsen and Andersen (2020). Salinity and temperature measurements from buoys, ice-tethered profiles and ship expeditions in the Arctic Ocean are spatial and temporal unevenly 75 distributed and also depends on seasonal accessibility (Behrendt et al., 2017). Especially, the data density is poor in the shallow seas along the Siberian Coast (Ludwigsen and Andersen, 2020), which is cause to large uncertainties. Temperature and salinity data are interpolated by kriging into a monthly $50 \times 50 \text{ km}$ spatial grid on 41 depth levels. If values are more than 3σ away from the mean of neighbouring grid cells, values from the same month in adjacent years is used.

Following the notion of Gill and Niller (1973); Stammer (1997); Calafat et al. (2012); Ludwigsen and Andersen (2020), 80 the change in steric heights, η , are calculated as the sum of halosteric heights (the contribution from salinity change), η_S and thermosteric heights, η_T .

$$\dot{\eta} = \dot{\eta}_S + \dot{\eta}_T \quad (3)$$

Depth profiles from the temperature and salinity grids are used for computing the right-hand side of equation 3:

$$\eta_S = -\frac{1}{\rho_0} \int_{-H}^0 \beta S' dz \quad (4)$$

$$85 \quad \eta_T = \frac{1}{\rho_0} \int_{-H}^0 \alpha T' dz \quad (5)$$

where H denotes the minimum height (maximum depth (z)). S' and T' are defining salinity and temperature anomalies, with reference values used in Ludwigsen and Andersen (2020) are 0 C° and 35 psu . β is the saline contraction coefficient and α is the thermal expansion coefficient. The opposite sign of η_S is needed since β represents a contraction (opposite to thermal

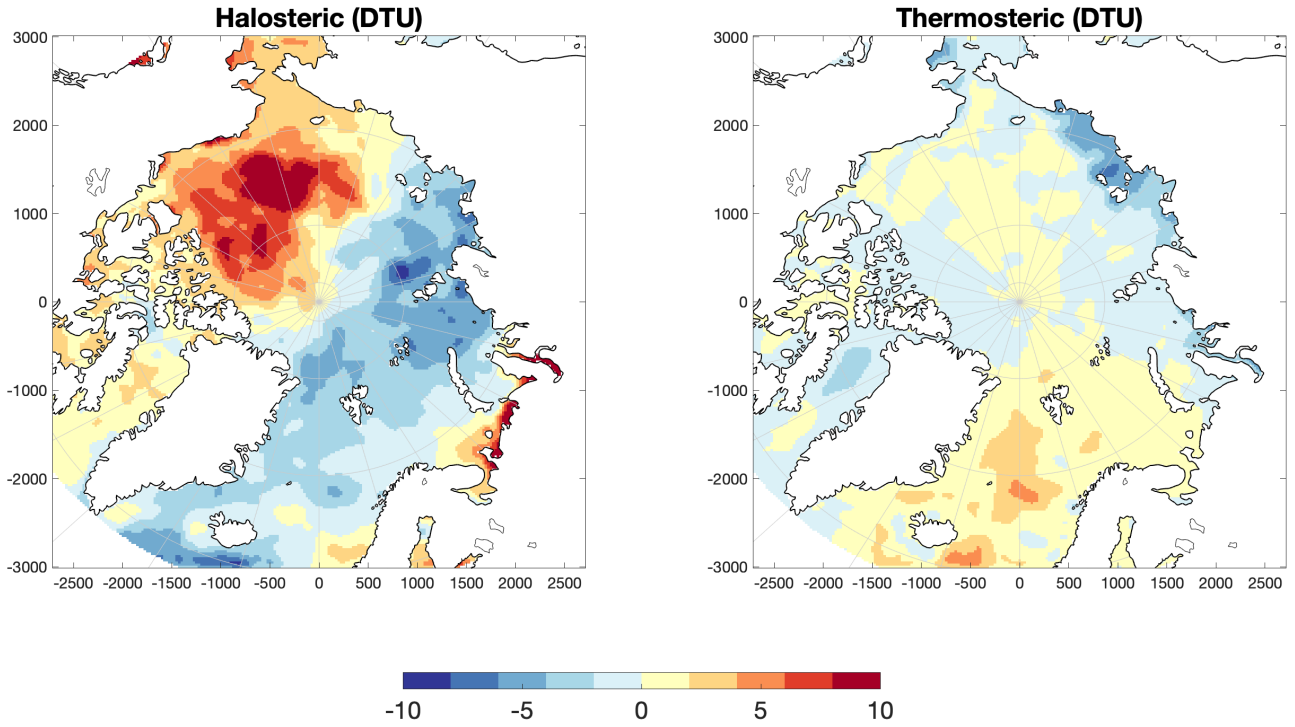


Figure 3. Halo- and thermosteric sea level trend [mm y^{-1}] from 1995-2015 derived from the DTU product which was used in Ludwigsen and Andersen (2020).

expansion). α and β are functions of absolute salinity, conservative temperature and pressure, and is determined with help from the freely available TEOS-10 software (Roquet et al., 2015). Map of $\dot{\eta}_S$ and $\dot{\eta}_T$ from 1995-2015 is shown in figure 3.

5 Mass contribution

Maps of the individual contributions to change in ocean mass is shown in figure 4. We divide the mass contributions into changes caused by changes in surface loading \dot{N} , from Greenland \dot{N}_{GRE} , Northern Hemisphere glaciers \dot{N}_{GNH} , Antarctica \dot{N}_{ANT} and GIA \dot{N}_{GIA} , and atmospheric pressure (IB) and a dynamic contribution ($D\dot{M}$).

$$95 \quad \text{Mass} = \dot{N}_{GRE} + \dot{N}_{GNH} + \dot{N}_{ANT} + \dot{N}_{GIA} + IB + D\dot{M} \quad (6)$$

Similar to the VLM-product (Ludwigsen et al., 2020a), the Regional Elastic Rebound Calculator (REAR) (Melini et al., 2015) is used to estimate elastic gravitational changes, \dot{G} , while gravitational changes from GIA is derived from the Caron2018-

model. \dot{N} is retrieved by adding the spatially constant c to the change of the geoid, \dot{G} ,

$$\dot{N} = \dot{G} + c \quad (7)$$

100 c is equal to the contribution to global mean sea level (Spada, 2017), and is defined as

$$c = -\frac{M_I \rho_w}{A_O} - \langle G - U \rangle \quad (8)$$

The used ice model with mass M_I , is a combined high resolution model for glacial estimates (Marzeion et al., 2012; Ludwigsen et al., 2020a) and Greenland ice caps and is here an extended version of the model used for calculations of VLM, U , in (Ludwigsen et al., 2020a). A_O is the global area of the ocean, while ρ_w is the average density of ocean water. $\langle \dots \rangle$,
105 denotes the average of the ocean surface.

The geoid perturbation of non-tidal ocean loading (NOL) (van Dam et al., 2012) and rotational feedback (RF) (King et al., 2012) is not shown since it is below 0.05 mm y^{-1} , but is included in \dot{N}_{GNH} . The change in surface mass, M_I , is zero for GIA, RF and NOL. The GIA contribution to global mean sea level (c) is 0.3 mm y^{-1} consistent with other studies (Peltier, 2009; Spada, 2017).

110 Inverse Barometer (IB) is estimated by the simple relationship derived from the hydro-static equation (Naeije et al., 2000; Pugh and Woodworth, 2014). Monthly averaged pressure estimates from National Center for Environmental Prediction (NCEP) are used for the change in surface pressure Δp :

$$\text{IB} = -9.948 [\text{mm/mbar}] \Delta p \quad (9)$$

Figure 4 also shows the mass-trends derived from Estimating the Circulation and Climate of the Ocean (ECCO) version
115 4 release 4 (Forget et al., 2015; Fukumori et al., 2019), which is used to estimate the dynamic contribution to sea level. The dynamic mass change is mainly a wind-driven effect that significantly changes the spatial distribution of ocean mass (Calafat et al., 2012; Dangendorf et al., 2014; Armitage et al., 2018) - also on secular time scales.

Because the ECCO-model is among other forced by wind (Forget et al., 2015), we use the difference between ECCO and the sum of \dot{N} and IB as an estimate of the dynamic contribution to mass ($D\dot{M}$, bottom right map of figure 4).

120 **6 Comparison of estimates of the Arctic Absolute Sea Level Trend**

Two derived trend estimates of the ASL budget is created from steric + mass ($\dot{\eta} + \dot{N} + \dot{IB}$) (without the dynamic component) and steric + mass (ECCO), where ECCO is used as the mass component and hence includes dynamic mass changes. They are compared to the independent estimates of ASL change from TG corrected for VLM and altimetry.

The two derived ASL-trend estimates are shown in figure 5. Since ECCO is partly assimilated with altimetry, only the mass
125 contribution without the dynamic component is truly independent from altimetry. On the scale shown in figure 5, we see that the differences are hardly recognizable.

Because of the sea ice bias before the launch of CryoSat-2 in end-2010, the values before 2011 are likely to be overestimated, which results in a 'flattening' of the trend. In particular, this seems to be the case in the Beaufort Sea (see figure 5), where

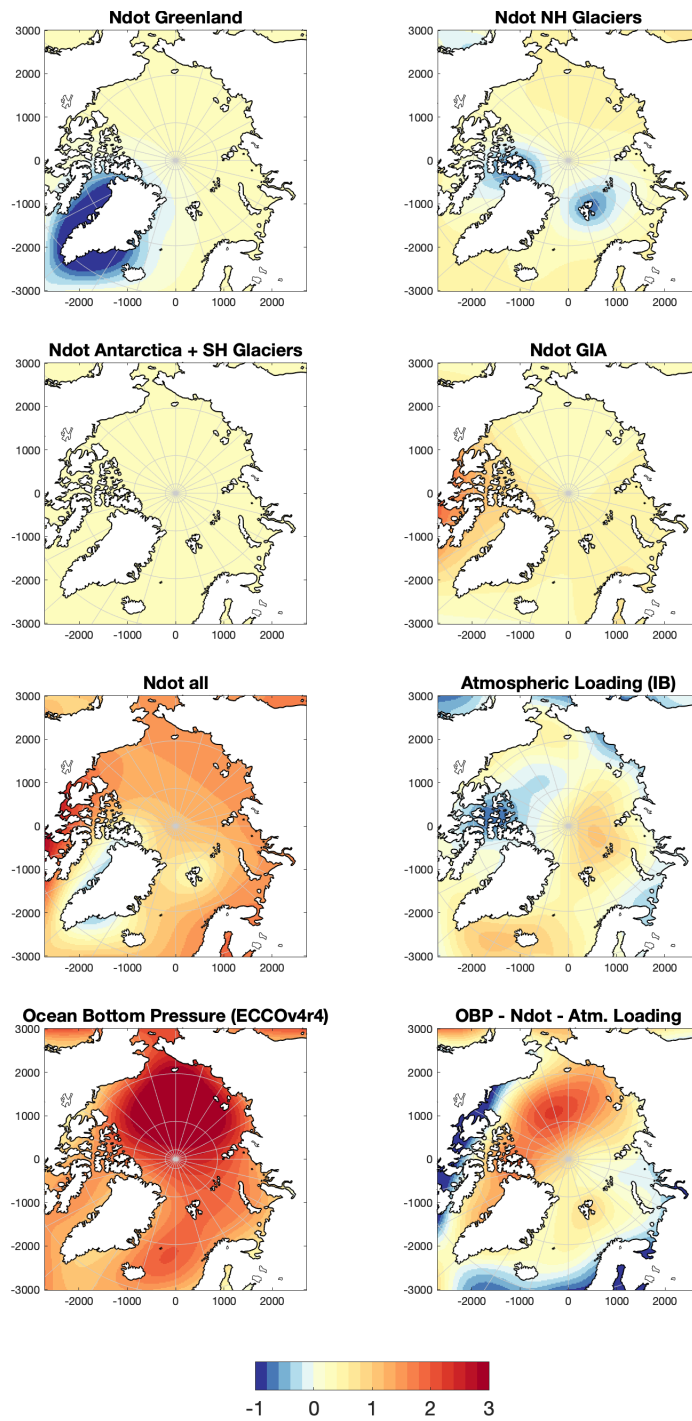


Figure 4. Mass contributions to Arctic Sea Level [mm y^{-1}] from 1995-2015. The top four maps shows the geoid perturbations (\dot{N}) due to changes in surface mass loading or ocean bottom changes. Third row left is the sum of the top four maps. Right is atmospheric loading or Inverse Barometer (IB). Bottom left is the modeled ocean bottom pressure from ECCO and left is the difference between OBP and \dot{N} + atm. loading from third row.

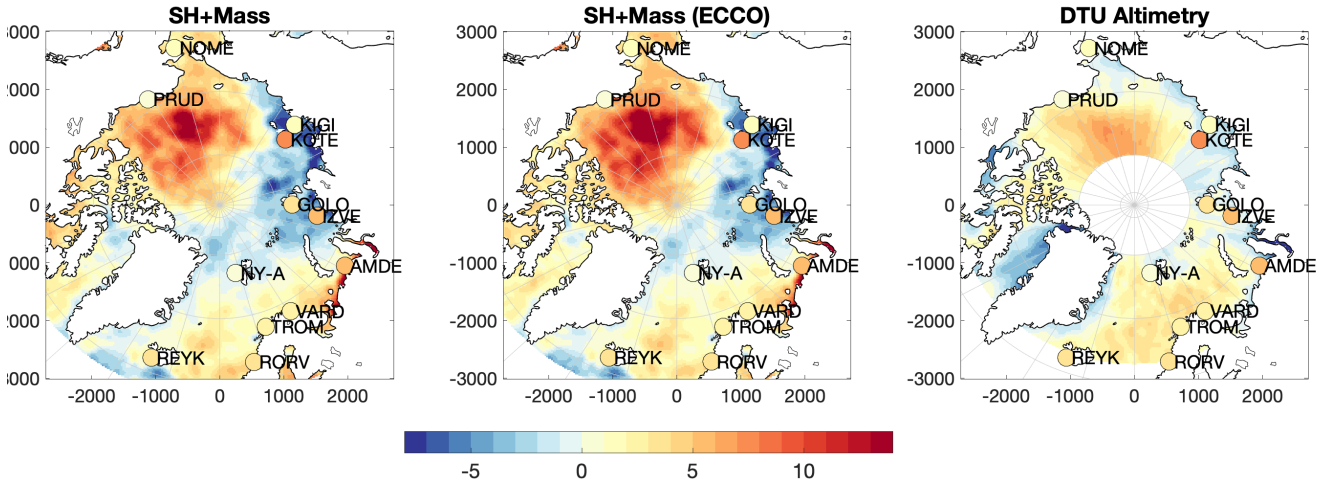


Figure 5. Absolute sea level trend from 1995-2015 [mm y^{-1}]. Left shows perturbation of the geoid + steric contribution, in the middle is OBP from ECCO combined with steric and right is altimetric sea level from Rose et al. (2019). The circles indicate the absolute sea level trend of tide gauges.

	TG RSL	VLM	TG ASL	Mass (\dot{N})	Mass (IB)	Mass (Dyn)	Steric	Mass+Steric	Altimetry
NOME	2.0 ± 1.3	-0.6 ± 0.9	1.4 ± 1.5	1.1 ± 0.3	0.1	0.8 ± 3.4	1.7 ± 12.9	3.6 ± 13.2	0.1 ± 1.0
PRUDHOE BAY	1.7 ± 1.0	-1.0 ± 1.3	0.7 ± 1.6	1.0 ± 0.5	0.4	1.0 ± 2.8	4.4 ± 14.2	6.4 ± 14.5	1.5 ± 1.1
REYKJAVIK	3.8 ± 0.7	0.0 ± 0.3	3.8 ± 0.8	0.3 ± 1.0	1.0	2.2 ± 4.6	-0.8 ± 2.8	1.7 ± 4.3	2.1 ± 0.7
RORVIK	-0.7 ± 1.0	4.5 ± 1.8	3.9 ± 2.1	1.3 ± 0.3	0.3	0.1 ± 2.9	1.9 ± 5.2	3.2 ± 6.1	2.6 ± 0.4
NY-ALESUND	-7.4 ± 0.8	8.0 ± 0.5	0.5 ± 0.9	0.1 ± 1.4	0.6	2.4 ± 4.0	-2.0 ± 2.2	0.4 ± 4.0	1.1 ± 0.3
TROMSO	-0.1 ± 0.9	2.5 ± 1.7	2.5 ± 1.9	1.1 ± 0.4	0.1	0.5 ± 3.2	-0.2 ± 1.9	1.4 ± 3.6	2.7 ± 0.4
VARDO	-0.0 ± 0.9	2.8 ± 1.4	2.8 ± 1.6	1.2 ± 0.4	-0.1	0.1 ± 2.9	0.7 ± 3.2	1.9 ± 4.5	3.8 ± 0.4
AMDERMA	4.9 ± 1.1	0.4 ± 1.1	5.2 ± 1.6	1.1 ± 0.3	-0.1	-0.1 ± 3.0	3.9 ± 11.1	4.9 ± 11.5	-0.7 ± 1.0
IZVESTIA TSIK	2.7 ± 1.0	2.5 ± 1.5	5.2 ± 1.8	1.1 ± 0.5	0.2	0.7 ± 4.4	-5.7 ± 8.0	-3.9 ± 8.6	0.6 ± 1.2
GOLOMIANYI	0.0 ± 0.8	3.0 ± 2.3	3.1 ± 2.5	0.9 ± 0.8	0.6	1.7 ± 4.4	-5.3 ± 7.9	-2.6 ± 8.5	-0.5 ± 1.3
KOTELNYI	7.7 ± 1.3	-0.4 ± 0.8	7.3 ± 1.5	1.1 ± 0.3	0.2	1.9 ± 3.6	-6.5 ± 15.3	-3.5 ± 15.6	-0.8 ± 1.2
KIGILIAH	1.7 ± 1.1	-0.2 ± 0.7	1.5 ± 1.3	1.2 ± 0.2	-0.1	0.9 ± 3.1	-8.0 ± 14.8	-5.9 ± 15.1	-1.5 ± 1.1

Table 1. 1995-2015 sea level trends [mm y^{-1}] of each contribution at the 12 tide gauge locations. The values (except VLM) represent a 100 km radius around the tide gauge. For VLM a 5 km radius is used and for Ny-Alesund and Reykjavik, VLM is taken from GNSS. The columns in bold indicate the estimates of Absolute Sea Level (ASL).

altimetry and the derived mass+steric product agree on the spatial extent of the dooming of the Beaufort Gyre, but altimetry is 5 mm y^{-1} lower than the mass + steric estimate. Another altimetry product from Armitage et al. (2016) has a larger trend in the Beaufort Gyre in alignment with the steric+mass products.

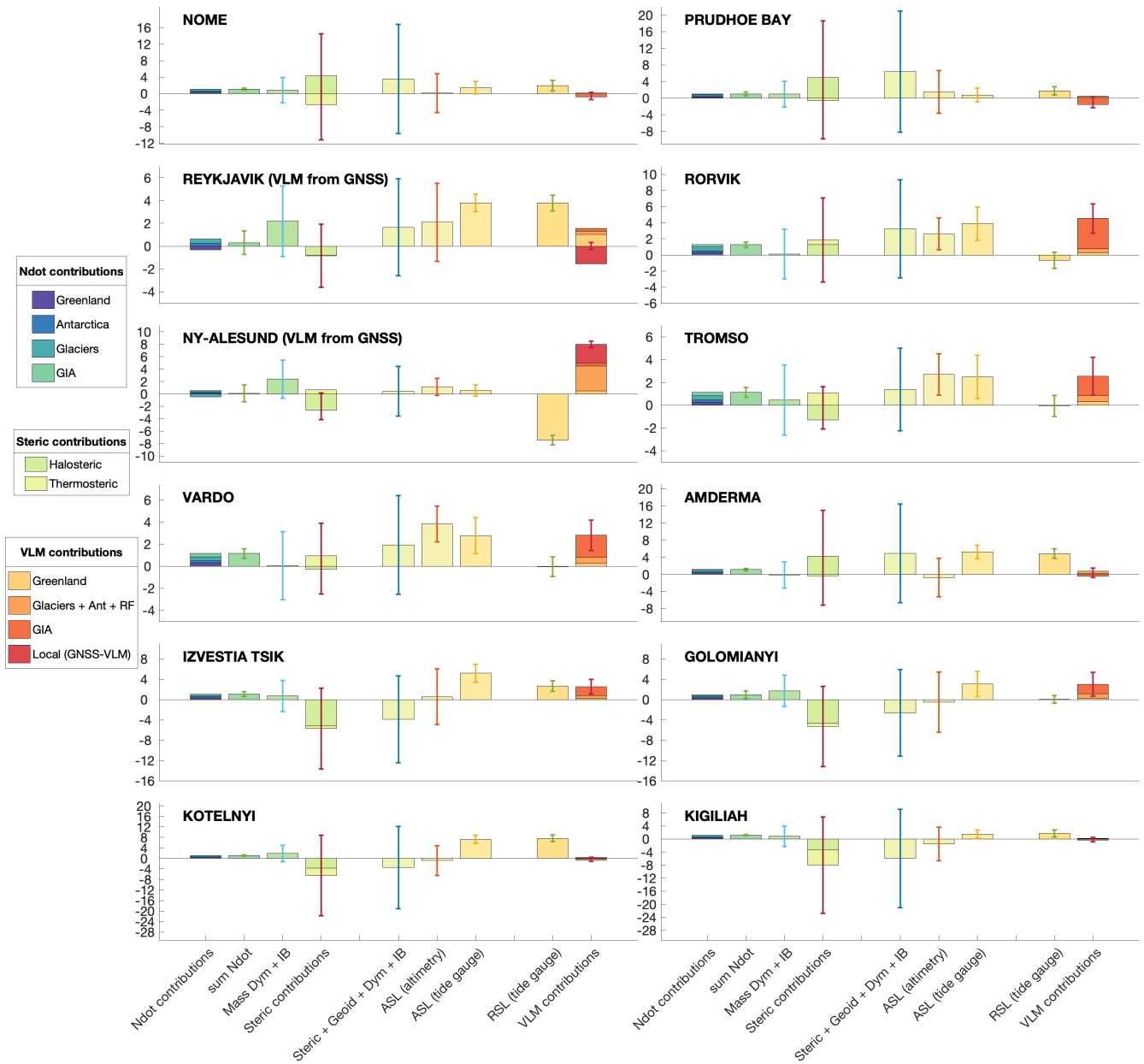


Figure 6. Components of sea level trend [mm y^{-1}] for each tide gauge from 1995-2015. The three bars in the middle (Steric+geoid+dyn, ASL (altimetry) and ASL (tide gauge)) are independent estimates of absolute sea level. The errorbars indicate one standard error (combined error from each component when relevant). The VLM component 'Local (GNSS-VLM)' is only relevant at Reykjavik and Ny Ålesund, because significant local properties causes VLM that is not present in the VLM-model (Ludwigsen et al., 2020b). Glacier component of VLM includes the effect of rotational feedback, ocean loading, and Antarctica which are less than 0.5 mm y^{-1} combined.

In the altimetric product a positive sea level trend extends in the Norwegian Sea until it reaches the average sea ice boundary, which (intentionally) coincides with the SAR-boundary of CryoSat-2. From altimetry it is unclear if this signal is a real physical signal or due to bias when different satellites and sea ice and open ocean regions are aligned in the DTU/TUM product. We see from the derived mass+steric product, that some of the positive sea level trends are restored in the Norwegian Sea by the thermosteric contribution (figure 3), thus is a warming of the ocean cause to sea level rise in the region. The boundary between sea ice and open ocean is however less significant.

Obviously, does tide gauges only measure sea level in coastal areas, and therefore not useful when analyzing spatial sea level trend patterns of the Arctic Ocean. Furthermore, is the coastal location often disturbed by the local environment that might be unknown (e.g. small river outflow, local construction, packing of sea ice etc.), which can influence both sea level measurements from tide gauge and altimetry.

In figure 6 and table 1, we quantify the contributions to sea level change explained in this chapter at each of the 12 tide gauge locations using a surrounding average of 100 km radius (5 km for GIA and elastic VLM). This radius ensures, that Rorvik, Nome and Reykjavik reaches the altimetric data, but few data points, might cause the data to be more variable and hence increase the uncertainty.

The Norwegian tide gauges (Rorvik, Tromso, Vardo) are considered the most stable. The derived product is in good agreement with the tide gauge and has for Tromso and Vardo better alignment with the TG-data than altimetry. This is also the region with highest density of hydrographical data and thus most reliable. We see that for Vardo and Rorvik, the sea level change is split between a steric and mass contribution of roughly the same size, which is similar to the share of the global sea level trend (Church and White, 2011; Group, 2018). At Tromso a negative halosteric signal (more saline water) is lowering the sea level trend.

Along the Siberian coast, multiple river outlets contributes to a freshening of the Arctic Ocean (Morison et al., 2012; Armitage et al., 2016), which is reflected by the positive halosteric trend. At Amderma TG, which is located on the coast between the Barents and Kara Sea, there is however no nearby major river outlet, but a significant halosteric signal is still present which matches the tide gauge-measured sea level. Ice loss from Novaya Zemlya contributes with over 1 gigaton of freshwater to the Kara Sea every year (Melkonian et al., 2016), but it is unclear if this is the reason for the halosteric sea level rise at Anderma, or if the halosteric signal is (falsely) extrapolated from the gulf of Ob which has mayor river outlets and the match with tide gauge is accidental. The altimetric signal reflects the mass contribution, which together with low hydrographic data density in the region, could indicate that both the tide gauge and halosteric sea level trends are overestimated.

The four other tide gauges along the Siberian coast all show a pattern, where mass+steric has a negative trend, altimetry has a slight negative or positive trend and the tide gauge has a clear positive trend. Due to poor hydrographic coverage along the Siberian coast (Ludwigsen and Andersen, 2020) it is difficult to estimate the 'true' sea level. The positive trend among tide gauges in the Siberian Seas is however consistent and has been recognized in other studies using an extended set of Siberian tide gauges (Proshutinsky et al., 2004; Henry et al., 2012). Remarkably is that the TG-trend at Kotelnyi and Kigiliah differ with almost 6 mm y⁻¹ despite being less than 250 km apart. This difference is only realistic if local circumstances is affecting the RSL.

Nome and Prudhoe Bay in Alaska both show a positive steric trend which is not reflected in sea level trends from altimetry or the tide gauge. The strong halosteric trend of the Beaufort Gyre, might be extrapolated towards the Alaskan coastline. Altimetry agrees reasonably well with the tide gauge trend.

170 Few hydrographic data around Reykjavik, makes the steric sea level rather uncertain as well. A negative halosteric contribution causes the steric+mass product to be too low compared to TG-data and altimetry.

At Ny-Ålesund on Svalbard, which like the other Norwegian TG-sites has good hydrographic data density, is the mass + steric contribution in agreement with the TG-trend. Ny-Ålesund is dominated by a large VLM caused by deglaciation in recent years and after the Little Ice Age that ended in the 19th century (Rajner, 2018; Ludwigsen et al., 2020a). This uplift
175 completely mitigates the large sea level fall measured by the tide gauge. A small mass upward trend is countered by a smaller steric downward trend, which in total agrees with the tide gauge measured sea level trend. Altimetry shows a slightly higher trend.

Generally the largest uncertainties (estimated as standard error of the trend) are found along the Siberian coast and in the interior of the Arctic where the largest sea level trend is present (see figure 7). The steric uncertainty, which in most cases is the
180 largest source of uncertainty, is computed as the standard deviation of the detrended and deseasoned time series, which naturally reflects if steric heights are unstable and poorly constrained. This method requires in principal temporal independence, which is not entirely true, since data from adjacent years are used instead of outliers. Furthermore, large influence by the non-periodic and non-linear Arctic Oscillation, would enhance the uncertainty, even though this is a real physical signal.

The mass contribution and VLM has naturally the largest uncertainties close to glaciated areas. Glacial ice loss on Baffin
185 Island is poorly constrained in the ice model, which is reflected in large uncertainties in this area. A significant uncertainty also originates in the dynamic mass loss, which probably also can be attributed to the Arctic Oscillation, which significantly changes wind patterns. Since no uncertainties are associated with the ECCO-product, we also here assume no temporal correlation, and calculate the standard deviation of the time series, even though the model likely has inter-annual correlations.

7 Conclusion

190 All significant contributions to the sea level change from 1995-2015 in the Arctic Ocean have been mapped and assessed at 12 tide gauges located throughout the Arctic, without the use of GRACE data or modeled steric data. Thereby are we able to attribute effects on Arctic Sea Level to their origin and thus understand the causes behind the observed sea level trend. By using a VLM-model that includes both GIA and elastic uplift, the TG-data can be utilized in locations if no reliable GNSS-data is present.

195 From figure 5 we clearly see that the general spatial pattern of altimetry is restored in the derived steric estimate and in the mass product. Figure 6 and 7 shows that steric sea level dominates the spatial variability and is also the main source of uncertainty. Some areas, in particular the Norwegian Sea and more interior of the Arctic Ocean, seems to be rather well constrained and understood from the individual contributions. The Siberian seas, are however poorly constrained and both the steric product, altimetry and tide gauges show large uncertainty. Figure 8 shows the spatial agreement between altimetry/tide

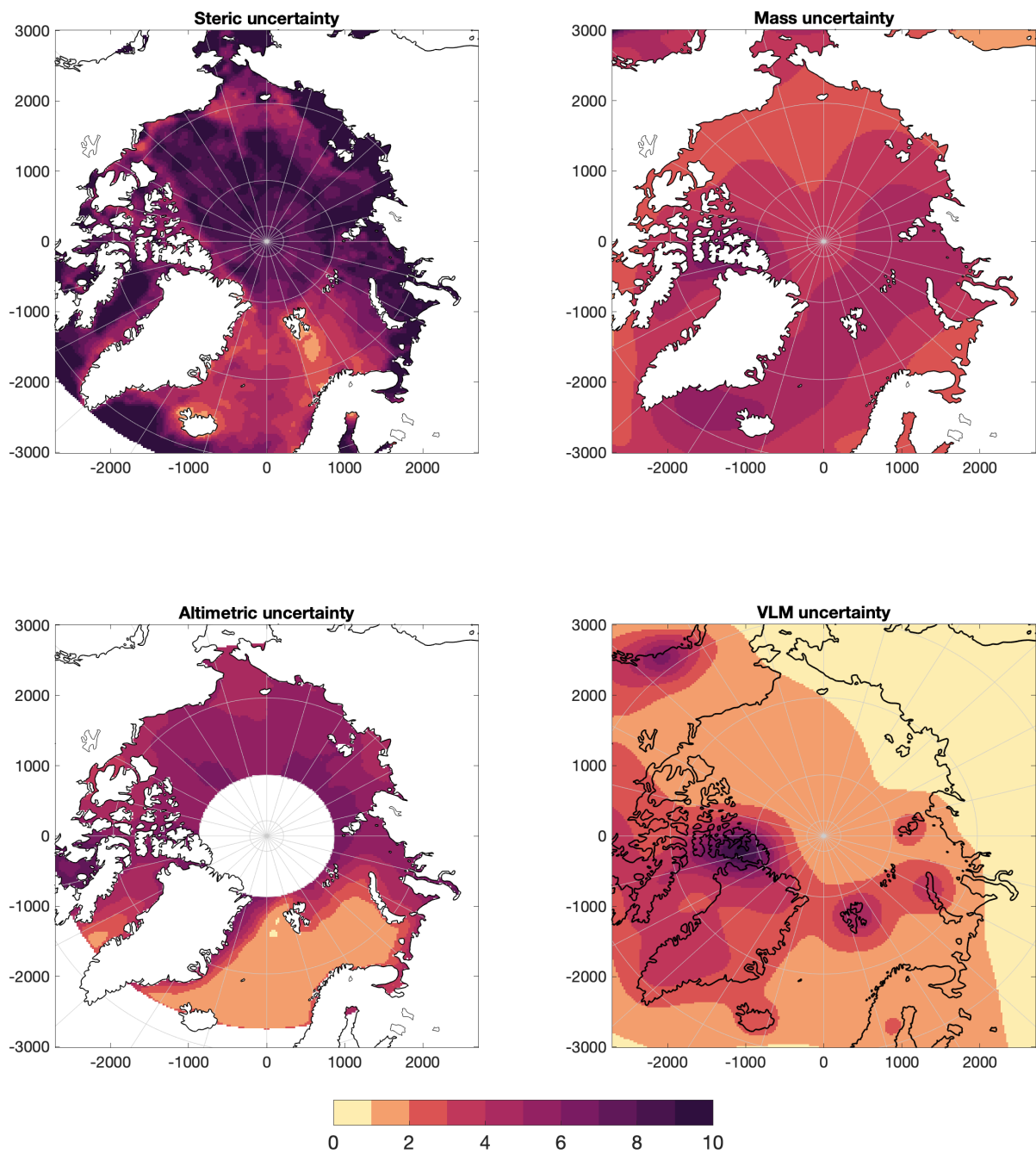


Figure 7. Maps of uncertainty (1 standard error) of the 1995-2015 trend [mm y^{-1}] for combined steric, combined \dot{N} + dynamic mass + IB, altimetry and combined VLM contributions.

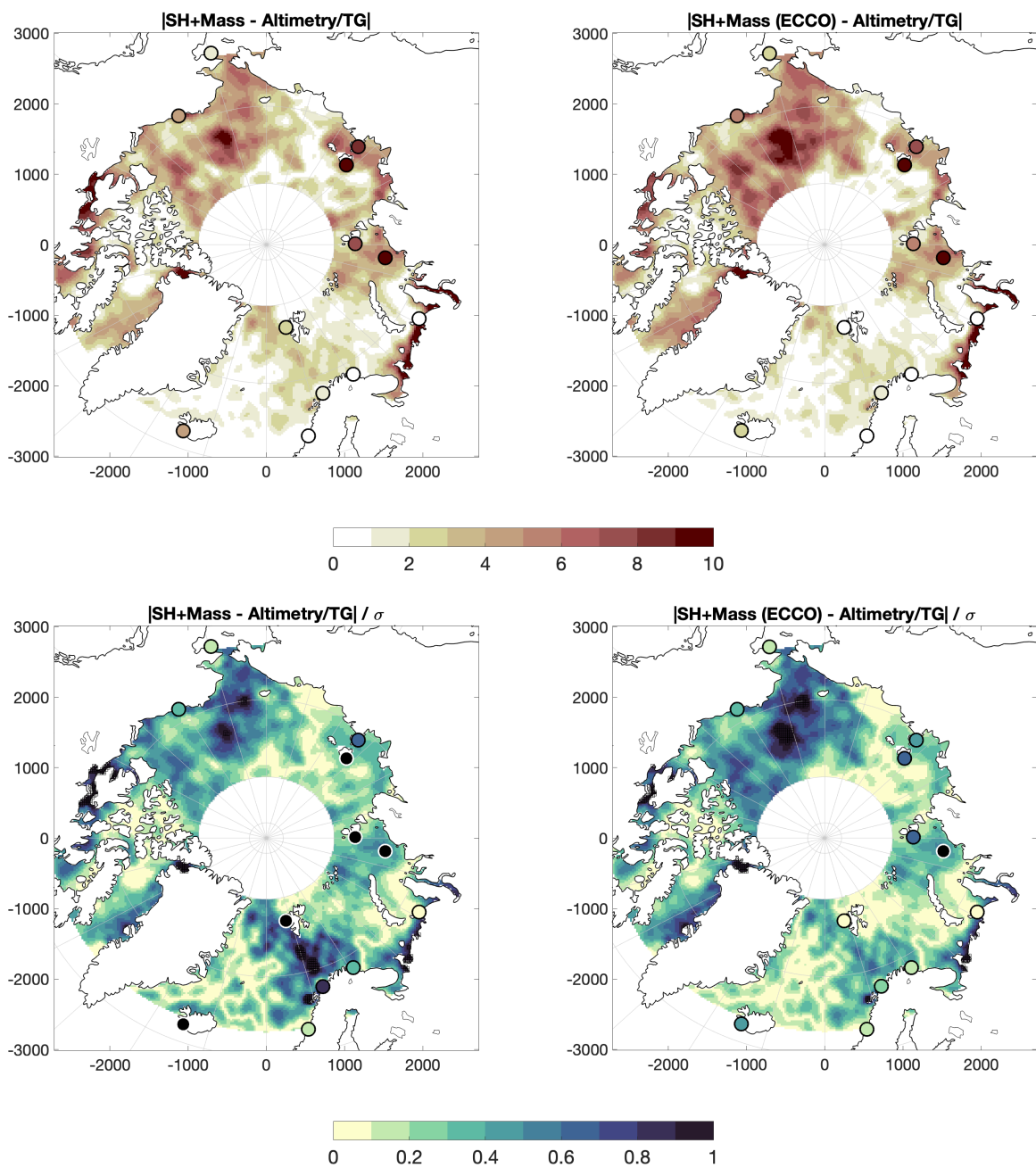


Figure 8. Map in the top row shows the absolute difference between altimetry and the steric+mass (no dynamic contribution) product (left column) and altimetry and the steric+mass from the ECCO-model (right column). Bottom row, shows the absolute difference relative to the combined uncertainty (σ). The dots show the difference to VLM-corrected tide gauges. At the tide gauges marked with black, is the difference larger than the combined uncertainty.

200 gauges and the steric+mass or steric+mass(ECCO) product within the combined uncertainty. Without the use of ECCO, the derived product agrees with altimetry at 98% of the area, while only 5 out of 12 of the TG-data agree with derived product. For the steric+mass(ECCO) product, the products agree at 99% of the area and at 11 out of 12 TG's. The areas of disagreement in the Norwegian Sea can be explained by the very low altimetric uncertainty in the area.

205 Our results show that the sea level budget is not closed or completely understood everywhere - likely because of poorly constrained steric data and uncertain dynamic contribution. However, from figure 8 we see that the uncertainties are in most of the Arctic significantly larger than the difference between a derived product and altimetry, including most of the Siberian Seas. More precise estimates of both the mass and steric product are necessary to get at complete understanding of what changes Arctic sea level and validate sea level trends observed by altimetry, which is not necessarily more accurate than the derived ASL-estimates.

210 *Author contributions.* CAL: Method, concept, data analysis and writing. OBA: Concept and editing. SKR: Providing altimetry data, validation and editing.

Competing interests. The authors declare no competing interests.

Acknowledgements. The authors want to thank Lambert Caron for creating the Caron2018 GIA-model, available at <https://vesl.jpl.nasa.gov/solid-earth/gia/>. Special thanks to Danielle Melini for creating the REAR-code (Melini et al., 2015). This research was funded by the 215 EU-INTAROS project (Grant agreement no. 727890) (CAL and OBA) and by the ESA-Climate Change Initiative Sea level budget closure (Expro RFP/3-14679/16/INB) (OBA and SKR).

References

- Armitage, T. W. K., Bacon, S., Ridout, A. L., Thomas, S. F., Aksenov, Y., and Wingham, D. J.: Arctic sea surface height variability and change from satellite radar altimetry and GRACE, 2003–2014, *Journal of Geophysical Research: Oceans*, 121, 4303–4322, <https://doi.org/10.1002/2015JC011579>, <https://agupubs.onlinelibrary.wiley.com/doi/abs/10.1002/2015JC011579>, 2016.
- Armitage, T. W. K., Bacon, S., and Kwok, R.: Arctic Sea Level and Surface Circulation Response to the Arctic Oscillation, *Geophysical Research Letters*, 45, 6576–6584, <https://doi.org/10.1029/2018GL078386>, <https://agupubs.onlinelibrary.wiley.com/doi/abs/10.1029/2018GL078386>, 2018.
- Behrendt, A., Sumata, H., Rabe, B., and Schauer, U.: A comprehensive, quality-controlled and up-to-date data set of temperature and salinity data for the Arctic Mediterranean Sea (Version 1.0), links to data files, <https://doi.org/10.1594/PANGAEA.872931>, <https://doi.org/10.1594/PANGAEA.872931>, supplement to: Behrendt, A et al. (2017): UDASH - Unified Database for Arctic and Subarctic Hydrography. *Earth System Science Data Discussions*, 37 pp, <https://doi.org/10.5194/essd-2017-92>, 2017.
- Calafat, F. M., Chambers, D. P., and Tsimplis, M. N.: Mechanisms of decadal sea level variability in the eastern North Atlantic and the Mediterranean Sea, *Journal of Geophysical Research: Oceans*, 117, <https://doi.org/10.1029/2012JC008285>, <https://agupubs.onlinelibrary.wiley.com/doi/abs/10.1029/2012JC008285>, 2012.
- Caron, L., Ivins, E. R., Larour, E., Adhikari, S., Nilsson, J., and Blewitt, G.: GIA Model Statistics for GRACE Hydrology, Cryosphere, and Ocean Science, *Geophysical Research Letters*, 45, 2203–2212, <https://doi.org/10.1002/2017GL076644>, <https://agupubs.onlinelibrary.wiley.com/doi/abs/10.1002/2017GL076644>, 2018.
- Carret, A., Johannessen, J. A., Andersen, O. B., Ablain, M., Prandi, P., Blazquez, A., and Cazenave, A.: Arctic Sea Level During the Satellite Altimetry Era, *Surveys in Geophysics*, 38, 251–275, <https://doi.org/10.1007/s10712-016-9390-2>, <https://doi.org/10.1007/s10712-016-9390-2>, 2017.
- Church, J. A. and White, N. J.: Sea-Level Rise from the Late 19th to the Early 21st Century, *Surveys in Geophysics*, 32, 585–602, <https://doi.org/10.1007/s10712-011-9119-1>, <https://doi.org/10.1007/s10712-011-9119-1>, 2011.
- Dangendorf, S., Calafat, F. M., Arns, A., Wahl, T., Haigh, I. D., and Jensen, J.: Mean sea level variability in the North Sea: Processes and implications, *Journal of Geophysical Research: Oceans*, 119, <https://doi.org/10.1002/2014JC009901>, <https://agupubs.onlinelibrary.wiley.com/doi/abs/10.1002/2014JC009901>, 2014.
- Forget, G., Campin, J.-M., Heimbach, P., Hill, C. N., Ponte, R. M., and Wunsch, C.: ECCO version 4: an integrated framework for non-linear inverse modeling and global ocean state estimation, *Geoscientific Model Development*, 8, 3071–3104, <https://doi.org/10.5194/gmd-8-3071-2015>, <https://gmd.copernicus.org/articles/8/3071/2015/>, 2015.
- Fukumori, I., Wang, O., Fenty, I., Forget, G., Heimbach, P., and Ponte, R. M.: ECCO Version 4 Release 4 Dataset, accessed: 2020-06-25, 2019.
- Gill, A. and Niller, P.: The theory of the seasonal variability in the ocean, *Deep Sea Research and Oceanographic Abstracts*, 20, 141 – 177, [https://doi.org/https://doi.org/10.1016/0011-7471\(73\)90049-1](https://doi.org/https://doi.org/10.1016/0011-7471(73)90049-1), <http://www.sciencedirect.com/science/article/pii/0011747173900491>, 1973.
- Group, W. G. S. L. B.: Global sea-level budget 1993–present, *Earth System Science Data*, 10, 1551–1590, <https://doi.org/10.5194/essd-10-1551-2018>, <https://essd.copernicus.org/articles/10/1551/2018/>, 2018.
- Henry, O., Prandi, P., Llovel, W., Cazenave, A., Jevrejeva, S., Stammer, D., Meyssignac, B., and Koldunov, N.: Tide gauge-based sea level variations since 1950 along the Norwegian and Russian coasts of the Arctic Ocean: Contribution of the steric and mass components,

- Journal of Geophysical Research: Oceans, 117, <https://doi.org/10.1029/2011JC007706>, <https://agupubs.onlinelibrary.wiley.com/doi/abs/10.1029/2011JC007706>, 2012.
- 255 Holgate, S. J., Matthews, A., Woodworth, P. L., Rickards, L. J., Tamisiea, M. E., Bradshaw, E., Foden, P. R., Gordon, K. M., Jevrejeva, S., and Pugh, J.: New Data Systems and Products at the Permanent Service for Mean Sea Level, *Journal of Coastal Research*, 29, 493–504, <https://doi.org/10.2112/JCOASTRES-D-12-00175.1>, <https://doi.org/10.2112/JCOASTRES-D-12-00175.1>, 2012.
- King, M. A., Keshin, M., Whitehouse, P. L., Thomas, I. D., Milne, G., and Riva, R. E. M.: Regional biases in absolute sea-
 260 level estimates from tide gauge data due to residual unmodeled vertical land movement, *Geophysical Research Letters*, 39, <https://doi.org/10.1029/2012GL052348>, <https://agupubs.onlinelibrary.wiley.com/doi/abs/10.1029/2012GL052348>, 2012.
- Limkilde Svendsen, P., Andersen, O. B., and Aasbjerg Nielsen, A.: Stable reconstruction of Arctic sea level for the 1950–2010 period, *Journal of Geophysical Research: Oceans*, 121, 5697–5710, <https://doi.org/10.1002/2016JC011685>, <https://agupubs.onlinelibrary.wiley.com/doi/abs/10.1002/2016JC011685>, 2016.
- 265 Ludwigsen, C., Khan, S. A., Andersen, O. B., and Marzeion, B.: Vertical Land Motion from present-day deglaciation in the wider Arctic, *Earth and Space Science Open Archive*, p. 18, <https://doi.org/10.1002/essoar.10502890.1>, <https://doi.org/10.1002/essoar.10502890.1>, 2020a.
- Ludwigsen, C. A. and Andersen, O. B.: Contributions to Arctic sea level from 2003 to 2015, *Advances in Space Research*, <https://doi.org/https://doi.org/10.1016/j.asr.2019.12.027>, <http://www.sciencedirect.com/science/article/pii/S0273117719309275>, 2020.
- 270 Ludwigsen, C. A., Andersen, O. B., Khan, S. A., and Marzeion, B.: Arctic Vertical Land Motion (5x5 km), <https://doi.org/10.11583/DTU.12554489.v1>, https://data.dtu.dk/articles/dataset/Arctic_Vertical_Land_Motion_5x5_km_/12554489, 2020b.
- Luthcke, S. B., Sabaka, T., Loomis, B., Arendt, A., McCarthy, J., and Camp, J.: Antarctica, Greenland and Gulf of Alaska land-ice evolution from an iterated GRACE global mascon solution, *Journal of Glaciology*, 59, 613–631, <https://doi.org/10.3189/2013JoG12J147>, 2013.
- 275 Marzeion, B., Jarosch, A. H., and Hofer, M.: Past and future sea-level change from the surface mass balance of glaciers, *The Cryosphere*, 6, 1295–1322, <https://doi.org/10.5194/tc-6-1295-2012>, <https://www.the-cryosphere.net/6/1295/2012/>, 2012.
- Melini, D., Spada, G., Gegout, P., and King, M.: REAR: a Regional ElAstic Rebound calculator. User manual for version 1.0, available on-line at: <http://hpc.rm.ingv.it/rear>, 2015.
- Melkonian, A. K., Willis, M. J., Pritchard, M. E., and Stewart, A. J.: Recent changes in glacier velocities and thinning at Novaya Zemlya, *Remote Sensing of Environment*, 174, 244 – 257, <https://doi.org/https://doi.org/10.1016/j.rse.2015.11.001>, <http://www.sciencedirect.com/science/article/pii/S0034425715301899>, 2016.
- 280 Morison, J., Kwok, R., Peralta-Ferriz, C., Alkire, M., Rigor, I., Andersen, R., and Steele, M.: Changing Arctic Ocean freshwater pathways, *Nature*, 481, 66–70, <https://doi.org/10.1038/nature10705>, <https://doi.org/10.1038/nature10705>, 2012.
- Naeije, M., Schrama, E., and Scharroo, R.: The radar Altimeter Database System project RADS, 2, 487 – 490 vol.2, <https://doi.org/10.1109/IGARSS.2000.861605>, 2000.
- 285 Peltier, W.: Closure of the budget of global sea level rise over the GRACE era: the importance and magnitudes of the required corrections for global glacial isostatic adjustment, *Quaternary Science Reviews*, 28, 1658 – 1674, <https://doi.org/https://doi.org/10.1016/j.quascirev.2009.04.004>, <http://www.sciencedirect.com/science/article/pii/S0277379109001218>, *quaternary Ice Sheet-Ocean Interactions and Landscape Responses*, 2009.

- 290 Proshutinsky, A., Ashik, I. M., Dvorkin, E. N., Häkkinen, S., Krishfield, R. A., and Peltier, W. R.: Secular sea level change in the Russian sector of the Arctic Ocean, *Journal of Geophysical Research: Oceans*, 109, <https://doi.org/10.1029/2003JC002007>, <https://agupubs.onlinelibrary.wiley.com/doi/abs/10.1029/2003JC002007>, 2004.
- Pugh, D. and Woodworth, P.: *Sea-Level Science: Understanding Tides, Surges, Tsunamis and Mean Sea-Level Changes*, Cambridge University Press, <https://doi.org/10.1017/CBO9781139235778>, 2014.
- 295 Raj, R. P., Andersen, O. B., Johannessen, J. A., Gutknecht, B. D., Chatterjee, S., Rose, S. K., Bonaduce, A., Horwath, M., Ranndal, H., Richter, K., Palanisamy, H., Ludwigsen, C. A., Bertino, L., Nilsen, J. E. , Knudsen, P., Hogg, A., Cazenave, A., and Benveniste, J.: Arctic Sea level Budget Assessment During the GRACE/Argo Time Period, *Remote Sensing*, 12, <https://doi.org/10.3390/rs12172837>, <https://www.mdpi.com/2072-4292/12/17/2837>, 2020.
- Rajner, M.: Detection of ice mass variation using gnss measurements at Svalbard, *Journal of Geodynamics*, 121, 20 – 25, <https://doi.org/https://doi.org/10.1016/j.jog.2018.06.001>, <http://www.sciencedirect.com/science/article/pii/S0264370718300450>, 2018.
- 300 Roquet, F., Madec, G., McDougall, T. J., and Barker, P. M.: Accurate polynomial expressions for the density and specific volume of seawater using the TEOS-10 standard, *Ocean Modelling*, 90, 29 – 43, <https://doi.org/https://doi.org/10.1016/j.ocemod.2015.04.002>, <http://www.sciencedirect.com/science/article/pii/S1463500315000566>, 2015.
- Rose, S. K., Andersen, O., Passaro, M., Ludwigsen, C., and Schwatke, C.: Arctic Ocean Sea Level Record from the Complete Radar Altimetry Era: 1991-2018, *Remote Sensing*, 11, <https://doi.org/10.3390/rs11141672>, 2019.
- 305 Save, H., Bettadpur, S., and Tapley, B. D.: High-resolution CSR GRACE RL05 mascons, *Journal of Geophysical Research: Solid Earth*, 121, 7547–7569, <https://doi.org/10.1002/2016JB013007>, <https://agupubs.onlinelibrary.wiley.com/doi/abs/10.1002/2016JB013007>, 2016.
- Spada, G.: Glacial Isostatic Adjustment and Contemporary Sea Level Rise: An Overview, *Surveys in Geophysics*, 38, 153–185, <https://doi.org/10.1007/s10712-016-9379-x>, <https://doi.org/10.1007/s10712-016-9379-x>, 2017.
- 310 Stammer, D.: Steric and wind-induced changes in TOPEX/POSEIDON large-scale sea surface topography observations, *Journal of Geophysical Research: Oceans*, 102, 20 987–21 009, <https://doi.org/10.1029/97JC01475>, <https://agupubs.onlinelibrary.wiley.com/doi/abs/10.1029/97JC01475>, 1997.
- van Dam, T., Collilieux, X., Wuite, J., Altamimi, Z., and Ray, J.: Nontidal ocean loading: amplitudes and potential effects in GPS height time series, *Journal of Geodesy*, 86, 1043–1057, <https://doi.org/10.1007/s00190-012-0564-5>, <https://doi.org/10.1007/s00190-012-0564-5>, 2012.
- 315 Wiese, D. N., Landerer, F. W., and Watkins, M. M.: Quantifying and reducing leakage errors in the JPL RL05M GRACE mascon solution, *Water Resources Research*, 52, 7490–7502, <https://doi.org/10.1002/2016WR019344>, <https://agupubs.onlinelibrary.wiley.com/doi/abs/10.1002/2016WR019344>, 2016.

7 Conclusions and outlook

The objective of this PhD thesis was to find new methods to investigate Arctic Ocean sea level change and help validate observed sea level change in one of the least accessible and harsh regions of the world. Data from in-situ measurements, satellite observations and modeling have been employed and combined to give an overview of Arctic sea level change.

From the research of this work, it is clear how the rapid warming of the Arctic leads to significant changes in the Arctic Ocean topography:

- Deglaciation of land and sea ice leads to freshening of the Arctic Ocean
- Warming of the Arctic and enhanced sun radiation warms the ocean
- Arctic land-to-ocean mass loss creates significant vertical deformation of land and ocean bottom of the Arctic
- Arctic land-to-ocean mass loss significantly changes the geoid
- Declining sea ice area enhances the dynamic effects of the Arctic Ocean

This thesis contributes with important findings in all of above topics, which has emerged into three papers, that combined gives a comprehensive analysis of the effects of climate change on the contributions to Arctic Ocean sea level.

The first paper (Ludwigsen and Andersen, 2020) presented the available sea level products in the Arctic Ocean in the era of the GRACE-satellites. In previous studies of the Arctic Ocean, the steric component was derived from models, which in early stages proved to be insufficient and not assembling the difference between GRACE-observed mass estimates and altimetry. Therefore was an Arctic steric product developed, *DTU Steric*, which integrated all available temperature and salinity profiles. The main findings of this work is:

1. Altimetric observations (from RADS (Scharroo et al., 2013), CPOM (Armitage et al., 2016) and DTU (Rose et al., 2019)) showed large variations - in particular in the extent of the Beaufort Gyre and in the Norwegian and Siberian Sea
2. Gravimetric observations from GRACE-mascon products showed very different mass-driven sea level patterns that in some regions showed difference with 10 mm y^{-1} , which the largest disagreement in the Beaufort Gyre
3. Steric calculations from modeled temperature and salinity profiles from ECCOv4r3 underestimates the halosteric signal in the Beaufort Gyre. Satellite-derived steric observations (Altimetry - GRACE) showed in Armitage et al. (2016) agrees well with changes estimated by DTU Steric.
4. Reasonable well spatial correlation was found between DTU Steric + JPL Mascons (Wiese et al., 2016) and CPOM altimetry (Armitage et al., 2016). The temporal correlation was however less significant, because the AO-driven sea level change is less pronounced in DTU Steric and JPL Mascons. Areas with disagreement coincides with areas of low hydrographic data density.
5. Other studies on Arctic sea level indicate that mass-driven sea level change dominates the sea level trend (e.g. (Carret et al., 2017; Raj et al., 2020)). However, the

results from the paper show that the halosteric contribution because of additional freshwater is the major driver of sea level change in the Arctic Ocean and that it is able to explain large parts of the spatial variability in the Arctic.

The second paper presents a major component of Arctic sea level measured at tide gauge. Because of climate change and resulting deglaciation of land ice, is the elastic vertical deformation that results after changed ice loading on land affecting the whole Arctic and is also having a significant impact in far field regions as the coastlines of United States or the North Sea region. A high-resolution ice model that reflects the spatial variability of mass loss of glaciers was created to compute elastic uplift in an equal high resolution. The high resolution of the VLM-model enables it to be used in glaciated regions, which would not be properly represented with the relative low spatial resolution of GRACE. Conclusions of this study were

1. GNSS-measurement throughout the wider Arctic showed that a combination of the GIA-model from Caron et al. (2018) and the produced elastic model was able to restore the GNSS-measured vertical deformation and clearly outperformed a GIA-only model.
2. Residuals between the combined VLM-model and GNSS was combined with information from other localized effects contributing to VLM. In Alaska a post-seismic signal from a major earthquake (M9.2) causes rapid uplift, Greenland and Svalbard experiences some viscoelastic deformation from deglaciation after the Little Ice Age and East-Greenland and Iceland has soft mantle structures, causing a more rapid uplift with a smaller footprint. The scale of the residuals matched the estimated VLM-estimates of the mentioned effects.
3. The elastic VLM has far-reaching effects and should be accounted for when projecting coastal sea level. In Denmark, about 30% of the sea level change from land-ice deglaciation is mitigated by elastic uplift.
4. Contrary GIA, is the elastic deformation time-varying and depends on glacial and icesheet mass balance. This is an important property in the future, where deglaciation is expected to accelerate, and the impact on tide-gauges might not be the same every year.
5. GIA-models are in some regions inadequate and it can be difficult to separate present-day elastic signals from viscoelastic deformation because of uncertain GIA estimates. A high resolution elastic VLM-model can help constrain GIA-models.

The third paper combined the research from the first and second paper. The VLM-model made it possible to integrate tide-gauge stations into the analysis of Arctic sea level. Instead of using GRACE for mass estimates, the sea level fingerprint of the ice model used in the second paper and GIA was used to estimate the mass component of Arctic Sea Level from 1995 to 2015. From the assessment we conclude that:

1. Large spatial variability of halosteric sea level change ($-5 - 15 \text{ mm y}^{-1}$) and a smaller mass component ($\simeq 1 \text{ mm y}^{-1}$) confirmed the analysis of the first paper.
2. In the Norwegian Sea, where steric component and VLM is well-constrained, the sea level measured from tide gauges are restored in the derived mass + steric sea level estimate. The sea level trend of the mass component equals the steric sea level change along the Norwegian coast.
3. A sea level rise in the Kara and Laptev seas because of freshwater outflow is

not captured by altimetry, but is clearly visible from the halosteric contribution and matches the sea level rise measured with tide gauges. A sea level decline in the East Siberian Seas in both the halo- and thermosteric sea level is not recognized by the tide gauges, which show a sea level rise. Large differences between neighboring tide gauges, indicate that tide gauges is affected by unknown local contributions. However, assessment of multiple Siberian tide-gauges show that the sea level rise on the Siberian Shelf has been consistent since the 1980's (Proshutinsky et al., 2004).

4. Large variability associated with the dynamic mass component is estimated from ECCOv4r4. It contributes to the general spatial (and temporal) variability of the Arctic Ocean. Dynamic changes are associated with Arctic Oscillation and is not necessarily a climate change signal.
5. The 1995-2015 sea level trend is explained within the uncertainty in 98% of the Arctic and at 11 out of 12 utilized tide gauges. However, large uncertainties in the steric and dynamic mass component contributes to the result. Large differences with altimetry are evident in particular in the Beaufort Gyre and Siberian Seas.

On basis of this research, and in particular from the third paper, is it clear that many of the observations and models are showing large uncertainties, mainly due to poor and inconsistent data from remote sensing and hydrographi T/S profiles that are difficult to validate. From the objective of understanding both temporal and spatial sea level change of the Arctic Ocean Sea, I list the following recommendations for future work:

1. Steric sea level from interpolated T/S has proven to be a good product that resembles the major spatial patterns of sea level change in the Arctic Ocean. Integrating satellite surface temperatures and salinity data (from SMOS), should improve the observed trends. Validating against models from latest release of ECCO (NASA JPL), GECCO (University of Hamburg) or EN4 (British Met Office), could further constrain the results of the 4D gridded temperature and salinity dataset used for steric calculations in DTU Steric.
2. Sea level observations from satellites are in constant development. The launch of IceSAT-2 and the upcoming Surface Water and Ocean Topography (SWOT)-mission significantly improves the spatial resolution of altimetric observations in the Arctic and should improve future versions of absolute sea level products from altimetry.
3. The calculated elastic mass component and VLM is not obtained by solving the sea level equation, which would also include the viscoelastic part of present-day ice loading change. Applying models of LIA-deglaciation and 3D-earth models could further help separate PDIL from past changes. Recent work by Shijie Zhong (CU Boulder, yet unpublished) significantly improved the computational workload needed to utilize high resolution 3D-models, which lightens the computational workload required. Applying the method by Caron et al. (2018) to create an statistical best-fit from multiple runs with different 3D-earth models, could be a way to constrain all available data.
4. The mass and VLM predictions did not include the effect of terrestrial water storage (TWS), which has limited effect in the Arctic, but is the largest land-to-ocean mass flux in mid and low-latitudes. TWS-estimates from GRACE could be used for the purpose of creating global predictions of VLM and mass-fingerprint.
5. If, in particular the steric contribution to sea level is improved, a complete Arctic sea

level budget assessment should include temporal variations. This would enable the possibility of accurately estimate freshwater in and outflow of the Arctic Ocean. Predicting the freshwater contribution that goes into the North Atlantic is important for predicting the behaviour of the Atlantic meridional overturning circulation (AMOC) and thus influences the Earth's climate system.

6. Analysis of Arctic Ocean wind-dynamics could constrain estimates of the dynamic mass contribution and thus improve a sea level budget assessment of the Arctic Ocean.

References

- Altamimi, Z., Collilieux, X., and Métivier, L. (2011). Itrf2008: an improved solution of the international terrestrial reference frame. *Journal of Geodesy*, 85(8):457–473.
- Amante, C. and Eakins, B. W. (2009). ETOPO1 Global Relief Model converted to PanMap layer format.
- AMAP (1998). *AMAP Assessment report: Artic pollution issues*. Norwegian Radiation Protection Authority,.
- Andersen, O. and Scharroo, R. (2011). *Range and geophysical corrections in coastal regions: and implications for mean sea surface determination*, pages 103–146. Springer.
- Armitage, T. W. K., Bacon, S., and Kwok, R. (2018). Arctic sea level and surface circulation response to the arctic oscillation. *Geophysical Research Letters*, 45(13):6576–6584.
- Armitage, T. W. K., Bacon, S., Ridout, A. L., Thomas, S. F., Aksenov, Y., and Wingham, D. J. (2016). Arctic sea surface height variability and change from satellite radar altimetry and grace, 2003–2014. *Journal of Geophysical Research: Oceans*, 121(6):4303–4322.
- Armitage, T. W. K. and Davidson, M. W. J. (2014). Using the interferometric capabilities of the esa cryosat-2 mission to improve the accuracy of sea ice freeboard retrievals. *IEEE Transactions on Geoscience and Remote Sensing*, 52(1):529–536.
- Bamber, J. and Riva, R. (2010). The sea level fingerprint of recent ice mass fluxes. *The Cryosphere*, 4(4):621–627.
- Barletta, V. R., Bevis, M., Smith, B. E., Wilson, T., Brown, A., Bordoni, A., Willis, M., Khan, S. A., Rovira-Navarro, M., Dalziel, I., Smalley, R., Kendrick, E., Konfal, S., Caccamise, D. J., Aster, R. C., Nyblade, A., and Wiens, D. A. (2018). Observed rapid bedrock uplift in amundsen sea embayment promotes ice-sheet stability. *Science*, 360(6395):1335–1339.
- Behrendt, A., Sumata, H., Rabe, B., and Schauer, U. (2017). A comprehensive, quality-controlled and up-to-date data set of temperature and salinity data for the Arctic Mediterranean Sea (Version 1.0), links to data files. Supplement to: Behrendt, A et al. (2017): UDASH - Unified Database for Arctic and Subarctic Hydrography. Earth System Science Data Discussions, 37 pp, <https://doi.org/10.5194/essd-2017-92>.
- Brown, G. (1977). The average impulse response of a rough surface and its applications. *IEEE Transactions on Antennas and Propagation*, 25(1):67–74.
- Calafat, F. M., Chambers, D. P., and Tsimplis, M. N. (2012). Mechanisms of decadal sea level variability in the eastern north atlantic and the mediterranean sea. *Journal of Geophysical Research: Oceans*, 117(C9).
- Caron, L., Ivins, E. R., Larour, E., Adhikari, S., Nilsson, J., and Blewitt, G. (2018). Gia model statistics for grace hydrology, cryosphere, and ocean science. *Geophysical Research Letters*, 45(5):2203–2212.
- Carret, A., Johannessen, J. A., Andersen, O. B., Ablain, M., Prandi, P., Blazquez, A., and Cazenave, A. (2017). Arctic sea level during the satellite altimetry era. *Surveys in Geophysics*, 38(1):251–275.

- Chen, J. L., Wilson, C. R., and Tapley, B. D. (2006). Satellite gravity measurements confirm accelerated melting of greenland ice sheet. *Science*, 313(5795):1958–1960.
- Cheng, Y., Andersen, O., and Knudsen, P. (2015). An improved 20-year arctic ocean altimetric sea level data record. *Marine Geodesy*, 38(2):146–162.
- Church, J. A. and White, N. J. (2011). Sea-level rise from the late 19th to the early 21st century. *Surveys in Geophysics*, 32(4):585–602.
- Ciraci, E., Velicogna, I., and Sutterley, T. C. (2018). Mass balance of novaya zemlya archipelago, russian high arctic, using time-variable gravity from grace and altimetry data from icesat and cryosat-2. *Remote Sensing*, 10(11).
- Clark, J. A. and Lingle, C. S. (1977). Future sea-level changes due to west antarctic ice sheet fluctuations. *Nature*, 269(5625):206–209.
- Cohen, J., Zhang, X., Francis, J., Jung, T., Kwok, R., Overland, J., Ballinger, T. J., Bhatt, U. S., Chen, H. W., Coumou, D., Feldstein, S., Gu, H., Handorf, D., Henderson, G., Ionita, M., Kretschmer, M., Laliberte, F., Lee, S., Linderholm, H. W., Maslowski, W., Peings, Y., Pfeiffer, K., Rigor, I., Semmler, T., Stroeve, J., Taylor, P. C., Vavrus, S., Vihma, T., Wang, S., Wendisch, M., Wu, Y., and Yoon, J. (2020). Divergent consensus on arctic amplification influence on midlatitude severe winter weather. *Nature Climate Change*, 10(1):20–29.
- Dangendorf, S., Calafat, F. M., Arns, A., Wahl, T., Haigh, I. D., and Jensen, J. (2014). Mean sea level variability in the north sea: Processes and implications. *Journal of Geophysical Research: Oceans*, 119(10).
- Dong, D., Yunck, T., and Heflin, M. (2003). Origin of the international terrestrial reference frame. *Journal of Geophysical Research: Solid Earth*, 108(B4).
- Dziewonski, A. M. and Anderson, D. L. (1981). Preliminary reference earth model. *Physics of the Earth and Planetary Interiors*, 25(4):297 – 356.
- Ewert, H., Groh, A., and Dietrich, R. (2012). Volume and mass changes of the Greenland ice sheet inferred from ICESat and GRACE. *Journal of Geodynamics*, 59-60:111–123.
- Farrell, W. E. (1972). Deformation of the earth by surface loads. *Reviews of Geophysics*, 10(3):761–797.
- Farrell, W. E. and Clark, J. A. (1976). On postglacial sea level. *Geophysical Journal of the Royal Astronomical Society*, 46(3):647–667.
- Fasullo, J. T. and Nerem, R. S. (2018). Altimeter-era emergence of the patterns of forced sea-level rise in climate models and implications for the future. *Proceedings of the National Academy of Sciences*, 115(51):12944–12949.
- Foresta, L., Gourmelen, N., Pálsson, F., Nienow, P., Björnsson, H., and Shepherd, A. (2016). Surface elevation change and mass balance of icelandic ice caps derived from swath mode cryosat-2 altimetry. *Geophysical Research Letters*, 43(23):12,138–12,145.
- Forget, G., Campin, J.-M., Heimbach, P., Hill, C. N., Ponte, R. M., and Wunsch, C. (2015). Ecco version 4: an integrated framework for non-linear inverse modeling and global ocean state estimation. *Geoscientific Model Development*, 8(10):3071–3104.
- Frederikse, T., Jevrejeva, S., Riva, R., and Dangendorf, S. (2018). A consistent sea-level reconstruction and its budget on basin and global scales over 1958-2014. *Journal of Climate*, 31(3):1267–1280. cited By 12.

- Frederikse, T., Landerer, F. W., and Caron, L. (2019). The imprints of contemporary mass redistribution on local sea level and vertical land motion observations. *Solid Earth*, 10(6):1971–1987.
- Fukumori, I., Wang, O., Fenty, I., Forget, G., Heimbach, P., and Ponte, R. M. (2019). Ecco version 4 release 4 dataset. Accessed: 2020-06-25.
- Giles, K. A., Laxon, S. W., Ridout, A. L., Wingham, D. J., and Bacon, S. (2012). Western arctic ocean freshwater storage increased by wind-driven spin-up of the beaufort gyre. *Nature Geoscience*, 5(3):194–197.
- Gill, A. and Niller, P. (1973). The theory of the seasonal variability in the ocean. *Deep Sea Research and Oceanographic Abstracts*, 20(2):141 – 177.
- Gregory, J. M., Griffies, S. M., Hughes, C. W., Lowe, J. A., Church, J. A., Fukimori, I., Gomez, N., Kopp, R. E., Landerer, F., Cozannet, G. L., Ponte, R. M., Stammer, D., Tamisiea, M. E., and van de Wal, R. S. W. (2019). Concepts and terminology for sea level: Mean, variability and change, both local and global. *Surveys in Geophysics*, 40(6):1251–1289.
- Hay, C. C., Lau, H. C. P., Gomez, N., Austermann, J., Powell, E., Mitrovica, J. X., Latychev, K., and Wiens, D. A. (2017). Sea level fingerprints in a region of complex earth structure: The case of wais. *Journal of Climate*, 30(6):1881–1892.
- Hayne, G. (1980). Radar altimeter mean return waveforms from near-normal-incidence ocean surface scattering. *IEEE Transactions on Antennas and Propagation*, 28(5):687–692.
- Helm, V., Humbert, A., and Miller, H. (2014). Elevation and elevation change of greenland and antarctica derived from cryosat-2. *The Cryosphere*, 8(4):1539–1559.
- Henry, O., Prandi, P., Llovel, W., Cazenave, A., Jevrejeva, S., Stammer, D., Meyssignac, B., and Koldunov, N. (2012). Tide gauge-based sea level variations since 1950 along the norwegian and russian coasts of the arctic ocean: Contribution of the steric and mass components. *Journal of Geophysical Research: Oceans*, 117(C6).
- Holgate, S. J., Matthews, A., Woodworth, P. L., Rickards, L. J., Tamisiea, M. E., Bradshaw, E., Foden, P. R., Gordon, K. M., Jevrejeva, S., and Pugh, J. (2012). New Data Systems and Products at the Permanent Service for Mean Sea Level. *Journal of Coastal Research*, 29(3):493–504.
- Jakobsson, M., Mayer, L., Coakley, B., Dowdeswell, J. A., Forbes, S., Fridman, B., Hodnesdal, H., Noormets, R., Pedersen, R., Rebesco, M., Schenke, H. W., Zarayskaya, Y., Accettella, D., Armstrong, A., Anderson, R. M., Bienhoff, P., Camerlenghi, A., Church, I., Edwards, M., Gardner, J. V., Hall, J. K., Hell, B., Hestvik, O., Kristoffersen, Y., Marcussen, C., Mohammad, R., Mosher, D., Nghiem, S. V., Pedrosa, M. T., Travaglini, P. G., and Weatherall, P. (2012). The international bathymetric chart of the arctic ocean (ibcao) version 3.0. *Geophysical Research Letters*, 39(12).
- James, R. H., Bousquet, P., Bussmann, I., Haeckel, M., Kipfer, R., Leifer, I., Niemann, H., Ostrovsky, I., Piskozub, J., Rehder, G., Treude, T., Vielstädte, L., and Greinert, J. (2016). Effects of climate change on methane emissions from seafloor sediments in the arctic ocean: A review. *Limnology and Oceanography*, 61(S1):S283–S299.
- Khan, S., Kjeldsen, K., Kjær, K., Bevan, S., Luckman, A., Aschwanden, A., Bjørk, A., Korsgaard, N., Box, J., van den Broeke, M., van Dam, T., and Fitzner, A. (2014). Glacier

dynamics at helheim and kangerdlugssuaq glaciers, southeast greenland, since the little ice age. *Cryosphere*, 8:1497–1507. CC Attribution 3.0 License.

- Khan, S. A., Liu, L., Wahr, J., Howat, I., Joughin, I., Dam, T. v., and Fleming, K. (2010). GPS measurements of crustal uplift near Jakobshavn Isbræ due to glacial ice mass loss. *Journal of Geophysical Research: Solid Earth (1978–2012)*, 115(B9).
- King, M. A., Keshin, M., Whitehouse, P. L., Thomas, I. D., Milne, G., and Riva, R. E. M. (2012). Regional biases in absolute sea-level estimates from tide gauge data due to residual unmodeled vertical land movement. *Geophysical Research Letters*, 39(14).
- King, M. A. and Watson, C. S. (2014). Geodetic vertical velocities affected by recent rapid changes in polar motion. *Geophysical Journal International*, 199(2):1161–1165.
- Kjeldsen, K. K., Khan, S. A., Wahr, J., Korsgaard, N. J., Kjær, K. H., Bjørk, A. A., Hurkmans, R., van den Broeke, M. R., Bamber, J. L., and van Angelen, J. H. (2013). Improved ice loss estimate of the northwestern greenland ice sheet. *Journal of Geophysical Research: Solid Earth*, 118(2):698–708.
- Krabill, W. B. (2011). Icebridge atm l2 icesn elevation, slope, and roughness, [1993–2012]. Boulder, Colorado: NASA Distributed Active Archive Center at the National Snow and Ice Data Center.
- Kustowski, B., Dziewoński, A. M., and Ekström, G. (2007). Nonlinear Crustal Corrections for Normal-Mode Seismograms. *Bulletin of the Seismological Society of America*, 97(5):1756–1762.
- Ludwigsen, C., Khan, S. A., Andersen, O. B., and Marzeion, B. (2020a). Vertical land motion from present-day deglaciation in the wider arctic. *Earth and Space Science Open Archive*, page 18.
- Ludwigsen, C. A. and Andersen, O. B. (2020). Contributions to arctic sea level from 2003 to 2015. *Advances in Space Research*.
- Ludwigsen, C. A., Andersen, O. B., Khan, S. A., and Marzeion, B. (2020b). Arctic Vertical Land Motion (5x5 km).
- Luthcke, S. B., Sabaka, T., Loomis, B., Arendt, A., McCarthy, J., and Camp, J. (2013). Antarctica, greenland and gulf of alaska land-ice evolution from an iterated grace global mascon solution. *Journal of Glaciology*, 59(216):613–631.
- Martin, T., Steele, M., and Zhang, J. (2014). Seasonality and long-term trend of arctic ocean surface stress in a model. *Journal of Geophysical Research: Oceans*, 119(3):1723–1738.
- Marzeion, B., Jarosch, A. H., and Hofer, M. (2012). Past and future sea-level change from the surface mass balance of glaciers. *The Cryosphere*, 6(6):1295–1322.
- Melini, D., Spada, G., Gegout, P., and King, M. (2015). Rear: a regional elastic rebound calculator. user manual for version 1.0, available on–line at: <http://hpc.rm.ingv.it/rear>.
- Meredith, M., Sommerkorn, M., Cassotta, S., Derksen, C., Ekaykin, A., Hollowed, A., Kofinas, G., Mackintosh, A., Melbourne-Thomas, J., Muelbert, M., Ottersen, G., Pritchard, H., and A.G., S. (2019). *Chapter 3: Polar Regions. IPCC Special Report on the Ocean and Cryosphere in a Changing Climate*.
- Milne, G. A. and Mitrovica, J. X. (1996). Postglacial sea-level change on a rotating Earth:

- first results from a gravitationally self-consistent sea-level equation. *Geophysical Journal International*, 126(3):F13–F20.
- Milne, G. A. and Mitrovica, J. X. (1998). Postglacial sea-level change on a rotating Earth. *Geophysical Journal International*, 133(1):1–19.
- Moon, T., Ahlstrøm, A., Goelzer, H., Lipscomb, W., and Nowicki, S. (2018). Rising oceans guaranteed: Arctic land ice loss and sea level rise. *Current Climate Change Reports*, 4(3):211–222.
- Morison, J., Kwok, R., Peralta-Ferriz, C., Alkire, M., Rigor, I., Andersen, R., and Steele, M. (2012). Changing arctic ocean freshwater pathways. *Nature*, 481(7379):66–70.
- Naeije, M., Schrama, E., and Scharroo, R. (2000). The radar altimeter database system project rads. 2:487 – 490 vol.2.
- NASA Jet Propulsion Laboratory (2020). Greenland ice loss 2002-2016. <https://gracefo.jpl.nasa.gov/resources/33/greenland-ice-loss-2002-2016/>.
- Nerem, R. S., Beckley, B. D., Fasullo, J. T., Hamlington, B. D., Masters, D., and Mitchum, G. T. (2018). Climate-change–driven accelerated sea-level rise detected in the altimeter era. *Proceedings of the National Academy of Sciences*, 115(9):2022–2025.
- Nuth, C., Moholdt, G., Kohler, J., Hagen, J. O., and Kääh, A. (2010). Svalbard glacier elevation changes and contribution to sea level rise. *Journal of Geophysical Research: Earth Surface*, 115(F1).
- Onarheim, I. H., Eldevik, T., Smedsrud, L. H., and Stroeve, J. C. (2018). Seasonal and Regional Manifestation of Arctic Sea Ice Loss. *Journal of Climate*, 31(12):4917–4932.
- Osadchiev, A. A., Pisareva, M. N., Spivak, E. A., Shchuka, S. A., and Semiletov, I. P. (2020). Freshwater transport between the kara, laptev, and east-siberian seas. *Scientific Reports*, 10(1):13041.
- Passaro, M., Nadzir, Z. A., and Quartly, G. D. (2018). Improving the precision of sea level data from satellite altimetry with high-frequency and regional sea state bias corrections. *Remote Sensing of Environment*, 218:245 – 254.
- Peacock, N. R. and Laxon, S. W. (2004). Sea surface height determination in the arctic ocean from ers altimetry. *Journal of Geophysical Research: Oceans*, 109(C7).
- Peltier, W. R. (1974). The impulse response of a maxwell earth. *Reviews of Geophysics*, 12(4):649–669.
- Peltier, W. R., Argus, D. F., and Drummond, R. (2015). Space geodesy constrains ice age terminal deglaciation: The global ice-6g_c (vm5a) model. *Journal of Geophysical Research: Solid Earth*, 120(1):450–487.
- Peltier, W. R., Argus, D. F., and Drummond, R. (2018). Comment on "An Assessment of the ICE-6G_C (VM5a) Glacial Isostatic Adjustment Model" by Purcell et al. *Journal of Geophysical Research (Solid Earth)*, 123(2):2019–2028.
- Pistone, K., Eisenman, I., and Ramanathan, V. (2019). Radiative heating of an ice-free arctic ocean. *Geophysical Research Letters*, 46(13):7474–7480.
- Povalishnikova, E. S., Frolova, N. L., Kireeva, M. B., Magritsky, D. V., Evstigneev, V. M., and Pakhomova, O. M. (2018). Long-term changes of river water inflow into the seas of the russian arctic sector, polarforschung. *Polarforschung*, 87(2):177–194.

- Powell, E., Gomez, N., Hay, C., Letychev, K., and Mitrovica, J. X. (2019). Viscous Effects in the Solid Earth Response to Modern Antarctic Ice Mass Flux: Implications for Geodetic Studies of WAIS Stability in a Warming World. *Journal of Climate*, 33(2):443–459.
- Prandi, P., Ablain, M., Cazenave, A., and Picot, N. (2012). A new estimation of mean sea level in the arctic ocean from satellite altimetry. *Marine Geodesy*, 35(sup1):61–81.
- Proshutinsky, A., Ashik, I. M., Dvorkin, E. N., Häkkinen, S., Krishfield, R. A., and Peltier, W. R. (2004). Secular sea level change in the russian sector of the arctic ocean. *Journal of Geophysical Research: Oceans*, 109(C3).
- Proshutinsky, A., Krishfield, R., Timmermans, M.-L., Toole, J., Carmack, E., McLaughlin, F., Williams, W. J., Zimmermann, S., Itoh, M., and Shimada, K. (2009). Beaufort gyre freshwater reservoir: State and variability from observations. *Journal of Geophysical Research: Oceans*, 114(C1).
- Quarty, G. D., Rinne, E., Passaro, M., Andersen, O. B., Dinardo, S., Fleury, S., Guillot, A., Hendricks, S., Kurekin, A. A., Müller, F. L., and et al. (2019). Retrieving sea level and freeboard in the arctic: A review of current radar altimetry methodologies and future perspectives. *Remote Sensing*, 11(7):881.
- Raj, R. P., Andersen, O. B., Johannessen, J. A., Gutknecht, B. D., Chatterjee, S., Rose, S. K., Bonaduce, A., Horwath, M., Ranndal, H., Richter, K., Palanisamy, H., Ludwigsen, C. A., Bertino, L., Nilsen, J. E. □., Knudsen, P., Hogg, A., Cazenave, A., and Benveniste, J. (2020). Arctic sea level budget assessment during the grace/argo time period. *Remote Sensing*, 12(17).
- Raney, R. K. (1998). The delay/doppler radar altimeter. *IEEE Transactions on Geoscience and Remote Sensing*, 36(5):1578–1588.
- Raney, R. K. (2012). Cryosat sar-mode looks revisited. *IEEE Geoscience and Remote Sensing Letters*, 9:393–397.
- Regan, H. C., Lique, C., and Armitage, T. W. K. (2019). The beaufort gyre extent, shape, and location between 2003 and 2014 from satellite observations. *Journal of Geophysical Research: Oceans*, 124(2):844–862.
- RGI Consortium (2017). Randolph Glacier Inventory – A Dataset of Global Glacier Outlines: Version 6.0: Technical Report. <https://doi.org/10.7265/N5-RGI-60>.
- Richter-Menge, J., Overland, J., Mathis, J., and Osborne, E. (2017). Arctic report card 2017.
- Riva, E., Frederikse, T., King, A., Marzeion, B., and Van Den Broeke, R. (2017). Brief communication: The global signature of post-1900 land ice wastage on vertical land motion. *Cryosphere*, 11(3):1327–1332. cited By 11.
- Roquet, F., Madec, G., McDougall, T. J., and Barker, P. M. (2015). Accurate polynomial expressions for the density and specific volume of seawater using the teos-10 standard. *Ocean Modelling*, 90:29 – 43.
- Rose, S. K., Andersen, O., Passaro, M., Ludwigsen, C., and Schwatke, C. (2019). Arctic ocean sea level record from the complete radar altimetry era: 1991-2018. *Remote Sensing*, 11(14).
- Santamaría-Gómez, A., Gravelle, M., Dangendorf, S., Marcos, M., Spada, G., and Wöp-

- pelmann, G. (2017a). Uncertainty of the 20th century sea-level rise due to vertical land motion errors. *Earth and Planetary Science Letters*, 473:24 – 32.
- Santamaría-Gómez, A., Gravelle, M., Dangendorf, S., Marcos, M., Spada, G., and Wöpelmann, G. (2017b). Uncertainty of the 20th century sea-level rise due to vertical land motion errors. *Earth and Planetary Science Letters*, 473:24 – 32.
- Save, H., Bettadpur, S., and Tapley, B. D. (2016). High-resolution csr grace rl05 mascons. *Journal of Geophysical Research: Solid Earth*, 121(10):7547–7569.
- Scharroo, R., Leuliette, E., Lillibridge, J., Byrne, D., Naeije, M., and Mitchum, G. (2013). RADS: Consistent Multi-Mission Products. 710:69.
- Schröder, L., Horwath, M., Dietrich, R., Helm, V., van den Broeke, M. R., and Ligtenberg, S. R. M. (2019). Four decades of antarctic surface elevation changes from multi-mission satellite altimetry. *The Cryosphere*, 13(2):427–449.
- Schumacher, M., King, M., Rougier, J., Sha, Z., Khan, S. A., and Bamber, J. (2018). A new global gps data set for testing and improving modelled glacial uplift rates. *Geophysical Journal International*, 214(3):2164–2176. cited By 5.
- Shepherd, A., Ivins, E., Rignot, E., Smith, B., van den Broeke, M., Velicogna, I., Whitehouse, P., Briggs, K., Joughin, I., Krinner, G., Nowicki, S., Payne, T., Scambos, T., Schlegel, N., A. G., Agosta, C., Ahlstrøm, A., Babonis, G., Barletta, V., Blazquez, A., Bonin, J., Csatho, B., Cullather, R., Felikson, D., Fettweis, X., Forsberg, R., Gallee, H., Gardner, A., Gilbert, L., Groh, A., Gunter, B., Hanna, E., Harig, C., Helm, V., Horwath, A., Horwath, M., Khan, S. A., K. Kjeldsen, K., Konrad, H., Langen, P., Lecavalier, B., Loomis, B., Luthcke, S., McMillan, M., Melini, D., Mernild, S., Mohajerani, Y., Moore, P., Mouginit, J., Moyano, G., Muir, A., Nagler, T., Nield, G., Nilsson, J., Noel, B., Otosaka, I., E. Pattle, M., Peltier, W., Pie, N., Rietbroek, R., Rott, H., Sandberg-Sørensen, L., Sasgen, I., Save, H., Scheuchl, B., Schrama, E., Schröder, L., Seo, K.-W., Simonsen, S., Slater, T., Spada, G., Sutterley, T., Talpe, M., Tarasov, L., van de Berg, W., van der Wal, W., van Wessem, M., Dutt Vishwakarma, B., Wiese, D., and Wouters, B. (2018). Mass balance of the antarctic ice sheet from 1992 to 2017. *Nature*, 558(7709):219–222.
- Smith, B. E., Fricker, H. A., Joughin, I. R., and Tulaczyk, S. (2009). An inventory of active subglacial lakes in antarctica detected by icesat (2003–2008). *Journal of Glaciology*, 55(192):573–595.
- Spada, G. (2017). Glacial isostatic adjustment and contemporary sea level rise: An overview. *Surveys in Geophysics*, 38(1):153–185.
- Stammer, D. (1997). Steric and wind-induced changes in topex/poseidon large-scale sea surface topography observations. *Journal of Geophysical Research: Oceans*, 102(C9):20987–21009.
- Stroeve, J. and Notz, D. (2018). Changing state of arctic sea ice across all seasons. *Environmental Research Letters*, 13(10):103001.
- Stuecker, M. F., Bitz, C. M., Armour, K. C., Proistosescu, C., Kang, S. M., Xie, S.-P., Kim, D., McGregor, S., Zhang, W., Zhao, S., Cai, W., Dong, Y., and Jin, F.-F. (2018). Polar amplification dominated by local forcing and feedbacks. *Nature Climate Change*, 8(12):1076–1081.
- Tapley, B. D., Bettadpur, S., Watkins, M., and Reigber, C. (2004). The gravity recovery

- and climate experiment: Mission overview and early results. *Geophysical Research Letters*, 31(9).
- Thompson, D. W. J. and Wallace, J. M. (1998). The arctic oscillation signature in the wintertime geopotential height and temperature fields. *Geophysical Research Letters*, 25(9):1297–1300.
- Tilling, R. L., Ridout, A., and Shepherd, A. (2018). Estimating arctic sea ice thickness and volume using cryosat-2 radar altimeter data. *Advances in Space Research*, 62(6):1203 – 1225. The CryoSat Satellite Altimetry Mission: Eight Years of Scientific Exploitation.
- van Dam, T., Collilieux, X., Wuite, J., Altamimi, Z., and Ray, J. (2012). Nontidal ocean loading: amplitudes and potential effects in gps height time series. *Journal of Geodesy*, 86(11):1043–1057.
- Veng, T. and Andersen, O. (2020). Consolidating sea level acceleration estimates from satellite altimetry. *Advances in Space Research*.
- Wake, L. M., Lecavalier, B. S., and Bevis, M. (2016). Glacial isostatic adjustment (gia) in greenland: a review. *Current Climate Change Reports*, 2(3):101–111.
- Wallace, J. M. and Gutzler, D. S. (1981). Teleconnections in the Geopotential Height Field during the Northern Hemisphere Winter. *Monthly Weather Review*, 109(4):784–812.
- Watanabe, E. and Hasumi, H. (2005). Arctic sea ice response to wind stress variations. *Journal of Geophysical Research: Oceans*, 110(C11).
- Watkins, M. M., Wiese, D. N., Yuan, D.-N., Boening, C., and Landerer, F. W. (2015). Improved methods for observing earth’s time variable mass distribution with grace using spherical cap mascons. *Journal of Geophysical Research: Solid Earth*, 120(4):2648–2671.
- WCRP, G. S. L. B. G. (2018). Global sea-level budget 1993–present. *Earth System Science Data*, 10(3):1551–1590.
- Whitehouse, P. L., Allen, M. B., and Milne, G. A. (2007). Glacial isostatic adjustment as a control on coastal processes: An example from the Siberian Arctic. *Geology*, 35(8):747–750.
- Wiese, D. N., Landerer, F. W., and Watkins, M. M. (2016). Quantifying and reducing leakage errors in the jpl rl05m grace mascon solution. *Water Resources Research*, 52(9):7490–7502.
- Wingham, D., Francis, C., Baker, S., Bouzinac, C., Brockley, D., Cullen, R., de Chateau-Thierry, P., Laxon, S., Mallow, U., Mavrocordatos, C., Phalippou, L., Ratier, G., Rey, L., Rostan, F., Viau, P., and Wallis, D. (2006). Cryosat: A mission to determine the fluctuations in earth’s land and marine ice fields. *Advances in Space Research*, 37(4):841–871. cited By 298.
- WMO (2020). Reported new record temperature of 38c north of arctic circle.
- Wouters, B., Gardner, A. S., and Moholdt, G. (2019). Global glacier mass loss during the grace satellite mission (2002-2016). *Frontiers in Earth Science*, 7:96.
- Wu, X., Ray, J., and Van Dam, T. (2012). Geocenter motion and its geodetic and geophysical implications. *Journal of Geodynamics*, 58:44–61.

- Wöppelmann, G., Letetrel, C., Santamaria, A., Bouin, M.-N., Collilieux, X., Altamimi, Z., Williams, S., and Martin Miguez, B. (2009). Rates of sea-level change over the past century in a geocentric reference frame. *Geophysical Research Letters*, 36(12). cited By 130.
- Wöppelmann, G., Martin Miguez, B., Bouin, M.-N., and Altamimi, Z. (2007). Geocentric sea-level trend estimates from gps analyses at relevant tide gauges world-wide. *Global and Planetary Change*, 57(3):396 – 406.
- Zemp, M., Huss, M., Thibert, E., Eckert, N., McNabb, R., Huber, J., Barandun, M., Machguth, H., Nussbaumer, S. U., Gärtner-Roer, I., Thomson, L., Paul, F., Maussion, F., Kutuzov, S., and Cogley, J. G. (2019). Global glacier mass changes and their contributions to sea-level rise from 1961 to 2016. *Nature*, 568(7752):382–386.
- Zwally, H. J., Schutz, R., Bentley, C., Buffon, J., Herring, T., Minster, J., Spinhirne, J., and Thomas, R. (2011). *Glaciersat I2 antarctic and greenland ice sheet altimetry data v031*. Boulder, Colorado: NASA Distributed Active Archive Center at the National Snow and Ice Data Center.

Technical
University of
Denmark

Elektrovej, Building 328
2800 Kgs. Lyngby
Tlf. 4525 1700

www.space.dtu.dk